
Transient Nuclear Criticality Analysis of Aqueous Fissile Solutions Using Point Nuclear Reactor Kinetics and Phenomenological Thermal-Hydraulic Feedback Models

Academic Supervisors:

Dr Matthew Eaton

Dr Michael Bluck

Industrial Supervisor:

Mr Chris Ryden

Author:

George Edward Winter

Department of Mechanical Engineering

A thesis submitted in partial fulfilment of the requirements for the degree of Doctor of Philosophy
and the Diploma of Imperial College London

November 2019

Authorship Declaration

I hereby certify that this thesis has been composed solely by myself and that its contents are my own original work, except where otherwise indicated by reference or acknowledgement. Any use of works by any other author is properly acknowledged at the point of use.

George Edward Winter

Copyright Notice

The copyright of this thesis rests with the author. Unless otherwise indicated, its contents are licensed under a Creative Commons Attribution-Non Commercial 4.0 International Licence (CC BY-NC).

Under this licence, you may copy and redistribute the material in any medium or format. You may also create and distribute modified versions of the work. This is on the condition that: you credit the author and do not use it, or any derivative works, for a commercial purpose.

When reusing or sharing this work, ensure you make the licence terms clear to others by naming the licence and linking to the licence text. Where a work has been adapted, you should indicate that the work has been changed and describe those changes.

Please seek permission from the copyright holder for uses of this work that are not included in this licence or permitted under UK Copyright Law.

Acknowledgements

I would like to thank my academic supervisors Dr Matthew Eaton and Dr Mike Bluck, as well as my industrial supervisor Mr Chris Ryden, for their help and support throughout my PhD. I would also like to thank Dr Chris Cooling and Emeritus Prof M.M.R. Williams for their invaluable advice and guidance. I would like to acknowledge the financial support of the Engineering and Physical Sciences Research Council (EPSRC) and AWE plc through an Industrial CASE studentship.

Abstract

This thesis presents a range of mathematical and computational models for use in transient nuclear criticality safety assessment. A mathematical model for quantifying the uncertainty in the wait-time probability distributions of criticality excursions initiated in the presence of weak intrinsic neutron sources is presented. This model is used to demonstrate the potential influence of parametric uncertainty on the wait-time probability distributions of the 1958 Y-12 criticality accident and experiments on the Caliban reactor.

Also presented in this thesis is a new mathematical and computational model of radiolytic gas production and evolution in fissile liquids. This model has been validated against nuclear criticality safety benchmark experiments on fissile solution reactors and has been shown to accurately predict features of the fission power profiles related to the appearance and advection of radiolytic gas voids in the solution. The model has also demonstrated efficacy in predicting the timing and magnitude of secondary peaks in the fission power output. The purpose of this new mathematical and computational radiolytic gas model was to improve the simulation of fissile liquid criticality transients while removing the need for the adjustable heuristic parameters used by existing fissile liquid simulation codes. These parameters, which must be appropriately adjusted to criticality safety benchmark experiments, are dependent on the geometry and composition of the system being analysed. The need for these heuristic parameters therefore precludes the use of these codes as predictive modelling and simulation tools. The new mathematical and computational model, presented in this thesis, offers valuable insights into the behaviour of radiolytic gas in fissile liquid systems.

Contents

1 Introduction	37
1.1 Introduction to Criticality Accidents	37
1.1.1 Definition of Criticality	38
1.1.2 Examples of Criticality Accidents	40
1.1.2.1 1958 Accident at the Y-12 National Security Complex	40
1.1.2.2 1999 Accident at the JCO Fuel Fabrication Plant in Tokaimura	41
1.1.3 Need for Accurate Modelling	41
1.2 Predicting Criticality	42
1.2.1 The Neutron Transport Equation	43
1.2.2 Neutron Diffusion	44
1.2.3 Hand Calculation Methods	45
1.3 Transient Nuclear Reactor Kinetics of Fissile Solutions	47
1.3.1 Reactivity Feedbacks	47
1.3.2 Quasi-Steady-State Method	48
1.3.3 Deterministic Point Nuclear Reactor Kinetics	49
1.3.4 Stochastic Point Nuclear Reactor Kinetics	50
1.3.5 Current and Historical Codes used for Modelling and Simulating Transient Nuclear Criticality Excursions in Aqueous Fissile Solutions	52

2 Power Excursions in the Presence of a Weak Neutron Source	55
2.1 Introduction	55
2.1.1 Relative Strength of an Intrinsic Neutron Source	55
2.1.2 The Wait-Time	56
2.1.3 Methods for Predicting the Wait-Time Probability Distribution	57
2.1.4 Types of Uncertainty	58
2.1.5 Objectives	58
2.2 Methodology	59
2.2.1 Gamma Distribution Method	59
2.2.2 Saddlepoint Method	61
2.2.2.1 Method Overview	61
2.2.2.2 Finding the Value of z_0	62
2.2.3 Range of Applicability of the Gamma Distribution Method	63
2.2.3.1 Verification with Monte Carlo Simulation	67
2.2.4 Uncertainty Quantification	69
2.2.4.1 Types of Uncertainty	69
2.2.4.2 The Monte Carlo Code	69
2.2.4.3 Mean and Standard Deviation of the Distributions	71
2.3 Case Study I: The Y-12 Accident	71
2.3.1 Description of the Accident	72
2.3.2 Model Parameters	72
2.3.3 Parametric Uncertainty	74
2.3.4 Deterministic Wait-Time and Aleatoric Uncertainty	74
2.3.5 Parametric Uncertainty Quantification	75
2.3.6 Summary of Results	77

2.4 Case Study II: The Caliban Experiments	78
2.4.1 Description of the Experiments	78
2.4.2 Model Parameters	79
2.4.3 Parametric Uncertainty	80
2.4.4 Deterministic Wait-Time and Aleatoric Uncertainty	81
2.4.5 Parametric Uncertainty Quantification	81
2.4.5.1 Safety Block Manipulation Time	81
2.4.5.2 Delayed Neutron Precursor Yields	83
2.4.6 Summary of Results	83
2.4.7 Convergence of the Monte Carlo Method	84
2.5 Conclusions	85

3 Linear Energy Transfer (LET) of Fission Fragments of ^{235}U and Nucleation of Gas Bubbles in Aqueous Solutions of Uranyl Nitrate **87**

3.1 Introduction	87
3.1.1 Nucleation of Bubbles in Aqueous Fissile Solutions	87
3.1.2 Linear Energy Transfer of Charged Particles	90
3.2 Methodology and Data	91
3.2.1 Predicting the Size of Bubbles on Fission Tracks	92
3.2.1.1 Steam Bubbles Before Condensation	92
3.2.1.2 Gas Bubbles Remaining Following Steam Condensation	95
3.2.1.3 Experimental Basis	96
3.2.2 Predicting the Linear Energy Transfer of a Fission Fragment	99
3.2.3 Input Parameters	100
3.2.3.1 Enthalpy of Reaction	100
3.2.3.2 Fuel Solution Density	100

3.2.3.3 Fuel Solution Surface Tension	101
3.2.3.4 Enthalpy of Vaporisation	101
3.2.3.5 Radiolytic Gas Generation Coefficient	101
3.2.3.6 Adjustment of G_{H_2} for Fission Tracks	103
3.2.3.7 Henry's Law Constant	104
3.3 Results	104
3.3.1 Sensitivity of Nucleation Bubble Radius to Solution Properties	104
3.3.2 Empirical Correlation for the Gas Bubble Nucleation Radius as a Function of Solution Temperature and Particle LET	108
3.3.3 Predicted LET Profiles of Fission Fragments in Uranyl Nitrate	110
3.3.4 Bubble Size Distribution in Aqueous Fissile Solutions	112
3.3.5 Empirical Correlation for the Gas Bubble Nucleation Radius Based on the Maxi- mum LET of Fission Fragments in Uranyl Nitrate	114
3.3.6 Estimates of Uncertainty in the Bubble Nucleation Radius	115
3.3.6.1 Fission Track Length	115
3.3.6.2 Fission Fragment LET	116
3.3.6.3 Interpolation Error	117
3.4 Comparison of LET Profiles Calculated Using SRIM and the Tables of Northcliffe and Schilling	117
3.5 Conclusions	120

4 Phenomenological Model Simulating the Dynamics of Bubble Formation Along Fission Tracks and Saturation of a Fissile Solution with Dissolved Radiolytic Gas 123

4.1 Introduction	123
4.1.1 Radiochemical Considerations	124
4.1.2 Theories and Mathematical Models of Bubble Growth	126
4.1.3 Bubble Nucleation Sites	127

4.1.4 Existing Approaches to Radiolytic Gas Models in Point-Kinetics Calculations . .	128
4.2 A Numerical (Monte Carlo) Model of Bubble Nucleation	129
4.2.1 Concept and Overview	129
4.2.2 Point Kinetics Model	131
4.2.3 Initial Conditions	134
4.2.4 Advection	135
4.2.5 Bubble Growth and Collapse	136
4.2.6 Bubble Generation Due to Radiolysis	138
4.2.7 Mass Transfer of Hydrogen Within the Aqueous Solution	138
4.2.8 Solubility of Hydrogen in Aqueous Salt Solutions	139
4.2.9 Radiolytic Gas Generation Coefficient	142
4.2.10 A Note on System Reactivity and Feedback Coefficients	142
4.2.11 A Note on Convection, Coalescence and Break-Up	143
4.2.12 Algorithm Summary	143
4.3 Numerical Results	146
4.3.1 Power Density and Reactivity	146
4.3.2 Reactivity Feedback as a function of Total Energy	150
4.3.3 Formation of Stable Bubbles at Saturation	153
4.3.3.1 Number of Stable Bubbles Produced	157
4.3.3.2 A Model of Bubble Stability	158
4.3.3.3 Rate of Bubble Collapse	164
4.3.4 Bubble Growth and Size Distribution	166
4.3.5 Rate of Appearance of Radiolytic Gas Voids	170
4.3.6 Summary of Selected Data	174
4.4 Further Observations	177

4.4.1 Effects of Non-Uniform Spatial Distribution of Bubbles	177
4.4.2 Effects of Statistical Variation in the Monte Carlo Model	179
4.5 Conclusions	180

5 A Point Kinetics Model with Physical Representation of Bubble Formation, Growth and Removal 183

5.1 Model Description	184
5.1.1 Point Kinetics Equations and Flux Shape	185
5.1.2 Vertical Discretisation	185
5.1.3 Bubble Population and Size	186
5.1.3.1 Stable Bubble Formation	187
5.1.3.2 Mixing and Advection	187
5.1.3.3 Break Up and Coalescence	188
5.1.4 Dissolved Gas Production	190
5.1.5 Dissolved Gas Mass Transfer	192
5.1.6 Critical Concentration with Multiple Dissolved Gases	193
5.1.7 Bubble Velocity	195
5.1.8 Heat Loss	198
5.1.8.1 From the Reactor to the Surroundings	198
5.1.8.2 From the Fuel Solution to the Reactor Vessel	199
5.1.8.3 From the Fuel Solution Surface to the Plenum Gas	202
5.1.9 Mixing	204
5.1.10 Modelling the Addition of the Fuel to the Solution	205
5.1.11 Solubility of Dissolved Gases	206
5.1.12 Radiolytic Gas Generation Coefficient	206
5.1.13 Summary of Principal Governing Equations	206

5.2 Simulation of the SILENE S3-258 Experiment	209
5.2.1 Reactivity and Delayed Neutrons	209
5.2.2 Reactivity Feedback Coefficients	210
5.2.3 Intrinsic Neutron Source and Initiation Time	210
5.2.4 Summary of Inputs	211
5.2.5 Model Results	212
5.3 Simulation of the CRAC-29 Experiment	216
5.3.1 Delayed Neutrons and Reactivity	217
5.3.2 Void Feedback Coefficient	218
5.3.3 Thermal Feedback Coefficient	219
5.3.4 Summary of Inputs	221
5.3.5 Model Results	221
5.3.6 Sensitivity to the Mixing Coefficient	226
5.4 Simulation of the TRACY R76 Experiment	227
5.4.1 Reactivity and Delayed Neutrons	227
5.4.2 Reactivity Feedback Coefficients	228
5.4.3 Radiolytic Gas Generation Coefficients	229
5.4.4 Summary of Inputs	229
5.4.5 Model Results	229
5.5 Application to the Y-12 Accident	234
5.5.1 Methodology	234
5.5.2 Input Data	235
5.5.3 Results	236
5.5.3.1 Effects of Initiation Time	236
5.5.3.2 Predictions of the Radiolytic Gas Model	240

5.6 Conclusions	241
6 Conclusions and Future Work	243
6.1 Thesis Summary	243
6.2 Insights Gained	245
6.3 Future Work	246
A Solubility Unit Conversions	263
B Details of MCNP Inputs Used to Model the CRAC and TRACY Experimental Reactors	265
B.1 CRAC 300 mm	265
B.1.1 Geometry and Compositions	265
B.1.2 Thermal Feedback Coefficient	267
B.2 TRACY	267
B.2.1 Geometry and Compositions	267
C Estimating the Solubility of H₂ and O₂ in Solutions of Uranyl Nitrate	269
D A Note on Sloshing	275
E Density Correlation for Aqueous Solutions of Uranyl Nitrate	277

List of Figures

2.2.1 Comparison of mean wait-times and standard deviations predicted by the gamma and saddlepoint methods for a 0.7\$ reactivity step insertion over a range of intrinsic neutron source strengths.	64
2.2.2 Wait-time probability distributions predicted by the saddlepoint (dashed) and gamma distribution (solid) methods for reactivity step insertions of 0.1\$, 0.2\$, 0.3\$ and 0.5\$, with a neutron source strength of 30 n/s.	65
2.2.3 Wait-time probability distributions predicted by the saddlepoint (dashed) and gamma distribution (solid) methods for reactivity step insertions of 0.1\$ and 0.5\$, with a neutron source strength of 90 n/s.	66
2.2.4 Minimum source strengths required for the gamma distribution method to predict a mean wait-time within 2% of the value predicted by the saddlepoint method. Results shown for varying reactivity insertion rates and a constant prompt neutron lifetime of 45 μ s. The reactivity insertion rate is the total insertion size divided by the insertion time stated.	66
2.2.5 Minimum source strengths required for the gamma distribution method to predict a mean wait-time within 2% of the value predicted by the saddlepoint method. Results shown for a reactivity step insertion with a range of prompt neutron lifetimes.	67
2.2.6 Wait-time probability distributions predicted by the gamma distribution method, saddlepoint method and a Monte Carlo simulation (5,000 realisations), for a reactivity step insertion of 0.7\$ and neutron source strength of 90 n/s.	68
2.3.1 Reactivity as a function of time, showing maximum and minimum values corresponding to $\alpha=0.9$ and $\alpha=1.1$	75

2.3.2 Wait-time probability distributions for the time taken between reaching criticality and the fission rate exceeding 2×10^9 fissions per second in the Y-12 accident.	76
2.3.3 Wait-time probability distributions for the Y-12 accident comparing the deterministic wait-time with models including parametric uncertainty in the reactivity insertion rate, aleatoric uncertainty, and combined parametric-aleatoric uncertainty.	77
2.4.1 Photograph of the Caliban reactor. Reproduced from Authier et al. (2014) with permission of the rights holder, Taylor & Francis (www.tandfonline.com).	78
2.4.2 Wait-time probability distribution for a cumulative detector count corresponding to a fission rate of 2×10^9 fissions per second with prompt neutron lifetimes of 12 ns and 65 μ s.	80
2.4.3 Deterministic wait-time and aleatoric wait-time probability distributions for a cumulative detector count corresponding to a fission rate of 2×10^9 fissions per second in the Caliban experiment.	82
2.4.4 Wait-time probability distributions for the Caliban experiment comparing the deterministic wait-time with models including parametric uncertainty in the timing of the safety block movement, aleatoric uncertainty, and combined parametric-aleatoric uncertainty.	82
2.4.5 Wait-time probability distributions for the Caliban experiment comparing the deterministic wait-time with models including parametric uncertainty in the delayed neutron precursor group yields, aleatoric uncertainty, and combined parametric-aleatoric uncertainty.	83
2.4.6 Evolution of the mean and standard deviation of the aleatoric-parametric wait-time probability distribution and the parametric probability distribution, with increasing number of Monte Carlo realisations, for the Y-12 accident simulation. Points shown at intervals of 25 realisations.	85
3.2.1 Superheat required for nucleation of steam bubbles by fission fragments in water. Experimental results and model predictions of Deitrich and Connolly (1973) shown with values predicted using Equations 3.2.7 and 3.2.17.	96
3.2.2 Experimental data from Lane et al. (1958) showing G_{H_2} as a function of uranyl nitrate concentration with correlation based on Equation 3.2.26.	102
3.3.1 Radius of bubble nucleus as a function of fission fragment LET and solution temperature	105

3.3.2 Critical concentration of dissolved hydrogen gas as a function of fission fragment LET	106
3.3.3 Bubble nucleation radius and critical concentration of dissolved hydrogen gas as a function of solution temperature for a fission fragment with maximum LET of 8 MeV μm^{-1}	106
3.3.4 Bubble nucleation radius as a function of the radiolytic gas generation coefficient	107
3.3.5 Variation of predicted gas bubble radius with changing concentration of uranyl nitrate	108
3.3.6 Radius of bubble nucleus as a function of liquid pressure	108
3.3.7 LET profiles at 298K for pure water, calculated using data from SRIM for the stopping power of fission fragments with the 250 highest yields from fission of ^{235}U .	110
3.3.8 LET profiles at 298K for an aqueous solution containing 1000 mol m^{-3} of uranyl nitrate, calculated using data from SRIM for the stopping power of fission fragments with the 250 highest yields from fission of ^{235}U .	111
3.3.9 Predicted bubble radius as a function of the vapour track length	115
3.3.10 Predicted bubble radius at atmospheric pressure and 298K for a fission fragment LET of 8 MeV $\mu\text{m}^{-1} \pm 7.3\%$.	116
3.4.1 LET profiles at 298K for pure water, calculated using the tables of Northcliffe & Schilling and the software package SRIM.	118
3.4.2 LET profiles at 298K for a solution containing 1000 mol m^{-3} of uranyl nitrate, calculated using the tables of Northcliffe & Schilling and the software package SRIM.	119
4.2.1 Model of bubbles inside a small volume within a larger vessel of fissile solution.	130
4.2.2 Stokes' Law advection velocity as a function of bubble radius.	136
4.2.3 Henry's law constants for hydrogen gas in aqueous solutions of various salts Washburn (2003), Pray and Stephan (1953), Pray and Stephan (1954).	140
4.2.4 Henry's law constant for hydrogen gas in various salts over concentrations ranging from 0 to 2.0 mol dm^{-3} .	141
4.2.5 Flow diagram summarising the algorithm followed by the numerical simulation.	145
4.3.1 Simulated fission power profiles for the 2.0\$ step insertion case in the SOL-C fuel solution and the 3.5\$ step insertion case in the SOL-B fuel solution.	147

4.3.2 Simulated void and thermal reactivity feedback for the 2.0\$ step insertion case in the SOL-C fuel solution and the 3.5\$ step insertion case in the SOL-B fuel solution.	147
4.3.3 Fission power density as a function of time.	148
4.3.4 Total fission energy released as a function of time.	149
4.3.5 Energy required to negate external reactivity through thermal feedback, or thermal and void feedbacks combined.	151
4.3.6 Number of bubbles per cubic metre for the 2.0\$ step insertion case in the SOL-C fuel solution and the 3.5\$ step insertion case in the SOL-B fuel solution.	154
4.3.7 Concentration of dissolved hydrogen gas for the 2.0\$ step insertion case in the SOL-C fuel solution and the 3.5\$ step insertion case in the SOL-B fuel solution.	154
4.3.8 Number of stable bubbles formed as a function of fission energy deposited during the saturation period for the 2.0\$ step insertion case in the SOL-C fuel solution.	155
4.3.9 Number of stable bubbles per unit volume as a function of time.	156
4.3.10 Number of bubbles per unit volume as a function of fission energy deposited per unit volume.	157
4.3.11 One-dimensional model of bubble collapse by diffusion. Growing bubbles are shown in blue while red indicates a collapsing bubble.	158
4.3.12 Number of stable bubbles per unit volume as a function of fission power density raised to the power of $3/2$	162
4.3.13 Equilibrium constant k_b obtained from the numerical model (yellow) and estimated using Equation 4.3.25 (blue).	163
4.3.14 Stable bubbles per unit volume (solid line) and predicted stable bubble number density (dashed line) based on Equations 4.3.23 and 4.3.25 for the 2.0\$ SOL-C and 3.5\$ SOL-B cases.	164
4.3.15 Number of stable bubbles per unit volume simulated by the numerical model (solid line) with collapse rate predicted using Equation 4.3.26.	165
4.3.16 Bubble size distribution moments before and after saturation of the SOL-C fuel solution with radiolytic gas during a 2.2 \$ reactivity step insertion case. Saturation occurs at $t = 79.1\text{ms}$	167

4.3.17 Distributions of bubble radius and dissolved gas concentration during the moments after saturation of the SOL-C fuel solution following a 1.8\$ reactivity step insertion at t_{crit}	168
4.3.18 Average radius of stable bubbles for the 2.0\$ step insertion case in the SOL-C fuel solution and the 3.5\$ step insertion case in the SOL-B fuel solution.	169
4.3.19 Average radius of stable bubbles during a 3.5\$ step reactivity insertion in the SOL-B fuel solution. Prediction of the numerical model compared to the value predicted by Equation 4.3.29.	170
4.3.20 Average radius of stable bubbles during the 2.0\$ step reactivity insertion in the SOL-C fuel solution. Prediction of the numerical model compared to the value predicted by Equation 4.3.29.	170
4.3.21 Total void fraction due to the presence of radiolytic gas voids for the 2.0\$ step insertion case in the SOL-C fuel solution and the 3.5\$ step insertion case in the SOL-B fuel solution.	171
4.3.22 Rate of disappearance of dissolved hydrogen gas for the 2.0\$ step insertion case in the SOL-C fuel solution and the 3.5\$ step insertion case in the SOL-B fuel solution.	172
4.3.23 Dissolved hydrogen gas concentration as a function of time.	173
4.3.24 Mass transfer rate constant α_c as a function of peak bubble number density during saturation of the fuel solution.	174
4.4.1 Change in bubble number density over time predicted by the numerical model of the 2.4\$ SOL-C step case, showing results of a Monte Carlo simulation and results of the predictive correlations.	177
4.4.2 Distribution of dissolved hydrogen gas concentrations within the simulated domain moments before and after saturation of the fuel solution for the 2.4\$ SOL-C case, showing two saturated regions which eventually merge into one.	178
4.4.3 Change in bubble number density over time predicted by the numerical model of the 3.5\$ SOL-B step case, showing results of a Monte Carlo simulation and results of the predictive correlations.	179
4.4.4 Change in bubble number density over time predicted by the numerical model of the 2.4\$ SOL-C step case, showing 5 independent Monte Carlo simulations with two different simulated domain volumes.	180

5.1.1 Selected rate constants for the decomposition of hydrogen peroxide in pure water and uranyl sulphate solution.	191
5.1.2 Acceleration rate of bubbles as a function of time for bubbles of various radii in uranyl nitrate solution at 298 K. Values calculated using Equation 5.1.27.	196
5.1.3 Error resulting from the use of the terminal velocity assumption in the case of a radiolytic gas bubble with radius 5×10^{-3} m in uranyl nitrate solution of concentration 932 mol m^{-3} at 298 K.	197
5.1.4 Maximum error resulting from the use of the terminal velocity assumption for bubbles of different sizes in uranyl nitrate solution of concentration 932 mol m^{-3} at 298 K. . .	197
5.1.5 Convective heat transfer coefficients for heat transfer between the fuel solution and the vessel wall, calculated using Equation 5.1.33.	200
5.1.6 Convective heat transfer coefficients for heat transfer between the fuel solution and the vessel wall, calculated using Equation 5.1.35 for stirred reactor vessels with cooling jackets.	202
5.1.7 Convective heat transfer coefficients for heat transfer between the surface of the fuel solution and the plenum gas, calculated using Equation 5.1.37 based on heat transfer to the air from a flat plate.	204
5.2.1 Probability distribution of the time to reach a power level of 1 Watt during the SILENE S3-258 experiment assuming an intrinsic neutron source strength of 250 n/s.	211
5.2.2 Experimental and predicted fission power profiles for SILENE S3-258. Experimental power profile digitised from Barbry (1994).	213
5.2.3 Predicted concentrations of dissolved hydrogen and oxygen, as well as the critical concentration, for SILENE experiment n°S3-258. Multiple lines shown to indicate the range of concentrations across each discretised section of the fuel solution.	214
5.2.4 Number of bubbles predicted by the model for SILENE experiment n°S3-258.	214
5.2.5 Radius of bubbles predicted by the model for SILENE experiment n°S3-258. Multiple lines shown to indicate the range of bubble sizes across each discretised section of the fuel solution.	215
5.2.6 Experimental and predicted temperature of the fuel solution and vessel wall for SILENE S3-258. Experimental temperature profile digitised from Barbry (1994).	216

5.2.7 Individual contributions and total reactivity predicted by the model for SILENE experiment n°S3-258.	216
5.3.1 MCNP simulation to determine the reactivity of CRAC29 as a function of the fuel solution level in the vessel.	218
5.3.2 Fission power output and solution temperature from experimental reports of the CRAC-29 experiment.	220
5.3.3 Estimate of the thermal feedback coefficient for CRAC-29.	220
5.3.4 Experimental and predicted fission power profiles for the CRAC-29 experiment. Experimental power profile digitised from Barbry et al. (1973).	223
5.3.5 Predicted concentrations of dissolved hydrogen and oxygen, as well as the critical concentration, for the CRAC-29 experiment. Area shaded in grey indicates the range of concentrations across each discretised section of the fuel solution.	223
5.3.6 Total number of bubbles predicted by the model for the CRAC-29 experiment.	224
5.3.7 Radius of bubbles predicted by the model for the CRAC-29 experiment in each vertically discretised region of the fuel solution. Regions are numbered from the bottom of the fuel solution (Region 1) to the top (Region 15).	224
5.3.8 Experimental and predicted temperature of the fuel solution and vessel wall for the CRAC-29 experiment. Experimental temperature profile digitised from Barbry et al. (1973).	225
5.3.9 Individual contributions and total reactivity predicted by the model for the CRAC-29 experiment.	225
5.3.10 Predicted power profiles simulated with two different mixing coefficients.	226
5.4.1 Calculated time-dependent reactivity profile for TRACY R76.	228
5.4.2 Experimental and predicted fission power profiles for the TRACY R76 experiment. Experimental power profile digitised from Nakajima et al. (2002c).	231
5.4.3 Predicted concentrations of dissolved hydrogen and oxygen, as well as the critical concentration, for the TRACY R76 experiment.	231

5.4.4 Predicted bubble radius in each discretised region of the fuel solution, throughout the duration of the experiment (left) and after the end of fission power oscillations (right). Regions are numbered from the bottom of the fuel solution (Region 1) to the top (Region 15).	232
5.4.5 Predicted number of bubbles in each discretised region of the fuel solution, throughout the duration of the experiment (left) and after the end of fission power oscillations (right). Regions are numbered from the bottom of the fuel solution (Region 1) to the top (Region 15).	232
5.4.6 Individual contributions and total reactivity predicted by the model for the TRACY R76 experiment.	233
5.4.7 Experimental and predicted temperature of the fuel solution for the TRACY R76 experiment. Experimental temperature profile digitised from Nakajima et al. (2002c).	234
5.5.1 Wait-time probability distribution for the fission power during the Y-12 accident to exceed a threshold value of 1 Watt.	236
5.5.2 Predicted fission power profile of the Y-12 accident.	238
5.5.3 Predicted solution temperature as a function of time during the Y-12 criticality accident.	239
5.5.4 Number of bubbles predicted in each vertically discretised region as a function of time during the Y-12 criticality accident. Regions are numbered from the bottom of the fuel solution (Region 1) to the top (Region 15).	240
5.5.5 Average bubble radius predicted in each vertically discretised region as a function of time during the Y-12 criticality accident. Regions are numbered from the bottom of the fuel solution (Region 1) to the top (Region 15).	241
B.1 Geometry of the CRAC 300 mm core as modelled in MCNP based on dimensions shown in Barbry et al. (1973). [†] Assumed value.	266
B.1 Geometry of the TRACY reactor as modelled in MCNP based on dimensions shown in Nakajima et al. (2002c).	268
C.1 Solubility of H ₂ and O ₂ as a function of temperature in pure water using the correlation of Harvey (1996) and the constants of Fernández-Prini et al. (2003).	270

C.2 Solubility of H_2 and O_2 in nitric acid based on data from International Critical Tables (Washburn (2003)).	271
C.3 Solubility of H_2 in nitrate salts based on data from International Critical Tables (Wash- burn (2003)).	271
C.4 Solubility of H_2 and O_2 in chloride based on data from International Critical Tables (Washburn (2003)).	272
D.1 Period of sloshing predicted using a correlation from Housner (1963) for liquids in a partially filled cylindrical tank.	276
E.1 Density of aqueous solutions of uranyl nitrate at various temperatures and uranyl nitrate concentrations, Grant et al. (1948)	277
E.2 Comparison of measured solution densities from fissile solution experiments on CRAC, SILENE and TRACY with densities predicted using Equations E.1 and E.2.	278

List of Tables

2.1 Mean wait-times and standard deviations predicted by the gamma and saddlepoint methods for a neutron source strength of 30 n/s.	65
2.2 Mean wait-times and standard deviations predicted by the gamma distribution and saddlepoint methods for a neutron source strength of 90 n/s.	68
2.3 Summary of calculated wait-times to reach a fission rate $2 \times 10^9 \text{ s}^{-1}$ for the simulation of the Y-12 accident. Mean values shown with standard deviation in brackets.	77
2.4 Upper and lower bounds of randomised delayed neutron precursor yields.	81
2.5 Summary of calculated wait-times to reach a fission rate $2 \times 10^9 \text{ s}^{-1}$ for the simulation of the Caliban experiments. Mean values shown with standard deviation in brackets.	84
3.1 G_{H_2} for aqueous solutions of varying uranyl nitrate and nitric acid concentrations. Data from Lane et al. (1958) with nitric acid concentrations estimated based on solution pH.	103
3.2 Standard calculation conditions, applied to all calculations in Section 3.3.1, except where otherwise indicated.	105
3.3 Predicted bubble sizes and associated fission fragment LET using Equation 3.3.1 for pure water at atmospheric pressure.	113
3.4 Predicted bubble sizes and associated fission fragment LET using Equation 3.3.1 for aqueous solutions of uranyl nitrate across a range of concentrations at atmospheric pressure and 298K.	113
4.1 Delayed neutron group yields (β_i) and decay constants (λ_i) for fuel solution SOL-A.	132
4.2 Delayed neutron group yields (β_i) and decay constants (λ_i) for fuel solution SOL-B.	133
4.3 Delayed neutron group yields (β_i) and decay constants (λ_i) for fuel solution SOL-C.	133

4.4 Delayed neutron group yields (β_i) and decay constants (λ_i) for fuel solution SOL-D. . .	133
4.5 Point kinetic parameters and properties for fuel solutions based on SILENE, TRACY and CRAC.	134
4.6 Values of the constant of proportionality k_b determined from the results of the numerical model, radiolytic gas generation coefficients and average diffusion coefficients for each of the four simulated fuel solutions.	161
4.7 Summary of selected data for simulations in the SOL-A fuel solution.	175
4.8 Summary of selected data for simulations in the SOL-D fuel solution.	175
4.9 Summary of selected data for simulations in the SOL-B fuel solution.	176
4.10 Summary of selected data for simulations in the SOL-C fuel solution.	176
5.1 Delayed neutron group yields (β_i) and decay constants (λ_i) for the SILENE fuel solution with a concentration of 71 gU/L based on data from Barbry (1994).	210
5.2 Summary of model inputs and initial values.	212
5.3 Delayed neutron group yields (β_i) and decay constants (λ_i) for the CRAC-29 fuel solution modelled using MCNP.	217
5.4 Thermal feedback coefficients for CRAC-29 at maximum liquid level estimated using MCNP and from experimental data.	221
5.5 Summary of model inputs and initial values.	222
5.6 Delayed neutron group yields (β_i) and decay constants (λ_i) for the TRACY fuel solution estimated using MCNP.	228
5.7 Summary of model inputs and initial values.	230
5.8 Summary of model inputs and initial values.	237
5.9 Peak fission rate and total number of fissions, values predicted by the point kinetics code compared to those reported in the literature.	238
B.I Fuel solution composition by atom fractions used for MCNP models of CRAC-29. . . .	266
B.II Composition of stainless steel SUS304L by atom fractions used for MCNP models. . .	266

B.III Thermal feedback coefficient using MCNP for the CRAC-29 experiment.	267
B.IV Fuel solution composition by atom fractions used for MCNP models of TRACY R76.	268
C.I Constants for use in Equation C.1 to evaluate the Henry's law solubility constants for hydrogen and oxygen in pure water.	269
E.I Composition and density data for various reactor fuel solutions with predicted densities using Equation E.2. Measured data obtained from Barbry et al. (1973), Barbry (1994), Nakajima et al. (2002b) and Nakajima et al. (2002c). [†] Assumed value.	279

Nomenclature

α_c	A mass transfer rate constant characterising the rate of change in the concentration of dissolved gas due to mass transfer to or from the gaseous phase
α_T	Thermal reactivity feedback coefficient
α_V	Void reactivity feedback coefficient
$\bar{\nu}_p$	Average number of prompt neutrons emitted per fission
$\bar{\nu}$	Average number of neutrons per fission
\bar{n}	Expected (mean) neutron population
\bar{Z}	Expected (mean) cumulative detector count
β	Total delayed neutron fraction
β_i	Proportion of fission neutrons which appear as delayed neutron precursors in group i
∇	The del operator
χ	Energy spectrum of fission neutrons
ΔH_r	Enthalpy of reaction
ΔH_{vap}	Enthalpy of vaporisation
δ	Extrapolation distance
\dot{E}	Linear energy transfer ($= \frac{dE}{dx}$)
ϵ	Energy released per fission
ϵ	The fast fission factor
η	The number of fission neutrons produced per neutron absorbed in fissile material

$\Gamma(x)$	The gamma function
$\gamma(x, y)$	The lower incomplete gamma function
Λ	Neutron generation time
λ_i	Decay constant of delayed neutron precursors in group i
μ	Mean value
μ	Solution dynamic viscosity
ϕ	Neutron scalar flux
ϕ_w	An energy-dependent weighting flux
ψ	Neutron angular flux
ρ	System reactivity $\left(= \frac{k_{\text{eff}}-1}{k_{\text{eff}}}\right)$
ρ_i	Partial density of component i in the solution
ρ_s	Solution or liquid density
ρ_v	Vapour density
σ	Standard deviation
$\sigma(E)$	Microscopic neutron cross-section at energy E
Σ_a	Transport macroscopic neutron cross-section
Σ_f	Fission macroscopic neutron cross-section
σ_g	Collapsed microscopic neutron cross-section for energy group g
Σ_s	Scattering macroscopic neutron cross-section
σ_s	Solution surface tension
Σ_t	Transport macroscopic neutron cross-section
σ_{S-B}	The Stefan-Boltzmann constant
τ	Prompt neutron lifetime
τ_i	Characteristic lifetime of a delayed neutron precursor in group i

$\vec{\Omega}$	An angular vector
\vec{r}	A position vector
A_b	Bubble surface area
A_{vessel}	Surface area available for heat transfer between the vessel and the surrounding air
B_g^2	Geometric buckling
B_m^2	Material buckling
C_D	Drag coefficient of a bubble
C_i	Power contribution of delayed neutron precursors in group i
C_N	Molar concentration of nitric acid
C_p	Heat capacity at constant pressure
C_U	Molar concentration of uranyl nitrate
C_{crit}	Critical concentration of dissolved H_2 for the appearance of radiolytic gas voids
$C_{i(aq)}$	Concentration of dissolved component i
$c_{i,0}$	Probability that an absorption event leads to the creation of i prompt neutrons no delayed neutron precursors
$C_{i,eq}$	Equilibrium concentration of component i
$c_{i,j}$	Probability that an absorption event leads to the creation of i prompt neutrons and a delayed neutron precursor in group j
D	Neutron diffusion coefficient (neutronics) or mass diffusivity (molecular diffusion)
D_i	Mass diffusivity of component i
D_{FS}	Solution mixing coefficient
E	Energy
$E(t_{sat})$	Fission energy absorbed by the solution since the start of the transient or since the solution last become unsaturated with radiolytic gas
$E[X]$	Expected value of X

E_0	Eötvös number
E_b	Bubble energy of formation
$E_{k,\text{fiss}}$	Combined kinetic energy of the fission fragments following fission
E_{sat}	Energy required to saturate the solution with radiolytic gas
F	Fission rate
f	The thermal utilisation factor
f_i	Mass fraction of component i
g	Acceleration due to gravity
G_i	Radiolytic gas generation coefficient for component i
Gr	Grashof number
h_{boil}	Boiling heat transfer coefficient
H_v	Vessel height
h_{ext}	Heat transfer coefficient between the vessel and the surrounding air
h_{int}	Heat transfer coefficient between the solution and the vessel
$H_{i,\text{sol}}$	Henry's law constant of component i in the solution
k	Thermal diffusivity
k_b	Constant of proportionality relating the maximum stable number density of bubbles in solution to the fission power density
k'_b	Constant of proportionality relating the constant k_b to the mass diffusivity of dissolved gas and the radiolytic gas generation coefficient of the solution
k_c	Constant of proportionality relating the rate of bubble collapse to the degree of departure from the equilibrium number density of stable bubbles
k_D	Gas/liquid interface mass transfer coefficient
$k_{\text{H}_2\text{O}_2}$	Reaction rate constant for the decomposition of H_2O_2
k_∞	The infinite multiplication factor

k_{eff}	The effective multiplication factor
L	Track length associated with the formation of a bubble
l	Mean neutron lifetime
L^2	Diffusion length
M_i	Molecular weight of component i
M_{vessel}	Vessel mass
M_{sol}	Solution mass
n	Neutron population
n^*	Neutron population corresponding to the wait-time threshold
N_b	Number of bubbles
N_i	Number of moles of component i
N_{fiss}	Number of fissions
N_{RG}	Number of moles of radiolytic gas
Nu	Nusselt number
P	Fission power output
$P(n, \mathbf{m}, t)$	Probability of having n neutrons and \mathbf{m} delayed neutron precursors at time t
$P(x)$	Absolute probability of x
P_b	Bubble pressure
P_l	Hydrostatic pressure
$P_w(t)$	Probability density of crossing the wait-time threshold at time t
P_{H_2}	Partial pressure of H_2 gas
P_{fNL}	Fast non-leakage probability
P_{NL}	Total non-leakage probability
P_{thNL}	Thermal non-leakage probability

Pr	Prandtl number
Q	Rate of heat transfer
$Q(x)$	Probability that $X < x$ (cumulative probability of x)
Q_{sol}	Mass flow rate of solution
R	Universal gas constant
r	Radius
r_b	Bubble radius
r_e	Expanded bubble radius or radius of a bubble which has achieved equilibrium with its surroundings by consuming excess dissolved gas through expansion
r_v	Vessel radius
$R_{\$, (T+V)}$	Combined thermal and void reactivity feedback in units of dollars
$R_{\$, T}$	Thermal reactivity feedback in units of dollars
R_{ex}	External (inserted) reactivity during a criticality transient
r_{nucl}	Characteristic radius of the available bubble nucleation sites
Re	Reynolds number
Ri	Richardson number
Ro	Roshko number
S	Intrinsic neutron source strength
T	Solution temperature in Kelvin
t	Time
T_{Av}	Mass-weighted mean solution temperature
T_c	Solution temperature in degrees Celsius
T_{ext}	External temperature
T_{sat}	Saturation temperature
t_{sat}	Time at which the concentration of dissolved H_2 exceeds the critical concentration

t_{sat}	Time at which the solution becomes saturated with radiolytic gas
U_{surface}	Heat transfer coefficient between the solution and the gas above its surface
v	Neutron velocity
v_b	Bubble velocity
V_{RG}	Volume of radiolytic gas
X	Separation distance in the direction of the x axis
y_{H_2}	Mole fraction of H_2 in the gaseous phase
Z	Cumulative detector count
Z^*	Cumulative detector count corresponding to the wait-time threshold
amu	Atomic mass units
CFD	Computational Fluid Dynamics
DNP	Delayed Neutron Precursor
eV	Electron volt
HTC	Heat Transfer Coefficient
LET	Linear Energy Transfer
MIPR	Medical Isotope Production Reactor
MOC	Method of Characteristics

Chapter 1

Introduction

Aqueous fissile solutions are created in a wide variety of important processes throughout the nuclear industry and pose a particular set of hazards with respect to nuclear criticality safety. Fissile liquids are common in nuclear fuel fabrication and reprocessing, where solid fuels are dissolved in aqueous solutions containing acid for the purpose of homogeneous chemical processing. Fissile liquids also occur in Aqueous Homogeneous Reactors (AHR), a type of reactor in which the fuel solution and moderator comprise an aqueous solution of a uranium-containing salt, typically uranyl nitrate or uranyl sulphate. These reactors are expected to become an important future source of radionuclides for medical applications.

This thesis presents new mathematical and computational models for the analysis of nuclear criticality transients in aqueous solutions of fissile material. This begins with a method for quantifying the degree of uncertainty in the initiation time of fission power bursts in the presence of weak neutron sources, followed by examination of the mechanics of bubble formation in fissile liquids and the evolution of bubble growth during saturation of a fissile solution with radiolytic gas. Finally, this thesis presents a point kinetics model which incorporates a new set of equations for predicting the number and size of bubbles formed during nuclear criticality transients. This model is validated against criticality benchmark experiments with close agreement between the predicted and measured transient variables.

1.1 Introduction to Criticality Accidents

A criticality accident occurs when a critical mass or volume of fissile material is assembled inadvertently, resulting in an uncontrolled and unplanned nuclear chain reaction. These accidents can occur

in any type of operation handling fissile material, including liquid and solid systems. Liquid systems are particularly vulnerable to criticality accidents due to several factors, including the fact that the geometry of the fissile material can be changed simply by transferring the solution to another vessel. There are also many physical and chemical processes that can take place in aqueous solutions of fissile material, such as precipitation, evaporation and sedimentation, which can contribute to increasing the overall reactivity. In some circumstances, these processes can be difficult to foresee and have led to unplanned and uncontrolled nuclear criticality excursions.

1.1.1 Definition of Criticality

Criticality of a fissile system is defined as the state in which the rate of production of neutrons from fission equals the rate of removal of neutrons from the system from one generation of neutrons to the next. In an infinite system, neutrons can only be removed by absorption and the system is critical when the infinite multiplication factor (k_∞) is equal to unity:

$$k_\infty = \frac{\text{rate of neutron production}}{\text{rate of neutron absorption}}. \quad (1.1.1)$$

In a real system, neutrons can also be lost from the system by leaking into the surroundings. In this case, the infinite multiplication factor is replaced by the effective multiplication factor:

$$k_{\text{eff}} = \frac{\text{rate of neutron production}}{\text{rate of neutron absorption} + \text{leakage}}. \quad (1.1.2)$$

It is noted by Glasstone and Sesonske (1994) that the infinite multiplication factor is a function of the material properties only, whereas the effective multiplication factor is a function of the material properties and the system geometry.

These multiplication factors can be thought of as the product of the probabilities of various events which determine whether or not a neutron born in a fission event will go on to induce another such event in a fissile nucleus. The four-factor formula describes the infinite multiplication factor:

$$k_\infty = \eta f \epsilon p, \quad (1.1.3)$$

$$k_{\text{eff}} = k_\infty P_{\text{NL}}, \quad (1.1.4)$$

where η is the number of fission neutrons produced per neutron absorbed in fissile material, f is the thermal utilisation factor which corresponds to the fraction of absorbed neutrons which are captured by the fuel as opposed to non-fissile nuclides, ϵ is the fast fission factor or the fraction of fission neutrons causing fission before thermalisation, and p is the resonance escape probability. This last factor represents the probability that a fast neutron will reach a thermal energy level without being

absorbed in the resonance region where neutron capture cross-sections are highest. The non-leakage probability (P_{NL}) is included to convert the infinite multiplication factor to the effective multiplication factor for finite systems. This is sometimes split into a fast and thermal non-leakage probability resulting in an expression known as the six-factor formula (Knief et al. (1985)):

$$k_{\text{eff}} = \eta f \epsilon p P_{\text{fNL}} P_{\text{thNL}}, \quad (1.1.5)$$

where P_{fNL} and P_{thNL} are the fast and thermal non-leakage probabilities, respectively.

A description of the four-factor formula in Stacey (2007) discusses the effect by which separation (or “lumping”) of the fuel and moderator into a heterogeneous configuration can increase the value of p and therefore k_{eff} . This may also be an important phenomenon for fissile solutions, where the fuel and moderator may initially comprise a homogeneous mixture before separating due to precipitation or sedimentation, potentially leading to an increase in reactivity.

The four and six factor formulae serve to illustrate the important phenomena at the scale of neutrons and nuclei that contribute to establishing criticality. This translates, at the larger scale, to a range of macroscopic properties that influence the criticality of a fissile system. Clayton (1974) makes the following observation when discussing these factors:

“Criticality, then, depends not only on the quantity of fissile material present, but on the size, shape, and material of any containment vessel which may be used, on the nature of any solvents or diluents, and on the presence of any adjacent material which may possibly return neutrons through scattering back into the fissile material.”

The factors which influence the criticality of a fissile system are summarised by the well-known mnemonic MAGICMERV which stands for: **M**ass, **A**bsorbers, **G**eometry, **I**nteraction, **C**oncentration, **M**oderation, **E**nrichment, **R**eflection, **V**olume (NNSA (2008)). Many of these factors are somewhat interdependent, which can lead to complex and unpredictable behaviour. This is highlighted in Clayton (1974) and Clayton (2010) which explore so-called “anomalies of criticality”, where the changes in the k_{eff} of a fissile system may be particularly unintuitive.

Clayton details many examples of complex and unpredictable changes in the reactivity of a fissile system. In one example, it is shown how the presence of ^{240}Pu in a fissile solution containing a mixture of ^{239}Pu and ^{240}Pu leads to a situation where a solution with a given size and shape can be critical at three different plutonium concentrations. This is due to the relatively high thermal capture cross-section, and negligible thermal fission cross-section, of ^{240}Pu . A change to the dilution of the system effects the mass and concentration of fissile material, but it also affects the degree of moderation

and therefore the neutron energy spectrum. A shift towards thermal energies increases the chance of fission in ^{239}Pu but it also increases the chance of capture in ^{240}Pu , leading to a complex relationship between k_{eff} and solution concentration. In other cases, Clayton shows that it is theoretically possible to have a system with $k_{\infty} < k_{\text{eff}}$ in which criticality can be achieved with $k_{\infty} < 1$.

1.1.2 Examples of Criticality Accidents

It is useful to give a brief summary of some of the better known criticality accidents. The aim of this section is to demonstrate the consequences of criticality accidents and the broad range of circumstances in which unplanned criticality excursions have occurred in the past.

1.1.2.1 1958 Accident at the Y-12 National Security Complex

A very well-known criticality accident occurred on 16th June 1958 at the Y-12 National Security Complex in Oakridge, Tennessee. This accident resulted in significant radiation exposure to 8 workers. The exact radiation doses received by the workers are not known. However, estimates have been made indicating that at least 5 workers received doses in excess of 2 Sv. Knief et al. (1985) reports an absorbed dose of 365 Rads (~ 3.7 Sv) for the worker in closest proximity at the time of the accident, while McLaughlin et al. (2000) reports that this worker received a dose of 461 Rem (~ 4.6 Sv).

The accident occurred in a 208 litre drum that was being used to collect water drained from pipework during a leak test. In a report on the incident, issued at the time by the plant operator Union Carbide, Patton et al. (1958) states that the water used for leak testing was to be transferred to the drum via a system of pipes, however a leaking valve meant that these pipes had become filled with a solution of 90% highly enriched uranium (HEU) in the form of uranyl nitrate. The solution of HEU in the pipework was deposited in the drum and was followed by water from the leak testing. Initially, the HEU deposited in the drum remained subcritical, however as water from the leak test flowed into the drum, the degree of moderation was increased, causing the solution to become critical. Water from the leak test continued to flow, making the solution more dilute, and eventually the system became subcritical once again. The total yield was estimated at 1.3×10^{18} fissions, a particularly large yield relative to other criticality accidents.

A deterministic point kinetics model of the Y-12 accident has been presented by Zamacinski et al. (2014) and a stochastic treatment, of the initial phase of the accident, is presented in Chapter 2.

1.1.2.2 1999 Accident at the JCO Fuel Fabrication Plant in Tokaimura

A more recent criticality accident occurred in 1999 at a JCO fuel fabrication plant in the town of Tokaimura, Japan. The accident resulted in two fatalities due to radiation exposures reported (IAEA (1999)) to be in excess of 6 GyEq. The same report notes that a third plant worker received a dose in the range 1.2 to 5.5 GyEq and survived. Gamma and neutron dose rates as high as 0.84 and 4.5 mSv/hr, respectively, were measured outside the confines of the facility which is believed to have resulted in doses as high as 9.1 mGyEq among members of the public (IAEA (1999)). Doses as high as 119 mGyEq were also received by the workers who intervened to bring the accident under control. The Tokaimura accident is classified at Level 4 on the International Nuclear and Radiological Event Scale (INES).

The events of the accident are described in McLaughlin et al. (2000). The accident occurred while three workers were preparing a solution of 18.8% enriched uranyl nitrate. The workers deviated from the approved procedure by preparing the solution in a precipitation vessel, rather than the storage columns intended for that purpose. The cause of the accident was the geometry of the precipitation vessel, which was wider than the storage columns and resulted in a more compact configuration, providing the conditions for criticality once a sufficient volume of solution had been added to the vessel. If the solution had been prepared in the storage columns, the tall narrow geometry of these vessels would have prevented criticality from occurring.

The Tokaimura accident was a prolonged excursion lasting approximately 20 hours. This was largely due to the presence of a cooling jacket surrounding the precipitation vessel, which removed heat from the fissile liquid, lowering the temperature and reducing thermal reactivity feedback (Liem and Naito (2015)), as well as acting as a neutron moderator and reflector. The accident was eventually brought to an end when the cooling jacket was drained by plant operators.

A model of the Tokaimura accident using the TRACE code was presented in Yamane et al. (2000) and cited in Liem and Naito (2015). Pain et al. (2003) also present a model of the Tokaimura accident using the FETCH code.

1.1.3 Need for Accurate Modelling

In the UK, the conditions of the nuclear site licence require that nuclear sites regularly review their criticality safety measures, as well as assessing the risk of criticality each time a new facility is designed, or the design of an existing facility is changed (ONR (2016)). In order to make a useful assessment of criticality risk and safety measures in place, it is necessary to be able to predict the potential

consequences of any accidents that might occur. A number of simplified methods exist for predicting the consequences of criticality accidents and a review of these methods can be found in Nakajima (2003). However, these methods are associated with large uncertainties, leading to a requirement for increased safety margins, which can place severe restrictions on plant operations, and may make certain operations altogether unviable. The purpose of advanced criticality safety models is to provide criticality safety assessors with more precise estimates of the worst case accidents, as well as support emergency preparedness, safety and evacuation planning. This can contribute to the safe reduction of unnecessary safety margins and a more accurate assessment of criticality risk, as well as providing improved emergency safety and evacuation plans.

Modelling and simulation tools for aqueous fissile solutions also have a potential future use in the production of medical isotopes such as Technetium-99m ($^{99\text{m}}\text{Tc}$). The aqueous homogeneous reactor (AHR) is a nuclear reactor where the fuel and moderator comprise an aqueous solution of the fissile material, such as uranyl nitrate or uranyl sulphate. These types of reactor are currently under investigation as a potential technology for the production of short-lived radioisotopes, such as $^{99\text{m}}\text{Tc}$, for medical applications (IAEA (2009)).

1.2 Predicting Criticality

There are many different methods for estimating the effective neutron multiplication factor of a fissile system. These methods vary widely in their accuracy and the complexity and computational expense of the calculation. At one end of the scale, hand calculation methods can provide a rapid estimate for criticality safety assessment purposes. These calculations can be performed on a simple calculator but may be subject to significant margins of error. At the other end of the scale is the neutron transport equation, which can provide an extremely accurate prediction of k_{eff} but requires the use of advanced numerical methods and computational techniques to arrive at a solution efficiently.

The criticality of a fissile system consists of an eigenvalue problem, where the effective multiplication factor represents the eigenvalue of the fundamental mode of the system, and the neutron flux shape represents the eigenvector. The neutron scalar flux distribution corresponding to the fundamental eigenvector is determined using the neutron transport or neutron diffusion equations described below.

1.2.1 The Neutron Transport Equation

The neutron transport equation is a linearised form of the Boltzmann transport equation for the balance on the population of particles in a medium. In the case of neutron transport, the particles are neutrons and the assumption is made that the neutron density is small enough compared to atomic densities in the medium that neutron-neutron interactions can be neglected. The neutron transport equation was originally derived by Ornstein and Uhlenbeck (1937), and is discussed in numerous sources, including Beckurts and Wirtz (1964), Amaldi et al. (1959), Hébert (2009) and CEA (2015). It is shown below in its partial integro-differential form without delayed neutrons:

$$\begin{aligned}
\frac{1}{v} \frac{\partial}{\partial t} \psi(\vec{r}, E, \vec{\Omega}, t) + \vec{\Omega} \cdot \nabla \psi(\vec{r}, E, \vec{\Omega}, t) + \Sigma_t(\vec{r}, E) \psi(\vec{r}, E, \vec{\Omega}, t) \\
= \iint \Sigma_s(\vec{r}, E' \rightarrow E, \vec{\Omega}' \rightarrow \vec{\Omega}) \psi(\vec{r}, E', \vec{\Omega}', t) dE' d\Omega' \\
+ \frac{\chi(E)}{4\pi} \iint \bar{\nu} \Sigma_f(\vec{r}, E') \psi(\vec{r}, E', \vec{\Omega}', t) dE' d\Omega' \\
+ S(\vec{r}, E, \vec{\Omega}, t)
\end{aligned} \tag{1.2.1}$$

where ψ is the angular neutron flux, E is neutron energy, \vec{r} is a position vector defining a particular location in phase space, $\vec{\Omega}$ is vector defining a particular direction, Σ_t is the total macroscopic neutron cross-section and the sum of the scattering and absorption macroscopic neutron cross-sections, Σ_s is the macroscopic neutron scattering cross-section, Σ_f is the macroscopic neutron fission cross-section, $\bar{\nu}$ is the average number of neutrons per fission, χ is the energy spectrum of prompt fission neutrons, v is neutron velocity and S is an extraneous (or fixed) prescribed neutron source.

The neutron transport equation is computationally expensive to solve due to the large number of dimensions (location, energy, direction). Approximations are required to discretise the equation in each of these dimensions, introducing a discretisation error into the solution.

The neutron transport equation can be solved stochastically, using Monte Carlo codes such as the Monte Carlo N-Particle Transport Code (MCNP, LANL (2017)), MONK, TRIPOLI-4 and SERPENT, or using deterministic solvers such as Winfrith Improved Multigroup Scheme (WIMS), EVEn Parity Neutral particle Transport (EVENT, de Oliveira (1986)), APOLLO2 and CRONOS2. A detailed review of these methods can be found in CEA (2015). An advantage of stochastic solvers is that they have the potential to model the location, angle and energy dimensions continuously, without the need to introduce a discretisation error. However, this comes at the price of a statistical error which is inherent to the Monte Carlo method. One major advantage of Monte Carlo methods is that they can model most geometries exactly using combinatorial geometry of conic sections in 2D and quadric

surfaces in 3D. However, this can now be achieved using the very latest innovations in deterministic transport theory methods based on isogeometric analysis (IGA). IGA enables much more general non-uniform rational B-spline (NURBS) geometries, utilised in CAD software, to be used for the spatial and geometric discretisation of the neutron transport equation. Hall et al. (2012) demonstrated the use of this method to solve the diffusion equation and Owens et al. (2016) demonstrated its use for a first-order solution of the neutron transport equation.

In deterministic transport theory solvers, energy is typically treated using multiple discrete energy groups. A very large number of energy groups is required to accurately capture the effects of spatial and energy resonance self-shielding on the microscopic neutron cross-sections. Using lattice codes, these energy groups can be collapsed into a smaller number of broader groups. Methods for resolving the resonances include the Livolant-Jeanpierre Method (Livolant and Jeanpierre (1974)) and the Sub-Group Method (Cullen (1974)). A description of lattice codes can be found in Hébert (2009). Collapsed group microscopic neutron cross-sections take the following form (CEA (2015)):

$$\sigma_g = \frac{\int \sigma(E) \phi_w(E) dE}{\int_g \phi_w(E) dE}, \quad (1.2.2)$$

where σ is the microscopic neutron cross-section and ϕ_w is a weighting-flux that depends on the energy spectrum of the neutrons in the system.

Deterministic transport theory solvers also require a method for discretisation of the angle representing the direction of travel of neutrons. This has been achieved using methods such as spherical harmonics (P_N method), the method of characteristics (MOC) and discrete ordinates (S_N method).

1.2.2 Neutron Diffusion

The neutron diffusion equation is derived from the neutron transport equation by making the assumption that angular variation in the angular flux is linearly anisotropic. The behaviour of neutrons can then be approximated to the diffusion of chemical species in a continuous medium, i.e. that they tend to move down a concentration gradient from areas of high concentration to areas of low concentration. The steady-state neutron diffusion equation for a single energy group is shown below:

$$\nabla \cdot D(\vec{r}) \nabla \phi(\vec{r}) - \Sigma_a(\vec{r}) \phi(\vec{r}) + \bar{\nu} \Sigma_f(\vec{r}) \phi(\vec{r}) = 0, \quad (1.2.3)$$

which can also be expressed in multiple energy groups:

$$\begin{aligned} \nabla D(\vec{r}, E) \nabla \phi(\vec{r}, E) - \Sigma_t(\vec{r}, E) \phi(\vec{r}) + \int \Sigma_s(\vec{r}, E' \rightarrow E) \phi(\vec{r}, E') dE' \\ + \chi(E) \int \bar{\nu} \Sigma_f(\vec{r}, E') \phi(\vec{r}, E') dE' = 0, \end{aligned} \quad (1.2.4)$$

where D is the neutron diffusion coefficient of the medium.

The single and two-energy group formulations have analytical solutions for various simple geometries, including spheres and cylinders (Meem (1964)). These analytical solutions form the basis of several hand calculation methods for criticality safety assessment (Bowen and Busch (2006)) which are discussed below. The multi-energy group formulation provides relatively accurate results for many systems and has been widely used for reactor physics calculations (Lamarsh (1975)). It is still used in modern reactor physics codes today, such as PANTHER (“PANTHER - An Advanced 3D Nodal Code for Reactor Core Analysis”, 2018). In many cases, the use of neutron diffusion is enhanced by the application of neutron transport to parts of the problem where the diffusion approximation would lead to unacceptable errors.

The advantage of the neutron diffusion equation compared to neutron transport is that the number of dimensions is reduced by eliminating the angular dependence. However, Stacey (2007) highlights that the absorption cross-section is assumed much less than the scattering cross-section. Where this is not the case, in or close to strongly absorbing materials, the diffusion approximation will result in an inaccurate result. This is also true in cases where scattering may be particularly anisotropic, such as close to neutron sources, or close to discontinuities in the medium, such as vacuum boundaries.

1.2.3 Hand Calculation Methods

Numerous hand calculation methods exist for quickly determining the approximate k_{eff} of a fissile system. Reviews of these techniques can be found in Bowen and Busch (2006), Knief et al. (1985) and Thomas and Abbey (1973).

The one-group diffusion equation discussed above (see Equation 1.2.3) can be solved analytically for systems with simple geometries. A detailed summary of this method can be found in Bowen and Busch. The method is based around two properties of a fissile system known as the geometrical buckling and the material buckling. When these two quantities are equal, the system is critical with $k_{\text{eff}} = 1$. The material buckling is given by the expression:

$$B_m^2 = \frac{k_\infty - 1}{L^2}; \quad L^2 = \frac{D}{\Sigma_a}, \quad (1.2.5)$$

where B_m^2 is the material buckling and L^2 is ratio of the diffusion coefficient to the absorption cross-section and is known as the diffusion length. The expression for the geometrical buckling depends on the geometry of the particular system in question. The geometrical buckling for various geometries can be found in Knief et al. (1985). For a sphere it is given by:

$$B_g^2 = \left(\frac{\pi}{r + \delta} \right)^2; \quad \delta = 2D, \quad (1.2.6)$$

where r is the radius of the sphere and δ is the extrapolation distance. The critical radius of the sphere is the value of r for which $B_g^2 = B_m^2$.

Bowen and Busch warn that the one energy group diffusion based method described above should not be applied to thermal systems where the effect of the slowing down of neutron cannot be ignored. In thermal systems, modified diffusion theory offers an alternative via a two energy group approximation.

Another method related to neutron diffusion is the method of shape conversion. This technique converts the dimensions of one system to the dimensions of another system with known critical dimensions. The critical dimensions must be known for the particular material in the target geometry. Critical dimensions for various system materials and geometries can be found in Paxton and Pruvost (1987). For example, the geometric buckling of a cuboid is given by the following expression (Knief et al. (1985)):

$$B_g^2 = \left(\frac{\pi}{a + 2\delta} \right)^2 + \left(\frac{\pi}{b + 2\delta} \right)^2 + \left(\frac{\pi}{c + 2\delta} \right)^2, \quad (1.2.7)$$

where a , b and c are the dimensions of the cuboid. If the critical radius of a sphere made of the same material as the cuboid is known, then by equating Equations 1.2.6 and 1.2.7 the radius of an equivalent sphere can be determined for the cuboid. If this radius is greater than or equal to the critical radius of the sphere, the cuboid will be critical.

For more complex geometries the diffusion based methods described above would be impractical. The surface density method can provide an indication of criticality for complex geometries or even interacting arrays of loosely-coupled units. The method is based on the surface density of the system or array, which represents the amount of material that be in one unit area if the array were collapsed into the floor. The k_{eff} of the system is less than 0.9 if its surface density is less than σ (Knief et al. (1985)), where:

$$\sigma = 0.54\sigma_0(1 - 1.37f). \quad (1.2.8)$$

σ_0 is the surface density of a critical water-reflected infinite slab and f is the ratio of the mass of the system (or one unit in the array) to the critical mass of a sphere, known as the fraction critical.

These methods represent a small number of examples of the numerous hand calculation methods

that exist for estimating the criticality of a fissile system. While these methods are too imprecise to be used for detailed design or risk assessment calculations, they can provide a useful tool for rapidly estimating the criticality of a system and through their simplicity they highlight the extent to which the geometric parameters of a system contribute to criticality.

1.3 Transient Nuclear Reactor Kinetics of Fissile Solutions

The nuclear reactor kinetics of a criticality excursion transient in a fissile solution depend on the reactivity of the system and the evolution of the reactivity over time. Transient nuclear criticality excursions may be initiated by any event which increases the reactivity of the system to a supercritical state. Initiating events may include:

- the addition of fissile material to a vessel;
- the removal of a neutron absorber, such as a control rod;
- a change in geometry, for example by agitating the liquid or by transferring it to a different vessel;
- the mass transfer of fissile material from one phase to another.

1.3.1 Reactivity Feedbacks

Once a nuclear criticality excursion transient is initiated, physical processes associated with the transient itself will begin to affect the system reactivity. These processes are referred to as reactivity feedbacks and the two most important for a fissile solution are void feedback and thermal feedback.

Void feedback can be due to radiolytic gas bubbles, or steam in the case of a boiling fissile solution. The density of the gas or steam inside the bubbles is so low compared to the surrounding liquid that they are typically treated as voids, neglecting the small possibility of an interaction between a gas molecule and a neutron traversing the bubble. Voids effectively reduce the reactivity of a fissile solution by reducing the solution density. This reduces the total macroscopic neutron cross-section of the solution and increases the chance of neutron leakage.

Thermal feedback in aqueous fissile solutions acts through three mechanisms:

- solution density,

- Doppler broadening of neutron cross-sections,
- changes to thermal scattering cross-sections.

As the temperature of the solution increases, the liquid expands and its density decreases. This reduces the density of the solution which reduces system reactivity in the same manner as void feedback.

Doppler broadening refers to the phenomenon whereby the chance of an interaction between a neutron and a nucleus depends on the relative energy of the neutron with respect to the nucleus (Cacuci (2010)). At certain relative energies, known as resonances, the probability of interaction becomes extremely high. In a medium with temperature $T > 0$ K, the atoms within the medium have a distribution of energies and this distribution becomes broader with increasing temperature. This has the effect of broadening the range of neutron energies which are susceptible to a given resonance energy, thereby increasing the effective microscopic neutron cross-section.

Whether the effect of Doppler broadening is to increase or decrease the reactivity of the system depends on composition. The cross-section for all potential interactions is increased by Doppler broadening. Therefore, the effect will be positive if the increase in fission cross-section dominates, whereas the effect will be negative if the increase in capture cross-section dominates. The effect is negative for low-enriched uranium but it can be positive for high-enriched, heterogeneous systems, as demonstrated by Shiroya et al. (1996).

The temperature of the medium also affects the microscopic cross-sections for neutron scattering. Scattering of neutrons at high energies is usually treated as a collision between unbound particles, ignoring the wave-like properties of the neutron. However, at thermal neutron energies, the wavelength of the neutrons approaches the length scale of molecular bonds and the effects of chemical bonds within the scattering medium become significant. A description of the theory of neutron scattering and thermalisation can be found in Williams (1966).

1.3.2 Quasi-Steady-State Method

The quasi-steady-state method of criticality transient analysis was presented by Schulenberg and Döhler (1986) and was further developed by Nakajima et al. (2002a). The method works by calculating for each instant in time, the amount of thermal and void reactivity feedback that would be present due to the amount of fission energy deposited in the system. The method uses a pseudo-steady-state assumption in that the feedbacks are assumed to appear immediately so that the system remains in an exactly critical state at all times. The method cannot predict the detail of short-lived transient

effects, such as oscillations in reactivity due to the appearance and advection of gas voids. However, the method has been shown to be effective at estimating the average fission power output over longer timescales.

1.3.3 Deterministic Point Nuclear Reactor Kinetics

The point kinetics equations are based on the simplifying assumption that the space, energy and time-dependent neutron flux can be factorised into an amplitude function that varies only in time and a shape function that varies in space and energy. The shape function may also vary in time, however this variation is orders of magnitude slower than the variation in the amplitude function. This method is described in numerous sources, including Lamarsh (1975) and Ott and Neuhold (1985). The flux factorisation can be represented as follows:

$$\phi(\vec{r}, E, t) = N(t)\psi(\vec{r}, E, t), \quad (1.3.1)$$

where ϕ is the neutron flux, N is the amplitude function and ψ is the shape function. By making this assumption it is possible to derive an equation of the following form:

$$\frac{dP(t)}{dt} = \frac{\rho(t) - \beta(t)}{\Lambda(t)} P(t) + \sum_i \lambda_i C_i(t), \quad (1.3.2)$$

$$\frac{dC_i(t)}{dt} = -\lambda_i C_i(t) + \frac{\beta_i}{\Lambda} P(t), \quad (1.3.3)$$

where P is the fission power output, ρ is the system reactivity in dimensionless form, Λ is the generation time, C_i is the fission power worth of delayed neutron precursors in group i , λ_i is the decay constant of delayed neutron precursors in group i and β_i is the fraction of all neutrons that appear as delayed neutrons precursors in group i .

The point kinetics method can be derived from the neutron diffusion equation (Ott and Neuhold (1985)) or the neutron transport equation (Cacuci (2010)). It is capable of providing highly accurate results, even for systems with complex geometry such as full scale reactor cores, provided the point kinetics parameters (Λ , β) are appropriately weighted. This can be achieved by means of adjoint flux weighting. The method also requires the time-dependent reactivity of the system ($\rho(t)$) to be supplied as an input. This must be determined a priori using methods based on neutron transport or neutron diffusion.

The point kinetics method is particularly well suited to criticality safety problems involving containers of fissile liquid, where the geometry of the system may be relatively simple. In these cases, the neutron flux distribution can be well characterised using a shape function ψ based on an analyt-

ical solution to the neutron diffusion equation. Indeed, this is the method employed by many of the criticality safety code discussed in Section 1.3.5.

1.3.4 Stochastic Point Nuclear Reactor Kinetics

In many criticality safety problems it is necessary to consider the stochastic nature of branching fission chains. This is because the processes that lead to the branching and growth of neutrons chains (fission, capture, scattering) are inherently random events. When the neutron population is large, the combined effect of these random events is predictable and can be treated as deterministic. However, criticality accidents often occur in situations where the neutron population in the fissile material prior to the start of the accident is very small. In these cases, the likelihood of significant deviations from deterministic behaviour is relatively large and needs to be taken into account.

Equation 1.3.4 shows the forward probability balance for the neutron population in a point nuclear reactor model using the notation of Bell (1963):

$$\begin{aligned}
P(n, \mathbf{m}, t + dt) = & \left(1 - \frac{ndt}{l} - \sum_{i=1}^I \frac{m_i dt}{\tau_i} - \sum_{k=1}^K S_k dt \right) P(n, \mathbf{m}, t) \\
& + \sum_{j=0}^J (n - j + 1) \frac{c_{j,0}(t)dt}{l} P(n - j + 1, \mathbf{m}, t) \\
& + \sum_{j=0}^J \sum_{i=1}^I (n - j + 1) \frac{c_{j,i}(t)dt}{l} P(n - j + 1, \mathbf{m} - \delta_i, t) \\
& + \sum_{i=1}^I \frac{m_i}{\tau_i} dt P(n - 1, \mathbf{m} + \delta_i, t) + \sum_{k=1}^K S_k(t) dt P(n - k, \mathbf{m}, t),
\end{aligned} \tag{1.3.4}$$

where $P(n, \mathbf{m}, t)$ is the probability of having n neutrons and \mathbf{m} precursors in the system at time t , where I is the number of delayed neutron groups and \mathbf{m} is a vector of size I , l is the mean neutron lifetime, $c_{i,j}$ is the probability that an absorption event (capture or fission) produces i prompt neutrons and a delayed neutron precursor of group j , or no delayed neutron precursor if $j = 0$, and $S_k dt$ is the probability that a neutron source S produces k neutrons in the time interval dt .

Equation 1.3.4 constitutes an infinite system of equations where the probability of a having n neutrons in the system is a function of the probabilities of all other possible neutron population numbers. This equation can produce useful information for systems with small neutron populations where the infinite series can be truncated, but rapidly becomes too expensive to solve for systems with larger neutron populations. Another important property of Equation 1.3.4 is that the probabilities determining the next state of the system depend purely on the current state of the system and not the system history. This type of system is known as a Markov chain (Grinstead and Snell (2012)).

Application of the generating function to Equation 1.3.4 allows the infinite system of equations to be replaced with a single ODE, the generating function to the forward probability balance equation for a single energy group point model, shown in Equation 1.3.5:

$$\frac{\partial G}{\partial t} = \frac{1}{l} \left[-x + \sum_{j=0}^J x^j c_{j,0}(t) + \sum_{j=0}^J \sum_{i=0}^i x^i y_i c_{j,i}(t) \right] \frac{\partial G}{\partial x} + \sum_{i=1}^I \frac{1}{\tau_i} (x - y_i) \frac{\partial G}{\partial y_i} + \sum_{k=1}^K S_k(t) (x^k - 1) G, \quad (1.3.5)$$

where $G(x, \mathbf{y}, t)$ is the generating function for the probability distribution $P(n, \mathbf{m}, t)$, l is the mean neutron lifetime, τ_i is the mean lifetime of a delayed neutron precursor in group i and the other symbols are as defined in Equation 1.3.4.

The forward probability balance equation was originally proposed by Feynman (1946) and further developed by Courant and Wallace (1947). It is generally used for single energy group point models, however it can be extended to derive a multi-energy group, spatially-dependent form which was first derived by Govorkov (1963a, 1963b). Detailed discussions of the forward probability balance equation can be found in Osborn and Natelson (1965) and Williams (2009).

A backward form of the probability balance equation also exists and is known as the Pál-Bell Equation, after Pál (1958) and Bell (1965) who derived it independently. The Pál-Bell Equation constitutes an adjoint form of the forward probability balance equation discussed above. The Pál-Bell Equation is mathematically less complicated to solve with spatial and energy dependence than the forward form, and is widely applied for this purpose. Humbert (2003) used the PANDA neutron transport code to solve for the neutron survival probability and the first and second moments of the neutron number probability distribution using the spatially-dependent Pál-Bell Equation. Saxby et al. applied the energy-dependent Pál-Bell Equation to a point model examining the influence of neutron energy on survival probability (2016), later applying neutron diffusion theory with a single energy group (2017), and neutron transport theory with multiple energy groups (2018) to spatially-dependent models of subcritical spheres. Williams and Eaton (2018) also applied the Pál-Bell Equation with spatial dependence to a study of reactor start-up for slab, cylindrical and spherical geometries.

The generating functions of the probability balance equations are often relatively easy to compute, however a new challenge is created in the form of extracting useful information about the underlying probability distributions. Several techniques have been demonstrated for inverting the generating function to extract useful information, notably by Bell (1963), Hurwitz et al. (1963), Abate and Whitt (1992), Authier et al. (2014) and Williams and Eaton (2017). Some of these methods are discussed further and applied in Chapter 2.

A thorough survey of the mathematics governing the branching of neutron chains, can be found

in Pázsit and Pál (2008).

1.3.5 Current and Historical Codes used for Modelling and Simulating Transient Nuclear Criticality Excursions in Aqueous Fissile Solutions

One of the earliest examples of a fissile liquid code dates back to the 1960s, with the AIREK code of Atomics International (Blue et al. (1964)). Specially modified versions of the code were also designed, such as AIREK-KEWB to simulate a series of experiments known as the Kinetic Experiments on Water Boilers (KEWB). The complexity of these codes was limited by the computational power available at the time and the need for mathematical efficiency was a factor that strongly influenced their design. The AIREK code coupled point reactor kinetics with a zero-dimensional model of thermal and void feedback. Radiolytic gas production was assumed to occur once a threshold energy had been reached. This was based on observations showing a delay between the initiation of a criticality transient and the appearance of radiolytic gas.

The CRITEX code was developed in the 1980s as a computer code for simulating reactivity transients in fissile liquids. A description of the code can be found in Mather and Shaw (1986). It was the product of a collaboration between the Commissariat à l’Energie Atomique (CEA) in France and the United Kingdom Atomic Energy Authority (UKAEA). Experiments were carried out on the SILENE aqueous fissile solution reactor for the purpose of determining appropriate values for adjustable parameters contained in the empirical radiolytic gas model within CRITEX. These empirical parameters are adjusted to a particular set of experimental conditions. Therefore, they cannot be used for predictive purposes for aqueous fissile solutions with arbitrary solution composition and geometry. The details of these models are described in a joint CEA-UKAEA report (Barbry et al. (nd)). The thermal hydraulics model in CRITEX includes one-dimensional (1D) discretisation in the vertical direction. The fission rate in each region of the solution is determined from a point kinetics calculation and a shape function representing the fundamental mode of the neutron scalar flux. Neither AIREK nor CRITEX include models of solution boiling and steam production. CRITEX includes a model for the advection of bubbles leading to a decrease in the system voidage based on a user-specified bubble velocity, while AIREK models the creation of radiolytic gas voids but not their advection.

Simulation codes for fissile liquids developed more recently have built upon the methods of AIREK and CRITEX. A point kinetics code for simulation of the Medical Isotope Production Reactor (MIPR) was developed by Cooling (2014). Like CRITEX, it combines point reactor kinetics with a 1D thermal hydraulics model to calculate void and thermal feedback. However, it includes many significant advances in the thermal hydraulics models, removing the need for user-specified parameters. Cool-

ing's code also includes models of solution boiling, mixing and heat transfer to the surroundings. The AGNES model also combines point reactor kinetics with 1D thermal hydraulics (Yamane et al. (2005), Basoglu et al. (1998)) while the TRACE code combines point reactor kinetics with 2D (radially and axially discretised) thermal hydraulics. The thermal hydraulics model of TRACE is based on the radiolytic gas model of CRITEX (Liem and Naito (2015)).

The INCTAC code differs from those described above by including a spatially-dependent neutronics model based on the time-dependent neutron transport equation. The neutronics model is used to determine reactivity coefficients for point reactor kinetics based on a quasi-steady-state method, thus removing the need for external reactivity calculations and permitting the reactivity feedback coefficients to be time-dependent. A detailed description of this code is reported by Mitake et al. (2003) alongside benchmark results using experiments carried out on the TRACY aqueous fissile solution reactor.

The FETCH code comprises the neutron transport solver EVENT loosely coupled with a computational multiphase fluid dynamics (CMFD) code. A description of the FETCH code can be found in Pain et al. (2001) and an analysis of the 1999 Tokaimura criticality accident using FETCH can be found in Pain et al. (2003). The advantage of the detailed spatially-dependent multiphysics approach is the ability to model the multidimensional evolution, movement and transport of materials, including radiolytic gas bubbles and delayed neutron precursors, throughout the problem domain. In addition, such codes can also model the time and spatially-dependent variations in the fission power profile over the duration of the nuclear criticality excursion. However, the use of detailed multiphysics codes for criticality safety problems, often does not yield any additional information beyond that which phenomenological models can provide in a small fraction of the run time. The complex nature of codes of this type also makes it difficult to quantify the impact of each input parameter on the model output.

Many of the codes discussed above, including CRITEX and FETCH, are now relatively old and no longer represent the state-of-the-art. In particular, there have been major advances in the fields of CFD (Yeoh and Tu (2019)), neutronics (Owens et al. (2016)) and thermal hydraulics of aqueous fissile solutions (Cooling (2014)) since these codes were developed. The CRITEX, TRACE and FETCH codes all require calibration of their radiolytic gas models against experimental information of gas evolution. The code described in Cooling (2014) does not require calibration of its radiolytic gas model, however the model is a simplification of the physical reality and cannot capture some important effects of radiolytic gas in fissile solutions. The improvement of the radiolytic gas model was therefore identified by Cooling as an area for future development. The radiolytic gas model presented in this thesis is based on a mechanistic model of bubble formation, which allows it to capture important

effects resulting from radiolytic gas formation during nuclear criticality transients in fissile solutions, without the need for calibration against experimental data.

Chapter 2

Power Excursions in the Presence of a Weak Neutron Source

2.1 Introduction

Much of the work presented in this chapter, including tables and figures, is reproduced from Winter et al. (2018).

In a fissile system, the fluctuations in neutron population over time are driven by the branching of neutrons chains, an inherently random process. When the neutron population is large, the law of large numbers determines that the outcome of the many branching processes taking place in the system, will tend towards the average (or “expected”) behaviour; the likelihood of significant deviations from the expected behaviour is small and can often be neglected. However, it is well known that the behaviour of a fissile system when the neutron population is small, such as a reactor start-up in the presence of a “weak” neutron source, cannot be accurately modelled without considering the stochastic nature of the growth in these neutron chains. In these cases, significant deviations from the average behaviour are to be expected and a different modelling approach is required.

2.1.1 Relative Strength of an Intrinsic Neutron Source

A useful qualitative indication of the relative strength of a given neutron source was derived by Hansen (1960) who noted that a source should be considered weak if,

$$\frac{2S\tau}{\bar{\nu}\Gamma_2} \ll 1, \tag{2.1.1}$$

where S is the neutron source strength, τ is the prompt neutron lifetime, $\bar{\nu}$ is the average number of neutrons released per fission, and $\Gamma_2 = \overline{\nu(\nu - 1)}/\bar{\nu}^2$. This expression is approximately equivalent to the more simple inequality,

$$S\tau \ll 1. \quad (2.1.2)$$

2.1.2 The Wait-Time

The implications of a low neutron population are well documented and have been demonstrated experimentally, by Hansen (1960) and Authier et al. (2014), amongst others. In both examples, a fast burst reactor, GODIVA (Hansen) or Caliban (Authier et al.), was brought multiple times from a subcritical state to a delayed supercritical state, and the time taken to reach a pre-defined fission rate threshold was measured. The time taken to reach the threshold is known as the *wait-time* and it was shown to vary significantly between each realisation of the experiment, despite identical experimental conditions.

In a delayed supercritical system, the neutron population at any given moment consists of prompt neutrons emitted from fission and delayed neutrons emitted from those fission fragments which are delayed neutron precursors. In a delayed supercritical system, the population of delayed neutron precursors increases over time. This leads to an increase in the number of prompt neutron chains initiated and a corresponding increase in the fission rate and the prompt neutron population. The wait-time is the time taken for this build up in the neutron population to occur. It varies because the growth rate in the neutron population depends on the different events which can happen to each neutron emitted in the system (absorption, scattering, leakage, etc.) and these events are inherently random. The sequence of events can never be identical for two realisations of the same experiment and this can be observed on the macroscopic scale as variation in the wait-time.

The wait-time is an important concept that can have significant implications for the severity of accidental power excursions and for the safe start-up of nuclear reactors. During reactor startup, for example, control rods may be withdrawn to increase the reactivity of the system. Assuming the reactor behaves in a deterministic manner, the reactor power will begin to increase as soon as the system reactivity increases, and once the system is critical, an exponential increase in power should be observed. This will cause a rise in temperature, leading to negative reactivity feedback through material expansion and Doppler broadening, limiting the overall reactivity of the system and preventing an excessive increase in power. However, if the neutron source is too weak, or the withdrawal of the control rods too fast, there is likely to be a delay between reaching positive reactivity and any significant rise in reactor power. Meanwhile the reactivity of the system continues to rise

in the absence of any negative temperature feedback. When the power output does finally begin to rise, the system reactivity may already be large enough to produce a dangerous power excursion. One potential objective in seeking to characterise the wait-time is to know at what rate the control rod can be withdrawn so the probability of a dangerous power excursion remains below a specified “safety probability”, e.g. 10^{-8} .

2.1.3 Methods for Predicting the Wait-Time Probability Distribution

Methods for determining the wait-time probability distribution include Hansen’s method (Hansen (1960)), the Fourier series method (see Abate and Whitt (1992)) and the saddlepoint method of Hurwitz et al. (1963). Hansen’s method is approximative and based on neutron survival probabilities. Hansen’s method considers that the wait-time consists of two parts: the time taken before a persistent neutron chain is initiated and the time for the neutron population due to the first persistent chain to build up to the wait-time threshold. Persistent chains sponsored after the first are not considered to influence the wait-time significantly, because prompt neutron chains grow very rapidly; and unless the delay between the initiation of the first and second persistent chains were on the order of the generation time, the neutron population due to the second chain would be insignificant compared to that due to the first. Hansen notes that the initiation of a second persistent chain on this timescale is unlikely in a weak source scenario.

The Fourier series and saddlepoint methods rely on inversion of probability generating functions to obtain the probability distribution of the neutron population. This approach is more rigorous but also far more computationally expensive. These methods do not rely on the concept of the first persistent chain and are therefore able to account for the possibility of overlapping chains (initiated by different source neutrons) contributing to the neutron population at the moment the wait-time threshold is exceeded. This is important in delayed supercritical systems, where persistent fission chains consist of finite prompt chains linked by delayed neutron precursors. Since the delayed neutron precursors decay on a long timescale, compared to the generation time, overlapping fission chains become a significant possibility. The generating function methods can be applied to point models or space-dependent models. They can also be used with single or multiple energy groups.

A less expensive alternative to the generating function approach is to approximate the wait-time probability distribution using the gamma distribution method. This method was first proposed by Harris (1964) and relies on the fact that the neutron population in a multiplying system will tend towards a gamma distribution. There are cases when the neutron population does not conform to the gamma distribution so this method does not work for all scenarios, however it can be highly accurate

and fast when applied to certain problems. Authier et al. (2014) derived a mathematical basis for the use of the gamma distribution to model the wait-time in delayed supercritical systems. Using fitted parameters they showed that the distribution of wait-times observed during their experiments on the Caliban reactor conformed to a gamma distribution. Analysing the same experiments on Caliban, Williams (2016) showed that the probability distribution of the wait-times could be accurately predicted without the need for fitted parameters, using a gamma distribution characterised by the mean and standard deviation of the neutron population - see Section 2.1.5.

2.1.4 Types of Uncertainty

For the purposes of the discussion that follows, it will be useful to distinguish between **aleatoric uncertainty** and **parametric uncertainty**. Aleatoric uncertainty will hereafter refer to uncertainty resulting from the random, stochastic nature of the build-up of neutron chains in fissile systems, and parametric uncertainty will refer to that resulting from epistemic uncertainty in the input parameters. When calculating the wait-time probability distribution using any method, there will inevitably be some epistemic uncertainty in the input parameters, particularly when simulating accidental excursions where the exact chain of events may be unknown. The uncertainty in input parameters adds to the uncertainty already present due to aleatoric uncertainty.

This chapter presents a method for quantifying the impact of epistemic uncertainty in the input parameters. Uncertainty quantification (UQ) will be carried out using the Monte Carlo approach, which requires a fast method for determining the wait-time probability distribution, so that many calculations can be performed for a range of randomised sets of input parameters. The gamma distribution method will be used for this purpose, with verification of the predicted probability distribution using the saddlepoint method.

The ability to quantify the impact of epistemic uncertainty in the input parameters on the resulting wait-time probability distribution has important implications for criticality safety and safe reactor start-up.

2.1.5 Objectives

The method of uncertainty quantification presented in this chapter makes use of the gamma distribution using the method presented in Williams (2016). In his paper, Williams shows that the wait-time probability distributions observed during the experiments of Authier et al. (2014) on the Caliban reactor, can be accurately predicted using the gamma distribution method. Starting from the forward

form of the generating function equation, Williams derives equations for the mean neutron population, precursor group populations, detector counts and their corresponding covariances. These same equations will be used here as the basis for the gamma distribution method.

The purpose of this work is to incorporate the gamma distribution method demonstrated by Williams into a Monte Carlo algorithm, for the purpose of uncertainty quantification. The gamma distribution method for determining the wait-time probability distribution is particularly amenable to Monte Carlo uncertainty quantification due to its excellent computational efficiency compared to alternative, more rigorous methods.

The gamma distribution method has been shown to produce accurate results for certain scenarios, however it will be shown in Section 2.2.3 that the neutron population does not always conform to a gamma distribution. The parameters influencing the accuracy of the gamma distribution method will be examined in order to establish the range of transients to which this method of uncertainty quantification can be applied.

2.2 Methodology

The methods outlined in this section were solved numerically, using a new code developed in FORTRAN. The numerical solution of the saddlepoint method is readily amenable to parallelisation, which was exploited using OpenMP in order to minimise required execution times.

2.2.1 Gamma Distribution Method

The neutron population, n , is modelled by the following probability density function (the Gamma Distribution) in which n is approximated as a continuous random variable, with the time, t , as a parameter.

$$P(n, t) = \frac{\eta(t)}{\bar{n}(t)\Gamma(\eta(t))} \left(\frac{\eta(t)n}{\bar{n}(t)} \right)^{\eta(t)-1} \exp \left(-\frac{\eta(t)n}{\bar{n}(t)} \right), \quad (2.2.1)$$

The function $\Gamma(z)$ is the complete gamma function, defined as follows

$$\Gamma(z) = \int_0^{\infty} x^{z-1} e^{-x} dx. \quad (2.2.2)$$

Two incomplete gamma functions also exist: the lower and upper incomplete gamma functions, where the upper or lower limit of integration, respectively, is replaced with a finite limit. The lower incomplete

gamma function, for example, is defined as follows

$$\gamma(z, y) = \int_0^y x^{z-1} e^{-x} dx. \quad (2.2.3)$$

The time-dependent parameter $\eta(t)$ is the ratio of the squares of the mean and standard deviation,

$$\eta(t) = \frac{\bar{n}(t)^2}{\sigma_n(t)^2}. \quad (2.2.4)$$

The methodology described here for calculating the wait-time probability distribution from the gamma distribution is based on that described in Williams (2016) with some minor modifications. The probability distribution, $P_w(t)$, of the wait-time may be determined by differentiating the cumulative probability density function $Q(n^*, t)$, where n^* is the instantaneous neutron population corresponding to the wait-time threshold fission rate, with respect to time.

$$P_w(t) = -\frac{dQ(n^*, t)}{dt} \quad (2.2.5)$$

The values of $Q(n^*, t)$ are obtained directly from the ratio of incomplete and complete gamma functions, as follows,

$$Q(n^*, t) = \frac{\gamma(\eta(t), \eta(t)n^*/\bar{n}(t))}{\Gamma(\eta(t))}, \quad (2.2.6)$$

where $\gamma(x, y)$ and $\Gamma(x)$ are the lower incomplete and complete gamma functions discussed above.

The wait-time may also be calculated with respect to the cumulative detector count (Z^*), as in Williams (2016). In this case, the wait-time probability is obtained by differentiating the cumulative probability density function, $Q(Z^*, t)$, for the detector count, Z^* , corresponding to the wait-time threshold fission rate.

$$P_w(t) = -\frac{dQ(Z^*, t)}{dt}, \quad (2.2.7)$$

$$Q(Z^*, t) = \frac{\gamma(\eta_z(t), \eta_z(t)Z^*/\bar{Z}(t))}{\Gamma(\eta_z(t))}. \quad (2.2.8)$$

The parameter $\eta(t)$ is replaced by $\eta_z(t)$,

$$\eta_z(t) = \frac{\bar{Z}(t)^2}{\sigma_z(t)^2}. \quad (2.2.9)$$

The value of n^* or Z^* is determined from the pre-defined wait-time fission rate threshold by calculating the expected fission rate, $\bar{F}(t)$, using the following equation from Williams (2016),

$$\bar{F}(t) = \frac{k_{\text{eff}}(t)}{\bar{\nu}\tau} \bar{n}(t), \quad (2.2.10)$$

where $k_{\text{eff}}(t)$ is the time-dependent neutron multiplication factor, $\bar{\nu}$ is the mean number of neutrons

released per fission, τ is the prompt neutron lifetime and $\bar{n}(t)$ is the time-dependent neutron population. The value taken for n^* is the value of $\bar{n}(t)$ at the moment $\bar{F}(t)$ crosses the wait-time threshold. Likewise, if the wait-time is calculated based on cumulative detector count, then the value of Z^* is the value of $\bar{Z}(t)$ when $\bar{F}(t)$ crosses the fission rate threshold. The mean neutron population, cumulative detector count and their standard deviations were calculated by solving the system of ordinary differential equations found in Williams (2016) using the ODE solver of Shampine and Gordon (1975).

The model is zero-dimensional, one-speed and without thermal feedback. It is derived by differentiating the one-speed, point model forward equation (Bell (1963)), for the probability generating function.

2.2.2 Saddlepoint Method

2.2.2.1 Method Overview

The wait-time probability distributions calculated by the gamma distribution method were compared against calculations using the saddlepoint method to confirm their accuracy. A detailed description of the saddlepoint method can be found in Williams and Eaton (2017) and only a brief summary will be presented here. The cumulative probability density function $Q(n^*, t|s)$ is obtained from Equation 2.2.11. It represents the probability that the neutron population has not exceeded n^* at time t if a source was present since time s . It is equivalent to the $Q(n^*, t)$ of Equation 2.2.6 if s is equal to the start time.

$$Q(n^*, t|s) \approx \frac{1}{2\pi\sigma_0} \frac{G_S(z_0, t|s)}{z_0^{n^*} (1 - z_0)} \quad (2.2.11)$$

where $G_S(z_0, t|s)$ is the backward form of generating function for the probability distribution of the neutron population at time t , given a source present since time s , and σ_0 is given by,

$$\sigma_0 = \frac{n^*}{z_0^2} + \frac{1}{(1 - z_0)^2} - \left(\frac{G'_S(z_0, t|s)}{G_S(z_0, t|s)} \right)^2 + \frac{G''_S(z_0, t|s)}{G_S(z_0, t|s)} \quad (2.2.12)$$

where G'_S and G''_S are the first and second derivatives of the generating function G_S with respect to z . Finally, z_0 is the value of z which satisfies the equation,

$$\frac{n^*}{z_0} = \frac{1}{1 - z_0} + \frac{G'_S(z_0, t|s)}{G_S(z_0, t|s)}, \quad (2.2.13)$$

where n^* is the neutron population corresponding to the wait-time fission rate threshold. The backward generating functions for a point model were obtained from Williams and Eaton (2017) and solved using the ODE solver of Shampine and Gordon (1975).

The saddlepoint method is actually an approximation, albeit a very accurate one, because it relies

on the method of steepest descents to approximate a line integral before arriving at the expression in Equation 2.2.11. The error in the method does, however, become significant for values of $Q(n^*, t|s)$ close to unity, and Hurwitz notes that for values of $n^* \gg \bar{n}$, $Q(n^*, t|s)$ tends to $\frac{e}{\sqrt{2\pi}} = 1.08444\dots$. This results in a wait-time probability distribution whose integral is ~ 1.08 and it is therefore necessary to renormalise the distribution to have an integral of 1.0.

Notwithstanding these limitations, which result in a small, quantifiable error in the saddlepoint method's predictions, the accuracy of the saddlepoint method has been evaluated by Williams and Eaton (2017) who compared it to the exact Fourier series method, details of which can be found in Abate and Whitt (1992). Williams and Eaton found that the values of $Q(n^*, t|s)$ calculated using the saddlepoint method were within 0.5% of the exact values calculated using the Fourier series method, in all the cases they tested. It is therefore assumed throughout this chapter that the results of the saddlepoint method are close to the true wait-time probability distribution, and any significant discrepancies between the probability distributions predicted by the two methods are attributable to error in the gamma distribution method.

The reason that the saddlepoint method is valid in all cases, whereas the gamma distribution is not, is that the saddlepoint method inverts the generating function to obtain the neutron population probability distribution directly from known quantities (such as neutron cross-sections). The gamma distribution method, on the other hand, assumes a probability distribution for the neutron population based on its mean and standard deviation. While this method is accurate in many cases, it is known that the probability distribution for the neutron population can deviate significantly from the assumed distribution.

As an additional check to confirm the accuracy of the saddlepoint method, one set of data, for a situation where the gamma distribution method fails to give accurate results, was also compared against a Monte Carlo simulation. Details of this comparison can be found in Section 2.2.3.1.

2.2.2.2 Finding the Value of z_0

The value of z_0 required by Equation 2.2.12 is determined by finding the roots of Equation 2.2.13. Because the generating functions G_S and G'_S are functions of z_0 whose values can only be determined by solving a system of ODEs, the roots cannot be found analytically and an iterative solution is necessary. Determining the value of z_0 for all time steps can therefore be an expensive task. Hurwitz et al. (1963) provided the following approximation for z_0 which can be used as a starting guess for

iterations,

$$z_0 \approx \frac{n^*}{1 + n^*}. \quad (2.2.14)$$

The method of bisection is a reliable technique for finding the roots of Equation 2.2.13, and thereby determining z_0 . Nonetheless, this method requires a relatively large number of iterations to achieve the required accuracy in z_0 , leading to long computing times, particularly when modelling fast systems where the system of ODEs for the generating functions tends to be particularly stiff. A more efficient solution is proposed by Williams and Eaton (2017) who suggest that the roots of the equation could be found using Newton-Raphson iterations. This was found to reduce the number of required iterations dramatically; a typical simulation requiring approximately 20 – 30 iterations with bisection was found to need only 4 – 8 iterations using Newton-Raphson.

The Newton-Raphson method allows the roots of an equation $f(x) = 0$ to be determined through a series of iterations. In each iteration, an estimate for the value of the root x_n is calculated based on the value of the previous estimate x_{n-1} . In most cases, the estimate converges rapidly on the true value of the root. Each new estimate of the root x_n is determined from the following relation,

$$x_n = x_{n-1} - \frac{f(x_{n-1})}{f'(x_{n-1})}, \quad (2.2.15)$$

where $f'(x)$ is the first derivative of $f(x)$ with respect to x .

In order to implement the Newton-Raphson method to find z_0 it is necessary to express it in the form $f(z_0) = 0$ and this can be done in many ways. The form given in Equation 2.2.16 was chosen, from which the derivative in Equation 2.2.17 immediately follows.

$$f(z_0) = \frac{z_0}{1 - z_0} + \frac{G'_S}{G_S} z_0 - n^*, \quad (2.2.16)$$

$$f'(z_0) = \frac{1}{1 - 2z_0 + z_0^2} + \frac{(G''_S z_0 + G'_S)G_S - (G'_S)^2 z_0}{(G_S)^2}. \quad (2.2.17)$$

The second derivative of the generating function G''_S is already required in Equation 2.2.12 to determine σ_0 so no extension is required to the system of ODEs.

2.2.3 Range of Applicability of the Gamma Distribution Method

The gamma distribution method works well for simulating fissile systems in which the neutron population conforms to a gamma distribution. However, if this is not the case then the predicted wait-time probability distribution will not be correct. Therefore, it is necessary to determine the range of applicability of the gamma distribution method if it is to be used with confidence. This was achieved by

verifying the results of the gamma distribution method against the saddlepoint method for a range of different scenarios, varying the magnitude and rate of the reactivity insertion, as well as the prompt neutron lifetime and the neutron source strength. All calculations in this section include 6 groups of delayed neutrons.

Figure 2.2.1 shows mean wait-times and standard deviations predicted by the gamma and saddlepoint methods for a 0.7\$ step insertion over a range of different intrinsic neutron source strengths. The means and standard deviations predicted by the two methods converge as the neutron source strength is increased, showing that the accuracy of the gamma distribution method improves with increasing neutron source strength. The relative offset in the mean predicted wait-time converges to a value around 1.2%, indicating that the mean value predicted by the gamma distribution method is 1.2% larger than that predicted by the saddlepoint method. This is likely due to the previously mentioned weakness in the saddlepoint method, where the cumulative probability distribution for $\bar{n} \ll n^*$ tends to a value greater than unity. This skews the distribution towards lower values of n and leads to a slight underestimate of the overall mean of the wait-time probability distribution.

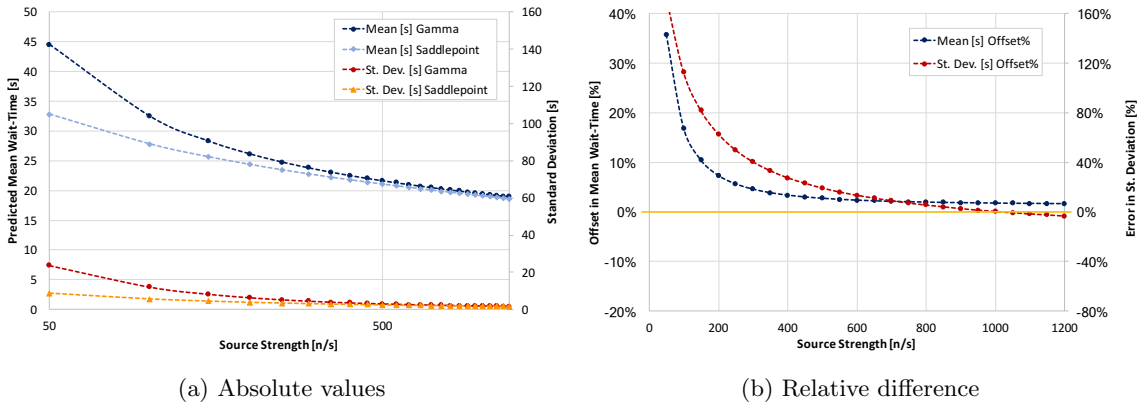


Fig. 2.2.1. Comparison of mean wait-times and standard deviations predicted by the gamma and saddlepoint methods for a 0.7\$ reactivity step insertion over a range of intrinsic neutron source strengths.

Figure 2.2.2 shows the wait-time probability distributions calculated using both the saddlepoint and gamma distribution methods for a range of reactivity step insertions in the presence of a neutron source emitting 30 n/s. The agreement between the two methods is very close for the 0.1\$ reactivity step insertion, however the gamma distribution method becomes progressively less accurate as the magnitude of the reactivity insertion increases. For the larger reactivity insertions, the gamma distribution method overestimates the likelihood of longer wait-times, resulting in higher means and standard deviations than those predicted by the saddlepoint method (see Table 2.1).

The accuracy of the gamma distribution method improves when the neutron source strength is

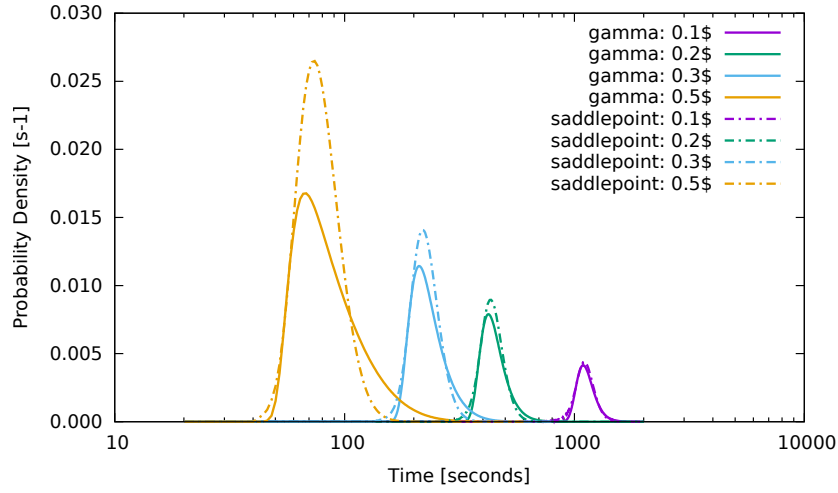


Fig. 2.2.2. Wait-time probability distributions predicted by the saddlepoint (dashed) and gamma distribution (solid) methods for reactivity step insertions of 0.1\$, 0.2\$, 0.3\$ and 0.5\$, with a neutron source strength of 30 n/s.

Reactivity Insertion [\$]	Mean (& St. Dev.) [s]	
	Gamma	Saddlepoint
0.1	1138 (117)	1122 (108)
0.2	456 (66)	445 (53)
0.3	242 (52)	230 (34)
0.5	101 (44)	82 (19)

TABLE 2.1

Mean wait-times and standard deviations predicted by the gamma and saddlepoint methods for a neutron source strength of 30 n/s.

increased to 90 n/s (see Figure 2.2.3). Significant inaccuracies are still observed, however, in the wait-times predicted for larger reactivity insertions.

Figure 2.2.4 shows the minimum source strengths required for the gamma distribution method to achieve acceptable accuracy over a range of reactivity step and ramp insertions. The system modelled in this figure has a prompt neutron lifetime of 45 μ s. Acceptable accuracy was defined as a mean wait-time predicted by the gamma distribution method that was within 2% of the mean wait-time predicted by the saddlepoint method. No criterion was imposed on the standard deviation because it was found that the standard deviations converged with the predicted means (see Figure 2.2.1).

Figure 2.2.4 shows that the minimum required source strength for the gamma distribution method to be close to the saddlepoint method increases with the magnitude of the reactivity insertion for step insertions and 1 s ramp insertions. The required minimum source strength also increases for a 10 s ramp insertion but the effect is smaller. For a 30 s ramp insertion, there is no correlation between the magnitude of the reactivity insertion and the minimum source strength required for accurate wait-time prediction by the gamma distribution method.

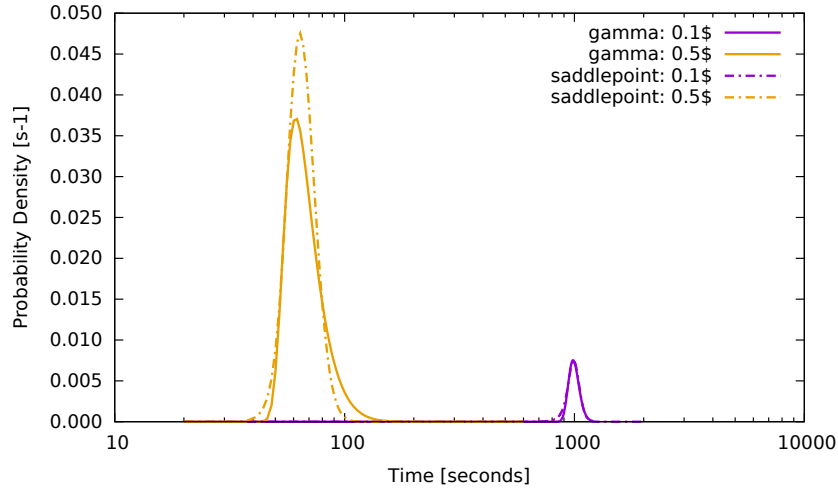


Fig. 2.2.3. Wait-time probability distributions predicted by the saddlepoint (dashed) and gamma distribution (solid) methods for reactivity step insertions of 0.1\$ and 0.5\$, with a neutron source strength of 90 n/s.

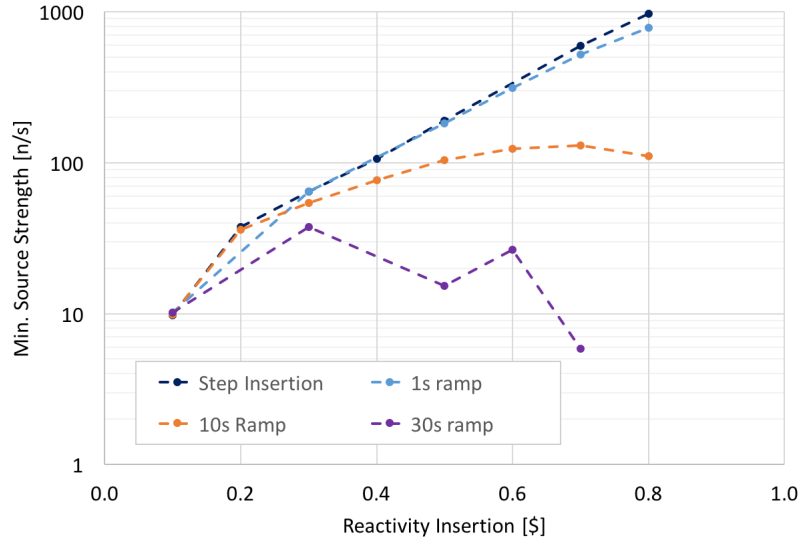


Fig. 2.2.4. Minimum source strengths required for the gamma distribution method to predict a mean wait-time within 2% of the value predicted by the saddlepoint method. Results shown for varying reactivity insertion rates and a constant prompt neutron lifetime of 45 μ s. The reactivity insertion rate is the total insertion size divided by the insertion time stated.

The minimum required source strength was also found to be a function of the prompt neutron lifetime. Figure 2.2.5 shows how the required minimum source strength varied with the magnitude of the reactivity insertion and the prompt neutron lifetime. The source strength corresponding to 2% accuracy initially increased with decreasing prompt neutron lifetime, however for prompt neutron lifetimes shorter than $\sim 10 \mu$ s, no significant further increase in the minimum required source strength was observed.

Figure 2.2.5 includes markers to show the source strength and reactivity insertion size correspond-

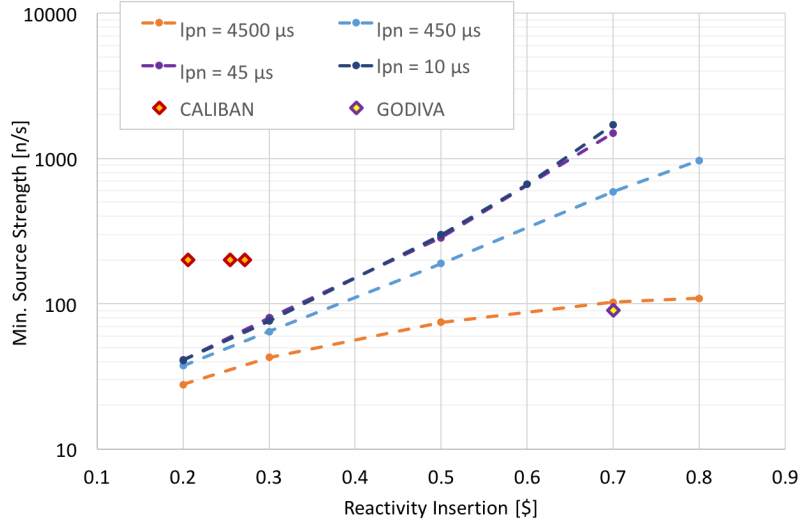


Fig. 2.2.5. Minimum source strengths required for the gamma distribution method to predict a mean wait-time within 2% of the value predicted by the saddlepoint method. Results shown for a reactivity step insertion with a range of prompt neutron lifetimes.

ing to two sets of burst wait-time experiments: the Caliban experiments of Authier et al. (2014) and the GODIVA experiment of Hansen (1960). From the figure it would be expected that the gamma distribution method would prove accurate for the Caliban experiments but not for Hansen’s experiment on GODIVA. Indeed this is the case: it has already been shown by Williams (2016) that the Caliban experiments can be modelled accurately using the gamma distribution method. Hansen’s experiment, on the other hand, requires a more rigorous method due to the combination of a relatively large and rapid reactivity insertion and a weak neutron source.

2.2.3.1 Verification with Monte Carlo Simulation

A 0.7\$ step insertion case was simulated using a Monte Carlo code and the results are shown in Figure 2.2.6. The Monte Carlo simulation was performed using the code described in Cooling et al. (2016). The code performs a large number of realisations (5,000 in this case), each with the same input parameters, and within each realisation, randomly determines the fate of each neutron produced at each time step according to the physical probabilities of different events.

The results match well with those of the saddlepoint method but not the gamma distribution method, which supports the hypothesis that the saddlepoint method works well even for scenarios where the gamma distribution method is not valid. The probability distribution generated by the Monte Carlo code is based on a relatively small number of data points compared to the distributions generated by the gamma distribution and saddlepoint codes. This is because the Monte Carlo code works by calculating the wait-times for a large number of system histories. In order to construct a

continuous probability distribution, it is necessary to group similar wait-times together into ‘bins’. The probability corresponding to each wait-time bin is then inferred from the proportion of system histories whose wait-time falls within each bin. Each data point in the Monte Carlo code therefore represents a relatively expensive calculation compared to the cost of calculating data points by the gamma distribution or saddlepoint methods.

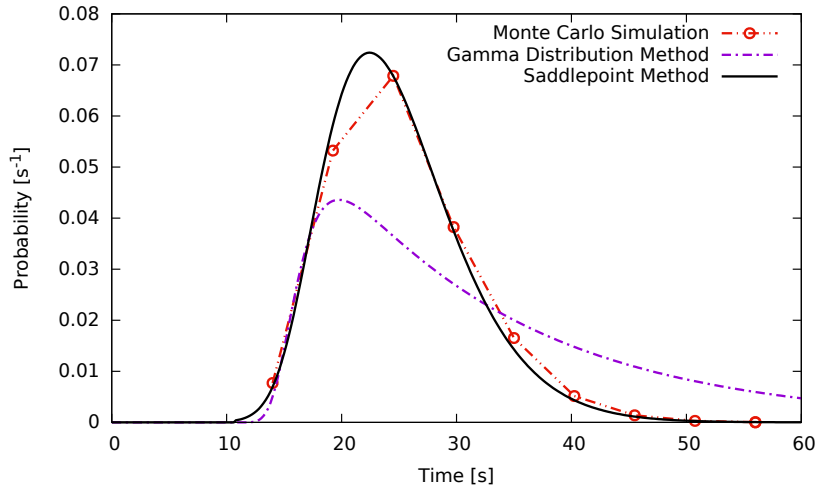


Fig. 2.2.6. Wait-time probability distributions predicted by the gamma distribution method, saddlepoint method and a Monte Carlo simulation (5,000 realisations), for a reactivity step insertion of 0.7\$ and neutron source strength of 90 n/s.

It was also attempted to use the code of Cooling et al. (2016) to simulate the 0.1\$ and 0.5\$ step insertion cases, however it was found that the value of N_{thresh} (see Cooling et al. (2016) for details) required to converge the resultant probability distribution was too large to allow the calculations to be run in a reasonable time. Essentially, the low reactivity in these cases allowed a large number of delayed neutron precursors to build up before the power increased to a level where its behaviour could be considered deterministic. Simulating the decay of such a large number of delayed neutron precursors proved too expensive in terms of computing time.

Reactivity Insertion [\$]	Mean (& St. Dev.) [s]		
	Gamma	Saddlepoint	Monte Carlo
0.1	998 (72)	991 (55)	—
0.5	70.7 (15)	66.7 (8.9)	—
0.7	33.4 (16.7)	25.0 (5.8)	25.2 (5.8)

TABLE 2.2

Mean wait-times and standard deviations predicted by the gamma distribution and saddlepoint methods for a neutron source strength of 90 n/s.

2.2.4 Uncertainty Quantification

2.2.4.1 Types of Uncertainty

Monte Carlo uncertainty quantification was carried out in two case studies to examine the impact of parametric uncertainty on the predicted wait-times. Four different wait-time probability distributions are presented:

- **Deterministic:** This probability distribution is a delta function, representing the expected wait-time when all uncertainty (both aleatoric and parametric) is neglected. The deterministic wait-time is the time at which the mean (or expected) fission rate crosses the fission rate threshold.
- **Aleatoric:** This is the distribution of wait-time probabilities resulting from the stochastic nature of the processes leading to the growth and branching of neutron chains. No uncertainty in input parameters is taken into account.
- **Parametric:** This is the distribution of deterministic wait-time probabilities when uncertainty is applied to one or more of the input parameters. No aleatoric uncertainty is taken into account.
- **Aleatoric-Parametric:** This is the wait-time probability distribution when aleatoric and parametric uncertainty are both taken into account. It is expected that the distribution incorporating the combined aleatoric and parametric uncertainties will be broader and less peaked than either the aleatoric or parametric distributions.

2.2.4.2 The Monte Carlo Code

A new version of the FORTRAN code was developed to implement Monte Carlo uncertainty quantification making use of the Message Passing Interface (MPI) to run multiple instances of the gamma wait-time code in parallel. In each instance, the Monte Carlo code randomised the variable to be made uncertain, before passing this to the gamma wait-time code, which returned either the deterministic wait-time or the calculated wait-time probability density function.

The parametric only probability distribution was then constructed by establishing wait-time bins of equal width across the range of expected wait-times. The MPI code was used to calculate 100,000 values of the deterministic wait-time by running 100,000 realisations of the wait-time code. These values were then sorted into the wait-time bins, and the probability distribution inferred from the proportion of values returned in each bin.

For the aleatoric-parametric probability distribution, the MPI code was used to calculate 10,000 aleatoric wait-time probability density functions by running 10,000 realisations of the gamma wait-time code. The combined probability density function was determined by calculating the sum of all 10,000 distributions and renormalising, so that for a given time t ,

$$P_w(t) = \frac{1}{N_{rn}} \sum_{i=1}^{N_{rn}} P_{w,i}(t), \quad (2.2.18)$$

where $P_w(t)$ is the probability of exceeding the wait-time threshold at time t , N_{rn} is the number of Monte Carlo realisations and $P_{w,i}(t)$ is the probability of exceeding the wait-time threshold at time t according to distribution i . Note that $P_w(t)$ is the wait-time probability across all realisations representing the full range of input parameters, whereas $P_{w,i}(t)$ is the wait-time probability for a single realisation with a single set of input parameters.

A larger number of realisations is required to obtain the parametric-only distribution than the parametric-aleatoric distribution. This is due to the need to sort the calculated deterministic wait-times into bins so that the continuous probability distribution can be approximated. The total number of realisations must be sufficiently large that the number of wait-time values in each bin is large compared to the standard deviation. The total number of realisations required depends on the number of bins used. On the other hand, each realisation of the parametric-aleatoric simulation produces a continuous probability distribution, therefore no binning is required and the number of realisations can be smaller. Nonetheless, it is important to run a sufficient number of realisations to ensure that the Monte Carlo simulation has fully captured the uncertainty in the resulting probability distribution. Convergence was verified by examining the evolution of the distribution mean and standard deviation as the number of Monte Carlo realisations was increased (see Section 2.4.7).

Execution times depended strongly on the scenario simulated. The simulations presented in the next section take approximately 60 minutes each, running on a 20-core desktop computer. This corresponds to 0.4 seconds per realisation for the aleatoric-parametric calculation and 0.04 seconds for the parametric only calculation. Individual realisations of the parametric only calculation are faster than the aleatoric-parametric calculation because only a single wait-time value is returned, whereas in the aleatoric-parametric calculation, gamma functions must be evaluated in order to construct the wait-time probability distribution for each realisation. Since the Monte Carlo method is easily parallelised, execution time decreases in inverse proportion to the number of cores available.

The prompt neutron lifetime has a particularly significant impact on the required computation time, as shorter prompt neutron lifetimes increase the stiffness of the ODEs that must be computed in order to calculate the gamma distributions. Williams (2016) observed that the wait-time proba-

bility distribution is sometimes insensitive to the prompt neutron lifetime; in cases where the relative standard deviation in the neutron population (or detector count) reaches a constant value before the probability of reaching the threshold value has risen above a negligible value. In these cases, the execution time can be reduced by selecting a longer prompt neutron lifetime, thereby reducing the stiffness of the system of ODEs. This technique was used to accelerate the execution of the simulations presented in Section 2.4.2.

2.2.4.3 Mean and Standard Deviation of the Distributions

The means and standard deviations were calculated for each of the wait-time probability density functions obtained from the Monte Carlo uncertainty quantification. The method used to calculate these values depended on the type of distribution.

For the aleatoric and aleatoric-parametric distributions, which are continuous distributions, the mean wait-times and standard deviations were calculated by numerically integrating the following expressions using Simpson's rule,

$$\mu = \int t' P(t') dt', \quad (2.2.19)$$

$$\sigma^2 = \int t'^2 P(t') dt' - \mu^2, \quad (2.2.20)$$

where μ is the mean wait-time, σ is the standard deviation in the wait-time and $P(t)$ is the absolute probability of exceeding the wait-time threshold at time t .

For the parametric only distributions, which are discrete, the mean wait-times and standard deviations were calculated from the following expressions,

$$\mu = \frac{1}{N_{rn}} \sum_{i=1}^{N_{rn}} t_i, \quad (2.2.21)$$

$$\sigma^2 = \frac{1}{N_{rn}} \sum_{i=1}^{N_{rn}} (t_i - \mu)^2, \quad (2.2.22)$$

where N_{rn} is the number of Monte Carlo realisations and t_i is the wait-time calculated in the i th realisation.

2.3 Case Study I: The Y-12 Accident

The gamma distribution method was applied to predict the timing of the first power excursion in the criticality accident that occurred in 1958 at the Y-12 National Security Complex in Oak Ridge,

Tennessee. As with most criticality accidents, there is some uncertainty around the exact conditions (flow rates, concentrations, etc.) prior to the accident. The impact of uncertainty in the flow rate of the uranium-rich solution will be examined by means of Monte Carlo uncertainty quantification.

2.3.1 Description of the Accident

Descriptions of the 1958 Y-12 accident can be found in Patton et al. (1958), Knief et al. (1985) and McLaughlin et al. (2000), among other sources, and a brief summary of the accident is given in Section 1.1.2.1. A description of the accident will not be repeated here, except to note an observation of McLaughlin et al. (2000) that the fissile liquid at Y-12 may have already reached a prompt critical configuration by the time of the first power peak. This feature makes an analysis using the method presented in this chapter highly relevant.

2.3.2 Model Parameters

The aim of the model is to obtain the probability distribution of the wait-time between the system reaching criticality and the fission rate exceeding some pre-defined threshold. It is estimated in Zamacinski et al. (2014) that the maximum fission rate during the first power peak was between 10^{16} and 10^{17} fissions per second. Preliminary calculations indicate that this fission rate is likely to have occurred after prompt criticality was reached. The gamma distribution method has not been validated in the prompt critical region so the threshold value will be set several orders of magnitude lower than the peak power level so that the delayed supercritical phase of the excursion may be examined.

The equations for the mean and covariances, derived in Williams (2016) from the forward form of the probability generating function, will be used to determine the time-dependent mean and standard deviation of the neutron population which characterise the gamma function. These equations do not include thermal-hydraulic feedback so they are only valid for the period before the fission power output rises to a level at which feedback becomes significant. This is another reason to set the wait-time fission rate threshold at a relatively low level so that the power output is low enough that thermal-hydraulic feedback may be neglected.

Delayed neutron precursors are represented in 6 groups using the same parameters as those used by Zamacinski et al. (2014) for their point kinetics model of Y-12. The reactivity profile as a function of time is also taken from Zamacinski et al. (2014), as is the mass and concentration of ^{235}U in the fuel solution. Zamacinski et al. determined that the prompt neutron lifetime varied approximately linearly from $4.1 \times 10^{-5}\text{s}$ at the start of the transient, to $5.5 \times 10^{-5}\text{s}$ at the end. Equation 54 from

Zamacinski et al. (2014) was used to model the prompt neutron lifetime in this analysis.

The probability distribution for the number of neutrons released per fission was taken from Table 1 of Zucker and Holden (1986).

An analysis of the various phenomena contributing to the intrinsic neutron source in uranium-fuelled reactors with non-irradiated fuel can be found in Harris (1960). The report identifies three main sources of neutrons,

1. spontaneous fission of ^{235}U and ^{238}U ,
2. (α, n) interactions where α particles emitted in radioactive decay of ^{238}U induce neutron emission in light nuclei,
3. cosmic ray induced emission of neutrons from within the fuel solution.

Experimental measurements of the intrinsic neutron source of solutions of uranyl nitrate can be found in Hankins (1966) and Seale and Anderson (1991). Hankins measured the intrinsic neutron source of a flask containing one litre of uranyl nitrate, with a concentration of 53 gU dm^{-3} and an enrichment of approximately 93%. The intrinsic neutron source measured was 5.6 n/s for the one litre volume of solution. Seale and Anderson measured the intrinsic neutron source of a much more concentrated solution of uranyl nitrate containing 420 gU dm^{-3} . The uranium enrichment was the same at 93%. The resulting intrinsic neutron source measured was equivalent to 21.4 n/s for a one litre volume of solution.

Of the two experiments, the concentration and enrichment of the Hankins experiment is far closer to the conditions of the Y-12 accident, as reported in Zamacinski et al. (2014): the concentration of uranium at the start of the accident is predicted to be approximately 40.1 gU dm^{-3} and the uranium enrichment was approximately 90%. Extrapolating the results of Hankins to the volume of solution at the start of the Y-12 accident ($V = 56.2 \text{ dm}^3$) gives a total intrinsic source of 315 n/s.

It should be noted that there is considerable uncertainty in this figure as it relates to the Y-12 accident. Firstly, it is not clear whether or not the uranyl nitrate solution present at the Y-12 accident had been previously irradiated. If it had been, there would be a higher concentration of radioactive isotopes, whose decay would contribute to an increased intrinsic neutron source through (α, n) reactions. Secondly, as noted above, the actual uranium concentration was slightly lower than the value in Hankins' experiment, which would be expected to reduce the intrinsic source due to reduced alpha emission from ^{238}U as well as reduced spontaneous fission.

Due to the uncertainty in the intrinsic neutron source, results will be presented for two intrinsic source strengths: 30 n/s and 315 n/s, so that the degree of sensitivity to the intrinsic source strength can be examined.

2.3.3 Parametric Uncertainty

In order to examine the impact of uncertainty in the fuel solution flow rate on the resulting wait-time probability distribution, uncertainty was applied to the reactivity insertion rate. The reactivity insertion rate was modelled using Equation 2.3.1, based on Equation 53 from Zamacinski et al. (2014), who calculated the reactivity as a function of time from the available hydraulic and geometric data using MCNP. The randomly varying parameter α was included to make the reactivity insertion rate uncertain. Its value was randomly varied between 0.9 and 1.1 according to a uniform probability distribution. The time axis of the equation has also been modified so that the system reaches criticality at $t = 0$.

$$R_{ex}(t) = 1.8636 \times 10^{-2}\alpha t - 5.5338 \times 10^{-5}(\alpha t)^2 + 6.8570 \times 10^{-8}(\alpha t)^3 \quad (2.3.1)$$

Figure 2.3.1 shows the system reactivity as a function of time, including the non-randomised reactivity profile corresponding to $\alpha = 1$, as well as minimum and maximum values corresponding to $\alpha = 0.9$ and $\alpha = 1.1$. Considering, for example, the effect of a value of $\alpha > 1$, two effects are notable. Not only does it result in the system reactivity rising faster, making shorter wait-times more likely, it also means the system is more deeply subcritical during the time before criticality is achieved. The latter effect offsets the first to some degree, because at the moment of criticality is reached, the population of delayed neutron precursors will be smaller in a system with large α than in a system with small α .

2.3.4 Deterministic Wait-Time and Aleatoric Uncertainty

The deterministic wait-time can be obtained by solving the system of ODEs referred to in Section 2.2.1 for the moment at which the expected fission rate $\bar{F}(t)$ crosses the wait-time threshold of 2×10^9 fissions per second. The value obtained is 45.7s for an intrinsic source strength of 30 n/s, and 43.0s for an intrinsic source strength of 315 n/s. Unsurprisingly, the stronger intrinsic source results in a shorter wait-time.

Figure 2.3.2 shows the aleatoric uncertainty associated with these wait-times; that is uncertainty due to the stochastic nature of fission chain growth, assuming certain input parameters. Wait-time

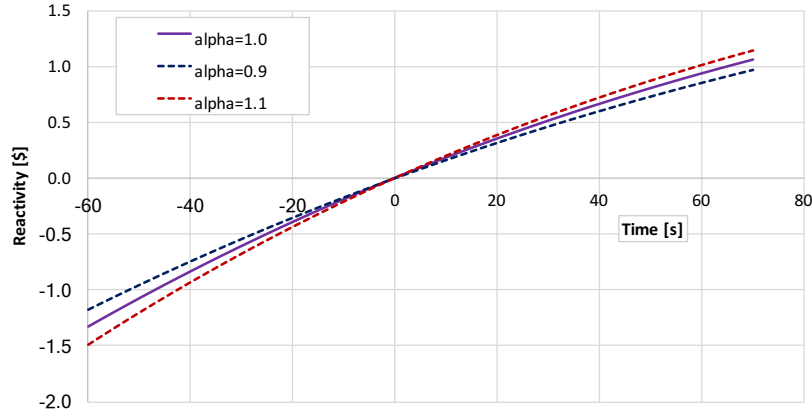


Fig. 2.3.1. Reactivity as a function of time, showing maximum and minimum values corresponding to $\alpha=0.9$ and $\alpha=1.1$.

probability distributions, calculated using the gamma distribution method and saddlepoint method, are shown for comparison. The predicted distributions are similar: for the 30 n/s case, the gamma distribution method gives a mean (and standard deviation) of 47.0s (2.1s) and the saddlepoint method predicts 47.1s (2.6s). For the 315 n/s case, the gamma distribution method gives a mean (and standard deviation) of 43.1s (0.8s) and the saddlepoint method predicts 43.0 (0.8s).

2.3.5 Parametric Uncertainty Quantification

Figure 2.3.3 shows the four probability distributions (deterministic, aleatoric, parametric and aleatoric-parametric) for the wait-time to reach 2×10^9 fissions per second in the Y-12 accident. Figure 2.3.3a shows the probability distributions for the case where the intrinsic neutron source strength is 30 n/s and Figure 2.3.3b shows the distributions for the 315 n/s case.

Despite the uniform probability distribution adopted for the randomisation of the reactivity insertion rate, the parametric wait-time probability distributions are slightly biased in favour of shorter wait-times. This is because the impact of varying α on the wait-time predicted by the deterministic model is not linear.

The parametric uncertainty makes the overall combined (aleatoric-parametric) probability distributions broader, compared to the aleatoric probability distributions, however, in both cases, there is no significant change in the mean. For 30 n/s case, the mean (and standard deviation) of the aleatoric-parametric wait-time probability distribution is 47.1s (2.9s) compared to 47.0s (2.1s) for the aleatoric distribution. For the 315 n/s, the aleatoric-parametric distribution has a mean (and standard deviation) of 43.3s (2.0s) compared to 43.1s (0.8s) for the aleatoric distribution.

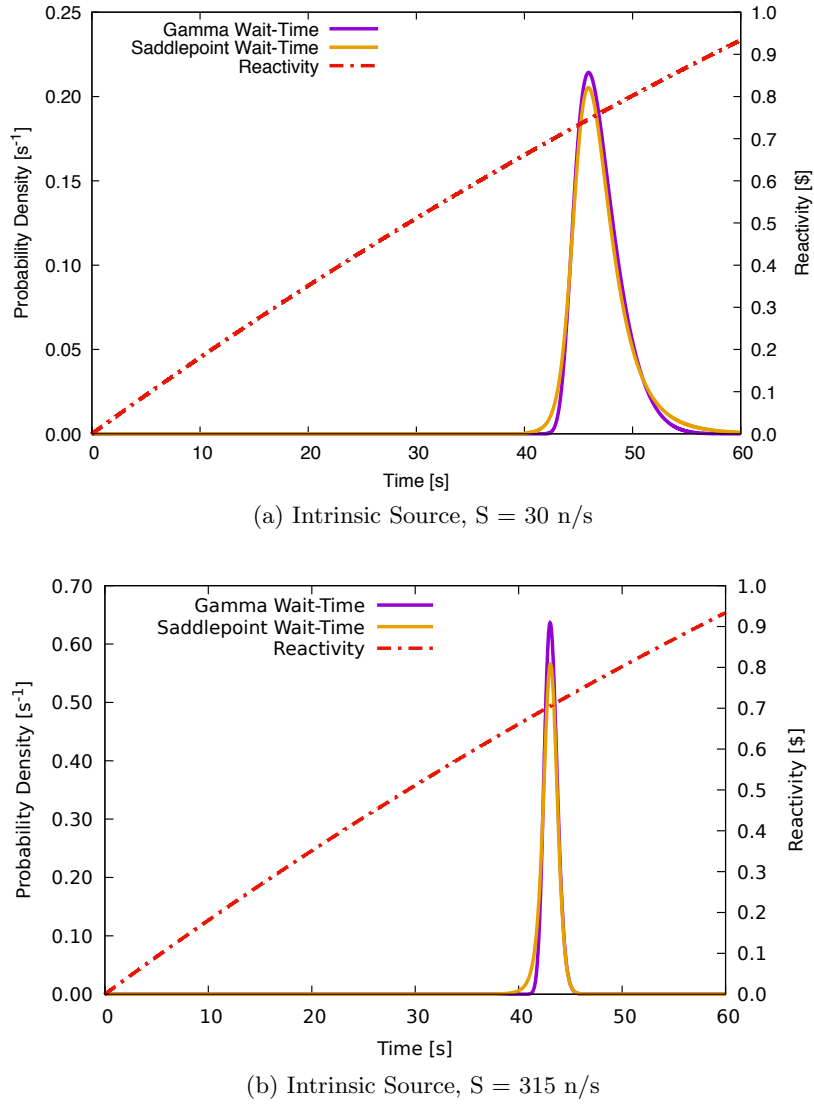
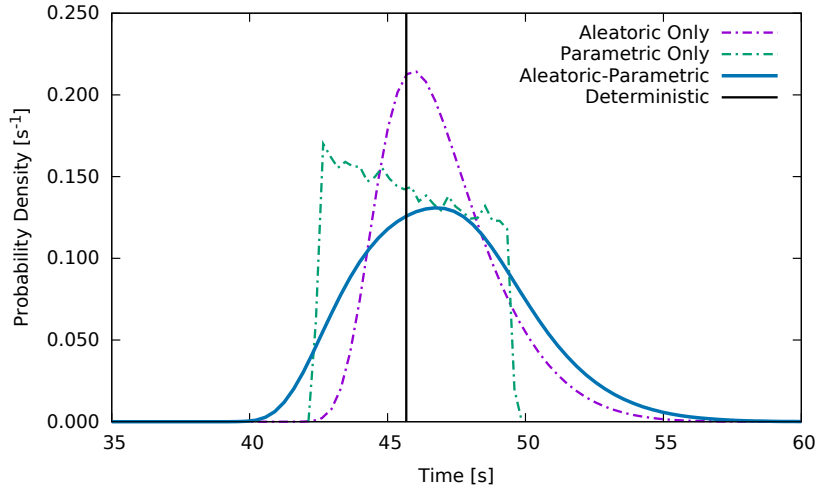


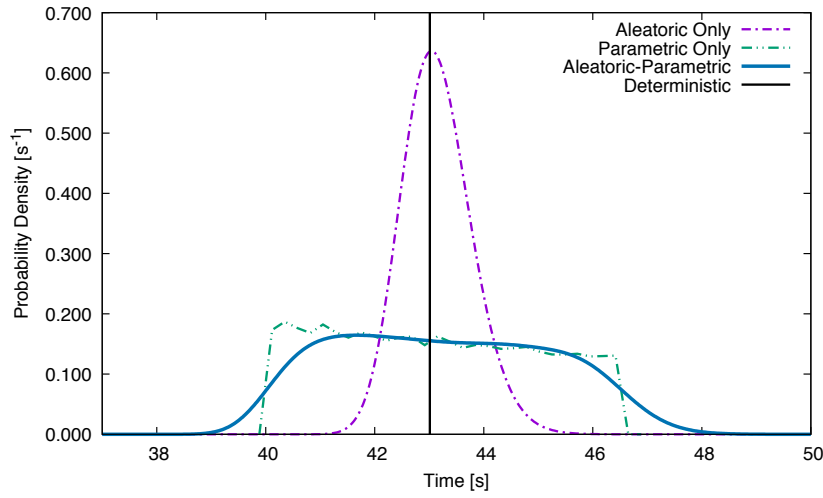
Fig. 2.3.2. Wait-time probability distributions for the time taken between reaching criticality and the fission rate exceeding 2×10^9 fissions per second in the Y-12 accident.

The parametric uncertainty has a greater impact on the standard deviation of the probability distribution in 315 n/s case. This is because there is less aleatoric uncertainty, so the parametric uncertainty is more significant by comparison. This effect is clearly visible in Figure 2.3.3b, where the combined aleatoric-parametric uncertainty is dominated by parametric uncertainty, whereas in Figure 2.3.3a, the combined aleatoric-parametric distribution is influenced in approximately equal parts by the aleatoric and parametric uncertainties.

These results show that a small degree of uncertainty in the reactivity insertion rate results in a significant increase in the overall uncertainty in the wait-time.



(a) Intrinsic Source, $S = 30$ n/s



(b) Intrinsic Source, $S = 315$ n/s

Fig. 2.3.3. Wait-time probability distributions for the Y-12 accident comparing the deterministic wait-time with models including parametric uncertainty in the reactivity insertion rate, aleatoric uncertainty, and combined parametric-aleatoric uncertainty.

2.3.6 Summary of Results

The mean wait-times and standard deviations discussed in this section are summarised in Table 2.3.

	Deterministic	Aleatoric	Parametric	Aleatoric-Parametric
Y-12 ($S=30$ n/s)	45.7s	47.0s (2.1s)	45.8s (2.0s)	47.1s (2.9s)
Y-12 ($S=315$ n/s)	43.0s	43.1s (0.8s)	43.1s (1.9s)	43.3s (2.0s)

TABLE 2.3

Summary of calculated wait-times to reach a fission rate 2×10^9 s⁻¹ for the simulation of the Y-12 accident. Mean values shown with standard deviation in brackets.

2.4 Case Study II: The Caliban Experiments

The Caliban reactor is a fast burst reactor constructed of solid metal disks of uranium/molybdenum with a ^{235}U enrichment of 93.5%. Authier et al. (2014) describe a series of experiments in which varying amounts of reactivity were inserted into the reactor so that the wait-time could be measured. It has already been demonstrated in Williams (2016) that the gamma distribution method to determine the wait-time probability distribution is accurate for these experiments and it is clear from Figure 2.2.5 that these experiments fall within the range of applicability of the gamma distribution method. A photograph of the Caliban reactor is shown in Figure 2.4.1.

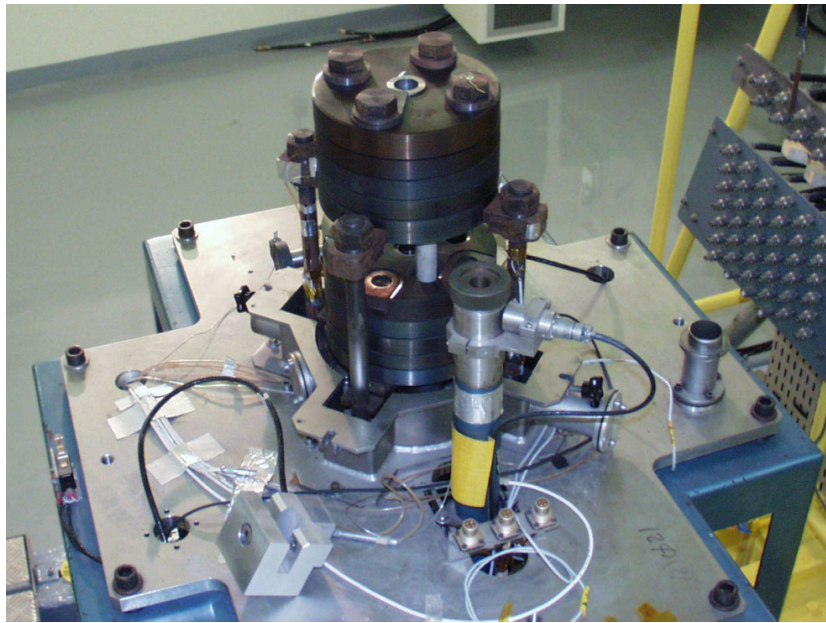


Fig. 2.4.1. Photograph of the Caliban reactor. Reproduced from Authier et al. (2014) with permission of the rights holder, Taylor & Francis (www.tandfonline.com).

2.4.1 Description of the Experiments

Full details of the experimental set-up can be found in Authier et al. (2014). Reactivity control in the Caliban reactor is achieved in part by means of calibration rods and a safety block. The calibration rods are set so that the desired degree of supercriticality is achieved when the safety block is lifted to its maximum position. The reactor is also equipped with a burst rod but this was not used for the delayed supercritical experiments modelled here.

Each delayed supercritical excursion was initiated by raising the safety block progressively closer to the reactor until it was in its maximum position. According to Figure 3 of Authier et al. (2014) the safety block is moved in 17 small movements over a period of 62 seconds until the block is in the

desired delayed supercritical position. In the model described here it was chosen to lump together some of these movements and the 17 movements of the safety block were approximated by 6 small ramp reactivity insertions (see Equation 2.4.1).

Authier et al. count the wait-time from the moment the safety block reaches its maximum position to the time at which the neutron detector indicates a fission rate of 2×10^9 fissions per second. According to Table I of Authier et al. (2014) the reactor reaches a supercritical configuration approximately 4 seconds before the safety block arrives at its maximum position.

2.4.2 Model Parameters

The experiment selected for uncertainty quantification was the 0.272\$ reactivity insertion. The wait-time threshold was set to 2×10^9 fissions per seconds, the same value used by Authier et al. (2014). Delayed neutron precursors are represented in 6 groups using the parameters for fast fission of ^{235}U from Keepin (1965).

$$R_{ex}(t) = \begin{cases} -16.7\$ & \text{for } t \leq -62.1s \\ -16.7\$ + \frac{t+62.1s}{16.7s} \times 1.7\$ & \text{for } -62.1s < t \leq -45.4s \\ -15.0\$ + \frac{t+45.4s}{16.7s} \times 3.6\$ & \text{for } -45.4s < t \leq -28.8s \\ -11.5\$ + \frac{t+28.8s}{16.7s} \times 6.6\$ & \text{for } -28.8s < t \leq -12.1s \\ -4.93\$ + \frac{t+12.1s}{8.1s} \times 4.9\$ & \text{for } -12.1s < t \leq -4.0s \\ 0.066\$ + \frac{t+4.0s}{4.0s} \times 0.206\$ & \text{for } -4.0s < t \leq 0.0s \\ 0.272\$ & \text{for } t > 0.0s \end{cases} \quad (2.4.1)$$

The reactivity profile is shown in Equation 2.4.1. It was constructed using data from Table 1 of Authier et al. (2014). The final reactivity increase in the table was omitted, as this corresponds to the insertion of the burst rod (prompt critical experiments only), and the reactivity values were adjusted by +0.077\$ so that the final reactivity corresponded to 0.272\$. The beta effective used in the model was 0.00659. For the intrinsic neutron source of the Caliban reactor, Authier et al. (2014) used a value of 200 n/s in their model, so the same value will be used for this analysis. No external source was present during the experiments.

The prompt neutron lifetime in the Caliban reactor has been evaluated as 1.2×10^{-8} s (see Casoli et al. (2009)). Attempting to model the reactor with such a short prompt neutron lifetime results in a stiff set of ODEs, which increases the computational expense of the Monte Carlo analysis and

limits the maximum number of realisations achievable. It is noted however, in Williams (2016), that the relative standard deviation in the cumulative detector count reaches a constant value, becoming insensitive to prompt neutron lifetime within 100 seconds of reaching criticality. This implies that the wait-time probability distribution is also insensitive to prompt neutron lifetime after this point. Since the expected wait-time is much longer than 100 seconds, it should be possible to increase the prompt neutron lifetime to reduce the execution time of the computational model, without any impact on the predicted wait-time probability distribution.

This hypothesis was tested by comparing the wait-time probability distribution predicted with a prompt neutron lifetime of 12 ns to a simulation with a prompt neutron lifetime of 65 μ s. The results, shown in Figure 2.4.2, confirm the insensitivity of the wait-time probability distribution predicted for the Caliban experiment to the prompt neutron lifetime.

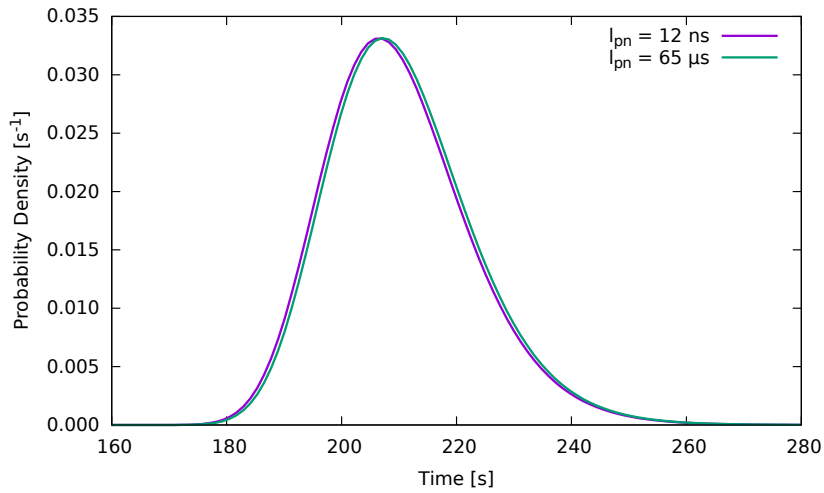


Fig. 2.4.2. Wait-time probability distribution for a cumulative detector count corresponding to a fission rate of 2×10^9 fissions per second with prompt neutron lifetimes of 12 ns and 65 μ s.

2.4.3 Parametric Uncertainty

Two areas of parametric uncertainty were examined for the Caliban experiments: time taken to move the safety block and the yields of the delayed neutron precursor (DNP) groups.

Equation 2.4.1 shows the reactivity profile representing the movement of the safety block in the Caliban experiments. The final ramp insertion lasts 4.0 seconds and takes the reactor from a slightly supercritical state (0.066\$) to the target reactivity of 0.272\$, for a reactivity insertion rate of 5.15×10^{-2} \$/s. The duration of this step was varied between 0 and 20 seconds according to a uniform probability distribution so that the reactivity insertion rate varied from a step to a ramp of 1.03×10^{-2} \$/s.

Group	Half-Life	Yield (β_i)	St. Dev.	Lower Bound	Upper Bound
	[s]	<i>dim.</i>	[s]	<i>dim.</i>	<i>dim.</i>
1	54.5	2.50×10^{-4}	0.003	2.16×10^{-4}	2.85×10^{-4}
2	21.8	1.40×10^{-3}	0.005	1.35×10^{-3}	1.46×10^{-3}
3	6.00	1.24×10^{-3}	0.016	1.06×10^{-3}	1.42×10^{-3}
4	2.23	2.68×10^{-3}	0.007	2.60×10^{-3}	2.76×10^{-3}
5	0.496	8.44×10^{-4}	0.008	7.52×10^{-4}	9.35×10^{-4}
6	0.179	1.71×10^{-4}	0.003	1.37×10^{-4}	2.06×10^{-4}

TABLE 2.4

Upper and lower bounds of randomised delayed neutron precursor yields.

The yields of the delayed neutron precursor groups are subject to some experimental uncertainty in their measurement. Table I of Keepin et al. (1957) states the standard deviation associated with each yield. From this value, an upper and lower bound (see Table 2.4) was calculated by assuming a uniform probability distribution. The values of each yield were then varied randomly within these ranges.

The total delayed neutron fraction, β , was calculated for each realisation as the sum of all precursor group yields. Its value therefore also varied, with a minimum of 0.00611 and a maximum of 0.00707. The reactivity profile was fixed before randomisation of the delayed neutron precursor yields so that the time-dependent k_{eff} was the same for each realisation. The reactivity of the reactor measured in dollars therefore varied with the changing value of β . For the safety block in its final position, the reactivity in dollars varied between a minimum of 0.254\$ and a maximum of 0.293\$.

2.4.4 Deterministic Wait-Time and Aleatoric Uncertainty

The deterministic wait-time for the system to reach 2×10^9 fissions per seconds is 207s. This value ignores both aleatoric, and any parametric uncertainty. When aleatoric uncertainty was modelled using the gamma distribution method, a probability distribution was obtained, with mean (and standard deviation) of 211s (12.8s). The distribution obtained is shown in Figure 2.4.3.

2.4.5 Parametric Uncertainty Quantification

2.4.5.1 Safety Block Manipulation Time

Adding parametric uncertainty to the timing of the safety block movement in the deterministic wait-time model produces the parametric probability distribution shown in Figure 2.4.4. The parametric probability distribution has mean (and standard deviation) of 202s (5.0s).

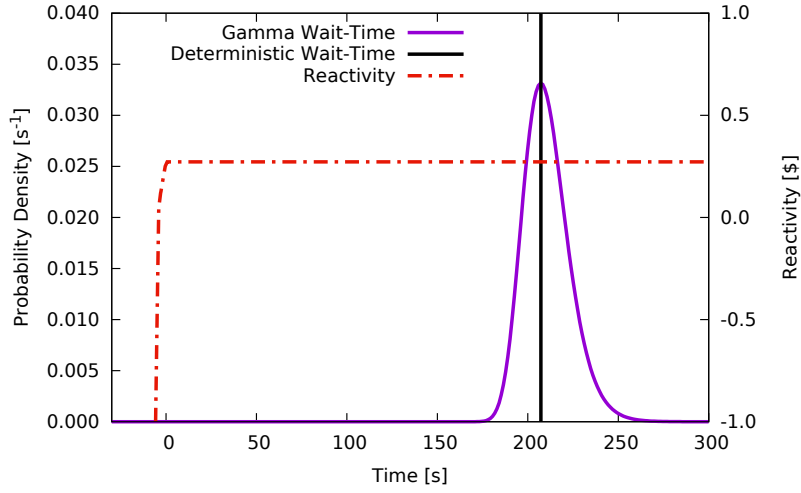


Fig. 2.4.3. Deterministic wait-time and aleatoric wait-time probability distributions for a cumulative detector count corresponding to a fission rate of 2×10^9 fissions per second in the Caliban experiment.

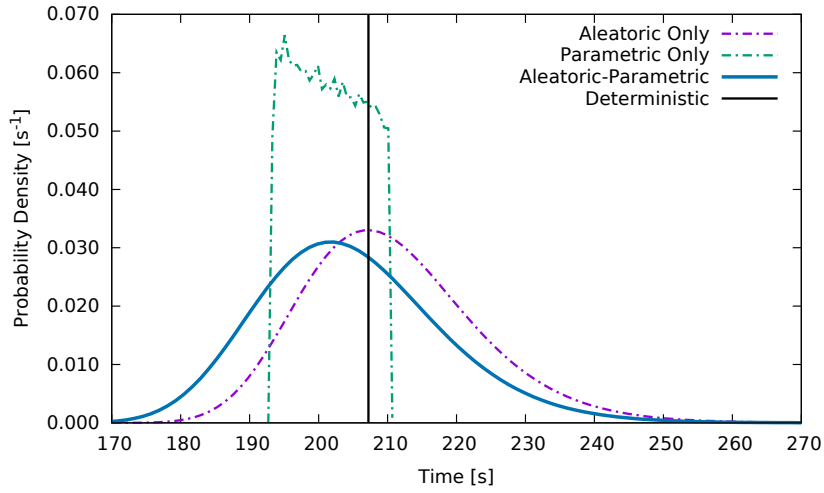


Fig. 2.4.4. Wait-time probability distributions for the Caliban experiment comparing the deterministic wait-time with models including parametric uncertainty in the timing of the safety block movement, aleatoric uncertainty, and combined parametric-aleatoric uncertainty.

The results confirm that the uncertainty applied to the timing of the final movement of the safety block has a significant impact on the resulting wait-time. This is because the system reaches criticality before the safety block reaches its final position. During this time the population of delayed neutron precursors in the system is increasing exponentially. The time taken to carry out this movement therefore will determine the delayed neutron precursor population at the start of the experiment with a resulting impact on the wait-time observed.

The aleatoric-parametric distribution shown in Figure 2.4.4 shows the impact of the parametric uncertainty when it is combined with the aleatoric uncertainty inherent in the neutron population growth rate. The aleatoric-parametric probability distribution has a mean (and standard deviation) of 205s (13.4s) so the effect of the parametric uncertainty is to make the probability distribution

broader and shift it slightly in favour of shorter wait-times.

2.4.5.2 Delayed Neutron Precursor Yields

The uncertainty applied to the yields of the delayed neutron precursor groups results in the parametric probability distribution shown in Figure 2.4.5. This parametric uncertainty applied to the deterministic wait-time (without aleatoric uncertainty) results in a mean (and standard deviation) of 207s (5.2s).

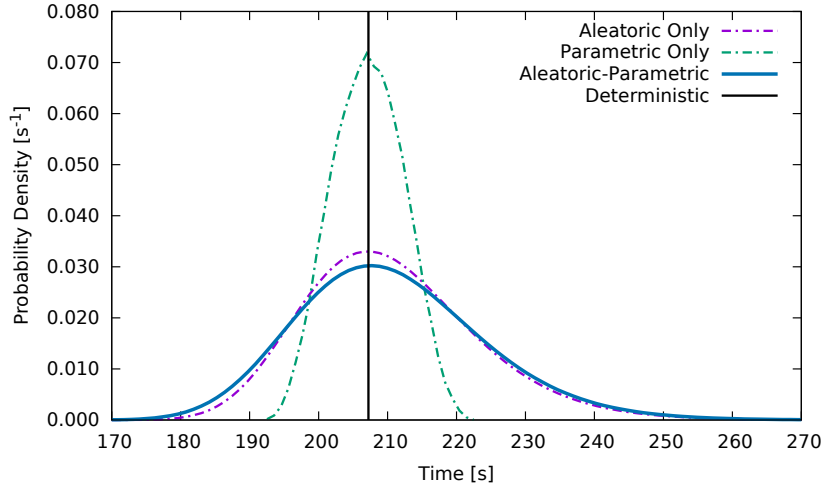


Fig. 2.4.5. Wait-time probability distributions for the Caliban experiment comparing the deterministic wait-time with models including parametric uncertainty in the delayed neutron precursor group yields, aleatoric uncertainty, and combined parametric-aleatoric uncertainty.

The aleatoric-parametric distribution shown in Figure 2.4.5 shows the impact of the parametric uncertainty when it is combined with the aleatoric uncertainty inherent in the neutron population growth rate. The aleatoric-parametric probability distribution has the same mean value of 211s as the aleatoric-only distribution but the standard deviation is increased slightly from 12.8s to 13.8s. The uncertainty in the measurement of the delayed neutron precursor yields therefore has a small but non-negligible impact on the overall wait-time probability distribution.

2.4.6 Summary of Results

The mean wait-times and standard deviations discussed in this section are summarised in Table 2.5.

	Deterministic	Aleatoric	Parametric	Aleatoric-Parametric
Caliban (safety block)	207s	211s (12.8s)	202s (5.0s)	205s (13.4s)
Caliban (DNP yields)			207s (5.2s)	211s (13.8s)

TABLE 2.5

Summary of calculated wait-times to reach a fission rate $2 \times 10^9 \text{ s}^{-1}$ for the simulation of the Caliban experiments. Mean values shown with standard deviation in brackets.

2.4.7 Convergence of the Monte Carlo Method

The convergence of the aleatoric and aleatoric-parametric distributions was tested by observing the evolution in the mean and standard deviation of the combined distribution as the number of realisations was increased. A sufficient number of realisations must be run so that the mean and standard deviation of the distributions become relatively constant, without any upwards or downwards trend.

Figure 2.4.6a shows the convergence of the mean and standard deviation for the aleatoric-parametric distribution predicted for the Y-12 accident. Significant variations are observed in the mean and standard deviation of the aleatoric-parametric distribution over the first 5,000 realisation and there is a notable downward trend in the standard deviation between 1,000 and 5,000 realisations. Beyond 5,000 realisations, the mean and standard deviation remain relatively constant, indicating that the Monte Carlo simulation has reached an acceptable degree of convergence.

The parametric distribution was calculated based on 100,000 realisations. Figure 2.4.6b indicates the degree of convergence in the mean and standard deviation for the Y-12 simulation.

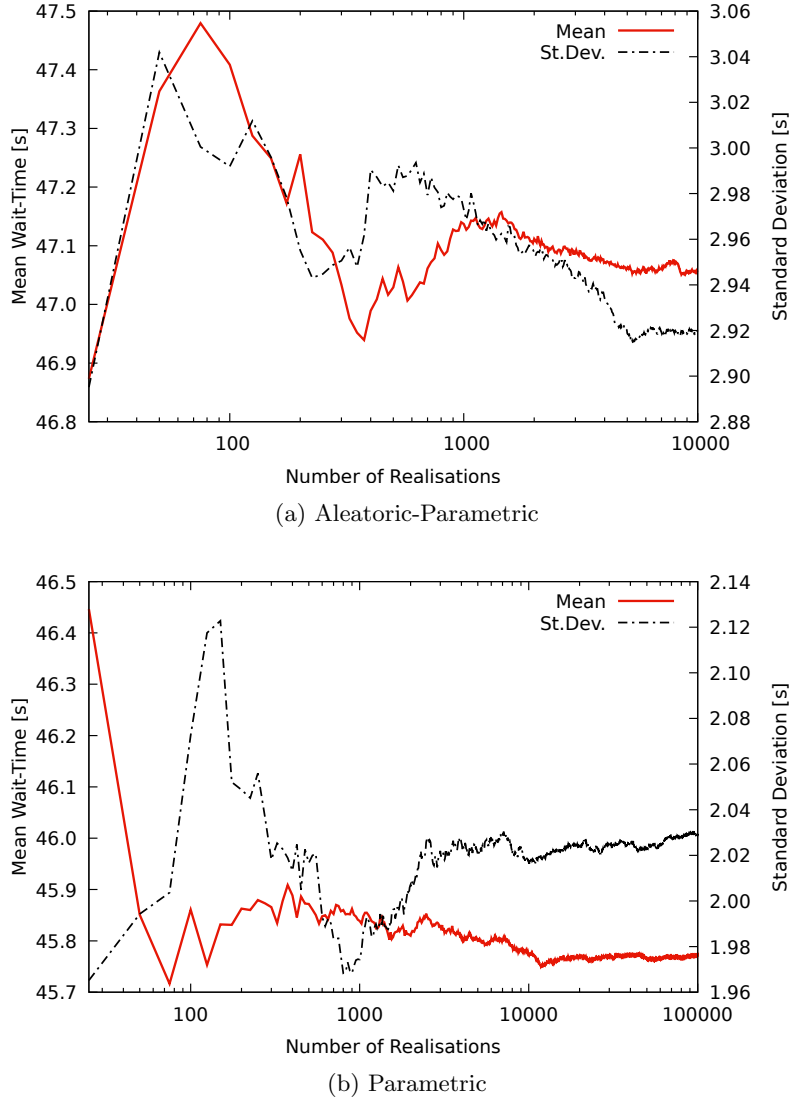


Fig. 2.4.6. Evolution of the mean and standard deviation of the aleatoric-parametric wait-time probability distribution and the parametric probability distribution, with increasing number of Monte Carlo realisations, for the Y-12 accident simulation. Points shown at intervals of 25 realisations.

2.5 Conclusions

A non-intrusive method has been demonstrated for quantifying the impact of parametric uncertainty on the probability distribution for the wait-time in a delayed supercritical system. The method makes use of the computational efficiency of the gamma distribution method to determine the wait-time probability distribution which makes uncertainty quantification feasible via the Monte Carlo method.

This method of uncertainty quantification has been applied to the criticality accident that occurred in 1958 at the Y-12 National Security Complex in Oak Ridge, Tennessee. Uncertainty in the flow rate of liquid into the drum was modelled by varying the reactivity insertion rate, and the resulting uncertainty in the predicted wait-time probability distribution was evaluated. Simulations were run

with two different values of the intrinsic neutron source strength in order to demonstrate the sensitivity of the wait-time probability distributions (aleatoric, parametric and combined aleatoric-parametric) to this parameter.

The method has also been applied to a model of an experiment on the Caliban reactor where two areas of uncertainty were examined. In the first case, the method was used to quantify the impact of uncertainty in the timing of the movement of the reactor safety block on the predicted wait-time probability distribution. The results show significant sensitivity of the wait-time probability distribution to the timing of the safety block movement. In the second Caliban case, the model was used to quantify the impact of epistemic uncertainty in the yields of delayed neutron precursor groups on the predicted wait-time probability distribution. The results show that reported uncertainty in the measurement of the delayed neutron precursor group yields is sufficient to have a small but significant impact on the wait-time probability distribution.

The range of applicability within which the gamma distribution method can be relied upon to produce an accurate prediction of the wait-time probability distribution has been examined. A range of applicability for a reactivity insertion in a hypothetical system is presented in terms of the magnitude and rate of the reactivity insertion, the strength of the neutron source and the lifetime of prompt neutrons in the system.

Wait-time probability distributions predicted by the gamma distribution method have been verified against predictions made using the more rigorous saddlepoint method. A method for rapid solution of the saddlepoint method using Newton-Raphson iterations to accelerate convergence has been demonstrated.

Chapter 3

Linear Energy Transfer (LET) of Fission Fragments of ^{235}U and Nucleation of Gas Bubbles in Aqueous Solutions of Uranyl Nitrate

3.1 Introduction

Much of the work presented in this chapter, including tables and figures, is reproduced from Winter et al. (2020a).

When the nucleus of a fissile atom undergoes nuclear fission in aqueous solution, the fully ionised fission fragments are emitted at high velocity from the site of fission. Except for a very small number of ternary and quaternary fissions (Gönnenwein (2004)), each fission event results in the creation of two charged fission fragments. These fragments travel in opposite directions to each other, creating tracks of radiolysis products in their wake. Lane et al. (1958) notes that the quantities and proportions of radiolysis products created depends on the linear energy transfer (LET) of the fission fragments.

3.1.1 Nucleation of Bubbles in Aqueous Fissile Solutions

Much work was done in the fifties, sixties and seventies to examine the mechanics of fission tracks in aqueous fissile solutions and their role as nucleation sites for bubbles of radiolytic gas and steam.

Ghormley (1958) of Oak Ridge National Laboratory exposed aqueous solutions of uranyl sulphate to fission recoil particles and measured the maximum superheat that could be applied before the appearance of stable bubbles. The purpose was to test the hypothesis that water vapour created due to the energy transfer from the fission recoil particles to the water would create tiny bubbles that could act as nucleation sites for boiling. It was noted that a significant superheat was required before visible bubbles appeared, from which it was concluded that bubbles measuring approximately $1.4\ \mu\text{m}$ in diameter were generated along the fission tracks and that visible bubbles would only be observed if the liquid superheat was sufficient for water to vaporise at the interface of bubbles of this size. The $1.4\ \mu\text{m}$ diameter of the fission track steam bubbles was inferred from the degree of superheat required for bubble nucleation. It was calculated that approximately 28 MeV would be required to vaporise enough water to create the bubble and that this amount of energy would be deposited by a fission recoil particle over approximately $4\ \mu\text{m}$ of track.

Ghormley's work was based on the thermal spike theory of bubble nucleation in fissile liquids. This work was extended by Norman and Spiegler (1963) who, using an energy balance for the creation of vapour bubbles in fissile aqueous solutions, predicted the size of bubbles deposited along the fission track as a function of LET. Norman and Spiegler notably extended the theory, previously concerned only with steam bubble generation in superheated solutions, to the formation of hydrogen gas bubbles in subcooled aqueous solutions.

Spiegler describes their theory of gas bubble formation in subcooled aqueous solutions in a technical report (Spiegler et al. (1962)). The theory can be summarised as follows:

- a jet of vapour is formed along the track of a fission fragment as energy is transferred from the fission fragment to the water surrounding it;
- the jet of water vapour breaks up into sections which become distinct vapour bubbles;
- if the solution is subcooled the water vapour condenses on a timescale of the order 10^{-8} seconds;
- a bubble of hydrogen is left which, in a solution where the dissolved gas concentration is relatively low, will collapse on a timescale of the order $\sim 10^{-6}$ seconds.

It is noted in Spiegler et al. (1962) that if the lifetime of the bubbles had been any longer than those indicated above, then a detectable rise in pressure would have been observed before the appearance of visible gas voids during their experiments on fissile solutions. The bubble lifetimes indicated are therefore inferred from the absence of a detectable rise in pressure.

The hydrogen bubble that remains will collapse unless the concentration of dissolved gas in solution

is sufficient to establish a net flow of gas into the bubble. At this “critical concentration”, the bubble will grow, leading to the appearance of voids due to radiolytic gas. The critical concentration of hydrogen in the liquid phase depends on the partial pressure of hydrogen gas in the bubble and the solubility of hydrogen in the fuel solution. Where no other gases are presented, it can be determined from:

$$C_{\text{crit}} = H_{\text{H}_2,\text{sol}} P_{\text{H}_2} = H_{\text{H}_2,\text{sol}} \left(P_l + \frac{2\sigma_s}{r_b} \right) y_{\text{H}_2} \quad (3.1.1)$$

where C_{crit} is the critical concentration of hydrogen gas in the fuel solution, $H_{\text{H}_2,\text{sol}}$ is the Henry’s law constant for the solubility of hydrogen in the solution, P_{H_2} is the partial pressure of hydrogen inside the bubble, P_l is the liquid pressure, σ_s is the fuel solution surface tension, r_b is the bubble radius and y_{H_2} is the mole fraction of hydrogen gas inside the bubble.

Up until this point, the discussion has been limited to hydrogen gas only. However, nitrogen gas is also produced as a direct product of radiolysis of uranyl nitrate solutions and will also influence the size of the gas bubbles deposited in the tracks of fission fragments. However, Bidwell et al. (1956) showed the amount of nitrogen gas produced to be two orders of magnitude less than the quantity of hydrogen produced. Any effect on the size of bubbles produced is therefore expected to be negligible and will not be considered here.

Oxygen gas is also produced during radiolysis of aqueous fissile solutions. However, it is not a direct radiolysis product but a product of ancillary reactions which take place later. Therefore, oxygen gas production will not affect the initial size of radiolysis bubbles but it will affect the critical concentration at which these bubbles begin to grow. Critical concentrations quoted in this chapter are calculated with the assumption that the solution contains no dissolved oxygen. However, the effect of oxygen on the critical concentration will be examined in Chapter 5.

The work of Norman and Spiegler was examined in a study by Deitrich and Connolly (1973). Their experiments supported the hypothesis that particle LET is the factor determining the size of bubbles generated along fission tracks. However, they noted that the values predicted by the theory of Norman and Spiegler overestimated the superheat required to nucleate steam bubbles in their own experiments, and they proposed a modification to the characteristic track length over which bubbles are formed (see Section 3.2.1).

The theory described above relies on the assumption that hydrogen gas will nucleate on the bubbles created by fission fragments at a lower concentration than that required for homogeneous nucleation. It is well known that homogeneous nucleation in certain gas/liquid systems tends to occur at lower concentrations than current theory predicts, and it is therefore useful to consider whether homogeneous nucleation might occur in the case of a fissile liquid at concentrations lower than the critical

concentration discussed above.

An extensive review by Lubetkin (2003) of numerous theories to explain the discrepancy between the predictions of the classical theory and the relative ease with which homogeneous nucleation seems to occur, concluded that dissolved gas molecules act as surfactants, reducing the liquid surface tension, which in turn, reduces the concentration required to bring about homogeneous nucleation. Lubetkin notes that the surfactant effect is smallest for helium and also very small for hydrogen. For example, carbon dioxide has been shown to undergo homogeneous nucleation at concentrations as low as 5.4 times its atmospheric saturation concentration, whereas Lubetkin (2003) reports that hydrogen gas was found to require a concentration of at least 80 times saturation.

According to data from Norman and Spiegler (1963) and Spiegler et al. (1962), the critical concentration required for heterogeneous nucleation of hydrogen bubbles on fission tracks is approximately 28 times the saturation concentration of the solution. This is well below the concentration required for homogeneous nucleation to occur. Homogeneous nucleation can therefore be ruled out as a factor in the formation of gas voids in fissile solutions, lending further credibility to the thermal spike model.

3.1.2 Linear Energy Transfer of Charged Particles

The size of bubbles created on the tracks of fission fragments depends on the LET of the fragments as this determines the quantities of water vapour and hydrogen gas created. This was confirmed experimentally by Deitrich and Connolly (1973).

The LET of a fission fragment varies along the fission track and is a complex function of particle velocity, the stopping power of the medium with respect to that particle and the charge of the ionised particle (Tavernier (2010)). Unlike smaller charged particles which tend to retain their charge until they are almost stopped, Chadderton (1988) notes that fission fragments, which have an exceptionally large initial charge, de-ionise continuously along the track.

While there is a relatively large body of experimental data available in the literature for protons, electrons and alpha particles, there is relatively less for larger charged particles. This motivated Northcliffe and Schilling (1970) to look at ways of predicting stopping powers for larger particles by extrapolation of the experimental data available at the time. While more recent stopping power tables have been compiled for some ions, those of Northcliffe and Schilling remain unmatched in the open literature for the range of charged particles and media covered.

A 2003 review by Helmut and Schinner (2003) of available data and models for calculating the stopping powers of heavy ions found that the Northcliffe and Schilling tables provided good accuracy

at reproducing the general trends in stopping power, while failing to reproduce the Z_1 - and Z_2 -oscillations in stopping power observed as a function of particle (Z_1 -) and target medium (Z_2 -) atomic numbers. This is not surprising, since Northcliffe and Schilling extrapolated their values by assuming that the stopping power was a smooth function of the atomic numbers of the particles and target media. For this reason it was chosen to model the fission fragment LET using the software package SRIM (Ziegler et al. (2010)). SRIM is capable of predicting the Z_1 - and Z_2 - oscillations noted by Helmut and Schinner. For comparison, the LET profiles of the 6 highest-yielding fission fragments of ^{235}U were calculated using both SRIM and the tables of Northcliffe and Schilling. The comparisons can be found in Section 3.4 and confirm a relatively close agreement with some notable differences between the two methods.

The LET of a heavy charged particle, such as a fission fragment, is quite different from that of smaller charged particles. With electrons, protons and alpha particles, the LET often starts relatively low, remaining relatively constant for most of the length of the particle track, before increasing sharply to a peak, then dropping to zero. This peak, known as the Bragg peak, occurs because, even as the particle is losing energy towards the end of the track, its reduced velocity increases its ability to interact with passing matter, leading to an increase in the rate of energy transfer from the particle to the medium.

Fission fragments may be emitted with energy on the same order of magnitude as an alpha particle, however, fission fragments have much greater mass, and therefore much lower velocities. Since it is velocity which determines the ability of the particle to interact with, and transfer energy to, the matter surrounding it, the LET of fission fragments starts close to its maximum, and Bragg peaks in the LET profiles are either absent or very small (see Section 3.3). A notable difference between the LET profiles calculated using Northcliffe and Schilling compared to SRIM was that plateaus or peaks due to the Bragg peak effect were significantly less pronounced in the LET profiles predicted by SRIM.

3.2 Methodology and Data

The following section presents the methodology used to predict values for fission fragment LET and the resulting distribution of bubble sizes created along the fission track. The methods are applied as indicated in the literature, subject to some modifications which are described below.

3.2.1 Predicting the Size of Bubbles on Fission Tracks

In a subcooled aqueous solution, free from dissolved gas, the collapse of the bubbles generated along the tracks of fission fragments is expected to take place in two stages: steam condensation followed by hydrogen dissolution in the liquid (see Section 3.1.1). The condensation of steam is expected to take place much faster than the mass transfer of hydrogen gas into the dissolved phase; thermal diffusivity in water is typically of the order $\sim 10^{-7} \text{ m}^2 \text{ s}^{-1}$ whereas the diffusivity of dissolved hydrogen gas is of the order $\sim 10^{-9} \text{ m}^2 \text{ s}^{-1}$. Furthermore, the partial pressure of hydrogen gas inside the steam bubble will be relatively low, limiting the rate at which hydrogen escapes the bubble, until most of the steam has condensed.

For this reason, the two processes can be considered to happen sequentially. This is important because it means that the nucleation of steam in a superheated solution will depend on the size of steam bubbles generated along the fission tracks, whereas the nucleation of gas bubbles in a solution saturated with dissolved gas will depend on the size of the much smaller gas bubbles left behind once the steam has condensed.

3.2.1.1 Steam Bubbles Before Condensation

Norman and Spiegler (1963) proposed that the radius of steam bubbles generated along the tracks of fission fragments in an aqueous solution could be predicted by means of an energy balance on the bubble. Equation 3.2.1 is based on their equation, with some minor adaptations to include the energy consumed by the radiolysis reaction, and an adjustment to account for the volume of hydrogen gas generated at the same time as the steam. The adapted energy balance equation is,

$$E_b = \frac{4}{3}\pi r_v^3 \rho_v \Delta H_{vap} + 4\pi r_b^2 \left(\sigma_s - T \frac{d\sigma_s}{dT} \right) + \frac{4}{3}\pi P_l r_b^3 + N_{\text{H}_2} \Delta H_r, \quad (3.2.1)$$

where E_b is the energy required to create the bubble, r_b is the radius of the bubble consisting of water vapour and hydrogen, r_v is the radius this bubble would have if it contained no hydrogen, ρ_v is the vapour density, P_l is the liquid pressure, σ_s is the liquid surface tension, N_{H_2} is the number of moles of hydrogen gas generated along with the water vapour and ΔH_r is the enthalpy of this reaction, per mole of hydrogen gas created.

The first term on the right-hand side of Equation 3.2.1 represents the energy required to vaporise the liquid water contained in the bubble. The second term represents the energy required to create the gas-liquid interface around the bubble.

The third term of Equation 3.2.1 gives the work done against the pressure of the liquid during

expansion of the bubble. This term was taken from a version of the energy balance equation used by Das and Sawamura (2004), among others. It is derived by integrating the force required to overcome the liquid pressure, over the distance of expansion, i.e. the radius of the bubble,

$$E = \int_0^{r_b} P_l 4\pi r^2 dr = \frac{4\pi}{3} P_l r_b^3 \quad (3.2.2)$$

where r_b is the radius of the bubble following expansion and P_l is the liquid pressure. This expansion term differs from that used by Norman and Spiegler (1963), as well as some other researchers (Deitrich and Connolly (1973) El-Nagdy and Harris (1971)), who instead seek to estimate the kinetic energy imparted to the liquid during bubble expansion. They estimate the kinetic energy as follows,

$$E_k = 2\pi\rho_s r_b^3 \dot{R}^2, \quad (3.2.3)$$

where \dot{R} is the rate of change in the bubble radius. This is determined from the rate of heat flow towards the bubble,

$$\dot{R} = \frac{dR}{dt} = \frac{4D}{\delta}, \quad (3.2.4)$$

where δ is the thermal film thickness. The difficulty with this approach is that the value of \dot{R} is relatively sensitive to the thermal film thickness, which is difficult to predict with accuracy. Norman and Spiegler (1963) point out that the fission fragment would initially leave a track of superheated liquid, through which heat must be transferred to the surrounding liquid. They point out that the thickness of this liquid can be determined as follows from the ratio of liquid and vapour densities:

$$R_l = R \left(\frac{\rho_v}{\rho_s} \right)^{1/3}, \quad (3.2.5)$$

where R_l is the radius of the cylindrical track of superheated liquid. According to Norman and Spiegler (1963), this value represents the minimum thermal film thickness, the maximum value being the final radius of the bubble. However, it seems equally possible that the expansion of the bubble would lead to a thinning of the thermal film, in which case R_l would be the maximum film thickness. This expression also neglects energy imparted to the liquid in other forms, such as compression.

It therefore seems likely that applying the kinetic energy expression (Equation 3.2.3) with $\delta = R_l$ will lead to an underestimate of the bubble formation energy. Since the kinetic energy imparted can only come from the work done against pressure during bubble expansion, the expression selected in Equation 3.2.1 is expected to provide a better estimate. In any case, the difference is expected to be small since the majority ($> 80\%$) of energy consumed during formation of the bubble is due to vaporisation of the liquid water, so the energy of formation of the bubble is not particularly sensitive to these assumptions.

The radius of the steam bubble generated is determined by equating the energy required to form the bubble, with the amount of energy transferred from the fission fragment to the liquid along the fission track. The total energy available depends on the LET of the fission fragment,

$$E_b = \dot{E}_{Av} \cdot L \quad (3.2.6)$$

where L is the length of track over which all water vapour and radiolysis products coalesce to form a single bubble, and \dot{E}_{Av} is the mean LET of the fission fragment over the track length L . The LET will hereafter be represented in equations as \dot{E} in order to simplify notation. The stopping power $(\frac{dE}{dx})$ is the same quantity measured with respect to the medium and is essentially interchangeable.

It was suggested by Norman and Spiegler (1963) that the track length should be approximately equal to the circumference of the bubble created, $L = 2\pi R$, citing a study by Rayleigh (1945) where this track length was found to correspond to a critical wavelength for break up of the vapour jet. However, Deitrich and Connolly (1973) conducted experiments to determine the characteristic radius for nucleation of steam bubbles in aqueous solutions and found that a value of $L = 3\pi R$ matched their results more closely. Citing Rayleigh's study, they noted that a value of $L = 4\pi R$ was also found to have physical significance as the track length corresponding to the most rapid break up of the vapour jet. They concluded that there is physical justification for a value of L that lies in the range $2\pi R \leq L \leq 4\pi R$.

Substituting Equation 3.2.6 into 3.2.1 gives,

$$\frac{4}{3}r_v^3\rho_v\Delta H_{vap} + 4(\sigma_s - T\frac{d\sigma_s}{dT})r_b^2 + \frac{4}{3}Plr_b^3 + 3\dot{E}(G_{H_2}\Delta H_r - 1)r_b = 0, \quad (3.2.7)$$

where $L = 3\pi R$ is the length of track contributing water vapour and radiolysis products to the bubble.

It is possible to simplify this equation without significant loss of accuracy by making the observation,

$$r_b = \left(r_v^3 + \frac{3}{4\pi} \frac{RT}{Pl} \dot{E} L G_{H_2} \right)^{\frac{1}{3}}. \quad (3.2.8)$$

The first term in the brackets is approximately 38 times larger than the second, and in practice $r_b \approx r_v$. Substituting r_v for r_b and cancelling reduces the equation from a cubic to a quadratic

$$\frac{4}{3}(\rho_v\Delta H_{vap} + Pl)r_v^2 + 4\left(\sigma_s - T\frac{dT}{dt}\right)r_v + 3\dot{E}(G_{H_2}\Delta H_r - 1) = 0. \quad (3.2.9)$$

Unfortunately this equation cannot simply be solved using the quadratic formula because the vapour density is a function of the bubble radius. Equation 3.2.9 was therefore solved iteratively using a Newton-Raphson algorithm.

3.2.1.2 Gas Bubbles Remaining Following Steam Condensation

The amount of gas remaining following condensation of the water vapour can be determined quite simply as the product of the radiolytic gas generation coefficient and the energy deposited during creation of the bubble,

$$N_{\text{H}_2} = G_{\text{H}_2} \dot{E}_{Av} L \quad (3.2.10)$$

where the average LET (\dot{E}_{Av}) and track length (L) are those values previously determined for the steam bubble. The radiolytic gas generation coefficient must be modified from its standard meaning to reflect the fact that not all fission energy is imparted to the fission fragments as kinetic energy. Further details can be found in Section 3.2.3.

The radius of the bubble that would contain this quantity of hydrogen gas can be determined from the ideal gas law,

$$N_{\text{H}_2} = \frac{P_b V_b}{RT}, \quad (3.2.11)$$

where P_b is the pressure inside the bubble, V_b is the bubble volume, R is the universal gas constant and T is the gas temperature.

The bubble pressure depends on the liquid surface tension as well as the external liquid pressure,

$$P_b = P_l + \frac{2\sigma_s}{r_b} \quad (3.2.12)$$

where σ_s is the liquid surface tension and r_b is the radius of the bubble. This equation is valid for $r_b \neq 0$, which poses no problem for the method presented in the current chapter where no bubbles are collapsing. However, it will be important to consider this possibility in the next chapter, which includes a model of bubble collapse.

Equating Equations 3.2.10 and 3.2.11 and substituting Equation 3.2.12 for the internal pressure of the bubble results in a cubic equation,

$$\frac{4\pi}{3RT} P_l r_b^3 + \frac{8\pi}{3RT} \sigma_s r_b^2 - G_{\text{H}_2} \dot{E} L = 0, \quad (3.2.13)$$

where r_b is the radius of the hydrogen gas bubble. This equation was solved iteratively using a Newton-Raphson algorithm.

Here we make the assumption that the bubble contains only hydrogen, with no other non-condensable gases present. This assumption is justified on the basis that hydrogen gas is known to be a direct product of radiolysis whereas oxygen gas is generated later through various side reactions, most notably the decomposition of hydrogen peroxide, both by thermal decomposition and the action of free radical

species (Lane et al. (1958), Allen (1961)). These reactions take place on a much longer timescale than the formation of the bubble.

3.2.1.3 Experimental Basis

Deitrich and Connolly (1973) used a method very similar to that set out in Section 3.2.1.1 to predict the superheat required to nucleate steam bubbles in a bubble chamber exposed to fission fragments. Their experimental results, along with their theoretical model, are shown in Figure 3.2.1.

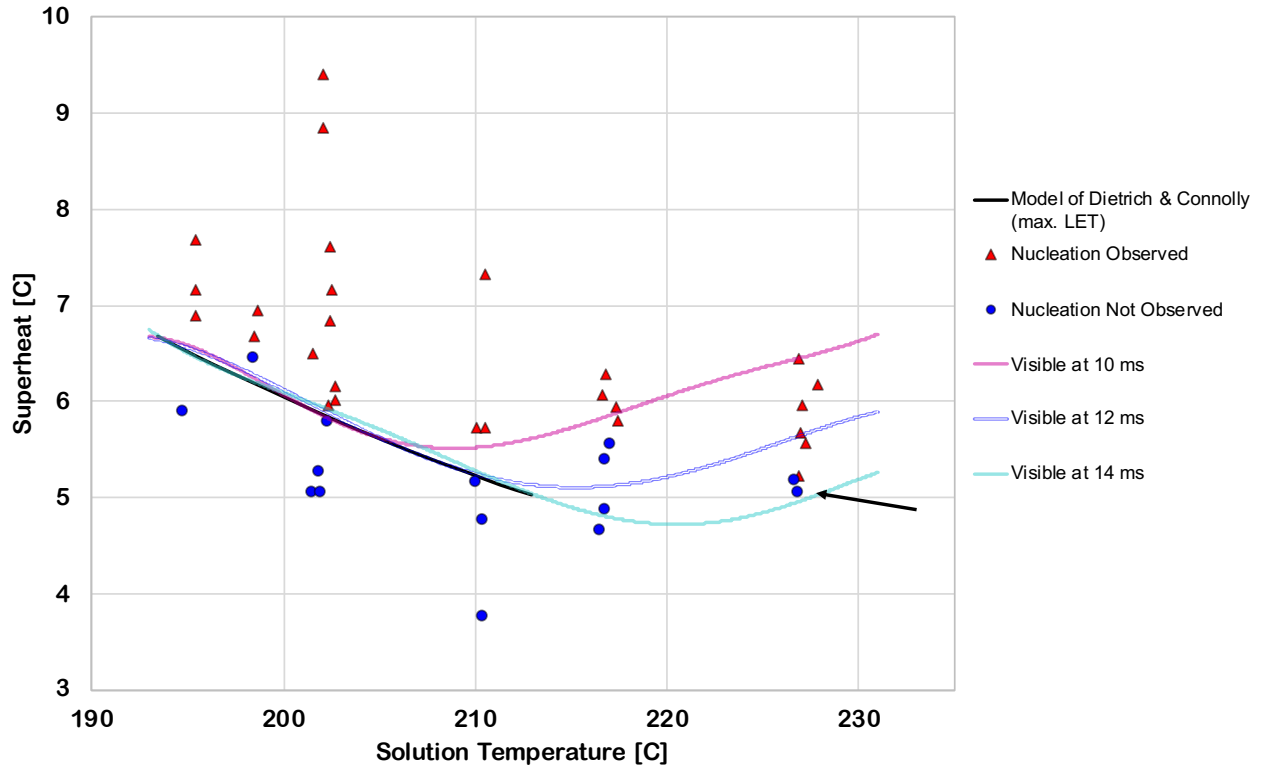


Fig. 3.2.1. Superheat required for nucleation of steam bubbles by fission fragments in water. Experimental results and model predictions of Deitrich and Connolly (1973) shown with values predicted using Equations 3.2.7 and 3.2.17.

Dietrich and Connolly concluded from these results that their theory of vapour bubble nucleation by fission fragments produced accurate predictions at lower temperatures and pressures, but noted that it appeared to lose accuracy in solution temperatures in excess of 210°C. The theory would therefore appear to offer a high degree of accuracy for the conditions encountered in most fissile liquid systems, where the system is at atmospheric pressure and boiling would be expected to occur at temperatures well below 210°C.

The theory may in fact be accurate at temperatures outside of this range as the discrepancies

noted at higher temperature may be explained by a significant decrease in the bubble growth rate as the liquid pressure increases. Dietrich and Connolly took a single photograph of the bubble chamber during each experiment, then examined the photograph for visible bubbles to determine whether or not nucleation had taken place. The photograph was taken a period of time following each application of the superheat (by depressurisation) which varied from one experiment to another. They report that bubbles were visible on the photographs once they reached a radius of 4×10^{-5} m.

The results shown on the left-hand side of Figure 3.2.1 were carried out at lower pressures, where surface tension effects still account for a significant proportion of the total pressure inside the small vapour bubble nuclei. This has the effect that once a bubble begins to expand, its internal pressure drops, leading to an increase in the rate of evaporation and the rate of expansion. These bubbles therefore reach a visible size relatively quickly.

Results on the right-hand side of Figure 3.2.1 were taken at pressures where surface tension effects are negligible compared to the external liquid pressure. Therefore, under experimental conditions close to the nucleation point, bubbles will expand extremely slowly. Dietrich and Connolly provide the oscillograph records for two of the experiments and it can be observed from these that the waiting times between depressurisation and taking the photograph were ~ 20 ms and ~ 40 ms for these two experiments. The data point corresponding to the 40ms case is indicated with an arrow in Figure 3.2.1. There are also two other data points taken at almost exactly the same temperature and superheat. In two of the three cases, no nucleation was observed, but in the other, visible bubbles did appear.

The rate of bubble growth due to evaporation is determined by the surface area available for boiling and the heat transfer coefficient at the gas/liquid interface. The latter parameter characterises the degree of resistance to heat transfer, which in a superheated liquid results from the formation of a film of subcooled liquid between the phase interface and the bulk liquid. The subcooled film occurs due to the latent heat of the evaporating liquid at the interface and it increases the resistance to heat transfer because heat from the liquid bulk must cross the subcooled film by conduction. Cooling (2014) calculated a boiling heat transfer coefficient of $12.8 \text{ kW m}^{-2} \text{ K}^{-1}$ for boiling heat transfer in fissile solutions. This heat transfer coefficient is based on data from Greenfield et al. (1954) for a boiling liquid, so it may be somewhat higher than the heat transfer coefficient for a single stationary bubble in an undisturbed environment. This is because the turbulent environment in a boiling liquid will help to prevent the build-up of the cool liquid film surrounding the bubbles. Nonetheless, it can be used to obtain an estimate of the minimum waiting time necessary to observe a bubble.

Starting with the rate of change in the number of moles of water vapour inside the bubble,

$$\frac{dn_{\text{H}_2\text{O}}}{dt} = \frac{Q}{\Delta H_{vap} M_{\text{H}_2\text{O}}} = \frac{h_{\text{boil}} 4\pi r_b^2 (T - T_{sat})}{\Delta H_{vap} M_{\text{H}_2\text{O}}}, \quad (3.2.14)$$

where $n_{\text{H}_2\text{O}}$ is the number of moles of water vapour in the bubble, Q is the rate of heat transfer into the bubble, ΔH_{vap} is the enthalpy of vaporisation of the fuel solution, $M_{\text{H}_2\text{O}}$ is the molecular weight of water, h_{boil} is the boiling heat transfer coefficient, r_b is the bubble radius and T and T_{sat} are the bulk temperature and saturation temperature of the fuel solution.

The rate of change in the bubble radius with respect to the number of moles of water vapour contained in the bubble can be obtained from the ideal gas law, taking into account the effect of surface tension on the bubble pressure,

$$n_{\text{H}_2\text{O}} = \frac{1}{3RT} (4\pi P_l r_b^3 + 8\pi \sigma_s r_b^2), \quad (3.2.15)$$

$$\frac{dn_{\text{H}_2\text{O}}}{dr_b} = \frac{1}{3RT} (12\pi P_l r_b^2 + 16\pi \sigma_s r_b), \quad (3.2.16)$$

where the symbols have the same meanings as in previous equations. The rate of change in the bubble radius with respect to time can therefore be deduced from the chain rule,

$$\frac{dr_b}{dt} = \frac{h_{\text{boil}} r_b (T - T_{sat}) 3RT}{\Delta H_{vap} M_{\text{H}_2\text{O}} (3P_l r_b + 4\sigma_s)}. \quad (3.2.17)$$

Using Equation 3.2.17, lines were added to Figure 3.2.1 indicating the degree of superheat required, as a function of solution temperature, for a visible bubble to appear within 10ms, 12ms or 14ms of depressurisation. The indicated data points fall just above the 14ms line, and since the oscillograph record shows that Dietrich and Connolly took their photograph approximately 40ms after depressurisation of the bubble chamber, these results would seem to suggest the waiting time was sufficient, at least for the 40ms case shown in the oscillograph record.

However, Figure 3.2.1 confirms that the anomalous results occurred in a region where bubble growth is slow; where experimental waiting times on the order of tens of milliseconds may not always be sufficient. On the left of the plot, where the results were in agreement with the theory, any waiting time greater than a few milliseconds would be sufficient to observe a bubble. Given the uncertainty previously noted in the boiling heat transfer coefficient of the bubbles, and the fact that oscillograph records confirm that Dietrich and Connolly varied the waiting time between experiments, and that these waiting times were relatively close to the minimum required values, it seems plausible that differences in bubble growth rates may explain the unexpected results observed at higher temperatures and pressures.

This observation provides further validation in support of the model of bubble nucleation, since not only does the model predict the required superheat for nucleation accurately over the range of temperatures 190°C to 210°C, as concluded by Dietrich and Connolly, it may also explain the behaviour observed at higher temperatures and pressures.

3.2.2 Predicting the Linear Energy Transfer of a Fission Fragment

Using tables of stopping power data it is possible to estimate the LET profile (LET with respect to distance travelled) of any fission fragment in any typical fissile aqueous solution. The objective is to obtain the particle energy (E) as a function of displacement (x) from the site of fission. This was achieved by solving the following ODE using an algorithm based on the 4th order Runge-Kutta method,

$$E(x) = - \int_0^x \frac{dE}{dx} dx, \quad (3.2.18)$$

where $\frac{dE}{dx}$ is the stopping power of the medium with respect to the charged particle, obtained from tables generated using SRIM. Since the medium consists of three covalently bonded species; water, UO_2^{2+} and NO_3^- , it is necessary to calculate a combined stopping power for the medium by adding together the individual contribution of each constituent, i.e.

$$\left(\frac{dE}{dx}\right)_{\text{medium}} = \sum_i \left(\frac{dE}{dx}\right)_i, \quad (3.2.19)$$

where $\left(\frac{dE}{dx}\right)_i$ represents the stopping power contribution of component i .

The initial condition is determined by the amount of total kinetic energy ($E_{k,\text{fiss}}$) shared between the fission fragments and the mass of each fragment (M). The total fission energy released in the form of kinetic energy of the fission fragments is approximately 169 MeV (Madland (2006)). This energy was assumed to be split so that momentum was conserved, resulting in the following equation for the initial kinetic energy (E_0) of the particle,

$$E_0 = \frac{E_{k,\text{fiss}}}{1 + \frac{M}{236 - \nu_p - M}}, \quad (3.2.20)$$

where ν_p is the number of prompt neutrons emitted in the fission event that created the fission fragment. Since the prompt neutrons are emitted on a very short timescale compared to the travel time of the fission fragment, these are treated as being emitted instantly at the moment of fission. An average value of $\nu_p = 2.43$ has been applied to calculate the initial particle energies throughout this paper.

The stopping power of the medium with respect to a charged particle varies as a function of the energy of that particle. SRIM was used to generate tabulated values corresponding to 167 particle energies ranging from 1.1×10^{-6} to 2.5 MeV amu⁻¹. These values were interpolated linearly to obtain the stopping powers required to solve Equation 3.2.18.

Stopping powers are tabulated in units of MeV mg⁻¹ cm². These values are multiplied by the partial density of each component in the medium to obtain a stopping power value in units of energy per distance travelled. The partial density is the product of the total solution density and the mass fraction of each component, e.g.

$$\rho_{\text{NO}_3} = f_{\text{NO}_3} \rho_s, \quad (3.2.21)$$

where ρ_{NO_3} is the partial density of nitrate in the solution, f_{NO_3} is the mass fraction of nitrate and ρ_s is the total solution density.

Stopping power depends on the ionic charge so values tabulated for one isotope can be applied to other isotopes of the same element, provided the mass is adjusted appropriately in the calculation. The same is true for isomers with the same mass and atomic number but different energy states.

3.2.3 Input Parameters

3.2.3.1 Enthalpy of Reaction

The enthalpy of reaction for the radiolysis of water was estimated from the enthalpies of formation of water and hydrogen peroxide, and the enthalpy of vaporisation of water, resulting in a value of 2.958×10^5 Joules per mole of hydrogen gas produced.

3.2.3.2 Fuel Solution Density

The density of the fuel solution was estimated using an empirical correlation derived from experimental data presented in Grant et al. (1948) and densities reported for the fuel solutions of various experimental reactors. The correlation is shown below and its justification is given in Appendix E:

$$\begin{aligned} \rho_s(T_c, C_U, C_N) = & 0.31635C_U - 3.5898 \times 10^{-3}T_c^2 - 4.7024 \times 10^{-2}T_c \\ & + 3.4663 \times 10^{-2}C_N + 1001.0, \end{aligned} \quad (3.2.22)$$

where ρ_s is the density of the solution in kg m⁻³, C_U and C_N are the concentrations of uranyl nitrate and nitric acid in mol m⁻³ and T_c is the solution temperature in °C. This expression is based on experimental data covering a range of uranyl nitrate concentrations up to 1650 mol m⁻³ and

temperatures ranging from 0°C to 100°C.

3.2.3.3 Fuel Solution Surface Tension

Surface tension was also estimated using an empirical equation derived from the data of Grant et al. (1948). The equation for surface tension was,

$$\begin{aligned}\sigma_s(T_c, C_U) = & -1.7160 \times 10^{-7} T_c^2 - 1.4427 \times 10^{-4} T_c + 2.0163 \times 10^{-6} C_U \\ & + 7.5725 \times 10^{-2},\end{aligned}\tag{3.2.23}$$

where σ_s is the surface tension of the solution in N m⁻¹, the symbols have the same meaning as in Equation 3.2.22.

The derivative of the surface tension with respect to temperature, required by Equation 3.2.1, was determined by differentiating Equation 3.2.24 as follows,

$$\frac{d\sigma_s}{dT_c}(T_c) = -3.4320 \times 10^{-7} T_c - 1.4427 \times 10^{-4}.\tag{3.2.24}$$

The expressions are based on experimental data from Grant et al. (1948) covering a range of uranyl nitrate concentrations up to 830 mol m⁻³ and temperatures ranging from 0°C to 100°C.

3.2.3.4 Enthalpy of Vaporisation

The enthalpy of vaporisation of water is widely available as tabulated data. The following correlation was used to estimate its variation with temperature,

$$\Delta H_{vap}(T) = -2.4367T + 3168.0,\tag{3.2.25}$$

where T is the solution temperature in Kelvin. This correlation is based on data for temperatures ranging from 0°C to 100°C.

3.2.3.5 Radiolytic Gas Generation Coefficient

The radiolytic gas coefficient is an important factor determining the size of gas bubbles deposited along fission fragment tracks. It has previously (Cooling (2014), Forehand (1981)) been estimated for solutions of uranyl nitrate based on data from Lane et al. (1958), which put the value of G_{H_2} for pure water at 1.8 molecules of H₂ per 100 eV of energy deposited, decreasing with increasing concentration of uranyl nitrate. The following correlation is based on the data from Lane et al. (1958) for the value

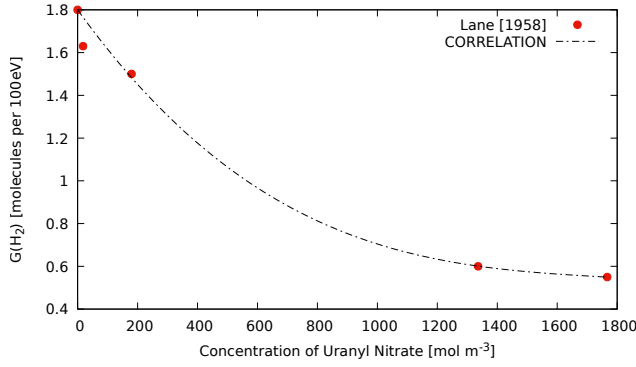


Fig. 3.2.2. Experimental data from Lane et al. (1958) showing G_{H_2} as a function of uranyl nitrate concentration with correlation based on Equation 3.2.26.

of G_{H_2} as a function of uranyl nitrate concentration:

$$G_{H_2} = 1.8 - 1.94451 \times 10^{-3}C_U + 1.04343 \times 10^{-6}C_U^2 - 1.94375 \times 10^{-10}C_U^3, \quad (3.2.26)$$

where G_{H_2} is in units of molecules per 100 eV, C_U is the concentration of uranyl nitrate in mol m⁻³.

Equation 3.2.26 was obtained by fitting a curve through the reported data and forcing the y-intercept to a value of 1.8, since this value for pure water is expected to constitute the maximum value (Forehand (1981)). The experimental data is for uranyl nitrate concentrations up to 1770 mol m⁻³. At concentrations in excess of this, Figure 3.2.2 appears to show that the value of G_{H_2} loses its sensitivity to the uranyl nitrate concentration, although further data at higher concentrations would be required to confirm this.

It is possible that the nitric acid concentration may also affect the value of G_{H_2} , independently of the concentration of uranyl nitrate. In general the concentration of nitric acid in a given fuel solution tends to increase with the concentration of uranyl nitrate because higher acid concentrations are needed to dissolve larger concentrations of uranyl nitrate. However, according to Youker et al. (2013), a range of nitric acid concentrations is possible, provided a pH of less than 3.0 is maintained to prevent the precipitation of uranium and fission products.

The concentrations of nitric acid corresponding to the data shown in Figure 3.2.2 are shown in Table 3.1. These have been estimated from the pH values quoted in Lane et al. (1958), using an acid dissociation constant $K_a = 35.5$ obtained from Levanov et al. (2017).

Unfortunately, there is insufficient data available in Lane et al. (1958) for a correlation that accounts for the concentration of both uranyl nitrate and nitric acid. It is therefore possible that the value of G_{H_2} may deviate from that predicted by Equation 3.2.26 where the concentration of nitric acid in the fuel solution differs significantly from the values listed in Table 3.1. The concentrations of nitric acid shown in Table 3.1 are significantly lower than the concentrations of the order 2000 mol m⁻³ which were typical of fissile solution reactors such as CRAC and TRACY (Barbry et al. (1973), Nakajima

Uranyl Nitrate Concentration	Nitric Acid Concentration	pH	G_{H_2}
mol m ⁻³	mol m ⁻³	–	molecules per 100eV
0	0	7.0	1.8
18.0234	UNKNOWN	UNKNOWN	1.63
179.809	17.8	2.05	1.5
1335.97	186.9	1.03	0.6
1766.71	504.2	0.6	0.55

TABLE 3.1

G_{H_2} for aqueous solutions of varying uranyl nitrate and nitric acid concentrations. Data from Lane et al. (1958) with nitric acid concentrations estimated based on solution pH.

et al. (2002c)). It is not clear to what degree these significant differences in the concentration of nitric acid would be expected to influence the value of G_{H_2} , or whether this influence would be negative or positive.

A more recent study by Yoshida et al. (2019) examining the radiolytic gas generation coefficient highlights the level of complexity required to accurately estimate the quantity of hydrogen gas produced during criticality transients in fissile liquids. In Yoshida et al. (2019), an advanced technique is used to estimate the amount of hydrogen gas produced during a transient on the TRACY reactor. Comparing these results to the data of Lane et al. (1958) appears to indicate that the amount of hydrogen gas produced was underestimated in the older data, highlighting considerable uncertainty in the true value of this parameter. Based on the findings of Yoshida et al. (2019), the values of G_{H_2} are expected to be at least as high as that predicted by Equation 3.2.26, and possibly higher.

Given the uncertainty highlighted above, Equation 3.2.26 will be used to illustrate the influence that solution composition may have on the size of radiolytic gas bubbles, via its influence of the value of G_{H_2} . However, more up-to-date values of G_{H_2} should always be chosen when available.

3.2.3.6 Adjustment of G_{H_2} for Fission Tracks

The radiolytic gas generation coefficient represents number of moles of hydrogen gas produced per unit of observable fission energy. Kopeikin et al. (2004) referred to the observable energy release as the *effective* fission energy, including the kinetic energy of the fission fragments and the energy of neutrons captured in the medium, but excluding the energy carried away by antineutrinos, beta particles and photons. They calculated the effective fission energy of ²³⁵U to be 193.37 MeV. Since radiolysis in fissile liquids is due almost entirely to the kinetic energy of the fission fragments Lane et al. (1958) (approximately 169.0 MeV) and not significantly associated with neutron capture events, the radiolytic gas coefficient applied in the calculations that follow must be multiplied by a factor $F = 193.37/169.0 = 1.14$.

3.2.3.7 Henry's Law Constant

A Henry's law constant of $6.5 \times 10^{-6} \text{ mol m}^{-3} \text{ Pa}^{-1}$ was assumed for dissolved H_2 gas in the uranyl nitrate solution. This is slightly lower than the value for pure water, chosen to reflect the fact that the presence of uranyl nitrate in the solution will reduce the solubility of hydrogen gas. In this chapter, the Henry's law constant is used only to provide an indication of the critical concentration resulting from a given bubble nucleation radius. A more detailed examination of the sensitivity of the Henry's law constant to solution temperature and concentration can be found in Appendix C.

3.3 Results

In this section results are presented for the LET of fission fragments in aqueous fissile solutions and the size of hydrogen gas bubbles deposited along those tracks. The size of vapour bubbles deposited along the fission tracks has already been thoroughly examined in the literature, as discussed in previous sections, and no further examination will be presented here. This section is concerned with the creation of hydrogen gas bubbles, along fission fragment tracks, and their potential to act as nucleation sites for the appearance and growth of gas voids in the solution.

Also examined in this section is the critical concentration of dissolved gas; that is the concentration of dissolved gas which must be reached before voids can be observed in a fissile solution. This quantity is directly related to the size of gas bubbles generated by fission fragments, as discussed in previous sections, and is a key parameter in criticality safety due to its importance in the kinetics of many nuclear criticality excursions. The size of the largest hydrogen gas bubble deposited by any fission fragment (that which determines the critical concentration) will hereafter be referred to as the nucleation bubble radius.

Except where indicated, all values shown in this section are calculated for the conditions shown in Table 3.2. The calculations are based on pure water, containing no uranyl nitrate. However, correction factors presented later (see Equation 3.3.3) allow the nucleation bubble radius to be adjusted as a function of the concentration of uranyl nitrate or the radiolytic gas generation coefficient of the solution.

3.3.1 Sensitivity of Nucleation Bubble Radius to Solution Properties

Equations 3.2.9 and 3.2.13 indicate that the nucleation bubble radius is a function of the properties of the fuel solution, notably its surface tension, density, pressure and temperature. It is also strongly

Mean LET (\dot{E}_{Av})	8	$MeV \mu m^{-1}$
Solution Temperature	298	K
Liquid Pressure	1	atm
Concentration of Uranyl Nitrate	0	$mol m^{-3}$
Concentration of Nitric acid	0	$mol m^{-3}$
Henry's Law Constant for H_2	6.5×10^{-6}	$mol m^{-3} Pa^{-1}$

TABLE 3.2

Standard calculation conditions, applied to all calculations in Section 3.3.1, except where otherwise indicated.

influenced by the radiolytic gas generation coefficient. These factors therefore also influence the critical concentration at which growing bubbles can be nucleated along the fission tracks.

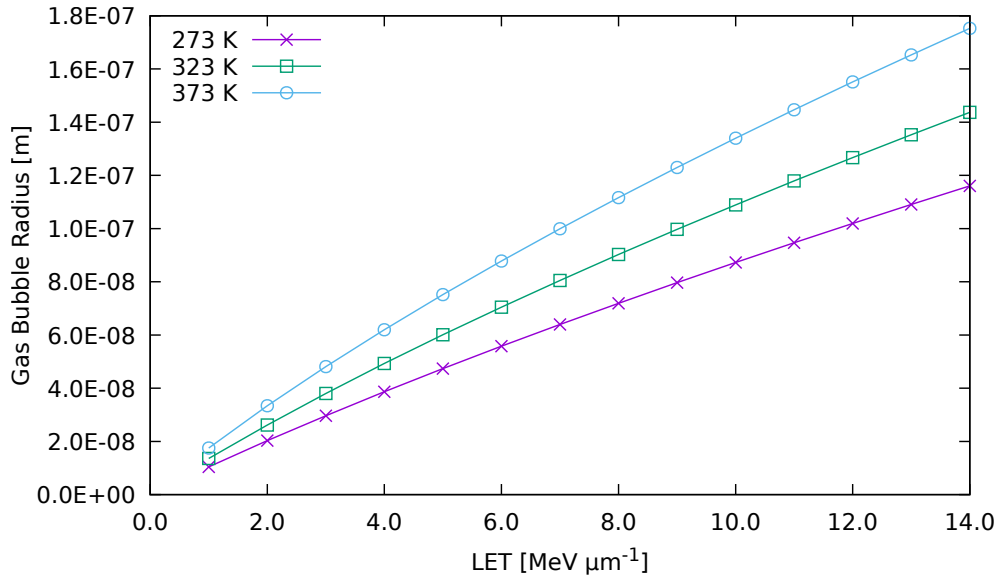


Fig. 3.3.1. Radius of bubble nucleus as a function of fission fragment LET and solution temperature

The influence of LET and temperature on the predicted size of gas bubbles nucleated is shown in Figure 3.3.1. The model predicts that the bubble size increases with the LET of the particle or fission fragment. This is consistent with the conclusions of Norman and Spiegler (1963) who present a plot of LET as a function of gas bubble size in their report.

The influence of temperature is due to two factors. Increasing the temperature reduces the latent heat of vaporisation of the liquid water, resulting in a larger vapour bubble. Because the model predicts the length of track along which the vapour bubble is formed is a function of the radius of the bubble formed ($L = 3\pi R$), a larger bubble means a longer track with more energy available to produce hydrogen gas.

Another factor is the solution surface tension, which decreases with increasing temperature. The surface tension contributes the majority of the pressure inside the bubble. A decrease in solution

surface tension therefore results in a larger bubble for the same quantity of hydrogen gas.

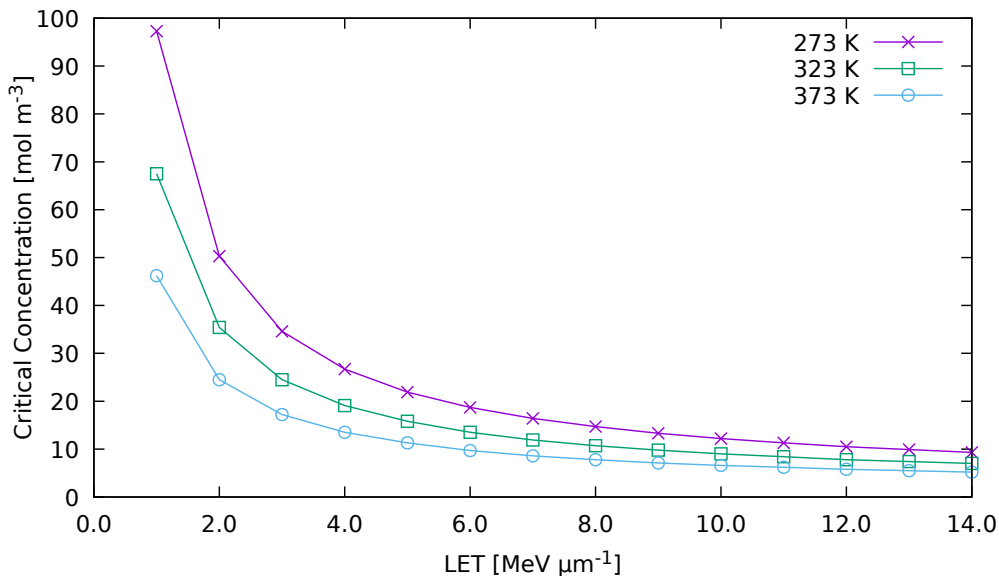


Fig. 3.3.2. Critical concentration of dissolved hydrogen gas as a function of fission fragment LET

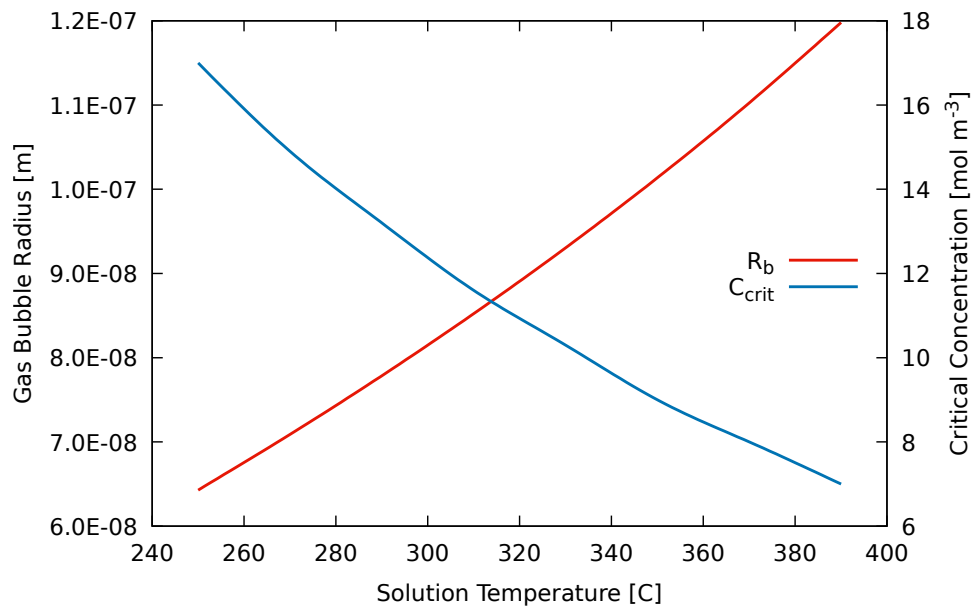


Fig. 3.3.3. Bubble nucleation radius and critical concentration of dissolved hydrogen gas as a function of solution temperature for a fission fragment with maximum LET of $8 \text{ MeV } \mu\text{m}^{-1}$

These results indicate that the critical concentration of hydrogen gas at which voids will appear in fissile aqueous solution will decrease with increasing solution temperature. Figure 3.3.2 shows the critical concentration predicted as a function of temperature and maximum particle LET. The values shown are based on a Henry's law constant for hydrogen of $6.5 \times 10^{-6} \text{ mol m}^{-3} \text{ Pa}^{-1}$. For a maximum particle LET of $8 \text{ MeV } \mu\text{m}^{-1}$, the model predicts a critical concentration of 15 mol m^{-3} at 273K,

decreasing to 8 mol m^{-3} at 373K.

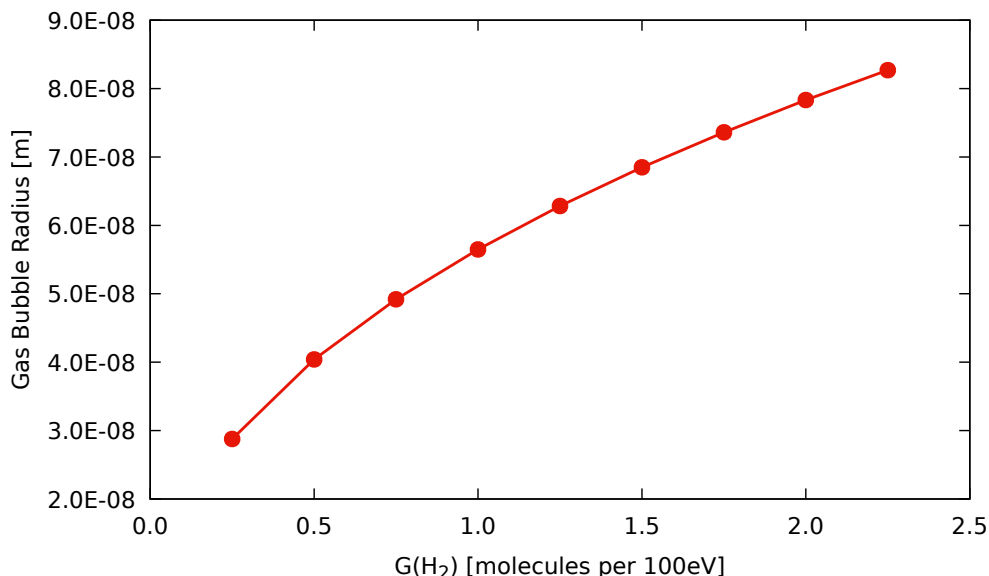


Fig. 3.3.4. Bubble nucleation radius as a function of the radiolytic gas generation coefficient

The sensitivity of the radius of hydrogen bubbles to the radiolytic gas generation coefficient is shown in Figure 3.3.4. It is not surprising that the size of bubbles produced is relatively sensitive to this parameter since it determines the quantity of hydrogen present. Since the radiolytic gas generation coefficient is affected by the concentration of uranyl nitrate, this also explains most of the sensitivity, shown in Figure 3.3.5, of the bubble radius and critical concentration to the concentration of uranyl nitrate in the solution. The sensitivity to uranyl nitrate concentration is also partly due to the increase in surface tension of the fuel solution as the concentration of uranyl nitrate increases, which would increase the internal pressure of the bubbles leading to a smaller bubble size. However, this effect is very small compared to the effect of the radiolytic gas generation coefficient, since the solution surface tension changes only by a relatively small degree with varying uranyl nitrate concentration (see Equation 3.2.23).

Figure 3.3.6 shows the influence of pressure on the predicted bubble size. A higher pressure compresses the bubbles, leading to a decrease in the size of hydrogen gas bubbles created. This would, in turn, lead to higher critical concentrations of hydrogen gas, potentially delaying the appearance of gas voids during a criticality transient.

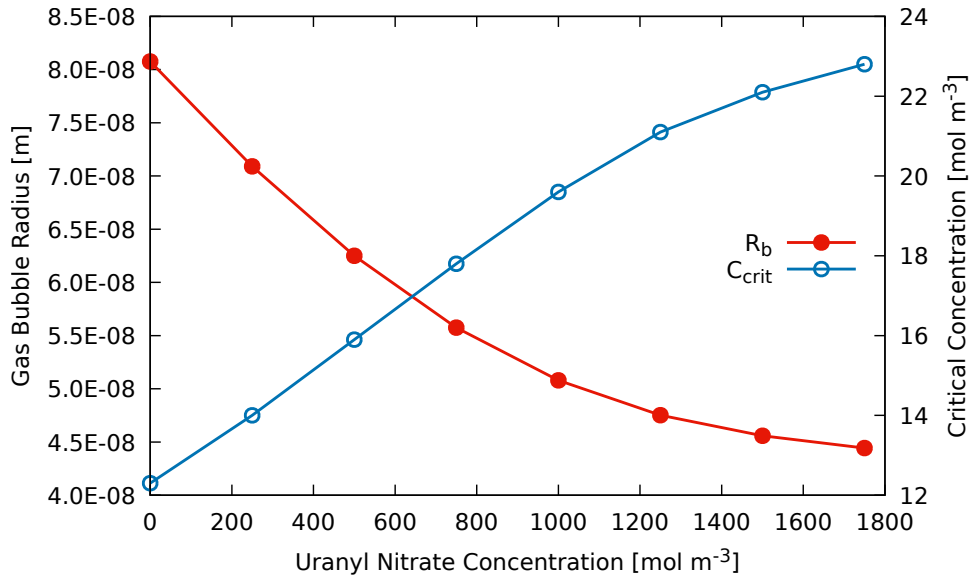


Fig. 3.3.5. Variation of predicted gas bubble radius with changing concentration of uranyl nitrate

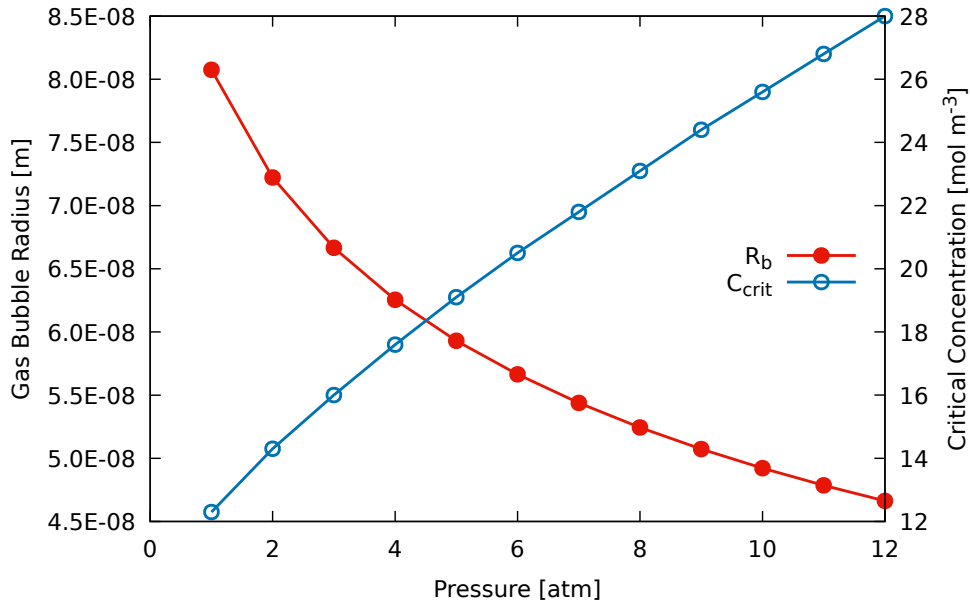


Fig. 3.3.6. Radius of bubble nucleus as a function of liquid pressure

3.3.2 Empirical Correlation for the Gas Bubble Nucleation Radius as a Function of Solution Temperature and Particle LET

It was observed in the last section that the model predicts that the radius of gas bubbles deposited along the tracks of a fission fragment in an aqueous solution of uranyl nitrate would be a strong function of the fission fragment LET, the solution temperature, the liquid pressure and the radiolytic gas generation coefficient (G_{H_2}). It is also affected by the concentration of uranyl nitrate in the fuel solution, mostly due to the effect this has on G_{H_2} .

Limiting the analysis to pure water systems at atmospheric pressure, an empirical correlation can be derived for the gas bubble nucleation radius as a function of temperature and LET. This results in Equation 3.3.1

$$\begin{aligned} r_{b,0} = & \left(-2.8632 \times 10^{-15} T^2 + 7.3996 \times 10^{-13} T - 9.9925 \times 10^{-11} \right) \dot{E}_{Av}^2 \\ & + \left(8.7907 \times 10^{-14} T^2 - 9.7928 \times 10^{-13} T + 3.4558 \times 10^{-9} \right) \dot{E}_{Av} \\ & + \left(9.7683 \times 10^{-14} T^2 - 4.0125 \times 10^{-11} T + 4.9092 \times 10^{-9} \right), \end{aligned} \quad (3.3.1)$$

where T is the temperature in Kelvin, $r_{b,0}$ is the bubble radius in metres for a pure water system, \dot{E}_{Av} is the rate of energy transfer from the particle to the medium, in units of MeV μm^{-1} , averaged over the distance L . This was calculated using

$$\dot{E}_{Av} = \frac{1}{L} \int_0^L \dot{E} dx, \quad (3.3.2)$$

where L is the length of track over which the original vapour bubble was formed.

The coefficients of Equation 3.3.1 were derived for pure water. However, because the value of G_{H_2} is affected by the composition of the solution, and particularly concentration of uranyl nitrate (see Equation 3.2.26), the value of r_b would also be expected to depend on solution composition (see Figure 3.3.5). In a solution with lower G_{H_2} , the vapour bubbles formed along the fission tracks will contain less hydrogen gas, and therefore collapse to smaller hydrogen gas bubbles upon condensation.

The following correction factor can be applied to predict the bubble nucleation radius in aqueous solutions of uranyl nitrate. This correction factor uses Equation 3.2.26 to predict the change in G_{H_2} as a function of uranyl nitrate concentration:

$$F_{\text{corr}} = 1.0 - 5.23 \times 10^{-4} C_U + 1.53 \times 10^{-7} C_U^2, \quad (3.3.3)$$

where $C_U < 1770 \text{ mol m}^{-3}$. Alternatively, the correction factor can be formulated in terms of G_{H_2} , thus removing the reliance on Equation 3.2.26, which as previously noted, is associated with a significant degree of uncertainty. The alternative formulation is as follows:

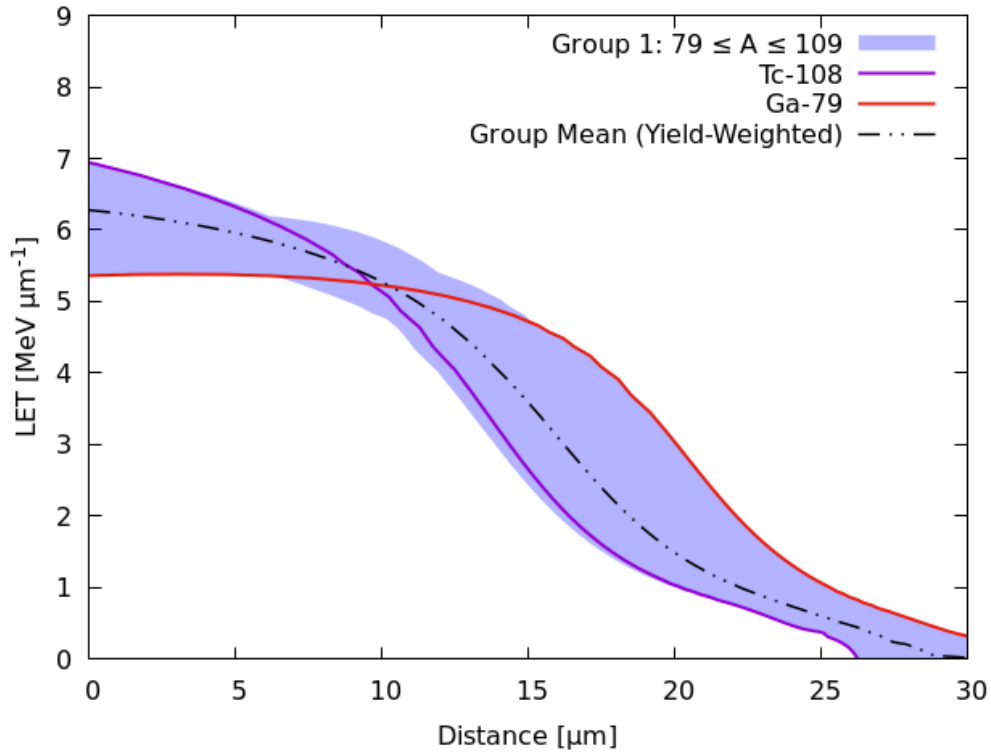
$$F_{\text{corr}} = 0.3554 + 0.4264 G_{H_2} - 0.0400 G_{H_2}^2, \quad (3.3.4)$$

where $0.5 < G_{H_2} < 4.5$ molecules per 100eV.

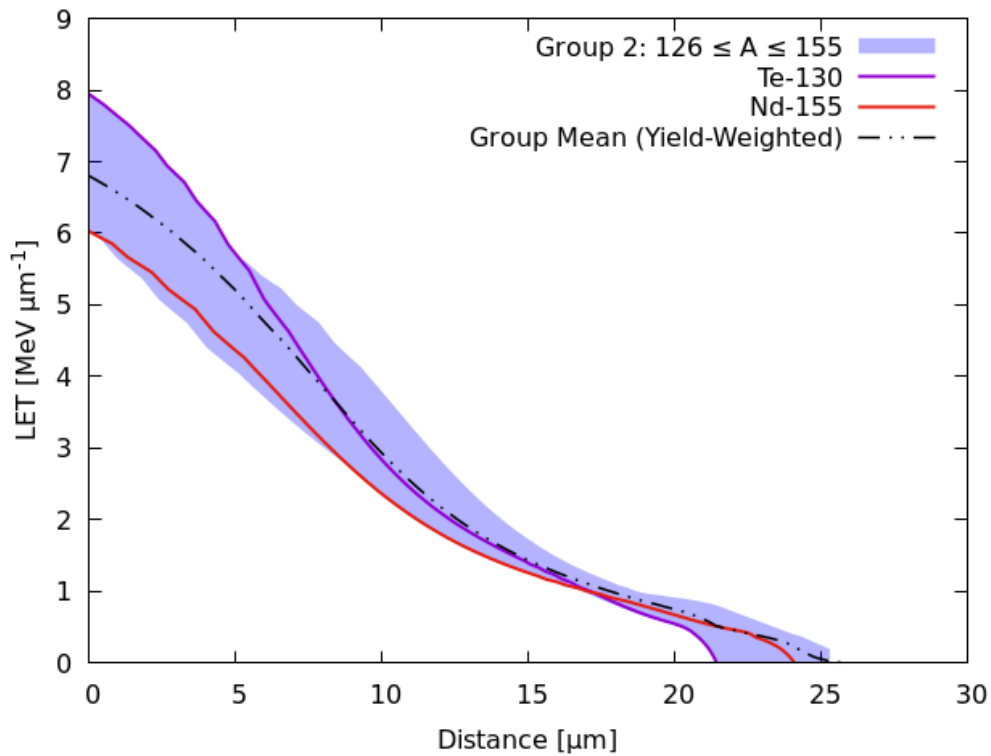
The value of r_b for a solution of uranyl nitrate is obtained using:

$$r_b = r_{b,0} F_{\text{corr}}. \quad (3.3.5)$$

3.3.3 Predicted LET Profiles of Fission Fragments in Uranyl Nitrate

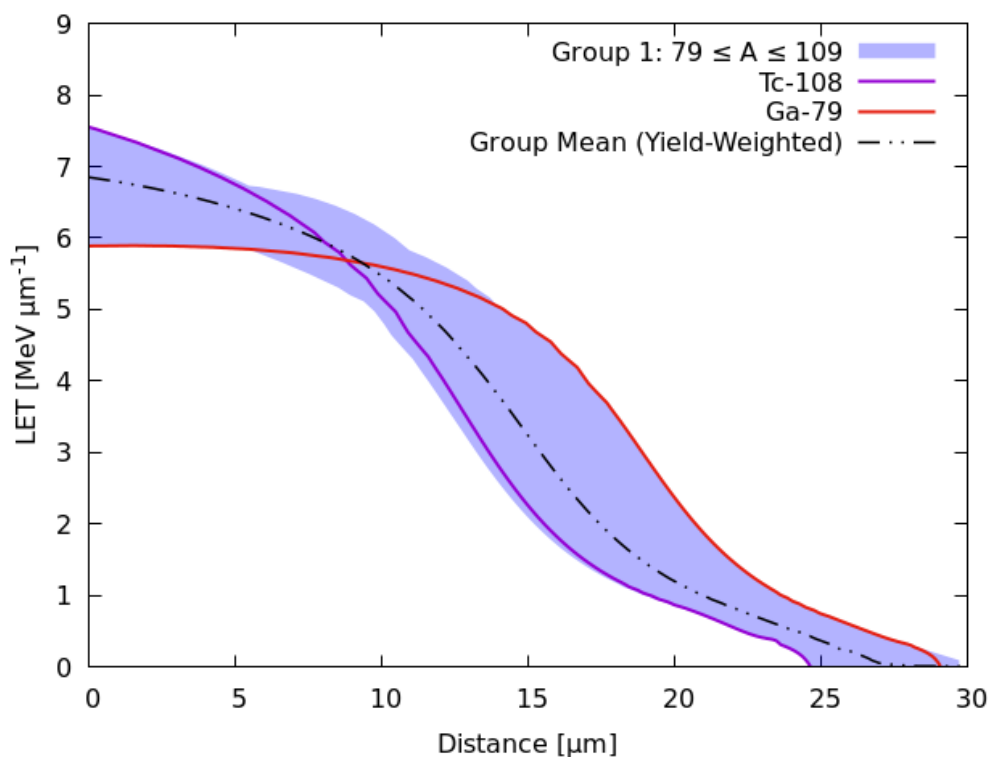


(a) Group 1: isotopes with mass number $79 \leq A \leq 109$

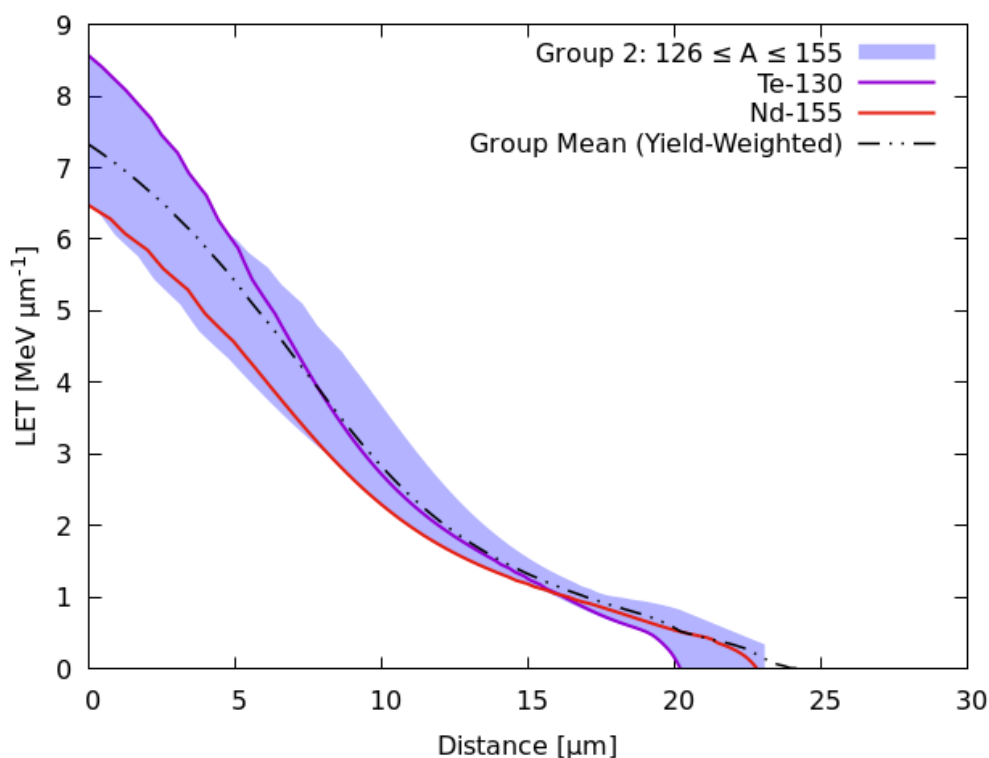


(b) Group 2: isotopes with mass number $126 \leq A \leq 155$

Fig. 3.3.7. LET profiles at 298K for pure water, calculated using data from SRIM for the stopping power of fission fragments with the 250 highest yields from fission of ^{235}U .



(a) Group 1: isotopes with mass number $79 \leq A \leq 109$



(b) Group 2: isotopes with mass number $126 \leq A \leq 155$

Fig. 3.3.8. LET profiles at 298K for an aqueous solution containing 1000 mol m^{-3} of uranyl nitrate, calculated using data from SRIM for the stopping power of fission fragments with the 250 highest yields from fission of ^{235}U .

LET profiles were calculated for the tracks of the 250 highest yielding fission products of ^{235}U . The list of fission products by yield was obtained from National Nuclear Data Center (2011) on the website of Brookhaven National Laboratory. The data show that these fission fragments account for more than 99.5% of the total fission yield. Some of the 250 fission products listed are different isomers of the same isotope. These can be treated identically for the purposes of calculating an LET profile so the original list of 250 fission products was reduced to a list of 215 distinct fission product isotopes.

The LET was calculated in the first instance for a pure water system, containing no uranyl nitrate or nitric acid. The results are shown in Figure 3.3.7 along with the yield-weighted mean. Figure 3.3.8 shows the same LET profiles calculated for an aqueous solution containing 1000 mol m^{-3} of uranyl nitrate with a ^{235}U enrichment of 90%.

Fission of ^{235}U usually results in the creation of two fission fragments; one larger fragment with mass number 125-155 atomic mass units (amu) and a smaller fragment with mass number 79-110amu. These two groups, corresponding to this bimodal distribution of fission fragments yields, have distinctly different LET profiles and are shown separately in Figures 3.3.7 and 3.3.8.

The lighter group of nuclei shown in Figures 3.3.7 and 3.3.8 has higher velocity at the start of the track and a few fission fragments in this group have not yet reached peak LET, although they are very close to it. The LET of a small proportion of the fission fragments in this group remains constant or increases slightly for the first 5-10 μm before it starts to decrease. The heavier group of nuclei has lower velocity at the start of the track and the LET of fission fragments in this group is already well past its peak. Their LET decreases monotonically for the entire length of the track.

The effect of uranyl nitrate concentration is indicated by comparing Figures 3.3.7 and 3.3.8. The LET of the fission fragments is increased by approximately $0.5 \text{ MeV } \mu\text{m}^{-1}$ in the uranyl nitrate solution compared to pure water, with a corresponding reduction in the range of the particles. This is due mainly to the increase in density of the fuel solution, which is a key parameter determining the LET of the fission fragments.

3.3.4 Bubble Size Distribution in Aqueous Fissile Solutions

The size of the largest bubble created by each fission fragment was determined using Equations 3.3.1 and 3.3.3 and the LET profiles generated using stopping power data from SRIM. Smaller bubbles formed at lower LET along the same fission track as larger bubbles are not of interest, since the presence of larger bubbles in close proximity means that these are not significant as nucleation sites for the appearance of gas voids.

	273K		323K		373K	
	r_b [m] $\times 10^{-8}$	\dot{E}_{Av} [MeV μm^{-1}]	r_b [m] $\times 10^{-8}$	\dot{E}_{Av} [MeV μm^{-1}]	r_b [m] $\times 10^{-8}$	\dot{E}_{Av} [MeV μm^{-1}]
Median	5.3	5.7	6.6	5.6	7.8	5.3
90th Percentile	5.6	6.0	6.9	5.9	8.3	5.6
95th Percentile	5.6	6.1	7.0	6.0	8.4	5.7
99th Percentile	5.8	6.3	7.2	6.2	8.7	6.0
Maximum	6.4	7.0	7.8	6.7	9.2	6.3

TABLE 3.3

Predicted bubble sizes and associated fission fragment LET using Equation 3.3.1 for pure water at atmospheric pressure.

Table 3.3 summarises the predicted bubble sizes for pure water across a range of temperatures. The lower temperature was chosen so that the results could be compared with those of Spiegler et al. (1962), who estimated from experimental measurements that hydrogen gas bubbles were nucleated with a maximum radius of 5×10^{-8} m at 273K. This appears to agree closely with the gas bubble radii predicted by the model, which gives a median bubble radius of 5.3×10^{-8} m and a maximum size of 6.4×10^{-8} at this temperature in pure water.

	0 mol m ⁻³		500 mol m ⁻³		1000 mol m ⁻³	
	r_b [m] $\times 10^{-8}$	\dot{E}_{Av} [MeV μm^{-1}]	r_b [m] $\times 10^{-8}$	\dot{E}_{Av} [MeV μm^{-1}]	r_b [m] $\times 10^{-8}$	\dot{E}_{Av} [MeV μm^{-1}]
Median	6.0	5.7	4.7	5.8	3.9	5.9
90th Percentile	6.2	5.9	5.0	6.2	4.2	6.4
95th Percentile	6.3	6.0	5.0	6.2	4.2	6.5
99th Percentile	6.5	6.3	5.2	6.5	4.4	6.7
Maximum	7.1	6.9	5.6	7.0	4.6	7.2

TABLE 3.4

Predicted bubble sizes and associated fission fragment LET using Equation 3.3.1 for aqueous solutions of uranyl nitrate across a range of concentrations at atmospheric pressure and 298K.

Spiegler posited that the radius of the gas bubbles would be insensitive to pressure and solution composition. He also noted, however, that this gas bubble size was at the limit of detection of the equipment used, so it is possible they were not able to measure the relatively small changes that the model predicts as a result of varying these parameters.

The results show that the gas bubble size increases significantly with increasing solution temperature. This has implications for the kinetics of nuclear criticality transients, because a larger gas bubble size means that gas voids will appear at lower dissolved gas concentrations. Void feedback may therefore appear earlier in solutions at higher temperatures compared to lower temperatures.

Tables 3.3 and 3.4 show the 90th, 95th and 99th percentile, as well as the maximum, gas bubble radius for each solution. These values are likely to have greater significance than the median or mean value since it is the largest bubbles that will determine the critical concentration of the solution.

3.3.5 Empirical Correlation for the Gas Bubble Nucleation Radius Based on the Maximum LET of Fission Fragments in Uranyl Nitrate

Using the data presented in the last section, which combines the LET profiles of Section 3.3.3 with the empirical correlation presented in Section 3.3.2, it is possible to derive a correlation for the bubble nucleation radius specific to fission of ^{235}U in uranyl nitrate solution. The correlation can be used to estimate the bubble nucleation radius directly from the solution temperature and uranyl nitrate concentration.

$$\begin{aligned} r_b = & \left(-2.0281 \times 10^{-19} T^2 + 1.6824 \times 10^{-16} T - 2.1277 \times 10^{-14} \right) C_U^2 \\ & - \left(1.2003 \times 10^{-13} T - 7.1969 \times 10^{-13} \right) C_U \\ & + 2.7697 \times 10^{-10} T - 1.1858 \times 10^{-8} \end{aligned} \quad (3.3.6)$$

where T is the solution temperature in Kelvin, C_U is the concentration of uranyl nitrate in mol m^{-3} and G_{H_2} is assumed to vary with uranyl nitrate concentration in accordance with Equation 3.2.26. This correlation is valid for solution temperatures in the range $273 \leq T \leq 373$, uranyl nitrate concentrations in the range $0 \leq C_U \leq 1770 \text{ mol m}^{-3}$, and nitric acid concentrations close to those shown in Table 3.1.

Equation 3.3.6 assumes that the radiolytic gas generation coefficient varies in accordance with Equation 3.2.26, which is associated with some significant uncertainty. In order to avoid this dependence, the following correlation can instead be used to obtain the expected fission fragment LET. Equation 3.3.1 can then be used to predict the resulting gas bubble radius:

$$\begin{aligned} \dot{E}_{Av}(C_U, T) = & \left(1.3387 \times 10^{-6} T - 3.4319 \times 10^{-5} \right) C_U \\ & - \left(6.6431 \times 10^{-3} T - 8.8142 \right), \end{aligned} \quad (3.3.7)$$

where C_U is in units of mol m^{-3} and T is in units of Kelvin.

Equation 3.3.7 does not consider the effect of nitric acid concentration on the LET of the fission fragments, however this influence is expected to be small compared to the influence of uranyl nitrate because one mole of nitric acid has a much smaller effect on the density of the solution than one mole of uranyl nitrate (see Equation 3.2.22) and this is the primary means by which the addition of uranyl nitrate increases the stopping power of an aqueous solution.

3.3.6 Estimates of Uncertainty in the Bubble Nucleation Radius

Uncertainty in the predicted bubble nucleation size derives primarily from two parameters: the length of track (L) which contributes water vapour and gas during formation of vapour bubbles along a fission track and the predicted LET of the fission fragment in the water or uranyl nitrate solution.

3.3.6.1 Fission Track Length

The most significant source of uncertainty in the predicted size of gas bubbles produced is the length of track contributing gas and steam to form a single bubble. As discussed in Section 3.2.1, there is some uncertainty around this parameter, with values ranging from $L = 2\pi R$ to $L = 4\pi R$ reported in the literature (Norman and Spiegler (1963), El-Nagdy and Harris (1971)). This wide range corresponds to a significant uncertainty in the predicted bubble size, however it should be noted that a strong experimental basis (Deitrich and Connolly (1973)) exists for the value chosen ($L = 3\pi R$) and large deviations from this value are therefore considered unlikely.

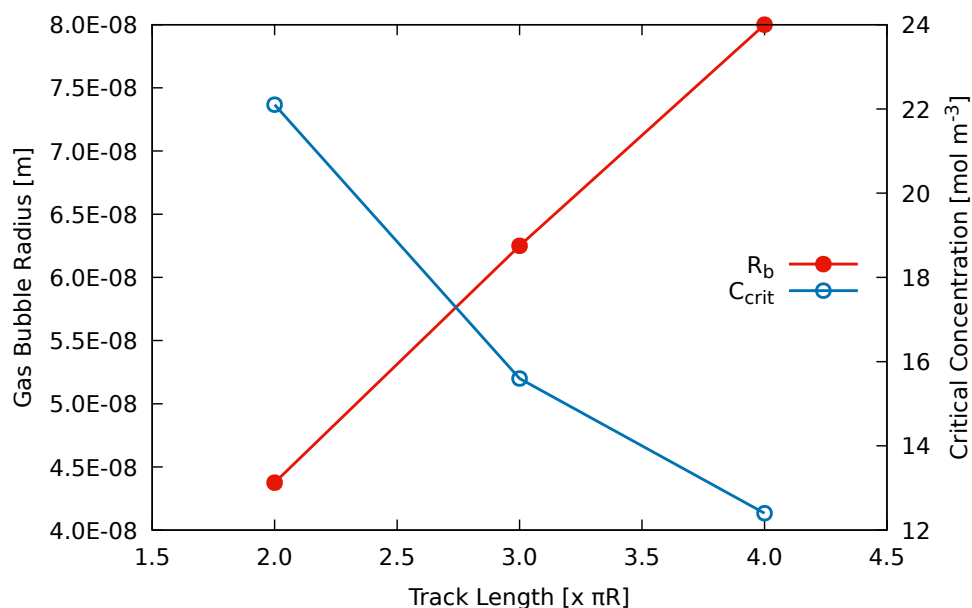


Fig. 3.3.9. Predicted bubble radius as a function of the vapour track length

One factor that determines the track length may be the rate of change in the particle LET during formation of the vapour bubble. Figures 3.3.7 and 3.3.8 show that lighter fission fragments in uranyl nitrate solution remain at or close to their maximum LET for up to $10 \mu\text{m}$ of track, whereas heavier fission fragments have monotonically decreasing LET profiles. If the lighter fragments leave a cylindrical region of superheated steam in their wake (while their LET is relatively constant), the heavier fragments would leave a tapered, conical region. It is possible this may explain the observed variation

in the track length, however without any experimental data relative to specific fission fragments it is not possible to conclude with any certainty.

Figure 3.3.9 shows the bubble radius predicted for a fission fragment with average LET, $\dot{E}_{Av} = 8 \text{ MeV } \mu\text{m}^{-1}$, at atmospheric pressure, fuel solution temperature 298K and a uranyl nitrate concentration of 500 mol m^{-3} . The predicted bubble radius varies from $4.4 \times 10^{-8} \text{ m}$ for $L = 2\pi R$ to $8.0 \times 10^{-8} \text{ m}$ for $L = 4\pi R$. Figure 3.3.9 also shows the difference this variation would make to the critical concentration of fuel solution with a Henry's law constant of $6.5 \times 10^{-6} \text{ mol m}^{-3} \text{ Pa}^{-1}$. The critical concentration is 22 mol m^{-3} in the case where $L = 2\pi R$, reducing to 16 mol m^{-3} if $L = 3\pi R$ and 12 mol m^{-3} if $L = 4\pi R$.

Taking into account the uncertainty highlighted, it is possible to conclude that the critical concentration at which voids will appear in a fissile solution is at least 20 times the saturation concentration for hydrogen gas at atmospheric pressure.

3.3.6.2 Fission Fragment LET

Figure 3.3.10 shows the uncertainty in the predicted bubble radius due to a 7.3% uncertainty in the LET of the fission fragment that created it. This uncertainty corresponds to the random error estimated by Helmut and Schinner (2003) for SRIM stopping powers in the energy range of fission fragments.

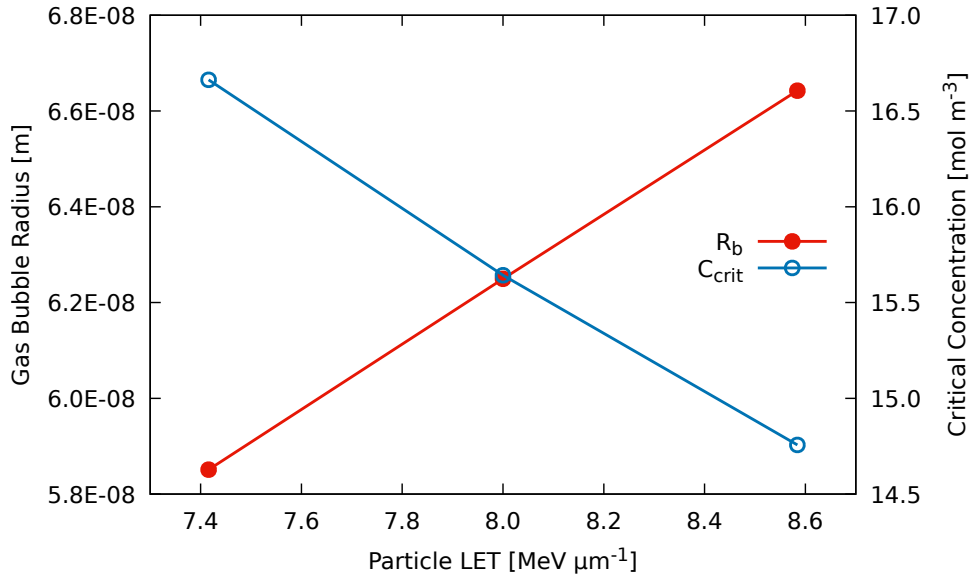


Fig. 3.3.10. Predicted bubble radius at atmospheric pressure and 298K for a fission fragment LET of $8 \text{ MeV } \mu\text{m}^{-1} \pm 7.3\%$.

The LET of the fission fragment has a linear relationship with the radius of the resulting gas bubble, producing a bubble size of $5.9 \times 10^{-8} \text{m}$ at a LET of $7.4 \text{ MeV } \mu\text{m}^{-1}$ and $6.6 \times 10^{-8} \text{m}$ at a LET of $8.6 \text{ MeV } \mu\text{m}^{-1}$. Assuming a Henry’s law constant of $6.5 \times 10^{-6} \text{ mol m}^{-3} \text{ Pa}^{-1}$, the variation in bubble radius corresponds to a critical concentration ranging from 15 mol m^{-3} to 17 mol m^{-3} .

3.3.6.3 Interpolation Error

The radiolytic gas bubble radius was calculated using Equations 3.3.7, 3.3.1 and 3.3.4 and the results were compared to the values computed directly by solution of the equations presented in Section 3.2. A total of forty-eight values were compared, for uranyl nitrate concentrations ranging from 0 to 1750 mol m^{-3} and solution temperatures ranging from 0 to 100°C . The maximum absolute error in the predicted bubble radius due to the correlations was $3.0 \times 10^{-9} \text{ m}$ and the root mean square (RMS) error was $1.4 \times 10^{-9} \text{ m}$.

3.4 Comparison of LET Profiles Calculated Using SRIM and the Tables of Northcliffe and Schilling

LET profiles were calculated using data from SRIM and from the tables of Northcliffe and Schilling (as described in Section 3.2.2), both for pure water and an aqueous solution containing 1000 mol m^{-3} of uranyl nitrate.

SRIM does not include uranyl nitrate in the compound library, however it is possible to build target compounds from their elemental constituents. For the uranyl nitrate solution, separate SRIM calculations were run to predict the stopping power of water, UO_2 and NO_3 species, with each contribution then added to arrive at a value for the uranyl nitrate solution. The calculation was carried out in this way because the software makes adjustments for the covalent bonds between atoms, whereas no such bonds exist between the water and the ionic constituents of the uranyl nitrate. The data from Northcliffe and Schilling were used to estimate stopping powers for U, H_2O , N and O; adding each contribution to arrive at the total stopping power for the uranyl nitrate solution. This method cannot account for the effects of covalent bonds, except those found in the water molecules.

It is not, as far as the authors are aware, possible to simulate the effect of ionic charges on the stopping power of uranyl nitrate using either Northcliffe and Schilling or SRIM. By attracting or repelling the fission fragment it is possible that ionic charge may increase or decrease the stopping power of a chemical species, however this effect is not accounted for in any of the results presented

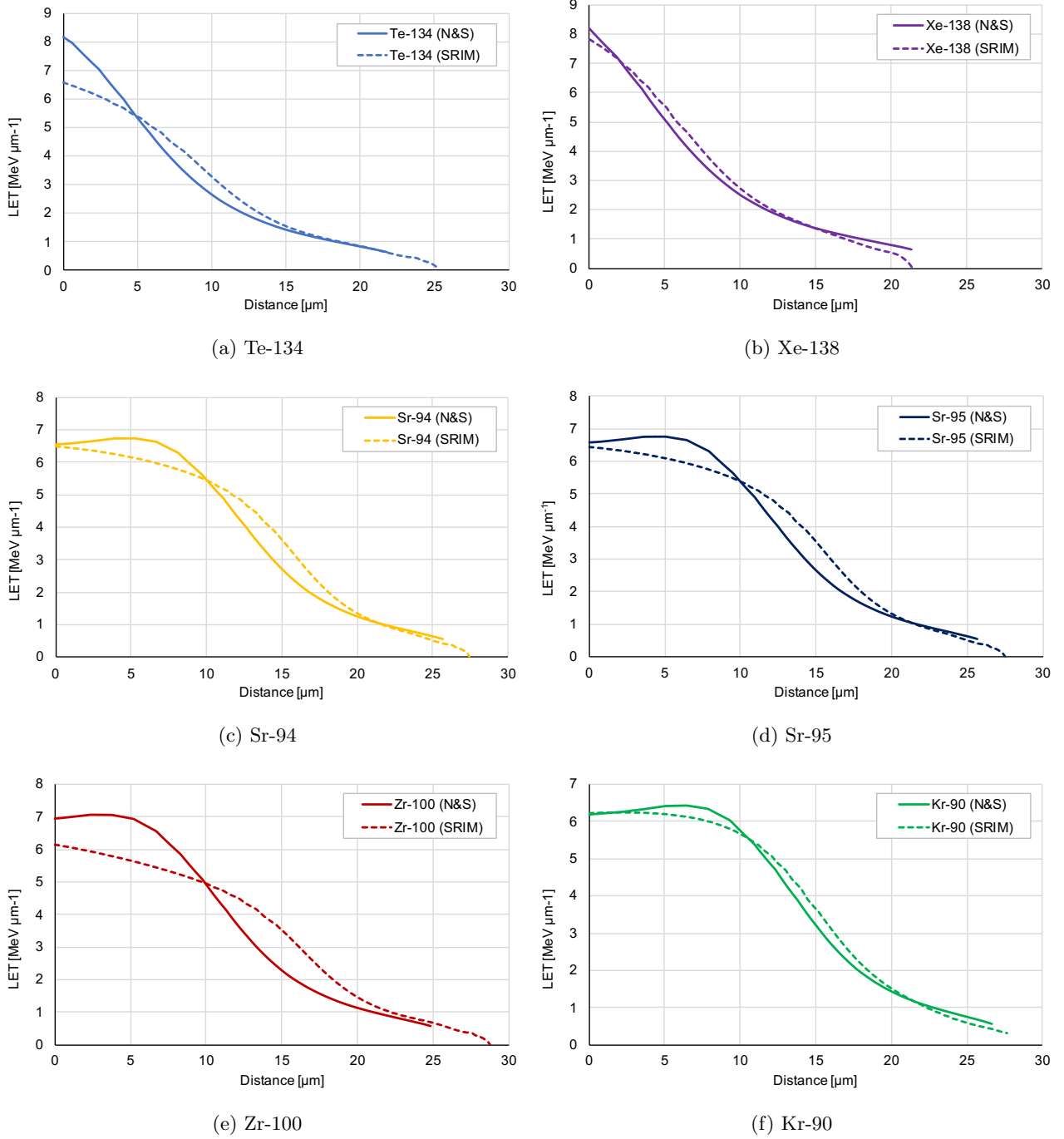


Fig. 3.4.1. LET profiles at 298K for pure water, calculated using the tables of Northcliffe & Schilling and the software package SRIM.

here.

The calculations of SRIM take into account both the electronic and the nuclear stopping power of the medium, whereas only the electronic stopping power is accounted for in the profiles calculated using Northcliffe and Schilling. The impact of nuclear stopping power is not significant to the objectives of this study, namely for predicting bubble sizes in the wake of fission fragments, because it is negligible

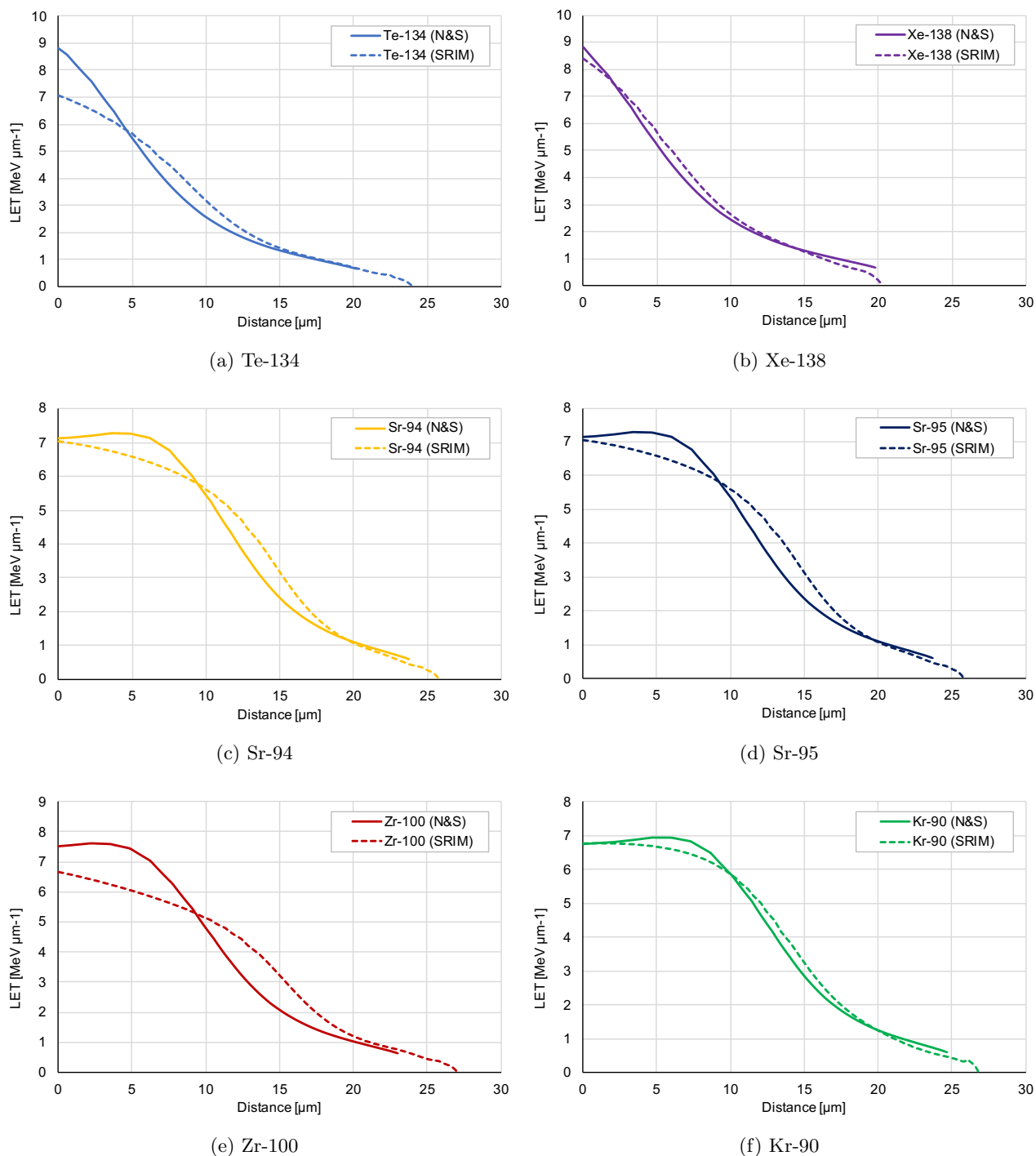


Fig. 3.4.2. LET profiles at 298K for a solution containing 1000 mol m^{-3} of uranyl nitrate, calculated using the tables of Northcliffe & Schilling and the software package SRIM.

compared to the electronic stopping power, except at the very end of the particle track. The effect is visible in Figures 3.4.1 and 3.4.2 as a small increase in the LET in the last 1-2 μm of track, before the particle energy falls to zero.

The agreement between the two methods is relatively close for ^{138}Xe , ^{94}Sr , ^{95}Sr and ^{90}Kr , while significant differences are noted between the two data sets for ^{134}Te and ^{100}Zr . It is possible that

these differences result from the Z_1 - oscillations, noted by Helmut and Schinner Helmut and Schinner (2003), and discussed earlier in Section 3.1.2.

3.5 Conclusions

The LET profiles of fission fragments in aqueous solutions of uranyl nitrate have been calculated and used to predict the distribution of bubble sizes generated along the tracks of these fragments as they travel through the solution. The critical concentration at which hydrogen gas appears as voids in a fissile solution is determined by the size and availability of nucleation sites where dissolved gas may come out of solution. The bubbles created in the wake of fission fragments can serve as nucleation sites and they are believed to be instrumental in the appearance of gas voids during nuclear criticality transients.

Stopping power data from SRIM have been used to predict the LET profiles of fission fragments constituting over 99.5% of the total fission yield of ^{235}U . Using a model adapted from those previously described in the literature, an empirical correlation is presented relating the fission fragment LET and solution properties to the size of gas bubble generated in an aqueous fissile solution. This correlation has been used to predict the distribution of bubble sizes, and therefore the critical concentration of dissolved hydrogen gas.

The critical concentration has been shown to vary significantly with the solution temperature and the concentration of uranyl nitrate in the solution. For pure water at 298K, the maximum predicted bubble radius was $7.1 \times 10^{-8}\text{m}$, associated with a particle LET of $6.9 \text{ MeV } \mu\text{m}^{-1}$. From this data it is possible to estimate a critical concentration of 14 mol m^{-3} of hydrogen gas, based on a Henry's constant of $6.5 \times 10^{-6} \text{ mol m}^{-3} \text{ Pa}^{-1}$. Adding uranyl nitrate to the solution to achieve a concentration of 500 mol m^{-3} is predicted to reduce the maximum gas bubble radius to $5.6 \times 10^{-8}\text{m}$, increasing the critical concentration of dissolved hydrogen to 17 mol m^{-3} .

These findings reveal significant sensitivity of the critical concentration of dissolved gas to the properties of the fuel solution. The sensitivity is due to the impact of solution properties on the LET of fission fragments, as well as the effect of solution properties on the mechanics of bubble formation. This has implications for criticality safety assessment, since the critical concentration often plays an important role in determining the timing and magnitude of the first power peak in accidental criticality transients.

Finally, a correlation has been presented combining the calculated LET profiles with the model of

bubble formation to predict the maximum fission track bubble radius based on solution composition and temperature.

Chapter 4

Phenomenological Model Simulating the Dynamics of Bubble Formation Along Fission Tracks and Saturation of a Fissile Solution with Dissolved Radiolytic Gas

4.1 Introduction

Much of the work presented in this chapter, including tables and figures, is reproduced from Winter et al. (2020b) (submitted for publication).

The process of radiolysis was described at the scale of individual bubble formation in Chapter 3. This chapter will explore the interaction between the bubbles formed in the context of a reactivity transient, the growth and collapse of these bubbles, how they interact with each other and how these processes influence the reactivity of the system.

Radiolysis takes place in all nuclear reactors but is of particular importance in Aqueous Homogeneous Reactors (AHR) or other fissile solutions due to the fact that, unlike solid-fuel reactors, fission fragments are in direct contact with water. By contrast, in a typical solid fuel reactor, any water would be separated from the fuel by cladding, which the fission fragments cannot penetrate. According to Neeb (1997), radiolysis in light water reactors is primarily due to collision of fast neutrons with

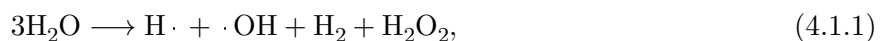
hydrogen atoms, producing recoil protons which then cause radiolysis of water molecules. Radiolysis in AHRs is quite different, being almost entirely due to fission fragments.

As explored in the previous chapter, the tendency of a particle to cause radiolysis depends on the rate of kinetic energy transfer, or LET, from the moving particle to the molecules of water. Fission fragments carry with them the vast majority ($\sim 87\%$) of the energy of fission and have a very high LET compared to other particles emitted during fission; they therefore account for the vast majority of all hydrogen gas produced by radiolysis in fissile solutions, approximately 96% according to Lane et al. (1958), the remaining 4% being due, in roughly equal parts, to neutrons and gamma rays.

Radiolytic gas production contributes to the overall voidage in a reactor or fissile solution and often has a major impact on the kinetics of the system. It is therefore necessary in most cases to account for the production of radiolytic gas when modelling reactivity excursions in fissile solutions. However, the formation and growth of bubbles in fissile solutions is an inherently spatial problem which is not easily represented with accuracy in typical criticality safety codes based on zero dimensional neutronics (point kinetics) coupled with one-dimensional thermal hydraulics. The aim of this chapter is to derive expressions that make it possible to achieve a good approximation of bubble formation and growth within a criticality safety code of this type.

4.1.1 Radiochemical Considerations

It is useful to begin by a brief summary of the principle chemical reactions involved in the formation of radiolytic gas in fissile solutions. The primary reaction leading to the production of gas is,



where a water molecule is broken up to form some combination of hydrogen gas, hydrogen peroxide and hydrogen and hydroxyl free radicals (see Lane et al. (1958)).

Radiolytic gas consists mostly of hydrogen and oxygen. Hydrogen gas is produced directly via the reaction shown in Equation 4.1.1 and oxygen gas is produced later from the decomposition of hydrogen peroxide via a series of subsequent reactions. The most straight-forward of these is thermal decomposition,



The previous chapter focussed on the formation of hydrogen gas, however radiolysis may also result in the production of other gases. Bidwell et al. (1956) measured the production of nitrogen gas during reactivity transients in solutions of uranyl nitrate. The amount of nitrogen gas produced was shown to

increase with increasing concentrations of uranyl nitrate. The total amount produced was on the order of 10^{-3} molecules per 100 eV compared to ~ 1 molecule per 100 eV typically expected of hydrogen gas. Since the quantity of nitrogen gas expected is very small compared to the quantity of hydrogen gas, nitrogen gas formation is not expected to significantly impact the formation of gas bubbles.

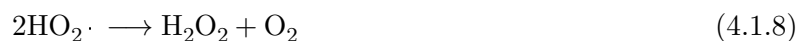
The population of free radical chemical species present in the fuel solution may be important in predicting the rate of production of oxygen gas. This is because these free radical chemical species are involved in a number of alternative routes leading to the decomposition of hydrogen peroxide. Free radicals are chemical species which have an unpaired electron, making them extremely reactive. They are identified in chemical equations by a dot next to the chemical symbol.



The free radical species $\text{HO}_2\cdot$ is formed from the decomposition of hydrogen peroxide by the $\cdot\text{OH}$ free radical and also by the interaction of the $\text{H}\cdot$ free radical with diatomic hydrogen, H_2 . Both diatomic hydrogen and oxygen can be broken down by interaction with free radical species.



Hydrogen peroxide can also be reformed by the interaction of two $\text{HO}_2\cdot$ free radicals. This reaction also produces a molecule of diatomic oxygen.



The amount of oxygen present in the radiolytic gas depends on the timescale of the transient. This is because hydrogen gas is produced immediately, whereas oxygen is produced through a series of reactions and thus takes longer to appear. Therefore, it follows that the radiolytic gas may be assumed to consist entirely of hydrogen if the transient is fast, or a mixture of hydrogen and oxygen gases in stoichiometric proportions if the transient is slow. The pure hydrogen assumption will be adopted throughout this chapter because the processes modelled are on a short timescale, however the role of oxygen will be considered in Chapter 5.

4.1.2 Theories and Mathematical Models of Bubble Growth

At the start of a transient, the fuel solution will typically contain very little dissolved hydrogen, so when radiolytic gas bubbles are produced, they will tend to collapse as the hydrogen gas dissolves. One model, initially proposed by Ghormley (1958) and developed by Norman and Spiegler (1963) was discussed in Chapter 3, however other mechanisms have also been proposed. For instance, Gamble (1959) proposed a model of bubble growth in which bubbles which are unsaturated with respect to their surroundings are assumed to have a lifetime in excess of 20 ms. This contrasts with the model of Norman and Spiegler, who used the equations of Epstein and Plesset (1951) to predict a bubble lifetime less than 10 μ s, for hydrogen gas concentrations up to 50% saturation.

The lifetime of unsaturated bubbles is important in determining models of void growth during transients in fissile solutions. Gamble concludes that bubble growth by diffusion would be too slow to explain the rapid negative reactivity feedback attributed to voidage in experiments they analysed on the KEWB-A reactor. In their model, bubble growth occurs, not by diffusion of dissolved gas from the fuel solution into the bubbles, but by collisions between fission tracks and existing bubbles in the solution. Bubbles intersected by fission tracks expand rapidly by consuming some of the gas left in the wake of the fission fragment. This model requires that bubbles in unsaturated solution collapse on the order of milliseconds, otherwise the probability of collisions between fission tracks and existing bubbles is insufficient to explain the observed rate of void growth.

The equations of Epstein and Plesset are based on a diffusion controlled model of bubble growth and shrinkage, whereas the model of Gamble (1959) posits that the surfactant effect, discussed in the previous chapter, leads to the creation of a relatively stable bubble, due to an accumulation of ions on the gas-liquid interface. The bubble created, sometimes referred to as a “nano-bubble” (Bunkin et al. (2016), Duval et al. (2012)), would remain stable or collapse far more slowly than diffusion theory predicts. However, as discussed in the previous chapter, data from Lubetkin (2003) shows that the surfactant effect is extremely weak in the case of hydrogen gas bubbles; only helium gas had a weaker effect among the gases studied. Furthermore, the hypothesis of a long lifetime for bubbles in unsaturated fissile solutions would appear to contradict experimental observations. In particular, the observations of Spiegler et al. (1962) during experiments on the KEWB-B reactor core, testing fission rates as high as 10^{19} fissions per second and observing no detectable rise in pressure before reaching the critical concentration of dissolved hydrogen in solution, they calculated that the bubble lifetime must have been on the order of microseconds, otherwise an observable rise in pressure would have occurred. The theory of Gamble (1959) is also incompatible with the experimental work of Deitrich and Connolly (1973), which showed that the growth of steam bubbles in superheated water exposed

to energetic particles was subject to a minimum superheat threshold.

It will be demonstrated in this chapter that bubble growth by diffusion, as proposed by Norman and Spiegler (1963), can indeed account for the rapid bubble growth, and resultant strong negative void feedback, observed during transients in fissile solutions and AHRs, such as KEWB-A, and indeed many other fissile solution reactors.

4.1.3 Bubble Nucleation Sites

The saturated (or “critical”) concentration of hydrogen in the fuel solution is the concentration at which hydrogen gas may come out of solution at the available nucleation sites. In a fissile solution, nucleation sites are provided by fission track bubbles (radiolytic gas bubbles formed along the fission tracks), imperfections on the surfaces of the vessel, and possibly on the surface of solid contaminants in the fuel solution. Nucleation sites reduce the activation energy required to form an interface between the gas and liquid phases. Gas bubbles may form in the absence of nucleation sites but this requires much larger concentrations of dissolved gas, as discussed in Chapter 3. The nature of the available nucleation sites is therefore the factor which determines the critical concentration of the solution.

Souto (2002) notes that the relative importance of fission track bubbles compared to surface imperfections as nucleation sites depends on the timescale of the transient. For slow transients, the concentration of dissolved gas builds slowly and there may be time for it to migrate towards imperfections on the vessel surfaces. For fast transients, the concentration of dissolved gas builds very rapidly until it is high enough to nucleate bubbles on the fission tracks bubbles.

The concentration at which bubbles can nucleate along the fission tracks is often referred to as the *critical concentration*. It can be determined using Henry’s law from the partial pressure of hydrogen inside a newly formed radiolytic gas bubble,

$$C_{crit} = H_{H_2, sol} P_{H_2}, \quad (4.1.9)$$

where $H_{H_2, sol}$ is the Henry’s law constant for hydrogen in the fuel solution. P_{H_2} is the partial pressure of hydrogen in the gas bubble, found by taking the product of the bubble pressure and the hydrogen mole fraction in the gas phase (y_{H_2}). The bubble pressure is dependent on the surface tension of the liquid (σ_s) and the bubble radius (r_b), as well as the external liquid pressure (P_l),

$$P_{H_2} = \left(\frac{2\sigma_s}{r_b} + P_l \right) y_{H_2}. \quad (4.1.10)$$

Therefore, the critical concentration depends on the radius of the gas bubbles acting as nucleation

sites. As shown in the previous chapter, the maximum bubble size created in the wake of a fission fragment depends on the solution properties, temperature and pressure, and is typically in the region $r_b = 5 \times 10^{-8}$ m. For a typical solution at atmospheric pressure, with a surface tension of 6.2×10^{-2} N m⁻¹, the pressure inside a newly formed bubble will be 2.58 MPa (25 times atmospheric pressure). Assuming a Henry's law constant equal to that of hydrogen gas in pure water (7.698×10^{-6} mol m⁻³ Pa⁻¹) the critical concentration would be 19.9 mol m⁻³. The critical concentration therefore refers to the concentration of hydrogen at which there is equilibrium between the gas and aqueous phases at the interface of the largest newly formed radiolytic gas bubbles.

As the concentration of dissolved hydrogen in the fuel solution approaches the critical concentration, the net flow of gas out of the bubble decreases and the lifetime of the collapsing bubbles increases. Assuming constant power, the rate of appearance of new bubbles remains the same, therefore, since their rate of disappearance is reducing, the number of bubbles in the system begins to increase. Once the concentration of dissolved hydrogen gas exceeds the critical concentration, the bubbles no longer collapse; instead they grow, taking in hydrogen from the solution around them. At this point, it is useful to define a new quantity, the equilibrium concentration. This is the concentration of hydrogen in the aqueous phase which is at equilibrium with the partial pressure of hydrogen in the gaseous phase. At first it is the same as the critical concentration, however as the bubbles grow in size, their internal pressure tends towards ambient pressure, and the concentration of dissolved gas tends towards the concentration in equilibrium with that pressure (~ 0.78 mol m⁻³, assuming the same values listed in the previous paragraph). The equilibrium concentration differs from the critical concentration, which is always defined with respect to the properties of newly formed radiolytic gas bubbles.

As the dissolved gas concentration drops below the critical concentration, new radiolytic gas bubbles are once again too small to act as nucleation sites, so they collapse. A population of larger bubbles in equilibrium with the concentration of dissolved gas in the fuel solution remains until they are removed by advection.

4.1.4 Existing Approaches to Radiolytic Gas Models in Point-Kinetics Calculations

Current models of radiolytic gas production in fissile solutions typically fall into one of two categories: models that assume instant saturation of the fuel solution, and models that assume a constant equilibrium concentration. In the latter case, the equilibrium concentration may be set at the value for atmospheric pressure (e.g. Souto (2002)), or the pressure inside a newly formed radiolytic gas bubble (e.g. Cooling (2014)). The value chosen will determine the delay between criticality and the

appearance of radiolytic gas; typically making a difference of several seconds for reactivity insertions up to a dollar in magnitude. Where the equilibrium concentration is assumed constant, at the value corresponding to atmospheric pressure, the total amount of gas produced will be accurate but the delay in its appearance will be underestimated. If the equilibrium concentration is assumed constant at the internal pressure of a radiolytic gas bubble, the amount of gas will be underestimated but the delay in its appearance will be closer to reality.

There is currently no way for models of fissile liquids based on point kinetics with one-dimensional thermal hydraulics to predict the number and size distribution of bubbles in a fissile solution. Without knowing the number and size of bubbles present, it is not possible to know exactly how much negative reactivity is induced per mole of gas produced. This is due to the surface tension effect (see Equation 4.1.10) which contributes to elevated internal pressure inside small bubbles compared to the external pressure.

Models of this type also neglect the influence of the bubble population on the rate of appearance of radiolytic gas. When the number of bubbles per unit volume (hereafter referred to as the “number density” of bubbles) is large, dissolved radiolytic gas has less distance to diffuse before it can come out of solution, resulting in a relatively fast rate of appearance of radiolytic gas voids. On the other hand, if the bubble number density is low, dissolved gas must diffuse further through the solution to find a bubble where it may come out of solution, resulting in a slower rate of appearance of radiolytic gas.

The work presented in this chapter aims to provide the information necessary to improve on the existing approaches to the handling of radiolytic gas and apply this new information in point kinetics simulations of criticality transients. The model should accurately predict the delay between criticality and the appearance of a radiolytic gas, as well as the quantity of gas produced, the volume it occupies, and its rate of appearance upon saturation of the fuel solution.

4.2 A Numerical (Monte Carlo) Model of Bubble Nucleation

4.2.1 Concept and Overview

The purpose of this chapter is to explore the mechanisms involved in saturation of a fissile solution with radiolytic gas and derive expressions which can be incorporated into a point kinetics model. The modelling of these processes using a point kinetics, or even one-dimensional approach, is not trivial because the formation and growth of bubbles from the microscopic gas bubbles deposited along

the tracks of fission fragments is a complex three dimensional process. The model presented in this chapter comprises a numerical simulation of bubble growth in a fissile solution during saturation of the solution with hydrogen gas from radiolysis. The results of Chapter 3 will be used to predict the fission track bubbles generated in the numerical simulation.

The numerical model simulates a small cube of fissile solution (hereafter referred to as “the simulated domain”) which represents a small volume within a larger volume of the solution, such as within an aqueous homogeneous reactor (AHR) or a container of fissile solution undergoing an unplanned criticality excursion (see Figure 4.2.1). Within this volume, the history of every bubble is simulated, from its birth by radiolysis, through growth and/or shrinkage to its possible collapse. The purpose of the numerical model is to simulate the many physical processes taking place at the centre of a fissile solution while the solution becomes saturated with radiolytic gas. The model is not intended to reproduce the behaviour of a full-scale fissile liquid system, but to provide the necessary inputs for such a model, which will be presented in Chapter 5.

The dimension of the simulated domain is variable, typically 1×10^{-4} m in the x- and y- dimensions, and up to 3×10^{-3} m in the z- (vertical) dimension, with a volume ranging from 2×10^{-12} m³ to 3×10^{-11} m³. The reason for making the simulated domain larger in the vertical direction was to allow sufficient distance for bubbles to advect. Simulations were also run with different dimensions to confirm a lack of sensitivity to these parameters.

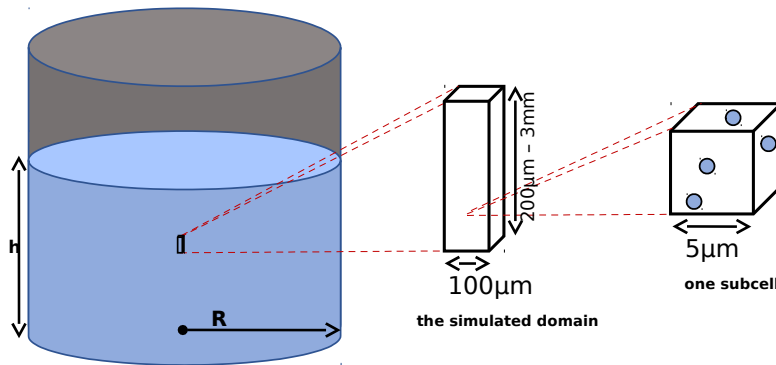


Fig. 4.2.1. Model of bubbles inside a small volume within a larger vessel of fissile solution.

Advection of the bubbles is calculated based on their size and the dimension of the simulated domain is determined so that the bubbles do not advect more than 50% of their way across it during the simulation time. Periodic boundary conditions are applied so that bubbles or molecules of gas, travelling out of the domain in one direction, re-enter the domain on the opposite side. The simulated region resembles an infinite system in the sense that no limits are set on the distance moved by bubbles of gas molecules in any direction. The probability of fission is uniform throughout the simulated region

since the volume simulated is very small and any influence of a non-uniform neutron flux shape is therefore negligible at the scale modelled.

The domain is subdivided into smaller regions (or “subcells”). The change in concentration of dissolved hydrogen gas in each subcell, due to bubble growth, shrinkage and collapse, is tracked, as well as the rate of diffusion between subcells. This makes it possible to model variations in concentration across the domain, resulting from stochasticity in the number, location and direction of fission tracks. The subcell dimension was fixed at $5 \times 10^{-6}\text{m}$ in all directions ($V = 1.25 \times 10^{-16}\text{m}^3$) and the number of subcells was determined according to the dimensions of the simulated domain. Simulations were also performed with different subcell dimensions to confirm the lack of any significant sensitivity to this parameter. If the selected subcell dimension were too large then a significant discretisation error would be introduced. The magnitude of the error would depend on the size of the subcells, which would result in sensitivity of the simulation results to the subcell dimension.

The simulation is relatively expensive and not easily amenable to parallelisation. The high computing cost is due to tracking the histories of a very large number of bubbles from birth to collapse. Execution time required to run the simulation increases with the volume of the simulated domain due to the resulting increase in the number of bubbles to be simulated and the number of liquid subcells. Total time required for a single simulation ranges from hours to days depending on the scenario.

The model resembles an Eulerian-Lagrangian scheme (Yeoh and Tu (2019)) in the sense that it consists of a continuous liquid phase (the solution) coupled to a dispersed phase (the bubbles). The continuous liquid phase is modelled on a fixed mesh whereas the bubbles are tracked individually as they move within the domain. The dispersed phase can exchange hydrogen gas with the continuous liquid phase, which is also exchanged between different volumes of the continuous phase by diffusion. Unlike computational fluid dynamics (CFD), this model does not track the movement of mass, momentum or energy within the continuous phase, only the local concentrations and diffusion of dissolved hydrogen gas.

4.2.2 Point Kinetics Model

A point kinetics model determines the power density of the fissile solution from a reactivity profile. The calculated power density determines the expected number of fission events occurring within the simulated domain in any given time step. The expected value defines a Poisson distribution which is sampled to determine the actual number of fissions in the time step.

The point kinetics equations were applied as follows,

$$\frac{dP(t)}{dt} = \sum_{i=1}^6 \lambda_i C_i(t) + \frac{\beta P(t)}{\Lambda} (R_{ex}(t) + \alpha_T(T(t) - T_0) + \alpha_V(V_{RG}(t) - V_{RG,0}) - 1) \quad (4.2.1)$$

$$\frac{dC_i(t)}{dt} = -\lambda_i C_i(t) + \frac{\beta_i}{\Lambda} P(t), \quad (4.2.2)$$

$$\frac{dT(t)}{dt} = \frac{P(t)}{M_{sol} C_p}, \quad (4.2.3)$$

where $P(t)$ is the fission power, β is the total delayed neutron fraction and β_i is the fraction of all neutrons in delayed neutron group i , Λ is the generation time, T is the temperature, V is the voidage, α_T and α_V are temperature and void feedback coefficients, respectively, λ_i is the decay constant of delayed neutron group i , M_{sol} is the mass of the fuel solution, C_p is the heat capacity of the fuel solution at constant pressure, T is the solution temperature and V_{RG} is the volume of radiolytic gas. A subscript zero indicates initial values.

The purpose of Equation 4.2.1 is to provide a power profile for simulations of the process of saturation with radiolytic gas, as well as bubble formation and growth. It uses feedback coefficients which have been adjusted for the size of the simulated domain (see Section 4.2.10), however it is not intended to provide an accurate model of a criticality transient in a full scale system.

The delayed neutron groups shown in Tables 4.2 to 4.4, as well as other parameters, were adapted from four reactor configurations from the literature: the SILENE reactor with uranyl nitrate concentrations of 300.9 mol m^{-3} (“SOL-A”) and 926.3 mol m^{-3} (“SOL-B”), the TRACY reactor with a uranyl nitrate concentration of $1632.8 \text{ mol m}^{-3}$ (“SOL-C”) and the CRAC reactor with a uranyl nitrate concentration of 860.2 mol m^{-3} (“SOL-D”).

	SOL-A	
i th Group	β_i	$\lambda_i \text{ [s}^{-1}\text{]}$
1	2.6934×10^{-4}	0.0124
2	1.7271×10^{-3}	0.0305
3	1.5908×10^{-3}	0.111
4	3.1059×10^{-3}	0.301
5	9.3428×10^{-4}	1.13
6	3.1263×10^{-4}	3.00
Source	Barbry (1994)	

TABLE 4.1

Delayed neutron group yields (β_i) and decay constants (λ_i) for fuel solution SOL-A.

The void volume is calculated by summing over the volume of all bubbles in the simulated domain. This is described in more detail Section 4.2.5. No expression is included for heat loss to surroundings

	SOL-B	
i th Group	β_i	λ_i [s ⁻¹]
1	2.8980×10^{-4}	0.0124
2	1.8487×10^{-3}	0.0305
3	1.7010×10^{-3}	0.111
4	3.3768×10^{-3}	0.301
5	9.9900×10^{-4}	1.13
6	3.1200×10^{-4}	3.00
Source	Barbry (1994)	

TABLE 4.2

Delayed neutron group yields (β_i) and decay constants (λ_i) for fuel solution SOL-B.

	SOL-C	
i th Group	β_i	λ_i [s ⁻¹]
1	2.5448×10^{-4}	0.0127
2	1.6498×10^{-3}	0.0317
3	1.4918×10^{-3}	0.1152
4	3.0008×10^{-3}	0.3116
5	8.8928×10^{-4}	1.4003
6	3.2365×10^{-4}	3.8939
Source	Miyoshi et al. (2009)	

TABLE 4.3

Delayed neutron group yields (β_i) and decay constants (λ_i) for fuel solution SOL-C.

	SOL-D	
i th Group	β_i	λ_i [s ⁻¹]
1	2.5×10^{-4}	0.01249
2	1.47×10^{-3}	0.03182
3	1.33×10^{-3}	0.10938
4	3.83×10^{-3}	0.31700
5	1.08×10^{-3}	1.35395
6	3.9×10^{-4}	8.63760
Source	Cooling (2014)	

TABLE 4.4

Delayed neutron group yields (β_i) and decay constants (λ_i) for fuel solution SOL-D.

because the rate of heat loss from a volume of liquid near the centre of the reactor is assumed to be negligible over the timescales considered.

The void and thermal feedback coefficients, and the generation time for each fuel solution are shown in Table 4.5.

The values of specific heat capacity (C_p) were estimated using the Equation 4.2.4, originally derived by Sugikawa et al. and cited in Yamane (2015),

$$C_p = 4186 \left(0.998 - 9.630 \times 10^{-4} C_U - 4.850 \times 10^{-2} C_N \right). \quad (4.2.4)$$

	SOL-A	SOL-B	SOL-C	SOL-D
Generation Time (s)	3.6×10^{-5}	1.3×10^{-5}	4.906×10^{-5}	1.279×10^{-5}
Thermal Feedback ($\$ K^{-1}$)	-6.4×10^{-2}	-2.2×10^{-2}	-3.3×10^{-2}	-1.1×10^{-2}
Void Feedback ($\$ m^{-3}$)	-2281	-2753.1	-387.67	-1200
$C(UO_2(NO_3)_2)$ (mol m^{-3})	300.9	926.3	1632.8	860.2
$C(HNO_3)$ (mol m^{-3})	2000	2840	580	2180
C_p (J $kg^{-1} K^{-1}$)	3598	2893	2495	2920
G_{H_2} (molecules per 100eV)	1.30	0.74	0.56	0.78
$\rho_s(25^\circ C)$ (kg m^{-3})	1218.8	1469.6	1550.7	1407.1
V_{FS} (m^3)	3.93×10^{-2}	2.44×10^{-2}	1.196×10^{-1}	7.09×10^{-2}

TABLE 4.5

Point kinetic parameters and properties for fuel solutions based on SILENE, TRACY and CRAC.

The radiolytic gas generation coefficient was estimated using Equation 3.2.26 based on the concentration of uranyl nitrate in the fuel solution. These values are shown in Table 4.5. The fuel solution density was calculated using Equation 3.2.22 and the surface tension was calculated dynamically by the model using Equation 3.2.23.

The fuel solution compositions based on the SILENE reactor were obtained from Barbry (1994), while the generation times, fuel solution volumes and thermal and void feedback coefficients were estimated based on data from Kornreich (1993). The feedback coefficients for the solution based on TRACY were obtained from Miyoshi et al. (2009) and those values for the solution based on CRAC, as well as the generation time, were obtained from Cooling (2014).

The purpose of selecting the four fuel solutions and corresponding input parameters summarised in Table 4.5 is not to determine anything in particular about the SILENE, CRAC or TRACY reactors. The purpose is to choose a broad and representative range of different fuel solution properties so that the influence of these properties on the results of the numerical model can be examined.

4.2.3 Initial Conditions

Simulations were started from steady-state ($\rho=0$) with a total reactor power output of $1 \times 10^{-6}W$, scaled to the volume of the simulated domain. For example, the SILENE reactor typically contains 24.4 L of fuel solution when running with the particular composition used here. For a simulated domain with dimensions $1 \times 10^{-4}m \times 1 \times 10^{-4}m \times 5 \times 10^{-4}m$ and total volume $5 \times 10^{-12}m^3$, Equation 4.2.1 would be initialised with a steady-state power level of $2.05 \times 10^{-16} W$.

4.2.4 Advection

Bubbles are assumed to reach terminal velocity instantly so that their advection velocity is assumed to equal their terminal velocity at all times. This assumption is tested in Section 5.1.7 and the associated error is shown to be small: e.g. for a bubble of radius 10^{-5} m, the error in the predicted displacement is $< 10^{-8}$ m.

The terminal velocity of a bubble is calculated by equating the drag and buoyancy forces acting on the bubble. The buoyancy force acting to accelerate the bubble upwards is the product of the mass of water displaced by the bubble (m_l) and the gravitational field strength (g):

$$F_{\text{buoyancy}} = m_l g, \quad (4.2.5)$$

where the mass of liquid displaced by the bubble is given by,

$$m_l = \frac{4}{3} \pi r_b^3 \rho_s. \quad (4.2.6)$$

The drag force acting on the bubble can be determined using the following expression obtained from Celata et al. (2007):

$$F_{\text{drag}} = \frac{\rho_s v_b^2 C_D \pi r_b^2}{2}, \quad (4.2.7)$$

where C_D is the drag coefficient, which for a spherical bubble can be approximated as $C_D = 24/Re_b$. This is valid for small bubbles with low terminal velocities, where the surface tension of the solution is sufficient to maintain a spherical bubble shape. On the other hand, larger bubbles advect at higher terminal velocities and require a more complex formulation for the drag coefficient due to the effect of deformation in their shape.

For the purposes of the numerical simulation presented in this chapter, where the period of interest is a very short time during which the fissile solution becomes saturated with radiolytic gas, the bubbles are not expected to grow to sizes at which significant deformation of their shape would occur. However, this effect is expected to be significant for the simulations presented in the next chapter, and a more complex model of bubble advection is discussed in Section 5.1.7.

Substituting $C_D = 24/Re_b$ into Equation 4.2.7, and setting Equation 4.2.7 equal to Equation 4.2.5, results in the following expression for the terminal velocity of a bubble,

$$v_b = \frac{2r_b^2 \rho_s g}{9\mu}, \quad (4.2.8)$$

where v_b is the velocity of the bubble presumed equal to the terminal velocity, μ is the dynamic viscosity of the fuel solution, ρ_s is the density of the fuel solution and g is the acceleration due to

gravity.

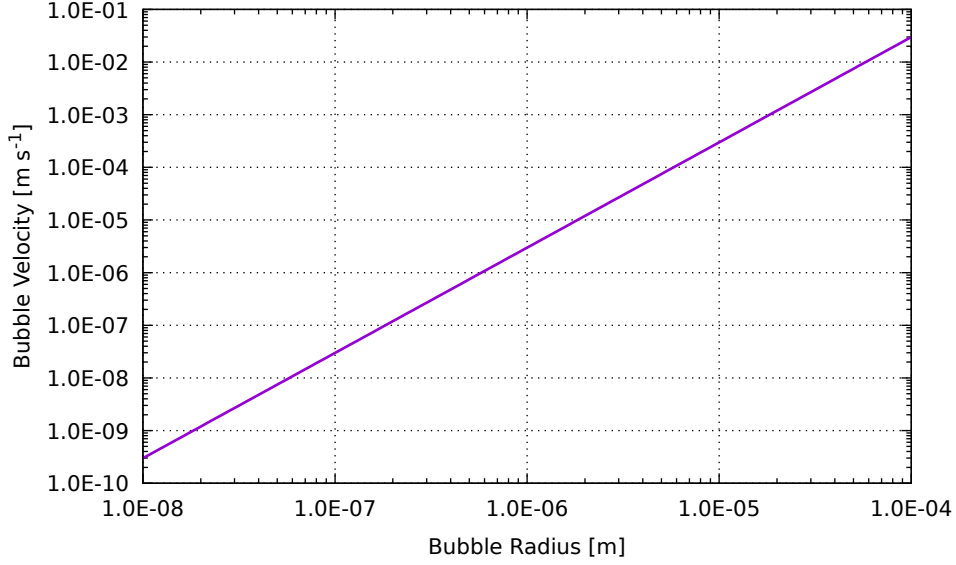


Fig. 4.2.2. Stokes' Law advection velocity as a function of bubble radius.

Terminal velocity as a function of bubble radius, calculated using Equation 4.2.8, is shown in Figure 4.2.2 for a solution of density 1218.8 kg m^{-3} and dynamic viscosity $8.9 \times 10^{-4} \text{ Pa s}$. It shows that a bubble of radius $1 \times 10^{-5} \text{ m}$ would travel approximately $300 \text{ }\mu\text{m}$ in one second, which is why in some simulations it is necessary to make the simulated domain significantly taller than it is wide, as indicated in Figure 4.2.1.

4.2.5 Bubble Growth and Collapse

The volume of radiolytic gas at any time is calculated by summing over the volume of all bubbles in the simulated domain,

$$V(t) = \sum_{i=1}^{N_b(t)} \frac{4}{3} \pi r_{b,i}^3, \quad (4.2.9)$$

where $N_b(t)$ is the number of bubbles in the simulated domain at time t and $r_{b,i}$ is the radius of bubble i . The radius of a single bubble is calculated from the number of moles of radiolytic gas it contains. This is done using a Newton-Raphson algorithm to solve the following expression, which was derived by substituting Equation 4.1.10 into the ideal gas law,

$$\left(P_l + \frac{2\sigma_s}{r_b} \right) \frac{4}{3} \pi r_b^3 - N_{\text{RG}} RT = 0, \quad (4.2.10)$$

where P_l is the liquid pressure around the bubble, σ_s is the liquid surface tension, r_b is the bubble radius, N_{RG} is the number of moles of radiolytic gas in the bubble and R is the universal gas constant.

The value of N_{RG} is calculated by the ODE solver, for each bubble individually, by tracking the rate of diffusion of gas into and out of the bubble. This is dependent on the concentration of dissolved gas in the region surrounding each bubble, the resistance to mass transfer across the gas/liquid interface at the bubble surface, and the partial pressure of gas inside the bubble, which determines the equilibrium concentration. The rate of mass transfer is given by,

$$\frac{dN_{\text{RG}}}{dt} = k_D A_b (C_{\text{H}_2(aq)} - C_{\text{H}_2,eq}), \quad (4.2.11)$$

where k_D is the mass transfer coefficient characterising the rate of mass transfer at the bubble gas/liquid interface, A_b is the surface area of the bubble, $C_{\text{H}_2(aq)}$ is the concentration of dissolved hydrogen in bulk liquid phase and $C_{\text{H}_2,eq}$ is the liquid phase concentration that would be in equilibrium with the partial pressure of hydrogen gas inside the bubble.

Equation 4.2.11 assumes a homogeneous gas inside the bubble with no significant resistance to mass transfer within the bubble. This is certainly justified in the case of radiolytic gas bubbles due to their small size. Resistance to mass transfer across the interface is presumed to behave in accordance with two-film theory, where resistance to mass transfer is assumed to reside in a stagnant liquid film on the liquid side of the interface.

Under steady-state conditions, it has been shown by Epstein and Plesset (1951) that the mass transfer coefficient is proportional to the diffusivity of the dissolved component in the liquid phase, and inversely proportional to the radius of the bubble and the thickness of the stagnant film:

$$k_D = D_i \left[\frac{1}{r_b} + \frac{1}{\delta} \right] = D_i \left[\frac{1}{r_b} + \frac{1}{\sqrt{\pi D_i \tau}} \right], \quad (4.2.12)$$

where r_b is the bubble radius, D_i is the diffusivity of component i in the liquid phase, δ is the thickness of the stagnant film and $\tau = r_b/v_b$ is the contact time of the bubble with the surrounding fluid as it moves by advection.

The Epstein-Plesset equation is a quasi-static approximation which may underestimate the mass transfer coefficients for rapidly expanding or shrinking bubbles. Peñas-López et al. (2016) propose a modified version of the Epstein-Plesset equation, incorporating a so-called “history term”, which accounts for the disruption to the stagnant film surrounding the bubble as the bubble itself expands or contracts. This work confirms that the Epstein-Plesset equation does indeed provide a conservative estimate of the mass transfer coefficient during the phase where the bubbles are growing rapidly. However, it will be shown later that, due to the large concentration of dissolved gas at the moment of saturation, the rate of bubble growth during this phase is so rapid that further increases in the mass transfer coefficient would have no discernible effect. The quasi-static version of the Epstein-Plesset

equation is therefore considered adequate.

4.2.6 Bubble Generation Due to Radiolysis

Fissions are assumed to occur at random locations within the simulated domain. The expected number of fissions is determined from the volume of the simulated domain and the reactor power density,

$$E[N_{\text{fiss}}] = \frac{P(t)\Delta t}{\epsilon}, \quad (4.2.13)$$

where ϵ is the energy released per fission and Δt is the length of the time step. The actual number of fission events within each timestep is determined by randomly sampling a Poisson distribution whose mean is N_{fiss} . The location of each fission event within the simulated domain is assumed random and determined by sampling a uniform probability distribution for the x , y and z coordinates.

Fission fragments are modelled at the site of each fission, leaving tracks of radiolytic gas in opposite directions from one another. The axis of the fission tracks is selected at random according to an isotropic distribution. Periodic boundary conditions are applied at the boundaries of the simulated domain so that fission tracks exiting on one side re-enter on the opposite side.

The size of the bubbles is determined by randomly assigning a fission fragment to each track from the 250 highest-yielding fission fragments of ^{235}U , according to data from the Brookhaven National Nuclear Data Center (2011). The LET of each fission fragment is estimated using the technique described in Section 3.2.2 and this is used to determine the size of bubbles produced in the fission fragment wake by applying Equation 3.3.1. The contents of any bubble with a radius less than $1 \times 10^{-8}\text{m}$ is assumed to dissolved instantly into the fuel solution.

The LET profiles of the 250 fission fragments are calculated according to the method detailed in Chapter 3. The profiles vary as a function of the system conditions, including uranyl nitrate concentration, system pressure and solution temperature. Since the solution temperature is varying during the transient, the LET profiles are updated for every 1°C increase in the fuel solution temperature.

4.2.7 Mass Transfer of Hydrogen Within the Aqueous Solution

The movement of dissolved hydrogen is assumed to take place by diffusion only and any convective transport is assumed insignificant. This is justified by the small length scale of the simulated domain, which means that relative movements within the simulated domain as a result of convection currents are likely to be small.

The diffusion of dissolved hydrogen between one subcell and its neighbours is calculated as follows,

$$\frac{\partial C_{\text{H}_2(aq)}(\vec{r}, t)}{\partial t} = D_{\text{H}_2}(t) \nabla^2 C_{\text{H}_2(aq)}(\vec{r}, t) \quad (4.2.14)$$

where $C_{\text{H}_2(aq)}(\vec{r}, t)$ is the concentration of dissolved hydrogen at a given point in space and time and $D_{\text{H}_2}(t)$ is the temperature-dependent diffusion coefficient for hydrogen in the fuel solution. The system of PDEs was discretised using a second-order finite volume method, in which the derivative terms were estimated using the central difference approximation.

The diffusion coefficient for hydrogen in pure water has been used in the absence of any data specific to a given fuel solution composition. Its variation with temperature has been modelled using the following correlation (Yaws (2009)):

$$\log_{10} D_{\text{H}_2} = A + \frac{B}{T}, \quad (4.2.15)$$

where T is the temperature of interest in units of Kelvin and $A = -1.46551 \text{ cm}^2 \text{ s}^{-1}$ and $B = -8.4259 \times 10^2 \text{ cm}^2 \text{ K s}^{-1}$ are constants specific to hydrogen in water.

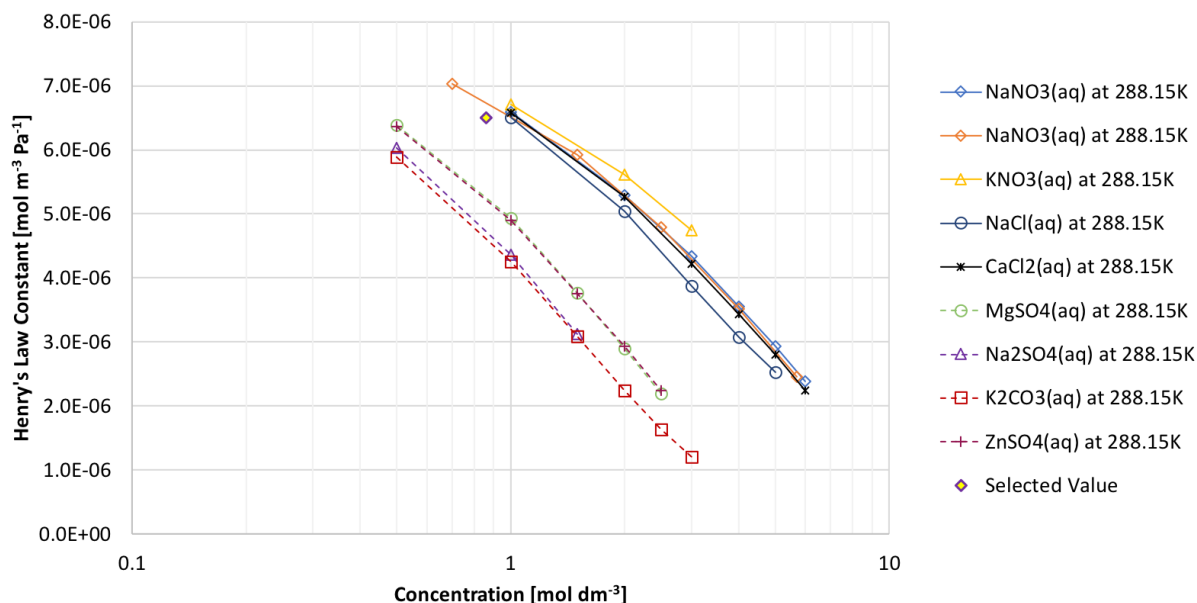
An indication of the error induced by neglecting the effect of fuel solution composition on the diffusion coefficient for hydrogen can be obtained by considering the available data for hydrogen diffusivity in salt water. Jähne et al. (1987) measured the diffusion coefficient of dissolved hydrogen at 25°C in pure water and in sea water, measuring values of $5.13 \times 10^{-9} \text{ m}^2 \text{ s}^{-1}$ for pure water and $4.91 \times 10^{-9} \text{ m}^2 \text{ s}^{-1}$ for sea water, a difference of approximately 4%. Sea water typically has a salinity of 600 mol m^{-3} .

4.2.8 Solubility of Hydrogen in Aqueous Salt Solutions

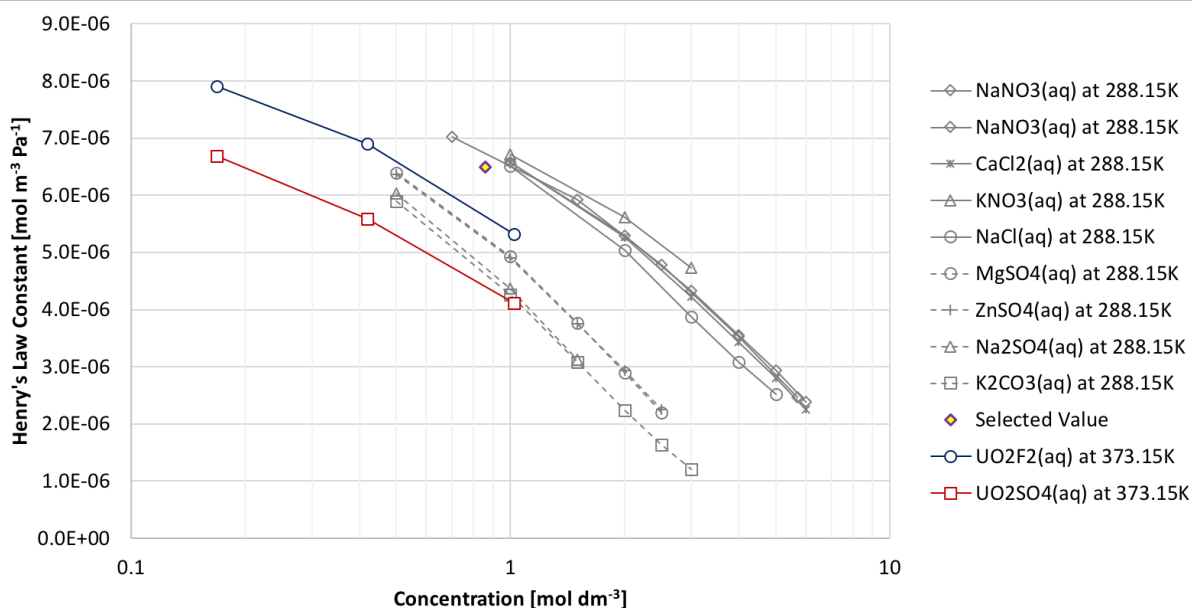
No data was found in the literature for the Henry’s law constant specific to hydrogen gas in solutions of uranyl nitrate. It is not known whether or not this has been experimentally determined. The Henry’s law constant for hydrogen gas in aqueous solutions of uranyl nitrate, at any given temperature, will decrease with increasing concentrations of uranyl nitrate. According to Engel et al. (1996), this is due to the “salting out” effect, which describes the tendency of an ion in solution to reduce the solubility of an another solute in the same solution. Engel et al. note that the salting out potential of an ion increases with ionic charge and reduces with ionic radius.

Figure 4.2.3a shows data from Washburn (2003) for the Henry’s law constant of hydrogen gas in aqueous solutions of various salts across a range of salt concentrations. Details of the unit conversions carried out can be found in Appendix A. Two groups clearly emerge from the data: salts with mono-

valent anions (shown with solid lines) and those with divalent anions (shown with dashed lines). This is because the divalent anions have a greater affinity for water molecules than the monovalent anions which means they compete more strongly with the hydrogen molecules.



(a) H_2 solubility in aqueous solutions of various salts



(b) H_2 solubility in aqueous solutions of uranyl sulphate and uranyl fluoride at elevated temperature and pressures

Fig. 4.2.3. Henry's law constants for hydrogen gas in aqueous solutions of various salts Washburn (2003), Pray and Stephan (1953), Pray and Stephan (1954).

Pray and Stephan measured the solubility of hydrogen in solutions of uranyl sulphate and uranyl fluoride (Pray and Stephan (1953, 1954)), at temperatures greater than 100°C and pressures in the range 20 to 100 atmospheres. Figure 4.2.3b shows the Henry's law constants, calculated using these

data, for hydrogen gas in uranyl sulphate and uranyl fluoride solutions. The Henry's law constants for other salts are included in grey for comparison.

The Henry's law constants calculated for uranyl sulphate and uranyl fluoride do not fit into the two groups identified in Figure 4.2.3a. One reason for this might be the pressure, since as explained above, these values are based on data for elevated pressures. However, examination of the data presented by Pray and Stephan shows a linear increase in liquid phase concentration with increasing hydrogen partial pressure across the full range of pressures tested, which would suggest the liquid phase concentration is not high enough in this pressure range to have a significant impact on solubility. A more likely explanation is temperature, since the Henry's law constant for hydrogen gas in pure water is significantly lower at 373K compared to 288K. Another explanation specific to the case of uranyl fluoride may be the small ionic radius of the fluoride ion, which would increase the salting out potential of uranyl fluoride relative to salts consisting of larger monovalent ions, such as nitrates.

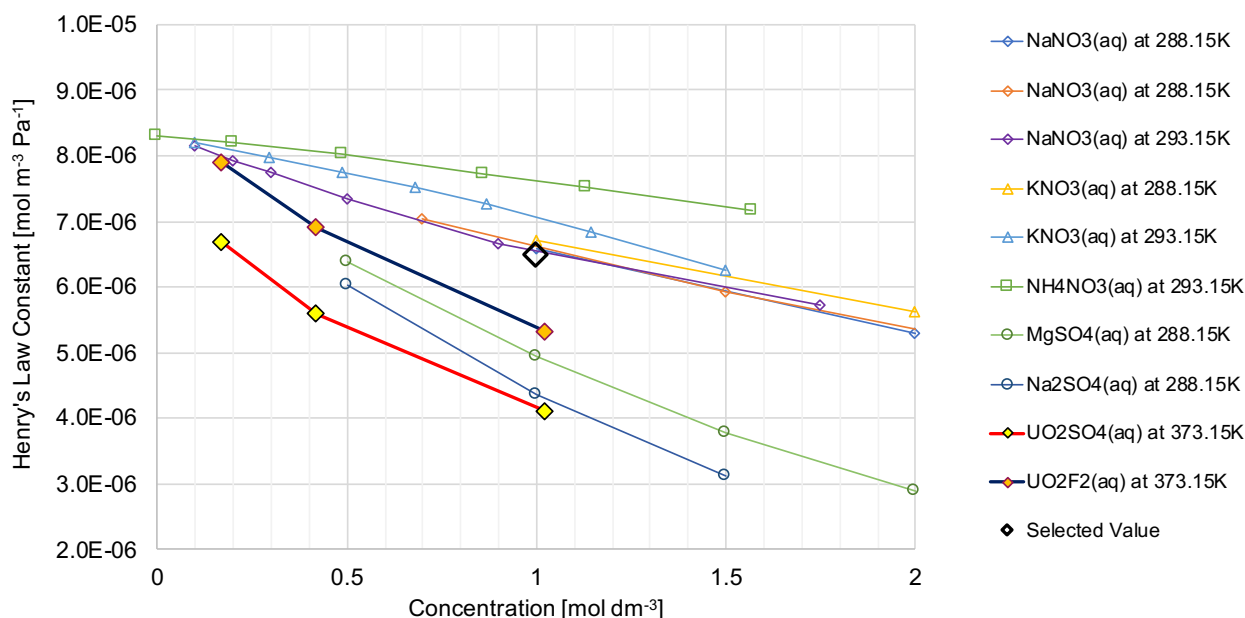


Fig. 4.2.4. Henry's law constant for hydrogen gas in various salts over concentrations ranging from 0 to 2.0 mol dm⁻³.

Figure 4.2.4 shows concentrations ranging from 0 to 2000 mol m⁻³ and the Henry's law constant in this range varies between 5.0×10^{-6} and 8.3×10^{-6} mol m⁻³ Pa⁻¹ for the nitrate salts. Appendix C explores the variation of hydrogen and oxygen solubility as a function of temperature and solute concentration for solutions of some of these salts and uses the data to derive a correlation which could be used to estimate a likely approximation to the Henry's law constant based on the limited data available. However, given the uncertainty due to the lack of specific experimental data, and the fact that effects due to variation in the uranyl nitrate concentration are not of interest to the model

presented in this chapter, a single constant value of $6.5 \times 10^{-6} \text{ mol m}^{-3} \text{ Pa}^{-1}$ (shown in figure) around the middle of the range for the nitrate salts has been selected.

4.2.9 Radiolytic Gas Generation Coefficient

Equation 3.2.26 in the previous chapter provides a correlation for the radiolytic gas generation coefficient for hydrogen (G_{H_2}) in uranyl nitrate solution, as a function of the concentration of uranyl nitrate. The correlation does not consider nitric acid, although it is possible this may also have an impact on the value of G_{H_2} . Souto (2002) notes that the presence of uranyl nitrate in the solution reduces the yield of hydrogen gas by destroying the free radical species which are products of the primary radiolysis reaction. In the case of hydrogen this would reduce the yield by preventing the recombination of H^\cdot free radicals in the fission track into molecular hydrogen.

The value of G_{H_2} in this model will affect both the rate of build-up of hydrogen gas in the fuel solution and the critical concentration at which hydrogen gas begins to move from the dissolved phase back into the gas phase. It affects the critical concentration because Equation 3.2.13 predicts that a higher G_{H_2} would result in the formation of larger gas bubbles along the fission tracks.

4.2.10 A Note on System Reactivity and Feedback Coefficients

Void and thermal reactivity feedback coefficients are required by Equation 4.2.1 in order to determine a power profile for each simulation. However, it is not the purpose of the numerical model to determine accurate reactivity and fission power profiles for a particular transient in a particular reactor; the purpose is to examine the process of bubble formation and growth during saturation of a fissile liquid with radiolytic gas.

The void and thermal reactivity coefficients have been based on values calculated for fuel solutions of the SILENE, TRACY and CRAC reactors. This was done in order to ensure that realistic values were chosen, however the exact values of these parameters are not particularly important since the objective is not to learn anything about these reactors in particular. Furthermore, the reactivities calculated in the numerical model should not be extrapolated to a larger system, since there are aspects of a full-scale system, such as mixing, convection and non-uniform flux distribution, which are not applicable on the scale of the simulated domain and therefore not included in the numerical model.

Since the model simulates only a small volume and not the entire volume of fissile solution, it is necessary to adapt the void feedback coefficient by applying it on a fractional basis, so that 1%

voidage in the simulated domain produces the same feedback as 1% voidage in the full scale system. For example, the SILENE reactor typically contains 24.4 L of fuel solution, resulting in a void feedback coefficient of $-2.7531 \times 10^3 \text{ } \$ \text{ m}^{-3}$. For a simulated domain of volume $2 \times 10^{-12} \text{ m}^3$, this gives an equivalent void reactivity feedback coefficient of $-3.36 \times 10^{13} \text{ } \$ \text{ m}^{-3}$ for use in Equation 4.2.1.

4.2.11 A Note on Convection, Coalescence and Break-Up

The numerical model presented in this chapter does not include convection because the simulated domain is small compared to the likely length-scale of a convection current or eddy. The effect of mixing within the fuel solution is, however, examined in Chapter 5 where the methods derived in this chapter are integrated into a point kinetics model of a full-scale system.

The numerical model does not include models of bubble coalescence or break-up because these phenomena are not expected to affect the behaviour of the type of system studied. Further justification of this is given in Section 5.1.3.3.

4.2.12 Algorithm Summary

Starting from the pre-defined start-time, t_0 , the model steps forward in time, taking even time steps. The time step selected must be shorter than the fastest collapse time of a radiolytic gas bubble in an unsaturated fuel solution, as this was found to produce the best numerical stability. The time step chosen was 10^{-6} s . The model proceeds as follows:

1. The ODE solver of Shampine and Gordon (1975) is called to step the system of point kinetics equations forwards by one time step. This includes Equations 4.2.1 to 4.2.3 from Section 4.2.2, Equation 4.2.11 from Section 4.2.5 and Equation 4.2.14 from Section 4.2.7.
2. Bubbles whose size has dropped below the pre-defined gas bubble cut-off radius ($1 \times 10^{-8} \text{ m}$) are removed from the system and the remaining radiolytic gas they contain is added to the dissolved gas concentration of the local subcell. This is important since it avoids the singularity in Equation 3.2.12 which could occur as $r_b \rightarrow 0$.
3. The expected number of fissions within the simulated domain, during the current time step, is calculated from Equation 4.2.13. A Poisson distribution is constructed with this value as its mean and this distribution is randomly sampled to obtain the actual number of fissions for the time step.

4. Each fission is given a random location with fission tracks extending in opposite directions along an axis whose orientation is randomly selected. Bubbles are added to the simulated domain along these fission tracks, their sizes and locations along the fission tracks determined according to the method described in the previous chapter.
5. The location of all bubbles is updated to reflect the distance advected during the time step. Bubble velocities are calculated using Equation 4.2.8.
6. Steps 1 - 5 are repeated until the pre-defined simulation end-time is reached.

A graphical summary of the algorithm is shown in Figure 4.2.5.

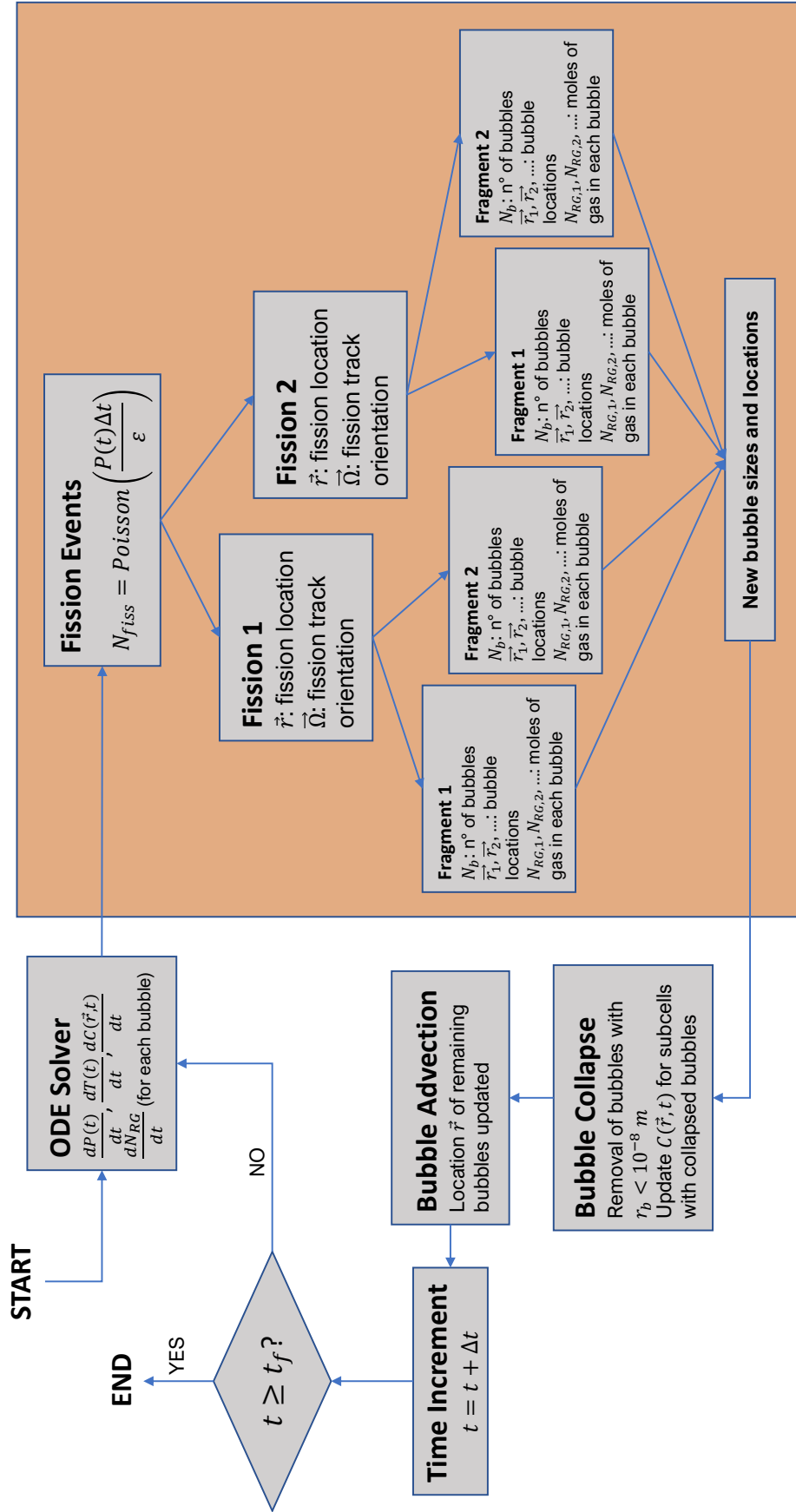


Fig. 4.2.5. Flow diagram summarising the algorithm followed by the numerical simulation.

4.3 Numerical Results

The numerical model produces a very large volume of data and it is useful to begin by analysing the data for a smaller number of cases in the first instance. This permits the key features and findings to be analysed before moving on to examine the trends across the full set of cases. Therefore, throughout this section the analysis will be begin by examining one or two cases which demonstrate the particular phenomena being discussed, before presenting the trends across the full set of data.

This section will examine two cases in particular: the 2.0\$ step insertion case in the SOL-C fuel solution and the 3.5\$ step insertion case in the SOL-B fuel solution. These cases, hereafter referred to as the “focussed cases”, have been chosen because they highlight quite different sets of behaviour.

Labels used on figures throughout this section ((1), (2), (A), (B), etc.) indicate notable features referred to in the text. These labels are not re-used within the section so when the same labels appear on a subsequent figures it indicates the influence of the same phenomenon on a different simulation variable.

4.3.1 Power Density and Reactivity

Figure 4.3.1 shows the simulated power density profiles for the two focussed cases. The 3.5\$ SOL-B case has a single peak (1) followed by a sharp decrease in fission power density, whereas the 2.0\$ case in SOL-C has an initial peak (2), followed by a plateau preceding a second sharp drop (3) in power density.

Figure 4.3.2 shows the simulated thermal and void reactivity feedback due to the rise in solution temperature and the rapid expansion of radiolytic gas bubbles. The reactivity feedback explains the observation in the power profiles that the 3.5\$ SOL-B case has a single peak, whereas the 2.0\$ SOL-C case has one peak followed by a second drop in power density. In both cases, thermal feedback appears earlier than void feedback, since thermal feedback emerges as soon as the solution temperature starts to rise, whereas void feedback only becomes significant once the critical concentration is reached. In the 3.5\$ SOL-B, the amount of thermal feedback at the moment the gas voids appear is still relatively small and insufficient to stop the power rising. A single peak is therefore observed as void feedback appears resulting in a sudden drop in reactivity. In the 2.0\$ SOL-C case, thermal feedback alone is sufficient to stop the rise in power, producing the first power peak (2). The power density then drops a second time once the critical concentration is reached resulting in the appearance of voids (3).

The power density and reactivity feedback profiles shown here do not represent those of a full-

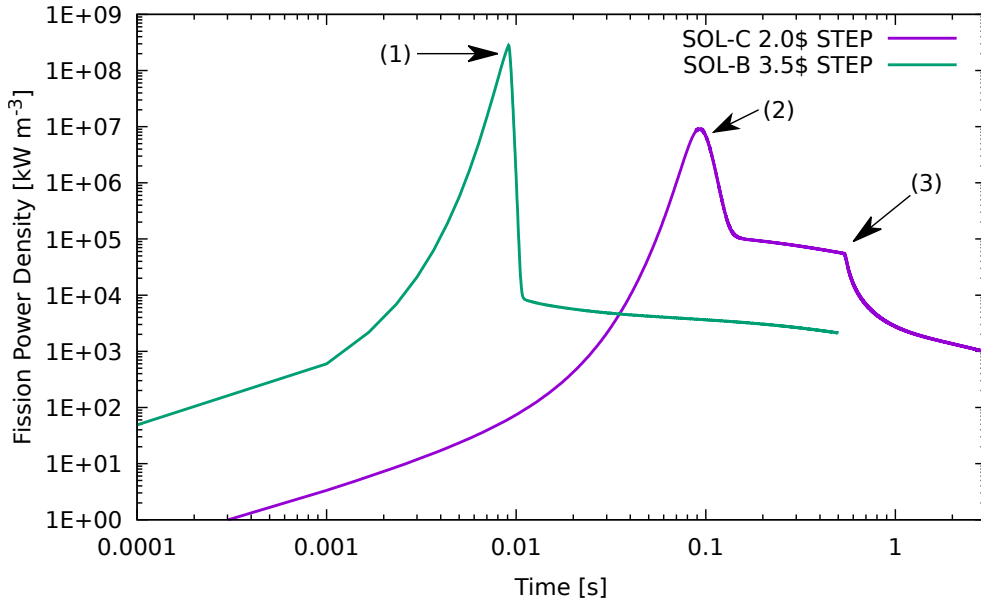


Fig. 4.3.1. Simulated fission power profiles for the 2.0\$ step insertion case in the SOL-C fuel solution and the 3.5\$ step insertion case in the SOL-B fuel solution.

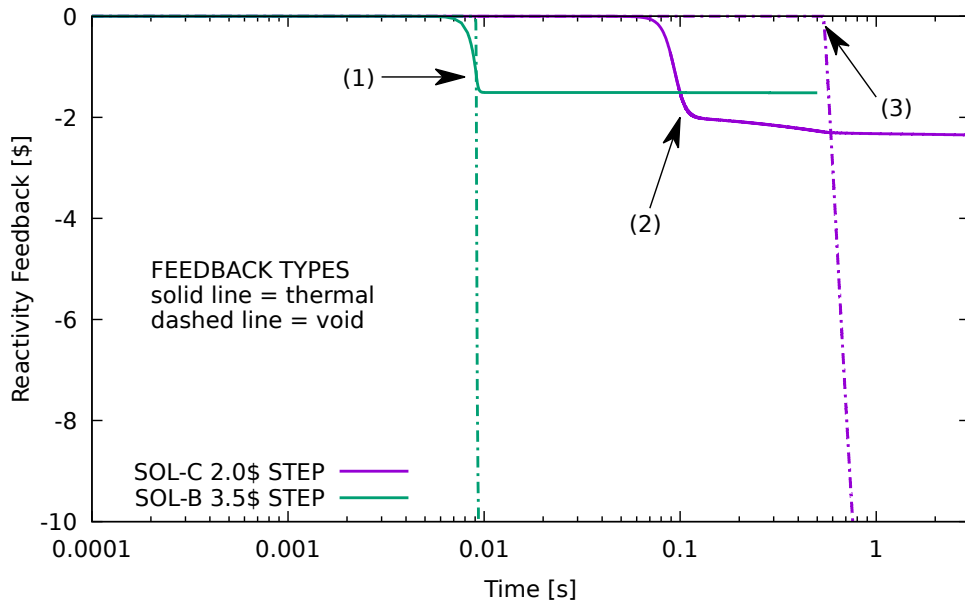


Fig. 4.3.2. Simulated void and thermal reactivity feedback for the 2.0\$ step insertion case in the SOL-C fuel solution and the 3.5\$ step insertion case in the SOL-B fuel solution.

scale system, rather they are local values for the fission power density and reactivity feedback in a microscopic volume of fuel solution, such as might exist at the centre of a larger fissile liquid system. It is possible that the power density may fall locally while the power density in wider system is rising. The impact of these local effects within a full-scale system will be examined in Chapter 5 while the current chapter will examine these local effects in detail.

The fission power density profiles for all transients simulated in the four different fuel solutions

are shown in Figure 4.3.3. As already noted above, the profiles of the larger reactivity insertions are defined by a single power peak coinciding with the appearance of voids due to radiolytic gas, whereas the smaller reactivity insertions produce an initial peak due to thermal feedback, followed by a plateau, then a secondary drop in power coinciding with the appearance of voids due to radiolytic gas.

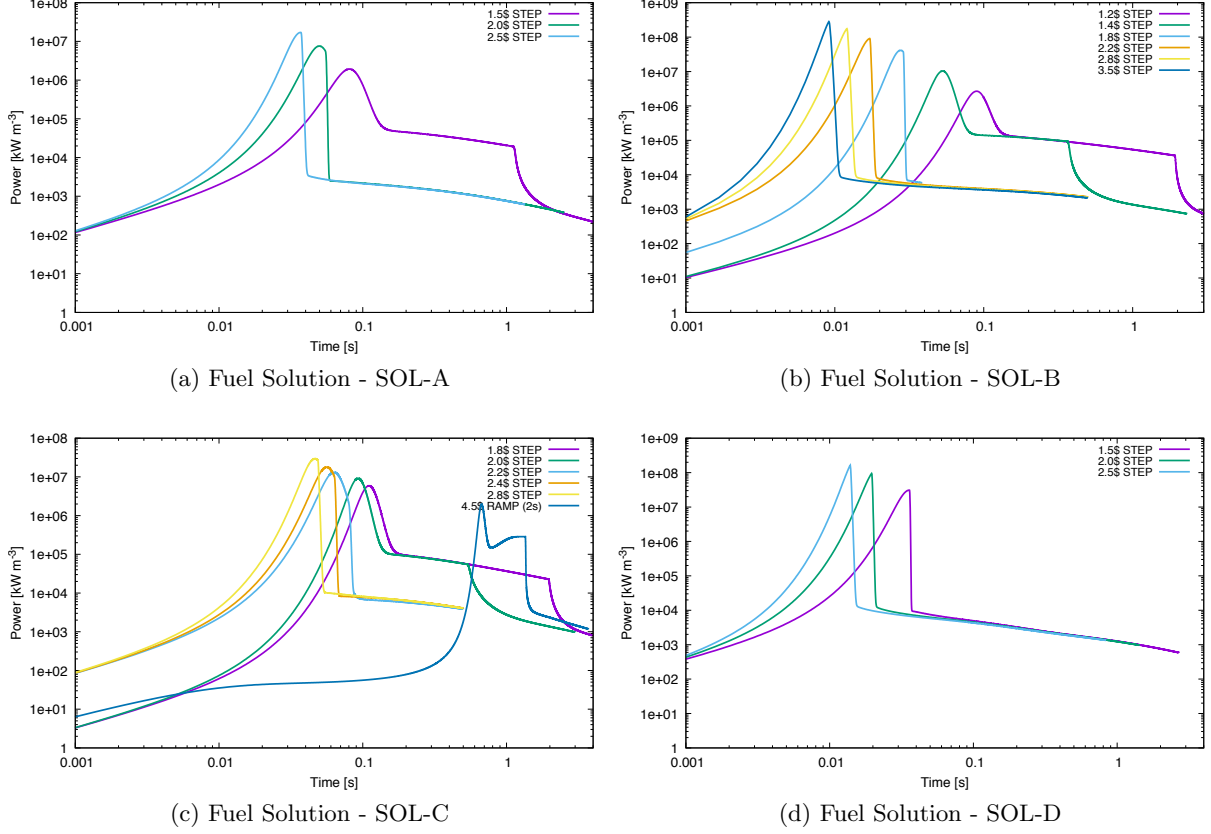


Fig. 4.3.3. Fission power density as a function of time.

Following the appearance of radiolytic gas voids, all the systems simulated become deeply sub-critical, and the total power output becomes dominated by the decay of delayed neutron precursors. An interesting feature of Figure 4.3.3 is that the fission power due to precursor decay after saturation is similar for all cases within the same fuel solution. This can be explained by considering Equation 4.3.1 which gives the population of delayed neutron precursors at the moment of saturation:

$$C_i(t_{sat}) = \frac{\beta_i}{\Lambda} \int_0^{t_{sat}} P(t') dt' - \lambda_i \int_0^{t_{sat}} C_i(t') dt', \quad (4.3.1)$$

where the symbols have the same meaning as in Equation 4.2.2. The first integral represents the fission energy deposited in the fuel solution up to the moment of saturation (saturation energy, E_{sat}). This is a function of the radiolytic gas generation coefficient and the solubility of hydrogen gas in the solution, and is therefore a function of the properties of a particular fuel solution. The second term

represents the decay of delayed neutron precursors during the time leading up to saturation. This latter term is close to zero for all cases shown in Figure 4.3.3 because the saturation time is very short.

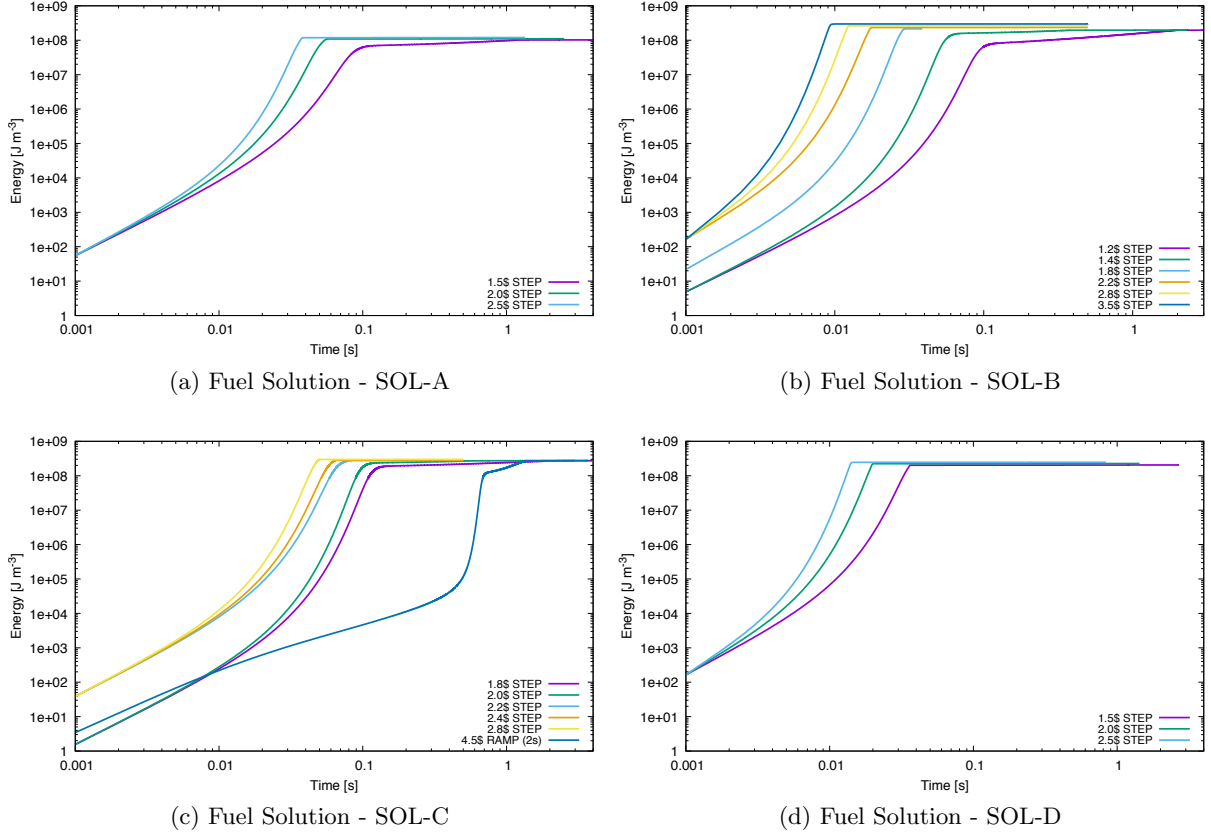


Fig. 4.3.4. Total fission energy released as a function of time.

Figure 4.3.4 shows the total fission energy released for all simulations. It confirms that the total energy released during saturation of the fuel solution is approximately constant for all transients within the same solution. However, there are small differences even within the same solution and this is due to the fact that the fuel solution does not saturate uniformly. Instead, the saturated region starts in one or two regions, which then draw dissolved gas away from other parts of the solution. The exact kinetics of this process will determine the precise energy required to saturate the fuel solution, but in general the value will be close to:

$$E_{sat} \approx \frac{V}{G_{H_2}} \left(P_l + \frac{2\sigma_s}{r_{nucl}} \right) H_{H_2,sol}, \quad (4.3.2)$$

where V is the volume of solution to be saturated, G_{H_2} is the radiolytic gas generation coefficient, σ_s is the fuel solution surface tension, r_{nucl} is the maximum characteristic radius of the available nucleation sites (fission track bubbles in this case) and $H_{H_2,sol}$ is the Henry's law constant for hydrogen gas in the fuel solution.

4.3.2 Reactivity Feedback as a function of Total Energy

Both thermal and void feedback increases with the amount of fission energy released into the solution. It is therefore possible, for a given reactivity transient, to predict the total fission energy released by that transient before the applied reactivity is cancelled out by feedback mechanisms. This was the basis of a fissile liquid model by Schulenberg and Döhler (1986) who used this technique to successfully predict the average fission power profiles of criticality transients in the CRAC reactor.

Figure 4.3.5 shows this relationship between energy released and reactivity feedback for the simulated domain, using the the fuel solution properties based on TRACY (SOL-C). The thermal feedback line on Figure 4.3.5 was derived from the thermal feedback term in the standard point kinetics equations (see Equation 4.2.1). Isolating the thermal feedback term from the point kinetics equation,

$$R_{\$,T} = \alpha_T(T(t) - T_0), \quad (4.3.3)$$

where $R_{\$,T}$ is the thermal reactivity feedback at a given temperature, T . A substitution for $T(t) - T_0$ can be found by integrating Equation 4.2.3. The following expression neglects heat loss from the solution since this is only significant for long transients:

$$\frac{dT}{dt} = \frac{P(t)}{M_{sol}C_p}, \quad (4.3.4)$$

$$M_{sol}C_p \int_{T_0}^{T(t)} dT = \int_0^t P(t)dt, \quad (4.3.5)$$

$$T(t) - T_0 = \frac{E(t)}{m_{fs}C_p}. \quad (4.3.6)$$

Substituting this into Equation 4.3.3, an expression is derived relating the fission energy deposited, E , to the thermal reactivity feedback, $R_{\$,T}$,

$$E = -\frac{M_{sol}C_p}{\alpha_T}R_{\$,T}. \quad (4.3.7)$$

The lines corresponding to combined thermal and void feedback were derived in a similar way, starting with the temperature and void feedback terms from Equation 4.2.1,

$$R_{\$(T+V)} = \alpha_T(T(t) - T_0) + \alpha_V(V_{RG}(t) - V_{RG,0}), \quad (4.3.8)$$

and substituting as above for $T(t) - T_0$, also substituting for $V_{RG}(t) - V_{RG,0}$ using the ideal gas law,

$$V_{RG}(t) - V_{RG,0} = \frac{N_{RG}(t)RT(t)}{P_b}, \quad (4.3.9)$$

where $N_{RG}(t)$ is the number of moles of radiolytic gas present and P_b is the pressure inside a radiolytic

gas bubble. The pressure inside a bubble is determined from the bubble radius using,

$$P_b = P_l + \frac{2\sigma_s}{r_b(t)}. \quad (4.3.10)$$

where r_b is the average radius of saturated radiolytic gas bubbles and P_l is the liquid pressure. This leads to the expression for the voidage $V_{RG}(t) - V_{RG,0}$ due to radiolytic gas,

$$V_{RG}(t) - V_{RG,0} = \frac{N_{RG}(t)RT}{P_l + \frac{2\sigma_s}{r_b(t)}}. \quad (4.3.11)$$

The number of moles of radiolytic gas, $N_{RG}(t)$, can be expressed as the product of the energy deposited and the radiolytic gas generation coefficient,

$$V_{RG}(t) - V_{RG,0} = \frac{E(t)G_{H_2}RT}{P_l + \frac{2\sigma_s}{r_b(t)}}. \quad (4.3.12)$$

Substituting Equations 4.3.6 and 4.3.12 into Equation 4.3.8, and rearranging in terms of fission energy deposited, E , yields the following equation for the combined thermal and void feedback lines,

$$E = -\frac{R_{\$, (T+V)}}{\frac{\alpha_T}{M_{sol}C_p} + \frac{\alpha_V G_{H_2} RT}{P_l + \frac{2\sigma_s}{r_b(t)}}}. \quad (4.3.13)$$

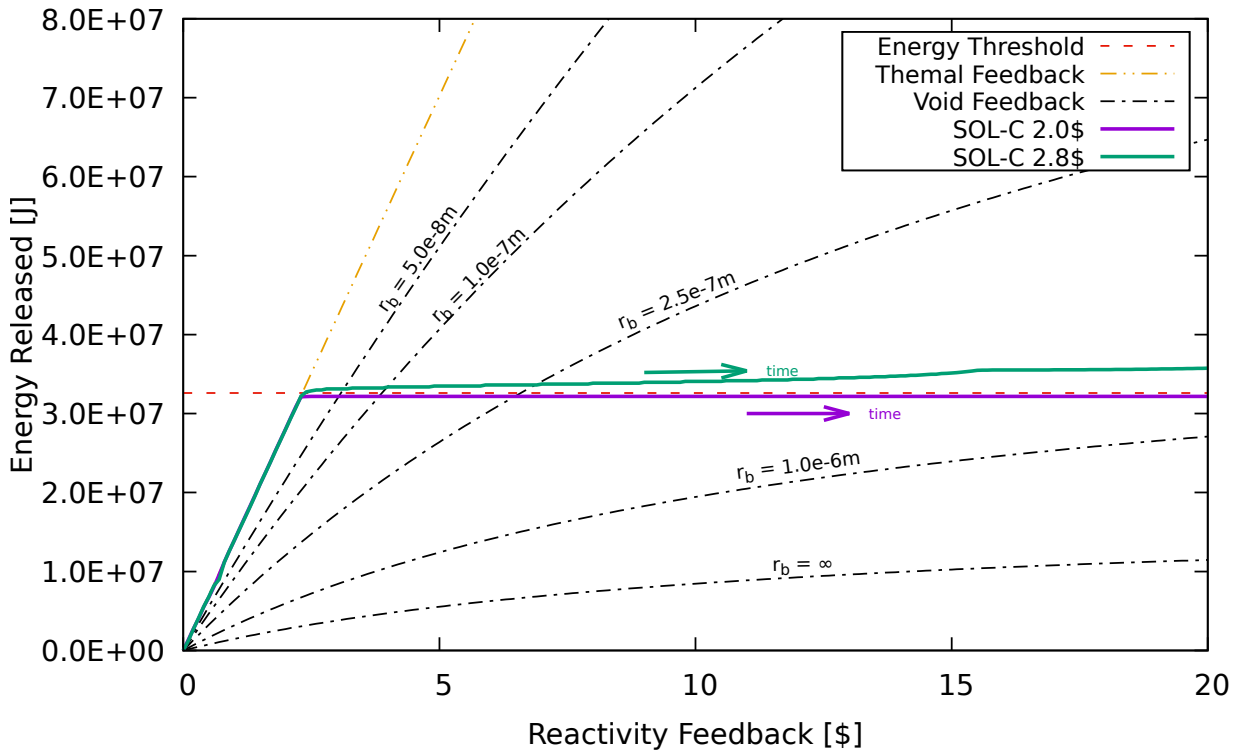


Fig. 4.3.5. Energy required to negate external reactivity through thermal feedback, or thermal and void feedbacks combined.

These lines are plotted in Figure 4.3.5 for the simulated domain based on the SOL-C fuel solution, with thermal feedback coefficient $-0.03295 \text{ } \$/\text{m}^{-3}$ and void feedback coefficient $-387.67 \text{ } \$/\text{m}^{-3}$ (adjusted for volume). The time-dependent reactivity feedback curve calculated by the numerical model for the SOL-C 2.0\$ step case is shown. The SOL-C 2.8\$ step case is included for comparison (the 3.5\$ SOL-B focussed case cannot be shown on the same plot because the fuel solution properties are not the same).

The line showing the reactivity curve for the SOL-C 2.0\$ step case (solid purple) indicates that reactivity feedback is initially driven by the rise in temperature of the fuel solution, then after saturation of the solution with radiolytic gas, reactivity feedback is driven by bubble expansion. The second phase of reactivity feedback requires no additional energy input as bubbles expand by consuming dissolved gas from the surrounding solution. This is shown by the fact that the reactivity feedback line for the SOL-C 2.0\$ case traces the energy threshold line without rising above it. In the SOL-C 2.8\$ step case, some additional energy input is required, as shown by the fact that the reactivity feedback line (solid green) departs from the energy threshold line as reactivity feedback increases. This is an interesting observation because it suggests that a different energy input is required to produce the same reactivity feedback for slightly different excursions in identical solutions. The reason that the 2.8\$ case requires more energy than the 2.0\$ case for the same reactivity feedback is that the 2.8\$ produces a larger number of bubbles, resulting in a smaller bubble size and a higher bubble pressure. The radiolytic gas is therefore more compressed and more of it is required to produce the same reactivity feedback as in the 2.0\$ case.

This effect is highlighted by the black dashed lines which show combined thermal and void feedback for various bubble radii, calculated using Equation 4.3.13. The energy required to negate a given reactivity insertion by void feedback depends strongly on the size of the radiolytic gas bubbles, with larger bubbles producing more reactivity feedback for the same energy deposition. This makes the size (and therefore number) of radiolytic gas bubbles an important parameter determining the magnitude of the first power peak during a criticality excursion.

Figure 4.3.5 shows that for the particular fuel solution modelled, transients resulting from reactivity insertions of less than $\sim 2.5\text{\$}$ would reach a peak due to thermal feedback only. In these cases, voids may still appear some time later but void feedback will not affect the kinetics of the first power peak. In transients resulting from larger reactivity insertions, the timing of the first power peak in this fuel solution would be expected to coincide with the appearance of gas voids. This is consistent with the observation made in Section 4.3.1 that the first power peak in the SOL-C 2.0\$ step insertion case is due to thermal feedback alone.

4.3.3 Formation of Stable Bubbles at Saturation

When analysing the number of bubbles present in the fuel solution, it is useful to distinguish between collapsing bubbles and stable bubbles. Collapsing bubbles may be present whenever the fission power density is greater than zero, as small bubbles are constantly added to the solution by radiolysis. The number of collapsing bubbles at a given time depends on the fission power density, which determines the rate at which new bubbles are created, and the degree of saturation of the fuel solution, which determines the time it takes for them to collapse. Stable bubbles (or growing bubbles) are only present once the fuel solution has become saturated.

A bubble can grow if it satisfies the inequality in Equation 4.3.14, i.e. if the local concentration of dissolved hydrogen is greater than or equal to that which would be in equilibrium with the partial pressure of hydrogen inside the bubble:

$$r_b \geq \frac{2\sigma_s(T)}{\frac{C_{\text{H}_2,\text{local}}}{H_{\text{H}_2,\text{sol}}} - P_l}, \quad (4.3.14)$$

where $\sigma_s(T)$ is the liquid surface tension, $C_{\text{H}_2,\text{local}}$ is the bulk liquid concentration of hydrogen in the subcell containing the bubble, $H_{\text{H}_2,\text{sol}}$ is the Henry's law constant for hydrogen gas in the fuel solution and P_l is the bulk liquid pressure. The majority of the collapsing bubbles which do not satisfy this inequality are so small that they do not contribute significantly to the total voidage, and have no discernible impact on the behaviour of the system.

The number of stable bubbles as a function of time for the two focussed cases is shown in Figure 4.3.6 and the concentration of dissolved hydrogen gas in the fuel solution is shown in Figure 4.3.7.

A notable difference between the cases shown is that in the 2.0\$ SOL-C case, the number density of bubbles rises to a value at which it remains relatively constant, whereas in the 3.5\$ SOL-B case, the number density rises to a peak value before declining sharply. The reasons for this are explored in Section 4.3.3.2.

There are four orders of magnitude difference in the peak bubble densities predicted for the two cases. In the 2.0\$ SOL-C case, the bubbles are separated by relatively large distances so it takes a relatively long time for dissolved gas to diffuse between them. In the 3.5\$ SOL-B case, the bubbles are more densely packed and diffusion times between adjacent bubbles are much shorter. In the latter case, the smallest bubbles collapse as large bubbles, which expand the most quickly, consume the dissolved gas in their surroundings until the smaller bubbles in the same region are no longer stable and start to collapse.

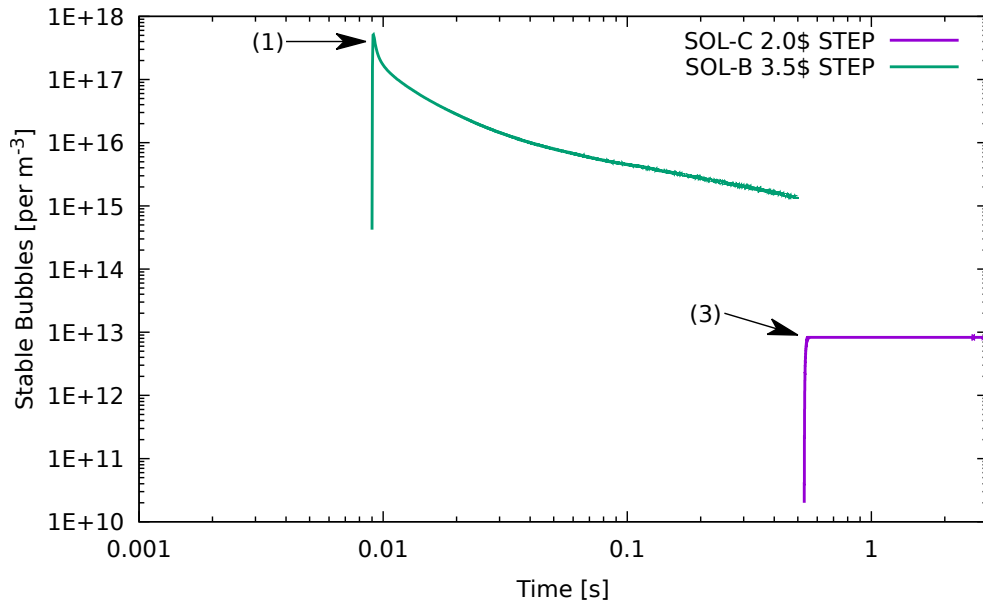


Fig. 4.3.6. Number of bubbles per cubic metre for the 2.0\$ step insertion case in the SOL-C fuel solution and the 3.5\$ step insertion case in the SOL-B fuel solution.

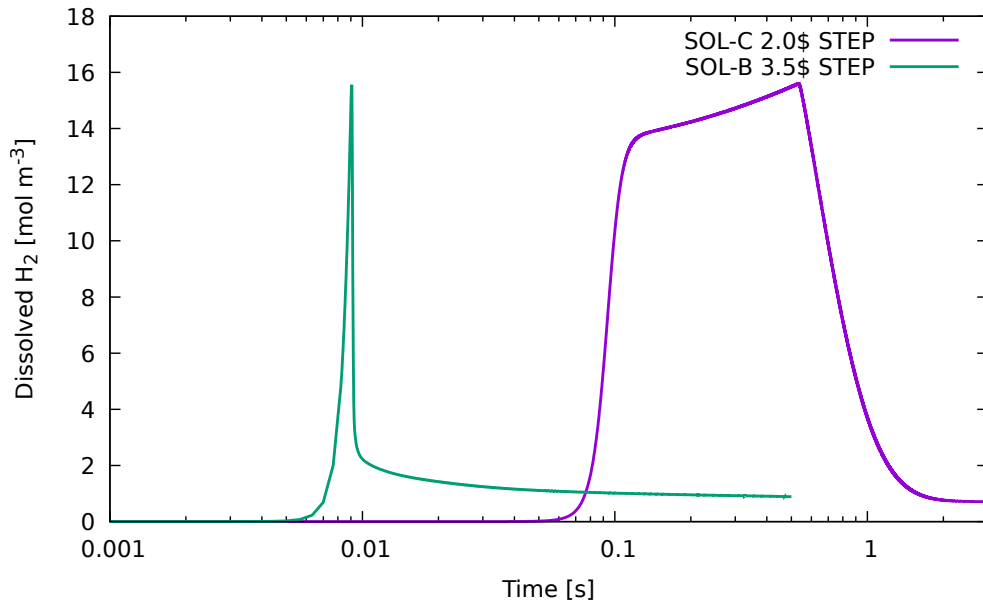


Fig. 4.3.7. Concentration of dissolved hydrogen gas for the 2.0\$ step insertion case in the SOL-C fuel solution and the 3.5\$ step insertion case in the SOL-B fuel solution.

In both cases, a large number of stable bubbles emerges extremely rapidly once the critical concentration of dissolved hydrogen is reached and a proportion of the fission track bubbles is able to grow. When the bubbles expand, they consume gas from the surrounding solution, resulting in a drop in the dissolved gas concentration (see Figure 4.3.7). Once the dissolved gas concentration has dropped back to a level below the critical concentration, the fission track bubbles are no longer large enough to grow and they begin to collapse once more. This means there is a relatively short saturation period

during which the local concentration exceeds the critical concentration, and new stable bubbles can form from the fission track bubbles. The numerical model indicates that saturation period lasts from a few microseconds up to a millisecond.

The number of stable bubbles formed during the saturation period depends on the number of available fission track bubbles of sufficient size deposited by fission fragments during the same period. This number depends on the total number of fission events occurring during the saturation period, which is proportional to the fission energy deposited. It is therefore useful to examine the relationship between the number of stable bubbles formed, and the fission energy deposited during the saturation period. This is shown in Figure 4.3.8 for the SOL-C 2.0\$ step case.

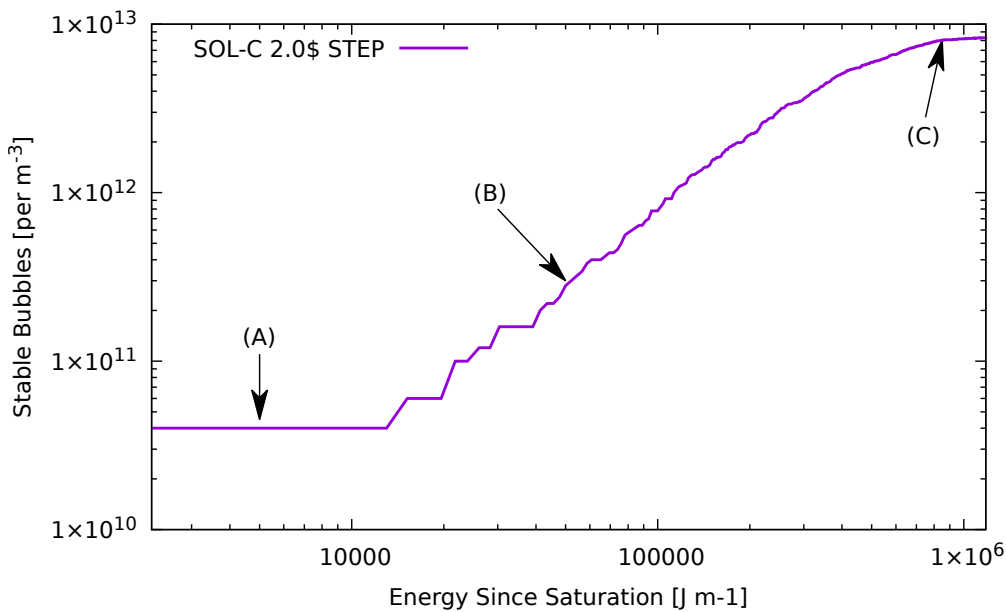


Fig. 4.3.8. Number of stable bubbles formed as a function of fission energy deposited during the saturation period for the 2.0\$ step insertion case in the SOL-C fuel solution.

The flat region marked (A) on Figure 4.3.8 is an artefact of the modelling technique. The number density of bubbles shown in this region corresponds to a single bubble present in the simulated domain. However, beyond this point it can be seen in region (B) that the number of stable bubbles increases steadily with the fission energy deposited. The line is straight on this part of the plot, indicating a power law relationship (since the scales are logarithmic).

Further to the right in region (C) of Figure 4.3.8, the number of stable bubbles appears to level off as the fission energy deposited continues to increase. This corresponds to the period during which bubble growth in certain areas of the simulated domain has reduced the concentration to below the critical concentration. The proportion of the simulated domain in which new stable bubble formation is still possible decreases to the extent that further addition of energy to the solution produces diminishing

returns in terms of the number of stable bubbles.

Figure 4.3.9 shows the number density of bubbles as a function of time for all transients simulated. As previously noted, the number of stable bubbles present evolves differently depending on the magnitude of the reactivity insertion. For the smaller reactivity insertion cases, a smaller number of stable bubbles is created during the saturation period but this number remains relatively constant after saturation. Let this type be called “Type A”. For the larger reactivity insertion cases, the number of stable bubbles rises to a peak, then decreases rapidly after saturation as the smallest bubbles collapse. Let this type be called “Type B”.

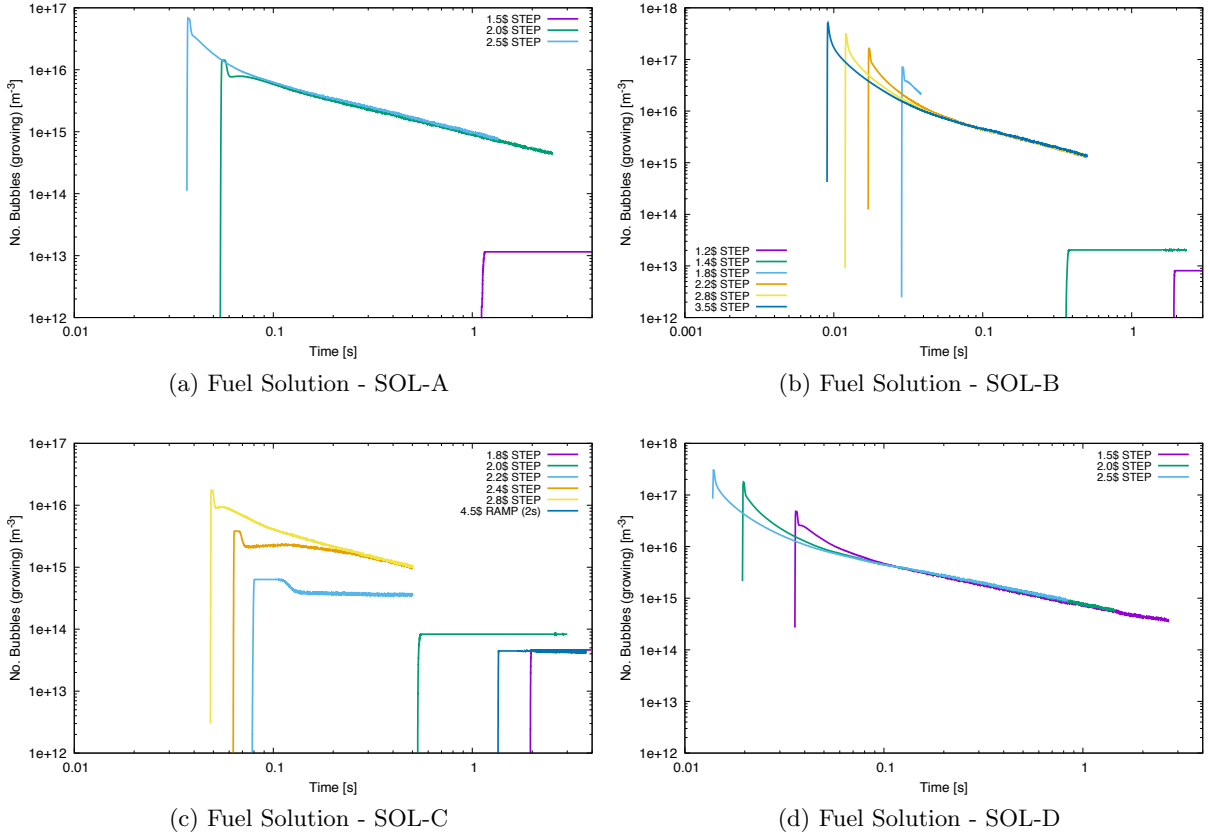


Fig. 4.3.9. Number of stable bubbles per unit volume as a function of time.

An interesting feature of the Type B cases, is that the number of stable bubbles per unit volume converges after saturation to approximately the same value. This can be explained by the observation already made in Section 4.3.1 that the fission power densities converge for all cases in the same fuel solution after saturation. The convergence in the stable bubble densities would therefore suggest that the density of stable bubbles after saturation is determined by the fission power density for Type B cases.

4.3.3.1 Number of Stable Bubbles Produced

The number of stable bubbles is a key parameter determining the rate of appearance of radiolytic gas voids, the extent to which these voids are compressed and the time taken for them to leave the system by advection. It would therefore be useful to be able to predict the number of stable bubbles created as a function of the conditions during saturation of the fuel solution.

It was shown in Figure 4.3.8 that the number of bubbles created during the saturation period increases with the amount of fission energy deposited in the fuel solution. The same data are shown in Figure 4.3.10 for all the transients simulated.

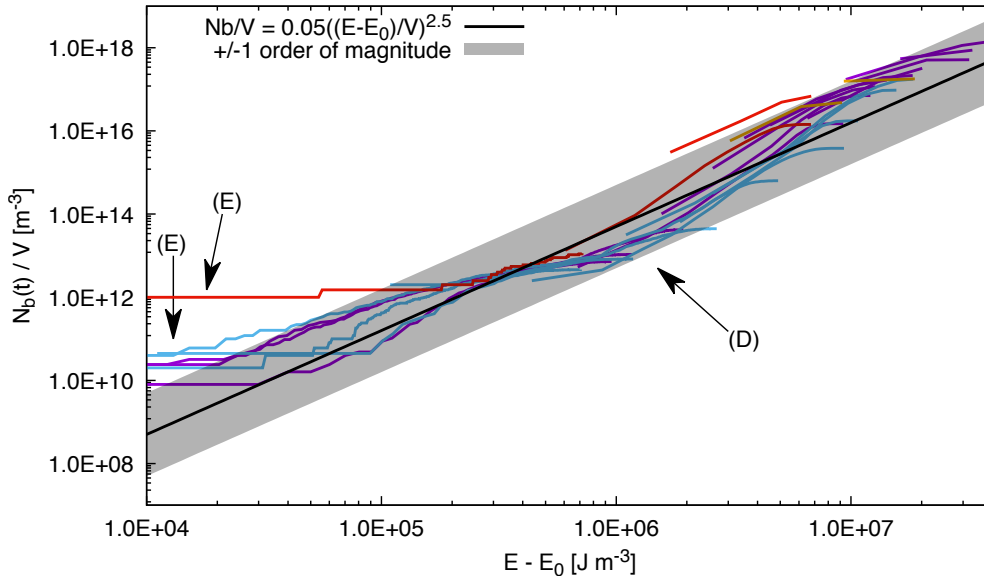


Fig. 4.3.10. Number of bubbles per unit volume as a function of fission energy deposited per unit volume.

Different fuel solutions in Figure 4.3.10 are indicated by different coloured lines but the purpose of the figure is not to examine individual transients or fuel solutions but to determine the general trend for all the data. The data is centered around a trendline with equation,

$$\frac{N_b(t)}{V} = 0.05 \left(\frac{E(t) - E(t_{sat})}{V} \right)^{2.5}, \quad (4.3.15)$$

where $E(t_{sat})$ is the energy released up to the point at which the first stable bubble appears. This equation is shown in Figure 4.3.10 as a solid black line.

There is a significant number of data points on either side of Equation 4.3.15. This is largely due to the fact that the trend for individual transients follows a S-shaped curve (as discussed in Section 4.3.3). The reason for the dip (D) in the centre of the figure is believed to be related to spatial effects

which are particularly prominent in transients in the intermediate intensity range. The effect is related to the appearance and subsequent merger of multiple regions of bubble growth within the simulated domain, leading to deviations from the behaviour that would be expected for a single region of bubble growth. These effects are discussed in Section 4.4.1.

Almost all the data points fall within one order of magnitude (region shaded in grey) of the value predicted by Equation 4.3.15 so this equation can provide a reasonable prediction of the number of bubbles created as a function of total energy deposited during the saturated period.

The outlying data points (E) on the left of Figure 4.3.10 are artefacts of the calculation method where there is only one stable bubble in the simulated domain, as explained previously. This could be tested by re-running the simulations with a larger domain size, in which case the trend highlighted by the grey region would be expected to extend further towards lower values of $E-E_0$.

4.3.3.2 A Model of Bubble Stability

It was noted in Section 4.3.3 that the number of stable bubbles in the fuel solution tends to remain relatively constant after saturation (for less powerful transients) or decrease after saturation (for more powerful transients), and that in the latter case where bubbles collapse after saturation, the total number of bubbles present tends towards a value determined by the fission power density. To understand this phenomenon, it is useful to consider an analytical model of bubble stability.

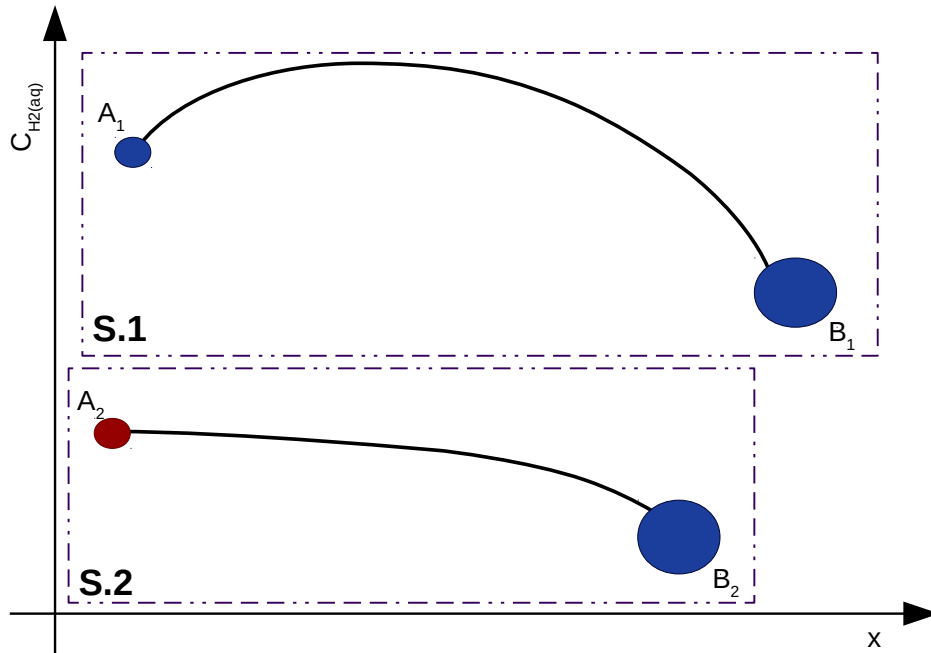


Fig. 4.3.11. One-dimensional model of bubble collapse by diffusion. Growing bubbles are shown in blue while red indicates a collapsing bubble.

For simplicity, the analytical model will consist of a one-dimensional system, containing only two adjacent bubbles, as shown in Figure 4.3.11. The two bubbles are located a certain distance, X , apart from each other. There exists a region between the two bubbles where the concentration of dissolved gas is influenced by ongoing radiolysis and the growth and/or collapse of the bubbles. In this region, the rate of change in the concentration profile due to diffusion is proportional to the second derivative of the concentration gradient (Fick's second law) and the rate of change due to radiolysis is equal to the product of the fission power density and the radiolytic gas generation coefficient,

$$\frac{\partial C_{\text{H}_2(\text{aq})}(x, t)}{\partial t} = D \frac{\partial^2 C_{\text{H}_2(\text{aq})}(x, t)}{\partial x^2} + G_{\text{H}_2} (P(t)/V), \quad (4.3.16)$$

where $C_{\text{H}_2(\text{aq})}(x, t)$ is the concentration of dissolved hydrogen at a location x along the domain and $P(t)/V$ is the fission power density.

The two bubbles can co-exist if a steady-state solution to Equation 4.3.16 exists in which both bubbles are growing. This is indicated by Scenario S.1 in Figure 4.3.11. In this case, the dissolved gas consumed by the growing bubbles is replaced by ongoing radiolysis, allowing both bubbles to grow at the same time. Alternatively, the generation of dissolved gas by radiolysis may be insufficient to replace the gas consumed by the growing bubbles. In this case, the smaller bubble will collapse, as shown in Scenario S.2 of Figure 4.3.11.

To solve for a steady-state, the time derivative on the left hand side of Equation 4.3.16 is set to zero. Robin boundary conditions applied at each end of the domain make use of Fick's first law, which relates the mass flux to the concentration gradient:

- **on the left ($x=0$):** $J = -D \left. \frac{\partial C_{\text{H}_2(\text{aq})}}{\partial x} \right|_{x=0} = -k_D (C_{\text{H}_2(\text{aq})}(0) - C_{b1:eq}),$
- **on the right ($x=X$):** $J = -D \left. \frac{\partial C_{\text{H}_2(\text{aq})}}{\partial x} \right|_{x=X} = k_D (C_{\text{H}_2(\text{aq})}(X) - C_{b2:eq}).$

where $C_{b1:eq}$ is the equilibrium concentration corresponding to the size of the bubble at location $x = 0$, $C_{b2:eq}$ is the equilibrium concentration corresponding to the size of the bubble at location $x = X$ and k_D is the mass transfer coefficient at the bubble interface. This equation has the following analytical solution,

$$C_{\text{H}_2(\text{aq})}(x) = -\frac{P(t)G_{\text{H}_2}}{2DV}x^2 + Y_1x + Y_2 \quad (4.3.17)$$

where

$$Y_1 = \frac{1}{1 + \frac{2D}{k_DX}} \left(\frac{C_{b2:eq} - C_{b1:eq}}{X} + \frac{P(t)G_{\text{H}_2}}{DV} \left(\frac{X}{2} + \frac{2D}{k_D} \right) \right)$$

$$Y_2 = \frac{D}{k_D} Y_1 + C_{b2:eq}$$

Because larger bubbles have lower equilibrium concentrations, unless all bubbles have identical

size, the population of bubbles in a solution with no source of dissolved gas will tend to one ($N_b \rightarrow 1$), as the growth of the largest bubbles tends to lower the concentration of dissolved gas below the equilibrium concentration of the smaller bubbles, leading them to collapse until there is only a single bubble remaining. A pair of adjacent bubbles of different sizes can coexist if there is a dissolved gas source, e.g. from radiolysis. The density of bubbles of different sizes that the solution can support depends on the fission power density, corresponding to the rate at which new radiolytic gas is required to meet the demands of the largest bubbles without reducing the concentration below the equilibrium concentration of the smaller bubbles. The required fission power density can be determined in the 1D model by differentiating Equation 4.3.17 and setting the derivative of the concentration to zero at the boundary on the side of the smaller bubble. This results in the following stability condition,

$$\frac{P}{V} = \frac{C_{b1:eq} - C_{b2:eq}}{G_{H_2} X \left(\frac{X}{2D} + \frac{1}{k_D} \right)} \quad (4.3.18)$$

where P/V is the fission power density in equilibrium with the number of bubbles present, $\Delta_C = |C_{b1:eq} - C_{b2:eq}|$ is the modulus of the difference in equilibrium concentrations for each of the two bubbles.

If the fission power density is known, then Equation 4.3.18 can be rearranged to give a quadratic expression for the bubble separation distance, X . This results in the following expression,

$$X = -\frac{D}{k_D} \pm \left(\sqrt{\frac{2D\Delta_C}{G_{H_2} (P/V)}} + \left(\frac{D}{k_D} \right)^2 \right). \quad (4.3.19)$$

The negative root can be discounted since it would result in a negative bubble separation. In most cases, the resistance to mass transfer at the bubble interface will be small compared to the resistance due to diffusion of dissolved gas through the solution: applying Eq. 4.2.12 it can be shown that $\lim_{r_b \rightarrow 0} \frac{D}{k_D} = r_b$ and $\lim_{r_b \rightarrow \infty} \frac{D}{k_D} = 0$. The resistance to mass transfer at the bubble interface can be neglected by taking the limit as $k_D \rightarrow \infty$, resulting in the following expression,

$$X = \sqrt{\frac{2D\Delta_C}{G_{H_2} (P/V)}}. \quad (4.3.20)$$

The equation can be used to find the stable bubble number density by substituting,

$$X = \sqrt[3]{\frac{V}{N_b}}, \quad (4.3.21)$$

where N_b/V is the stable bubble number density. This results in a relatively simple expression for the stable bubble number density as a function of the fission power density,

$$\left(\frac{N_b}{V} \right)_{eq} = \left(\frac{G_{H_2} P(t)}{2D\Delta_C V} \right)^{3/2}. \quad (4.3.22)$$

The difficulty with Equation 4.3.22 is that the parameter Δ_C is not easily obtained, even for the 1D scenario described. In a 3D system the value of Δ_C would depend on the distribution of dissolved gas concentration within the fuel solution. Its value would tend to increase with increasing fission power density, since stochasticity in the timing and location of fission events creates heterogeneity in the dissolved gas concentration, while diffusion of dissolved gas and mixing would make the solution more homogeneous.

Instead, using the results of the numerical model it is possible to estimate a constant of proportionality (let this be called k_b), which incorporates the Δ_C parameter, and links the stable bubble number density to the fission power density. Equation 4.3.22 then becomes,

$$\left(\frac{N_b}{V}\right)_{eq} = k_b \left(\frac{P}{V}\right)^{3/2} \quad (4.3.23)$$

Equation 4.3.22 would suggest that the constant of proportionality k_b is a function of the radiolytic gas generation coefficient and the dissolved gas diffusion coefficient,

$$k_b = k'_b \left(\frac{G_{H_2}}{D}\right)^{3/2}. \quad (4.3.24)$$

Figure 4.3.12 shows the values of $(N_b/V) / P^{3/2}$ as a function of time, predicted by the numerical model for a range of transients across all four simulated fuel solutions. From these figures it appears that k_b tends towards a constant value, which appears to be a function of the fuel solution properties, since different values emerge for each of the four simulated fuel solutions.

The values of k_b are shown in Table 4.6 along with the average saturation temperatures and dissolved gas diffusion coefficients for the four simulated fuel solutions. Also shown is the value of k'_b or $k_b/(G_{H_2}/D)^{3/2}$ since Equation 4.3.22 suggests that this value should be a constant.

Fuel Solution	k_b [$W^{3/2}$]	G_{H_2} [mol J ⁻¹]	T[sat] _{Av} [K]	D [m ² s ⁻¹]	$k_b / (G_{H_2}/D)^{3/2}$
SOL-A	1.58×10^{15}	1.35×10^{-7}	323	8.43×10^{-9}	2.47×10^{13}
SOL-B	3.79×10^{14}	7.67×10^{-8}	361	1.59×10^{-8}	3.57×10^{13}
SOL-C	1.23×10^{14}	5.80×10^{-8}	371	1.83×10^{-8}	2.19×10^{13}
SOL-D	6.01×10^{14}	8.08×10^{-8}	354	1.43×10^{-8}	4.45×10^{13}
Average	—				3.172×10^{13}

TABLE 4.6

Values of the constant of proportionality k_b determined from the results of the numerical model, radiolytic gas generation coefficients and average diffusion coefficients for each of the four simulated fuel solutions.

By taking the average value of k'_b it is possible to derive the following expression for the constant

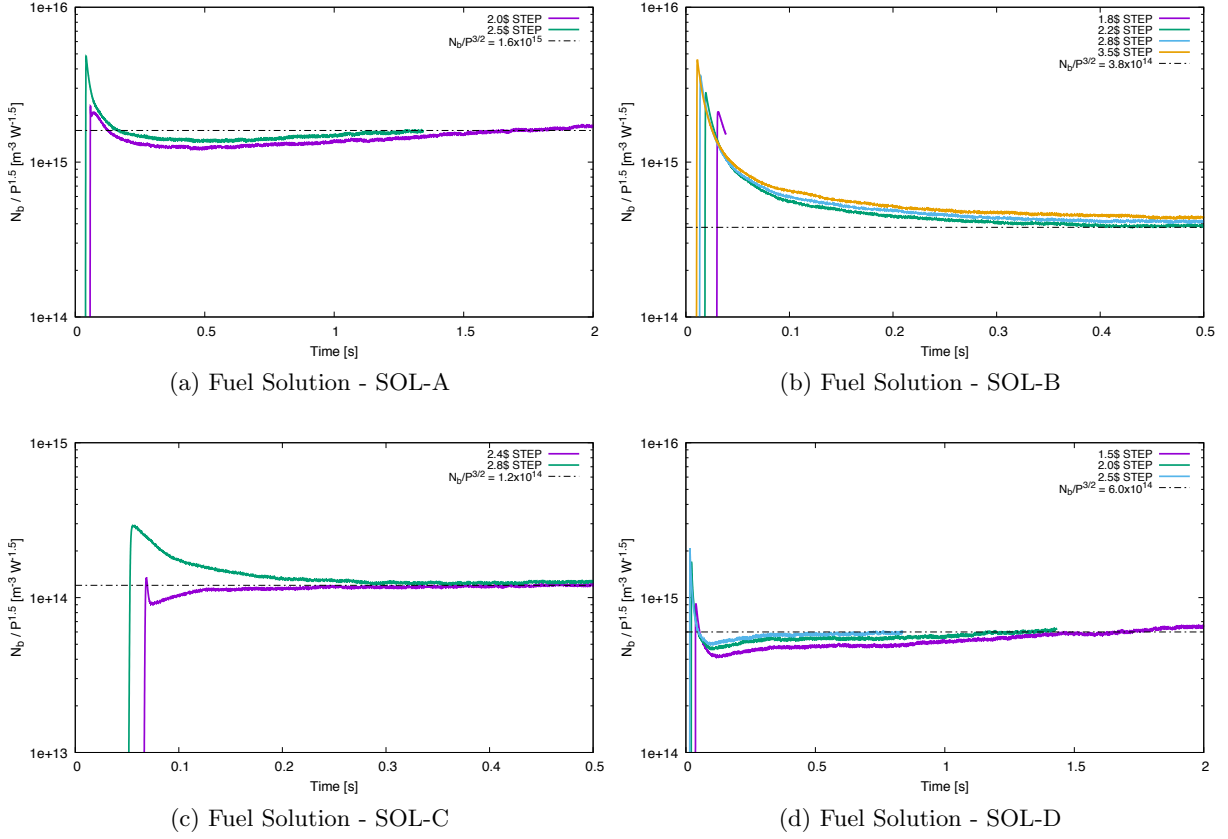


Fig. 4.3.12. Number of stable bubbles per unit volume as a function of fission power density raised to the power of $3/2$.

of proportionality k_b :

$$k_b = 3.172 \times 10^{13} \left(\frac{G_{H_2}}{D} \right)^{3/2}. \quad (4.3.25)$$

It is clear from Table 4.6 that there is some variation in the values of k'_b derived for the four different fuel solutions. To evaluate the influence of this variation on the predicted value of k_b , Equation 4.3.25 was used to predict k_b for all fuel solutions and these values are compared to those obtained from the numerical model in Figure 4.3.13.

Figure 4.3.13 shows that there is reasonable agreement between the values of the k_b obtained from the numerical model and the values predicted using Equation 4.3.25. This finding lends credibility to the proposed one-dimensional model of bubble stability and the validity of Equation 4.3.22 which indicates that the equilibrium number density of stable bubbles is related to the fission power density raised to the power of $3/2$. It also confirms that the variation in the values of the equilibrium number density from one fuel solution to another results largely from differences in the values of G_{H_2} and D .

Caution should be exercised when applying Equation 4.3.25 more widely to a range of different transients, especially when the fission power density remains high after saturation. This is because, as

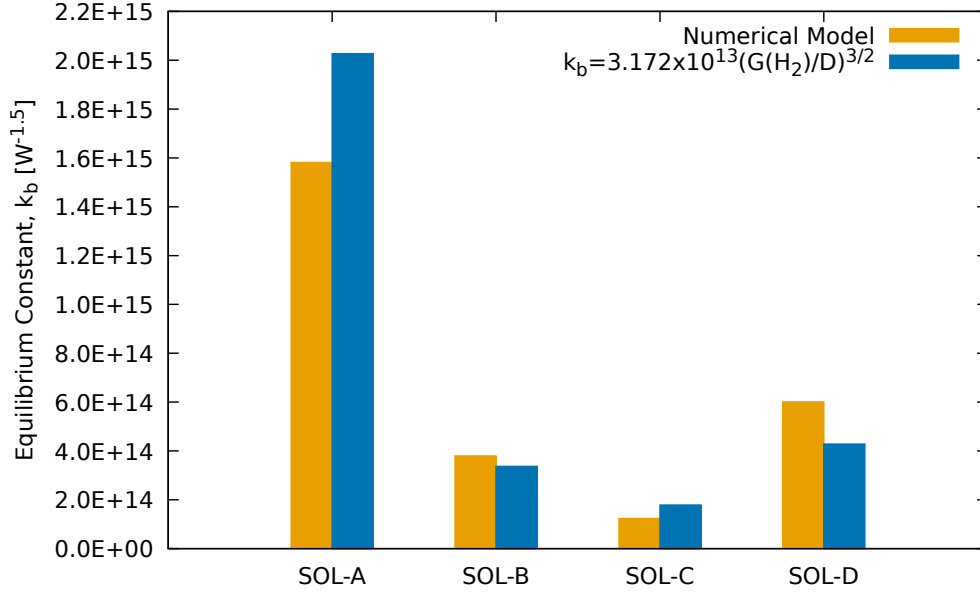


Fig. 4.3.13. Equilibrium constant k_b obtained from the numerical model (yellow) and estimated using Equation 4.3.25 (blue).

noted earlier, the parameter Δ_C is expected to be sensitive to the fission power density, which suggests that the fission power density after saturation may have some influence on the value of the constant k'_b in Equation 4.3.25. In this case, higher fission power densities may increase the heterogeneity in the dissolved gas concentration in the fuel solution, reducing the value of k'_b and reducing the number of stable bubbles the fuel solution can support. Nevertheless, this effect is likely to be relatively weak compared to the influence of the fission power density on the rate of radiolytic gas production, which is accounted for in Equation 4.3.23.

Figure 4.3.14 shows the stable bubble densities for the 2.0\$ SOL-C and 3.5\$ SOL-B cases, simulated by the numerical model and predicted based on Equations 4.3.23 and 4.3.25. In the 2.0\$ SOL-C case, the number of stable bubbles formed during saturation is less than the number of stable bubbles that the fuel solution can support at the fission power density after saturation, so the number of stable bubbles remains constant (F). In the 3.5\$ SOL-B case, the number of stable bubbles formed during saturation exceeds the number that the fuel solution can support once the fission power density has dropped following saturation. This leads to bubble collapse as the number of bubbles present in the fuel solution tends towards the stable equilibrium value predicted by Equation 4.3.23 (G).

There is one anomaly in Figure 4.3.14 where the number of stable bubbles in the 3.5\$ SOL-B fuel solution initially drops (H) while the equilibrium value predicted by Equation 4.3.25 is greater than the number actually present. This is likely to be due to spatial effects, where the bubbles formed during saturation are initially distributed in a non-uniform manner, so that the bubble number density

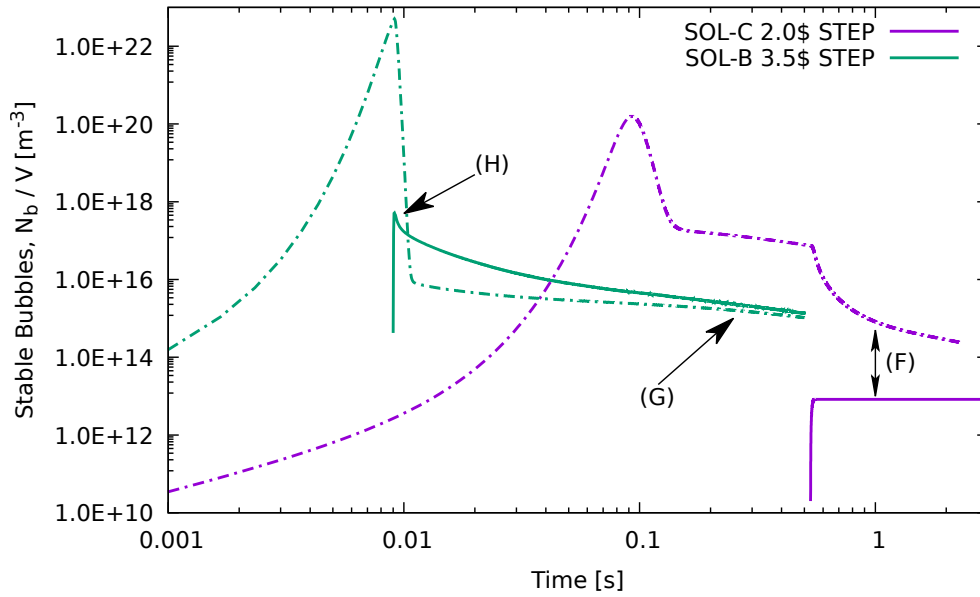


Fig. 4.3.14. Stable bubbles per unit volume (solid line) and predicted stable bubble number density (dashed line) based on Equations 4.3.23 and 4.3.25 for the 2.0% SOL-C and 3.5% SOL-B cases.

is higher in some places and lower in others, leading to bubble collapse when, on average, the system appears stable.

4.3.3.3 Rate of Bubble Collapse

Section 4.3.3.2 presents a method for predicting the number of stable bubbles that a fuel solution can support, as a function of the fission power density. As shown in Figure 4.3.14, the numerical model predicts that, when the number of stable bubbles per unit volume exceeds this value, bubbles will collapse so that the number of bubbles in the fuel solution tends towards the equilibrium value. The aim of this section is to provide an estimate for the time constant characterising this movement towards the equilibrium value.

The collapse of bubbles is driven by the fact that the density of stable bubbles (N_b/V) exceeds the value which would be in stable equilibrium with the current fission power density according to Equation 4.3.23. Collapse of the bubbles is due to diffusion, as dissolved gas diffuses towards larger expanding bubbles and away from smaller bubbles which then start to collapse. Since the rate of change in concentration due to diffusion is proportional to the second derivative of the concentration with respect to distance (Fick's Second Law), a reasonable approximation would be expected using

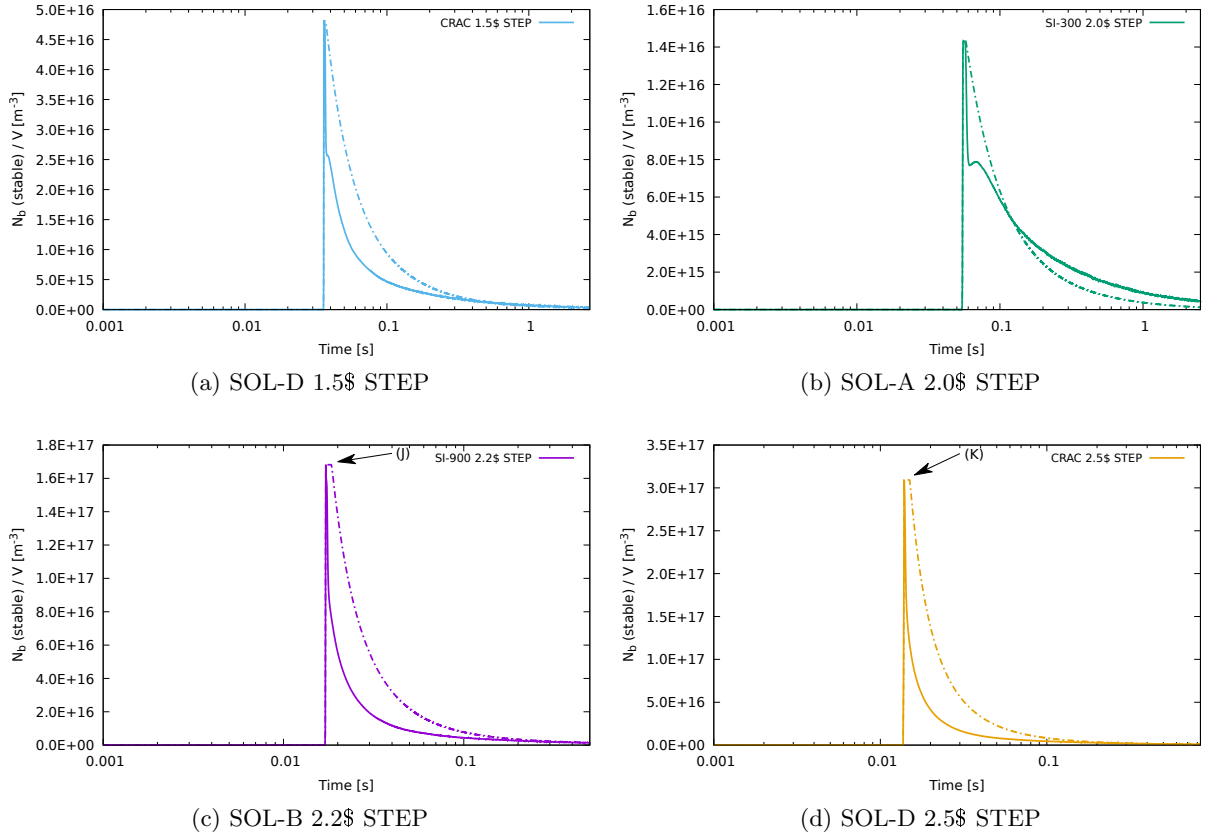


Fig. 4.3.15. Number of stable bubbles per unit volume simulated by the numerical model (solid line) with collapse rate predicted using Equation 4.3.26.

an expression of the following form:

$$\frac{dN_b}{dt} = \begin{cases} -\frac{k_c}{S(t)^2} \left[\frac{N_b(t)}{V} - k_b \left(\frac{P(t)}{V} \right)^{3/2} \right] V & \text{when } \frac{N_b(t)}{V} > k_b \left(\frac{P(t)}{V} \right)^{3/2}, \\ 0 & \text{otherwise,} \end{cases} \quad (4.3.26)$$

where all the symbols are as previously defined. This equation results in a collapse time constant k_c with the same units as the diffusion coefficient, i.e. $\text{m}^2 \text{s}^{-1}$. Equation 4.3.26 provides a reasonable fit to the results of the numerical model. A comparison showing four examples of transient simulations is shown in Figure 4.3.15.

One feature that Equation 4.3.26 cannot reproduce was already discussed in the previous section (see note (H) on Figure 4.3.14), where non-uniformity in the spatial distribution of bubbles immediately after saturation may lead to some immediate bubble collapse, even before the power has dropped such that the average bubble number density is below that required by Equation 4.3.26 for bubble collapse. This effect can be seen in Figure 4.3.15 as a short plateau (marked (J) and (K)) before the number of bubbles starts decreasing.

The time constant k_c was determined by calculating the value for each simulation which minimises

the following error indicator:

$$\text{ERR} = \int_0^{t_f} (t - t_{sat}) \left(\frac{N_b(t)}{V} - \frac{N_{b,pr}(t)}{V} \right)^2 dt, \quad (4.3.27)$$

where $N_b(t)$ is the number of bubbles at time t predicted by the numerical model and $N_{b,pr}(t)$ is the number of bubbles at time t predicted by Equation 4.3.26. The factor $(t - t_{sat})$ was included in Equation 4.3.27 in order to give preference to values of k_c that produce the best convergence, rather than favouring values which best matched the initial rate of collapse.

The average of all k_c values calculated was $5 \times 10^{-10} \text{ m}^2 \text{ s}^{-1}$ and this value was used to calculate the estimated bubble collapse rates shown in Figure 4.3.15. The value of this parameter corresponds to the rate at which bubbles will collapse due to diffusion when the density of bubbles in a volume of fuel solution exceeds that which is sustainable at the current fission power density.

4.3.4 Bubble Growth and Size Distribution

The numerical model produces snapshots of the distribution of bubble radii at fixed time intervals throughout the simulation. These snapshots can be used to observe the change in the bubble size distribution before, during and after the saturation period. Figure 4.3.16 shows the bubble size distribution during the moments before and after saturation of the SOL-C fuel solution during the SOL-C 2.2\$ step insertion case.

The bubble size distribution before saturation consists of a peak around $r_b = 5.0 \times 10^{-8} \text{ m}$, which corresponds to the approximate size of the first and largest bubble created along each fission track. There are no bubbles larger than $r_b = 5.5 \times 10^{-8} \text{ m}$ radius before saturation because the critical concentration of dissolved hydrogen has not yet been reached and all bubbles present in the simulated domain are collapsing. There is a population of bubbles with radius less than $r_b = 5.0 \times 10^{-8} \text{ m}$. These bubbles are collapsing as their gas dissolves into the surrounding solution. This is a relatively fast process with collapse times on the order of $10 \mu\text{s}$ (in agreement with Spiegler et al. (1962)).

Figure 4.3.17b shows the bubble size distribution 0.2ms after saturation has occurred. A distribution of larger bubble sizes has appeared with radii up to $2.5 \times 10^{-6} \text{ m}$. These bubbles result from fission events depositing bubbles in areas where the local dissolved gas concentration exceeds the critical concentration, leading to rapid expansion of these bubbles as they consume gas from their surroundings. There is still a large peak around $r_b = 5 \times 10^{-8} \text{ m}$ (truncated in the figure) as bubbles appearing in regions of low concentration continue to collapse.

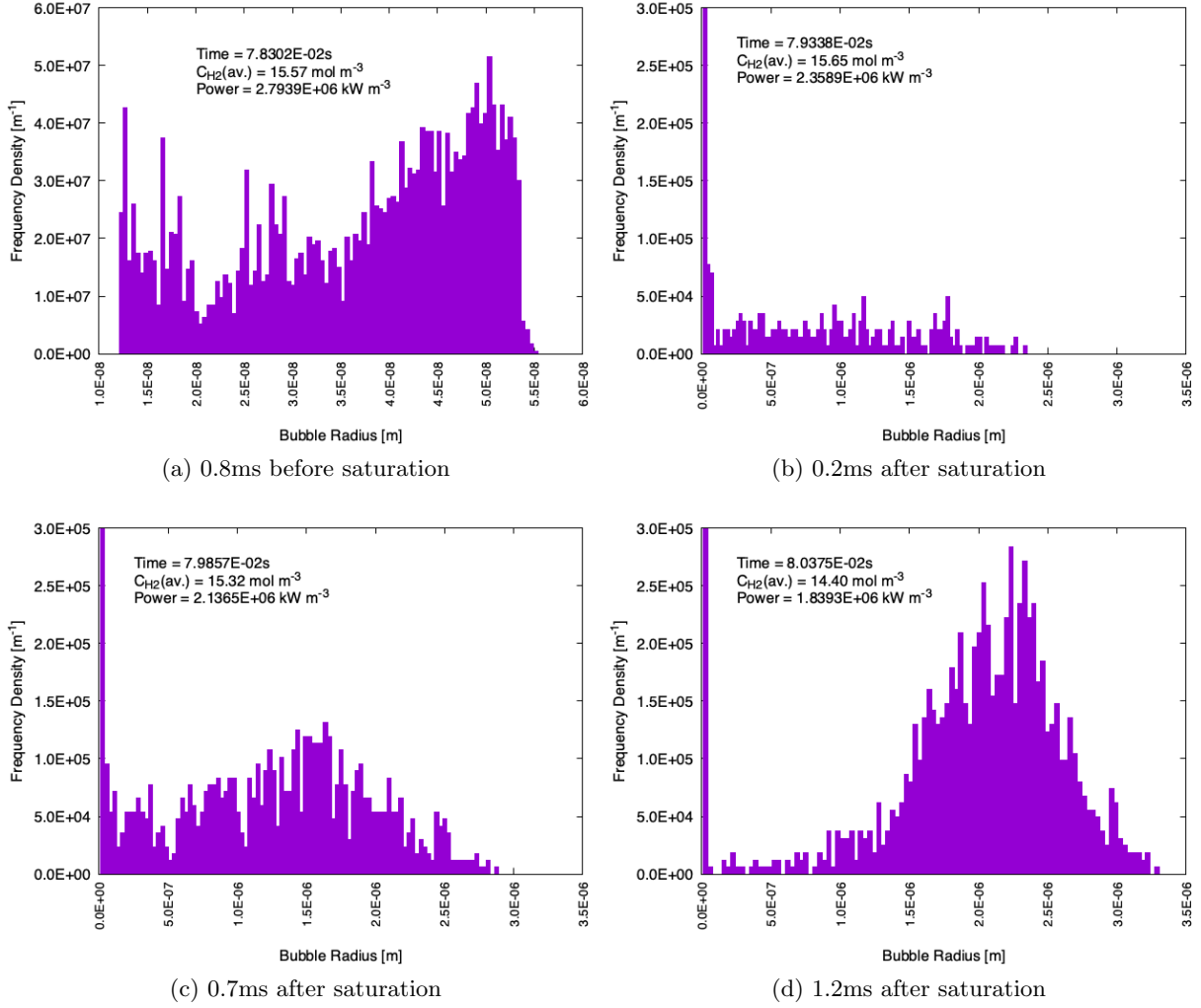


Fig. 4.3.16. Bubble size distribution moments before and after saturation of the SOL-C fuel solution with radiolytic gas during a 2.2 \$ reactivity step insertion case. Saturation occurs at $t = 79.1\text{ms}$

In Figure 4.3.16c, 0.7ms after saturation, the number of expanding bubbles has increased and a peak is beginning to form around $r_b = 1.6 \times 10^{-6}\text{m}$. The second peak consists of growing bubbles which are expanding as they consume dissolved gas from the fuel solution. The peak continues to become more pronounced in Figure 4.3.16d.

The numerical model can also produce snapshots of the distribution of dissolved gas concentrations at set time intervals. Bubbles will tend to expand until the partial pressure of hydrogen gas inside the bubble is in equilibrium with the concentration of dissolved hydrogen in the surrounding solution. The distribution of dissolved gas concentrations is therefore closely linked to the distribution of bubble sizes.

Figure 4.3.17 shows the evolution in the distributions of bubble radius and dissolved gas concentration for the SOL-C 1.8\$ step case. The bubble size distribution shifts towards larger bubble sizes

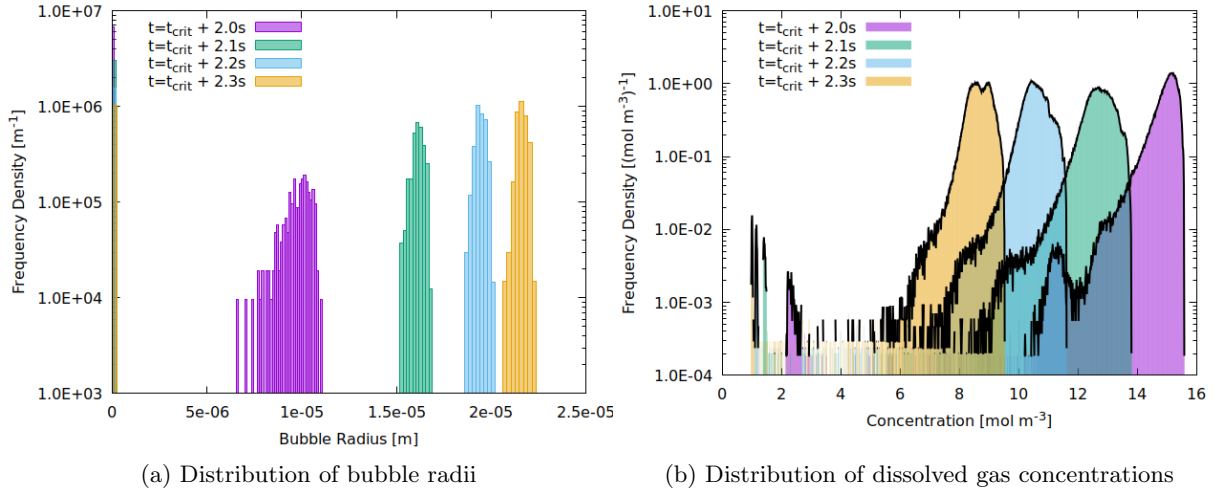


Fig. 4.3.17. Distributions of bubble radius and dissolved gas concentration during the moments after saturation of the SOL-C fuel solution following a 1.8\$ reactivity step insertion at t_{crit} .

while the distribution of dissolved gas concentrations shifts towards lower values.

The evolution in the size of stable bubbles can take different courses depending on the type of transient. Figure 4.3.18 shows the average stable bubble radius over time for the two focussed cases. In the 3.5\$ SOL-B case, the bubbles increase in size rapidly at first, their average radius rising almost two orders of magnitude from $\sim 5 \times 10^{-8} \text{m}$ to $\sim 1 \times 10^{-6} \text{m}$ in less than one millisecond. This initial rapid increase is followed by a much more gradual increase. In the 2.0\$ SOL-C case, the average radius of stable bubbles rises rapidly to a much larger size than in the SOL-B case, reaching a radius of $\sim 2 \times 10^{-5} \text{m}$ in just a few milliseconds. However, their expansion stops and their size remains relatively constant after that point.

In both cases, the fission power density has dropped to a very low level after the appearance of stable bubbles so the rate of addition of radiolytic gas to the solution is very small. The continued expansion after saturation of the stable bubbles in the 3.5\$ SOL-B case cannot therefore be explained by continued addition of gas to the solution by radiolysis. This secondary growth phase is instead due to bubble collapse.

Figure 4.3.6 showed that the number of bubbles in the 3.5\$ SOL-B case peaked at saturation before declining rapidly, whereas the number of stable bubbles in the 2.0\$ SOL-C case remained relatively constant. The expansion of stable bubbles in the SOL-B case is driven by the collapse of smaller bubbles in the solution, which release their gas back into the solution for the larger bubbles to consume.

In both cases, the initial rapid increase in stable bubble size is due to the consumption of dissolved

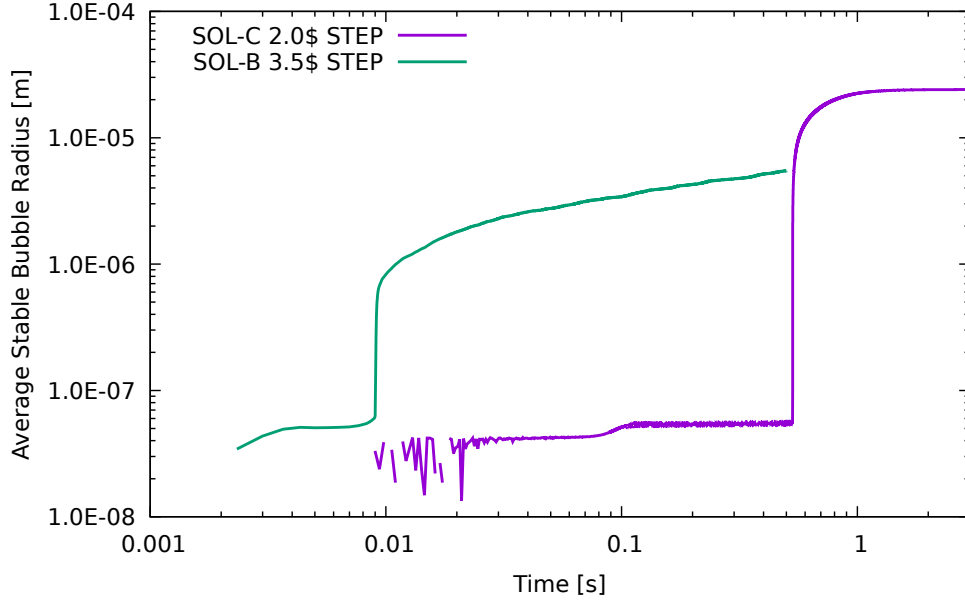


Fig. 4.3.18. Average radius of stable bubbles for the 2.0\$ step insertion case in the SOL-C fuel solution and the 3.5\$ step insertion case in the SOL-B fuel solution.

gas in the solution surrounding each bubble. This is why stable bubbles in the 2.0\$ SOL-C case are larger after the initial expansion phase than stable bubbles in the 3.5\$ SOL-B case - because the SOL-C case has fewer bubbles among which to share the available dissolved gas. The size of the bubbles after this initial expansion phase can be estimated, by considering that the concentration of dissolved gas after expansion is simply the critical concentration after deducting the number of moles of gas contained in the expanded bubbles. The radius of the bubble in equilibrium with this concentration (let this be called the “expanded bubble radius”, r_e) can therefore be found by solving,

$$C_{H_2,eq} = C_{crit} - \frac{N_b P_b V_b}{V RT}, \quad (4.3.28)$$

where $C_{H_2,eq}$ is the equilibrium concentration of the bubble, C_{crit} is the critical concentration, N_b/V is the number density of bubbles at saturation, P_b is the internal pressure of the bubble, V_b is the bubble volume, R is the universal gas constant and T is the temperature of the fuel solution. The second term on the right-hand side should strictly include a term to subtract the gas contained in the critical bubble nucleus at the moment of saturation. However, this term has a negligible impact on the radius of the expanded bubble ($\Delta r_e < 1\%$ for $r_e > 5 \times 10^{-7} \text{ m}$) and has therefore been omitted for simplicity.

Substituting expressions for the bubble pressure and volume in terms of the bubble radius, and for the critical concentration in terms of the nucleation radius, results in the following expression:

$$\left(P_l + \frac{2\sigma_s}{r_e}\right) H_{H_2,sol} = \left(P_l + \frac{2\sigma_s}{r_0}\right) H_{H_2,sol} - \frac{4\pi N_b}{3VRT} \left(P_l + \frac{2\sigma_s}{r_e}\right) r_e^3, \quad (4.3.29)$$

where r_0 is the radius of the fission track bubble which nucleated the expanding bubble and the other

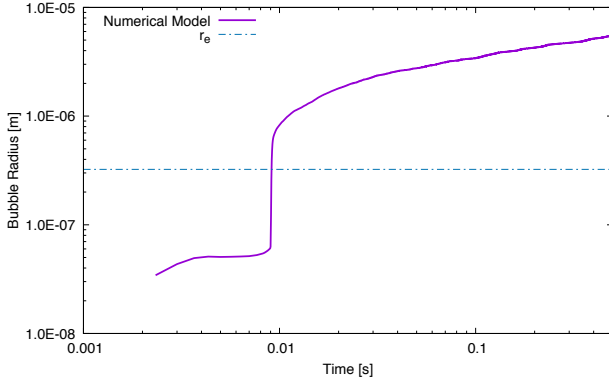


Fig. 4.3.19. Average radius of stable bubbles during a 3.5\$ step reactivity insertion in the SOL-B fuel solution. Prediction of the numerical model compared to the value predicted by Equation 4.3.29.

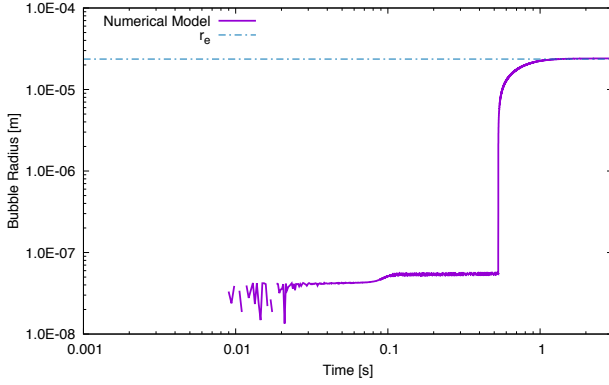


Fig. 4.3.20. Average radius of stable bubbles during the 2.0\$ step reactivity insertion in the SOL-C fuel solution. Prediction of the numerical model compared to the value predicted by Equation 4.3.29.

symbols are as previously defined.

By calculating the value of r_e using Equation 4.3.29 it is possible to confirm the above hypothesis regarding the mechanisms of bubble expansion. Figures 4.3.19 and 4.3.20 compare the values of r_e obtained using Equation 4.3.29 to the evolution in the stable bubble radius predicted by the numerical model. The values of r_e were calculated using the peak values for the number density of bubbles at saturation which can be found in Tables 4.7 to 4.10.

The expanded bubble radius coincides precisely with the maximum stable bubble radius in the SOL-C 2.0\$ case, confirming that in this case the expansion of the bubbles is due entirely to the consumption of excess dissolved gas in the fuel solution surrounding the bubbles. In the 3.5\$ SOL-B case, the bubbles continue to grow far beyond the value predicted using Equation 4.3.29, confirming that other processes (bubble collapse in this case) are also playing an important role.

4.3.5 Rate of Appearance of Radiolytic Gas Voids

The change in gas void fraction (voidage) in the simulated domain is shown as a function of time in Figure 4.3.21. The rates of increase in the voidage evolve differently for the two transients shown. In the 3.5\$ SOL-B case, the voidage increases rapidly from zero to ~ 0.20 , after which it continues to increase at a more gradual rate. In the 2.0\$ SOL-C case, the voidage increases at a slower rate which

it maintains until a voidage of ~ 0.42 is reached, at which point the voidage stops increasing.

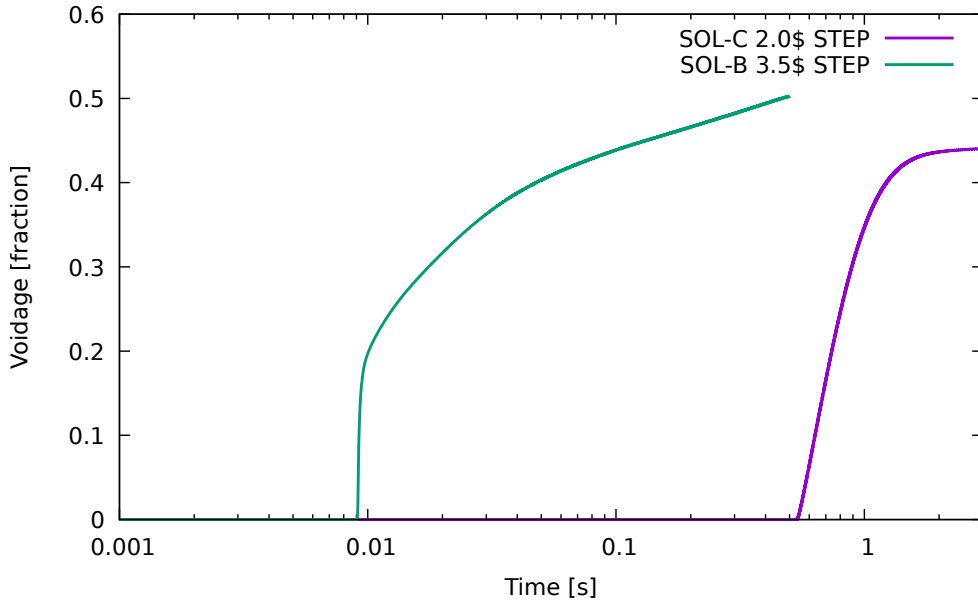


Fig. 4.3.21. Total void fraction due to the presence of radiolytic gas voids for the 2.0\$ step insertion case in the SOL-C fuel solution and the 3.5\$ step insertion case in the SOL-B fuel solution.

The voidage in the fissile solution is affected by two factors: the size of the gas bubbles and the number of moles of gas present. Both factors can be seen in the 3.5\$ SOL-B case where the initial rapid increase in the voidage coincides with a sudden drop in the dissolved gas concentration as hydrogen is transferred to the gaseous phase. The secondary, slower increase in voidage is due to the growth of radiolytic gas bubbles. As discussed in the previous section, this is primarily driven by the decrease in the total number of stable bubbles (mechanism described in Section 4.3.3) which leads to a smaller number of larger bubbles containing the same radiolytic gas. The bubbles are less compressed by surface tension effects due to their larger size which leads to an increase in voidage.

The voidage is therefore a relatively complex function of the number of moles of radiolytic gas produced and the number of bubbles present per unit volume. Figure 4.3.22 shows the amount of dissolved gas in the fuel solution as a function of time for the two focussed cases. This figure provides an indication of the rate at which radiolytic gas is transferred from the dissolved phase to the gaseous phase, where it can contribute to the growth of gas voids.

The evolution of the dissolved gas concentration after saturation of the fuel solution is a very close fit to an exponential decay of the form:

$$\frac{dC_{\text{H}_2(aq)}(t)}{dt} = -\alpha_c (C_{\text{H}_2(aq)}(t) - C_{\text{H}_2,eq}), \quad (4.3.30)$$

where $C_{\text{H}_2(aq)}(t)$ is the concentration of dissolved hydrogen gas at time t and $C_{\text{H}_2,eq}$ is the concentration

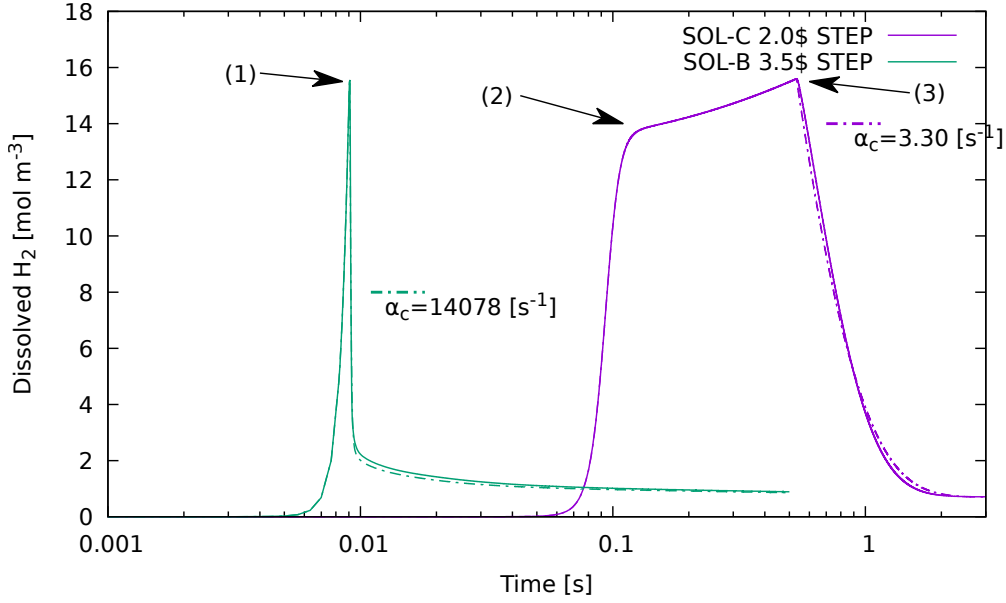


Fig. 4.3.22. Rate of disappearance of dissolved hydrogen gas for the 2.0\$ step insertion case in the SOL-C fuel solution and the 3.5\$ step insertion case in the SOL-B fuel solution.

of dissolved hydrogen gas in equilibrium with partial pressure of hydrogen gas inside the bubble. This is given by,

$$C_{H_2,eq} = y_{H_2} \left(P_l + \frac{2\sigma_s}{r_b} \right) H_{H_2,sol}, \quad (4.3.31)$$

where the symbols are as defined previously.

By comparing the values of α_c , shown in Figure 4.3.22 for the 2.0\$ SOL-C and 3.5\$ SOL-B cases, it is clear that there is a substantial difference between the two cases in the rates at which dissolved gas moves from the dissolved phase into the gaseous phase. This difference can be explained by comparing the stable bubble densities in the two cases. Since dissolved gas can only come out of solution when it encounters an expanding bubble, and the bubble number density in the 3.5\$ SOL-B case is four orders of magnitude larger than in the 2.0\$ SOL-C case, it takes longer for dissolved gas in the latter case to reach a bubble and come out of solution.

The evolution of the dissolved hydrogen concentration for all simulated transients is shown in Figure 4.3.23. The general trend across all simulations is similar to that described above, starting with an exponential rise in concentration resulting from the exponential rise in the fission power, followed by a sudden drop in concentration once the critical concentration has been reached. It is worth noting that the *average* dissolved gas concentration never actually exceeds the critical concentration; instead the critical concentration is exceeded in one, or possibly several, regions.

Figure 4.3.23 reinforces the observation that the rate of mass transfer of hydrogen gas from the dissolved phase to the gaseous phase varies substantially between different transients. The drop in

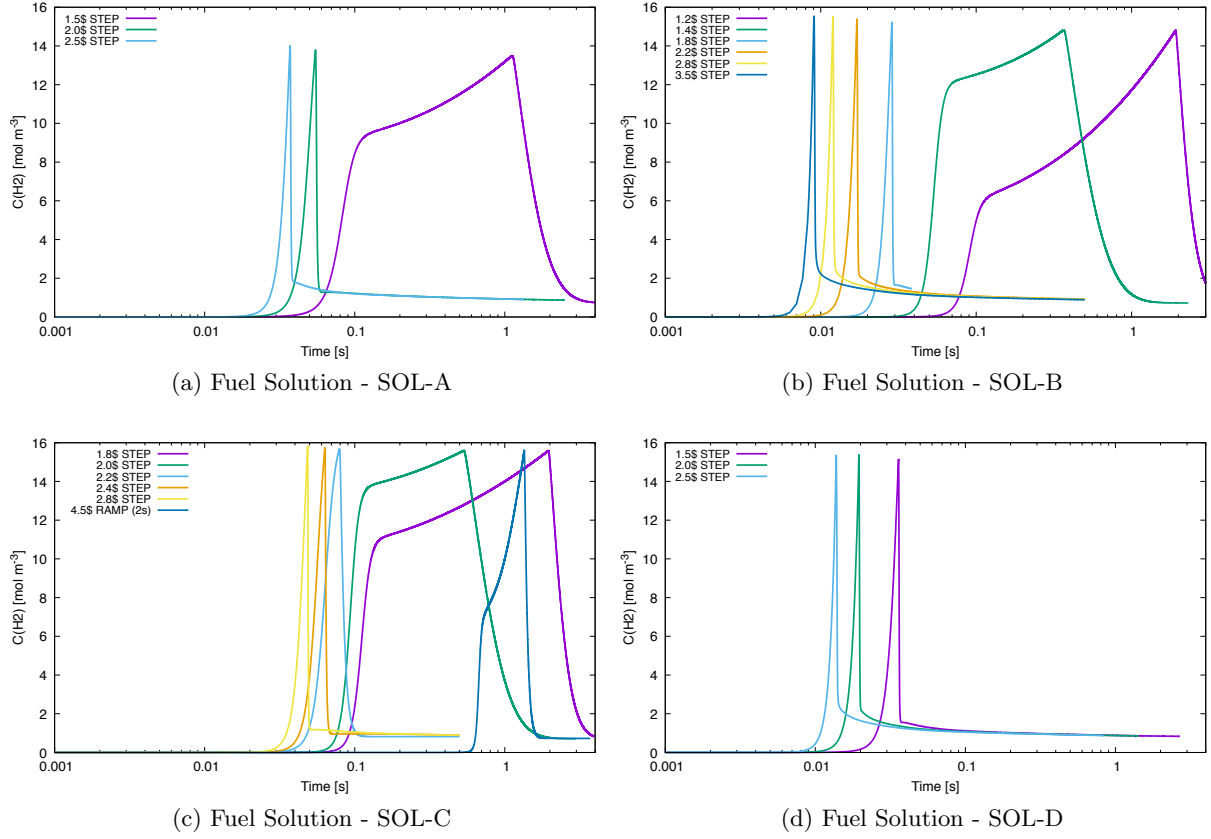


Fig. 4.3.23. Dissolved hydrogen gas concentration as a function of time.

dissolved gas concentration after saturation, from the critical concentration to a value less than ~ 1 mol m $^{-3}$ can be seen to take place in a time period ranging from a few microseconds up to a second.

It was previously hypothesised that the difference in the mass transfer rate was due to the difference in the number of bubbles per unit volume, since the presence of bubbles is required for dissolved gas to come out of solution. This hypothesis is confirmed by Figure 4.3.24 which shows the rate constant α_c (as defined by Equation 4.3.30) as a function of the peak bubble number density during the saturated period.

Figure 4.3.24 shows that the rate constant α_c increases with increasing bubble number density. The properties of the fuel solution do not appear to have a significant influence on the value of α_c since there is no clear difference between the sets of data for the different simulated solutions. The trendline shown in Figure 4.3.24 has the equation,

$$\alpha_c = 1.9436 \times 10^{-10} \left(\frac{N_b}{V} \right)^{0.78926}, \quad (4.3.32)$$

where N_b/V is the peak bubble number density to occur during the saturated period. The values of α_c shown were obtained by fitting Equation 4.3.30 to each set of results and adjusting α_c to minimise

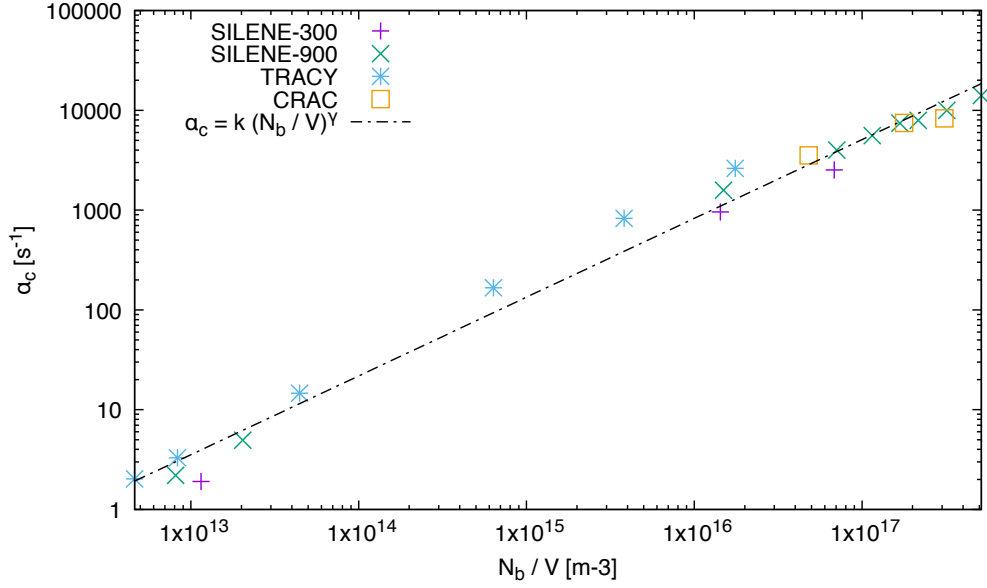


Fig. 4.3.24. Mass transfer rate constant α_c as a function of peak bubble number density during saturation of the fuel solution.

the error, as defined by the following indicator:

$$\text{ERR} = \int_0^{t_f} (C_{\text{H}_2(aq)}(t) - C_{\text{H}_2,pr}(t))^2 dt, \quad (4.3.33)$$

where $C_{\text{H}_2,pr}$ is the dissolved gas concentration predicted using Equation 4.3.30.

4.3.6 Summary of Selected Data

Table 4.9 provides a summary of some of the key parameters determined by the numerical model for each reactivity transient. The results corresponding to the time of saturation have been determined by taking the values which coincide with the peak concentration of dissolved hydrogen gas. However, it is not actually possible to define a single instant of saturation, since various regions within the simulated domain would often saturate at different times. The values listed therefore coincide with the moment at which the number of bubbles which are stable with respect to their local concentration is sufficient for rate of mass transfer from dissolved phase to gas phase to exceed the rate at which new dissolved radiolytic gas is deposited into the solution due to collapsing bubbles.

Transient N°	1	2	3
Reactivity Inserted	1.5\$	2.0\$	2.5\$
Insertion Rate [$\$ s^{-1}$]	STEP	STEP	STEP
$C(H_2)_{\max}$ [mol m^{-3}]	13.49	13.81	14.02
Time to $C(H_2)_{\max}$ [s]	1.1200	0.0548	0.0371
Power Density at $C(H_2)_{\max}$ [W m^{-3}]	1.892×10^7	5.737×10^9	1.699×10^{10}
Bubble Number Density at $C(H_2)_{\max}$ [m^{-3}]	2.000×10^{12}	5.324×10^{15}	4.898×10^{16}
Peak Power Density [W m^{-3}]	1.934×10^9	7.594×10^9	1.702×10^{10}
Time to Peak Power Density [s]	0.0807	0.0499	0.0369
Peak Bubble Number Density [m^{-3}]	1.150×10^{13}	1.432×10^{16}	6.829×10^{16}
Time to First Stable Bubble [s]	1.1103	0.0542	0.0368
Energy [J] at EOS ¹	1.026×10^8	1.107×10^8	1.200×10^8

TABLE 4.7

Summary of selected data for simulations in the SOL-A fuel solution.

Transient N°	1	2	3
Reactivity Inserted	1.5\$	2.0\$	2.5\$
Insertion Rate [$\$ s^{-1}$]	STEP	STEP	STEP
$C(H_2)_{\max}$ [mol m^{-3}]	15.17	15.39	15.38
Time to $C(H_2)_{\max}$ [s]	0.0359	0.0196	0.0138
Power Density at $C(H_2)_{\max}$ [W m^{-3}]	3.077×10^{10}	9.458×10^{10}	1.566×10^{11}
Bubble Number Density at $C(H_2)_{\max}$ [m^{-3}]	3.854×10^{16}	1.569×10^{17}	8.497×10^{16}
Peak Power Density [W m^{-3}]	3.084×10^{10}	9.458×10^{10}	1.632×10^{11}
Time to Peak Power Density [s]	0.0358	0.0196	0.0139
Peak Bubble Number Density [m^{-3}]	4.812×10^{16}	1.780×10^{17}	3.093×10^{17}
Time to First Stable Bubble [s]	0.0357	0.0195	0.0138
Energy [J] at EOS	2.059×10^8	2.263×10^8	2.465×10^8

TABLE 4.8

Summary of selected data for simulations in the SOL-D fuel solution.

¹End of Simulation

Transient N°	1	2	3	4	5	6	7	8	9
Reactivity Inserted	1.2\$	1.4\$	1.6\$	1.8\$	2.0\$	2.2\$	2.4\$	2.8\$	3.5\$
Insertion Rate [$\$ s^{-1}$]	STEP	STEP	STEP	STEP	STEP	STEP	STEP	STEP	STEP
$C(H_2)_{\max}$ [mol m $^{-3}$]	14.81	14.81	15.08	15.25	15.32	15.40	15.42	15.53	15.56
Time to $C(H_2)_{\max}$ [s]	1.9205	0.3648	0.0426	0.0287	0.0232	0.0171	0.0149	0.0120	0.0091
Power Density at $C(H_2)_{\max}$ [W m $^{-3}$]	3.616×10^7	9.312×10^7	1.272×10^{10}	3.816×10^{10}	6.435×10^{10}	9.105×10^{10}	1.175×10^{11}	1.721×10^{11}	2.759×10^{11}
Bubble Number Density at $C(H_2)_{\max}$ [m $^{-3}$]	1.289×10^{12}	3.363×10^{12}	4.733×10^{15}	4.019×10^{16}	5.182×10^{16}	1.278×10^{17}	9.522×10^{16}	1.582×10^{17}	5.050×10^{17}
Peak Power Density [W m $^{-3}$]	2.681×10^9	1.041×10^{10}	2.328×10^{10}	4.128×10^{10}	6.440×10^{10}	9.106×10^{10}	1.186×10^{11}	1.757×10^{11}	2.821×10^{11}
Time to Peak Power Density [s]	0.0896	0.0530	0.0384	0.0277	0.0232	0.0172	0.0150	0.0121	0.0091
Peak Bubble Number Density [m $^{-3}$]	8.104×10^{12}	2.037×10^{13}	1.495×10^{16}	7.073×10^{16}	1.150×10^{17}	1.682×10^{17}	2.161×10^{17}	3.199×10^{17}	5.142×10^{17}
Time to First Stable Bubble [s]	1.9156	0.3610	0.0422	0.0285	0.0231	0.0170	0.0148	0.0119	0.0090
Energy [J] at EOS	1.968×10^8	1.980×10^8	2.049×10^8	2.147×10^8	2.243×10^8	2.354×10^8	2.451×10^8	2.642×10^8	2.978×10^8

TABLE 4.9

Summary of selected data for simulations in the SOL-B fuel solution.

Transient N°	1	2	3	4	5	6
Reactivity Inserted	1.8\$	2.0\$	2.2\$	2.4\$	2.8\$	4.5
Insertion Rate [$\$ s^{-1}$]	STEP	STEP	STEP	STEP	STEP	RAMP (2s)
$C(H_2)_{\max}$ [mol m $^{-3}$]	15.59	15.60	15.67	15.75	15.84	15.61
Time to $C(H_2)_{\max}$ [s]	1.9596	0.5334	0.0791	0.0633	0.486	1.3487
Power Density at $C(H_2)_{\max}$ [W m $^{-3}$]	2.279×10^7	5.539×10^7	2.439×10^9	1.043×10^{10}	2.705×10^{10}	2.854×10^8
Bubble Number Density at $C(H_2)_{\max}$ [m $^{-3}$]	3.800×10^{11}	1.040×10^{12}	7.150×10^{13}	7.670×10^{14}	3.741×10^{15}	5.244×10^{12}
Peak Power Density [W m $^{-3}$]	5.905×10^9	9.184×10^9	1.319×10^{10}	1.793×10^{10}	2.958×10^{10}	1.962×10^9
Time to Peak Power Density [s]	0.1105	0.0928	0.0630	0.0562	0.0464	0.6703
Peak Bubble Number Density [m $^{-3}$]	4.620×10^{12}	8.320×10^{12}	6.350×10^{14}	3.822×10^{15}	1.754×10^{16}	4.444×10^{13}
Time to First Stable Bubble [s]	1.9553	0.5314	0.0784	0.0629	0.0484	1.3468
Energy [J] at EOS	2.715×10^8	2.758×10^8	2.774×10^8	2.864×10^8	2.995×10^8	2.760×10^8

TABLE 4.10

Summary of selected data for simulations in the SOL-C fuel solution.

4.4 Further Observations

Throughout this section the term “predictive correlations” will be used to refer to the expressions derived in the previous section to predict the bubble number density, bubble collapse rate, dissolved gas concentration, and other parameters relating to the saturation of a fuel solution with dissolved radiolytic gas. This includes Equations 4.3.15, 4.3.23, 4.3.26 and 4.3.30.

4.4.1 Effects of Non-Uniform Spatial Distribution of Bubbles

In some cases, there are differences between the numerical model and the predictive correlations developed in the previous section due to 3D spatial effects, which cannot be accounted for in the correlations because they approximate the saturated region to a single homogeneous region. For example, the trends in the stable bubble number density for the 2.4\$ SOL-C step case predicted by the numerical model and the correlations are shown in Figure 4.4.1. The numerical model predicts a bubble number density which peaks, followed by a decline (L) much more rapid than that predicted by the correlations. This is then followed by a short-lived recovery (M) in the bubble number density before the population proceeds to decrease at a rate closer to that predicted by the correlations.

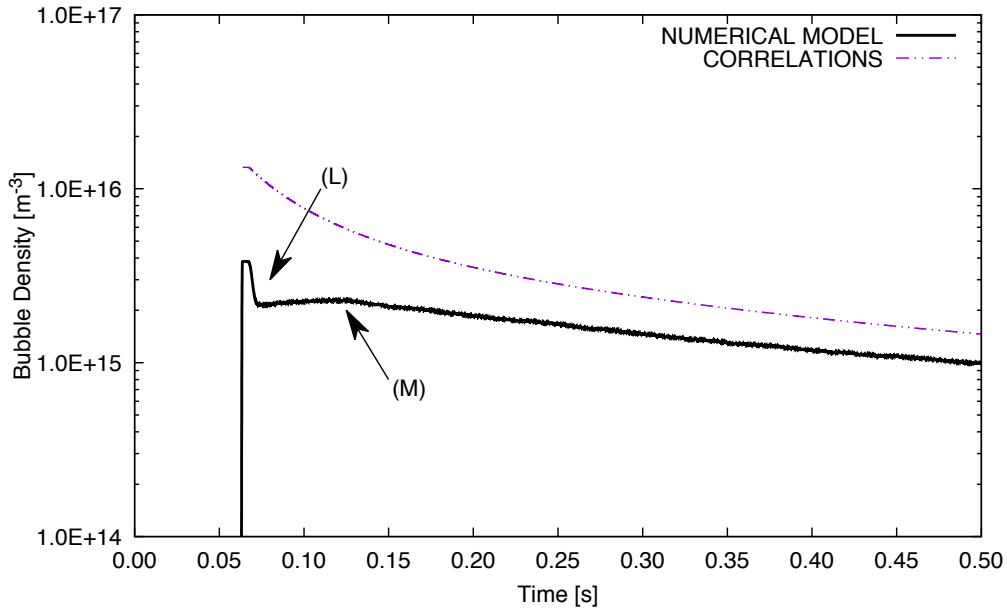


Fig. 4.4.1. Change in bubble number density over time predicted by the numerical model of the 2.4\$ SOL-C step case, showing results of a Monte Carlo simulation and results of the predictive correlations.

Analysis of the distribution of local concentrations predicted by the numerical model confirms this is indeed due to spatial effects. Figure 4.4.2 shows the distributions of dissolved gas concentrations around the moment of saturation for the same simulation in the SOL-C fuel solution. Moments before

saturation there is a single peak in the concentration distribution, however during saturation the distribution breaks up into two distinct peaks, corresponding to regions of the simulated domain with different concentrations of dissolved gas. A few moments later these two peaks merge as diffusion between the regions of the simulated domain evens out the dissolved gas concentration.

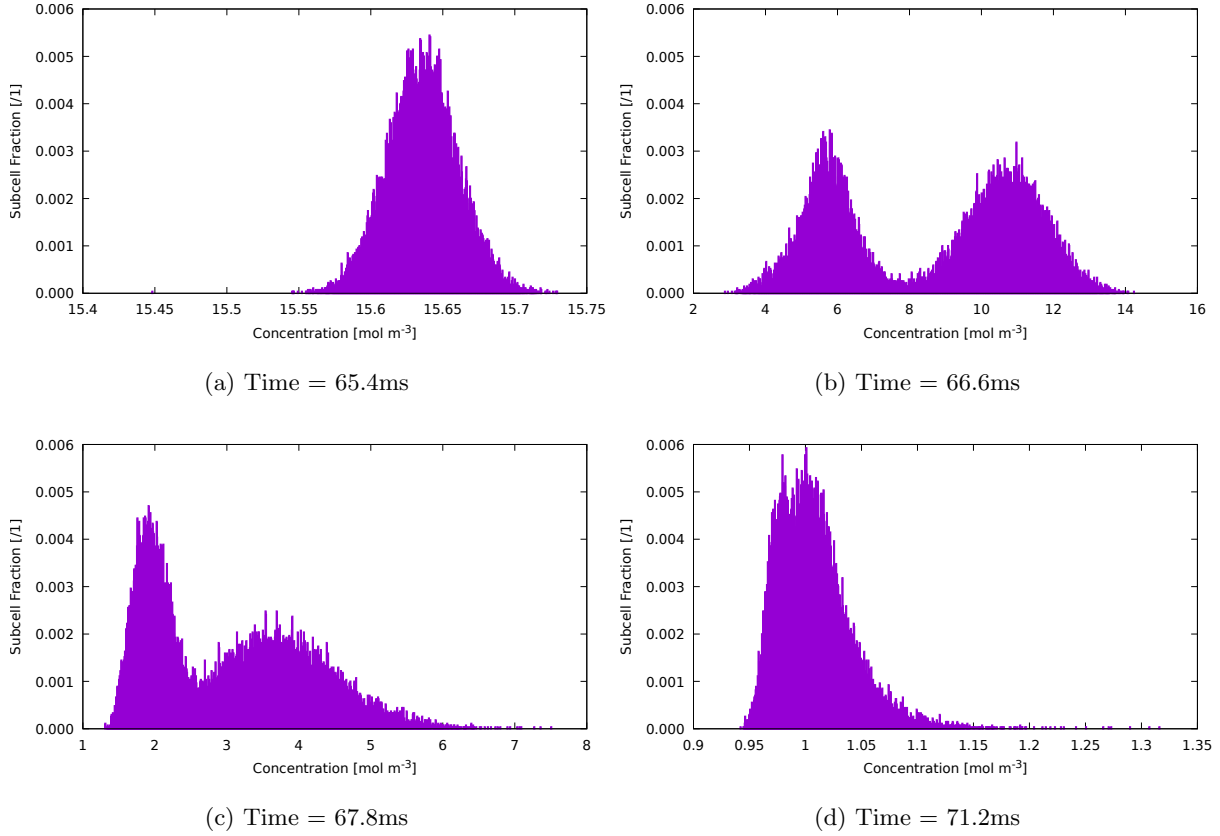


Fig. 4.4.2. Distribution of dissolved hydrogen gas concentrations within the simulated domain moments before and after saturation of the fuel solution for the 2.4\$ SOL-C case, showing two saturated regions which eventually merge into one.

In the case shown in Figure 4.4.2, the bubble number density is non-uniform, creating a region of low dissolved gas concentration where the bubble number density is highest and areas of high dissolved gas concentration where the bubble number density is lowest. This results in higher than expected rates of bubble collapse in the areas of high bubble number density and a higher than expected overall rate of bubble collapse. However, once the regions start to become more homogeneous due to the effects of diffusion and bubble collapse, the results of the numerical model converge towards those predicted by the correlations.

This effect appears to be less pronounced for cases of larger reactivity insertions. It is not visible at all in the SOL-B 3.5\$ simulation shown in Figure 4.4.3. This may be because the dissolved gas concentration rises faster in the more reactive transients. In these cases, a larger proportion of the

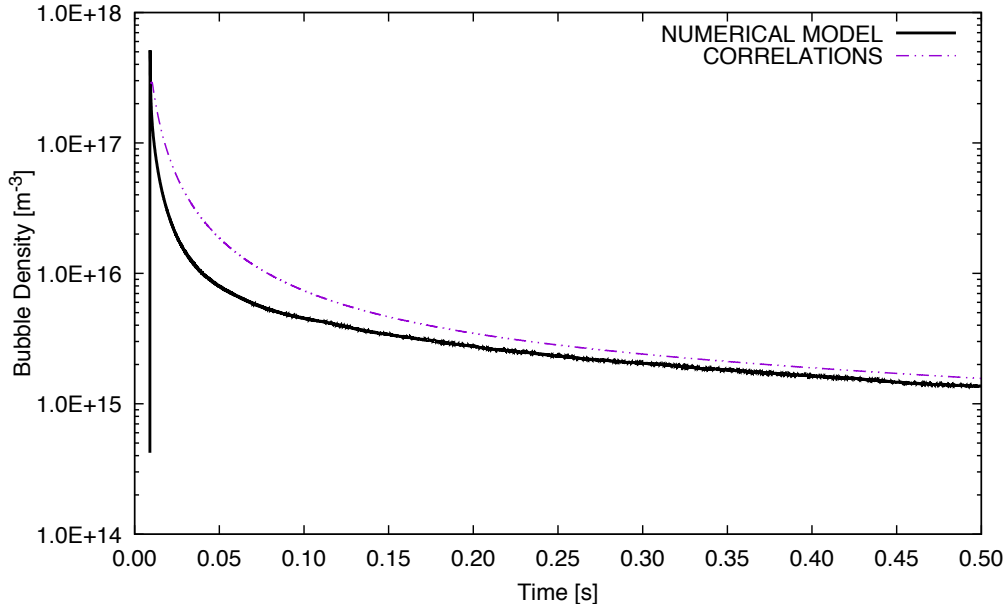


Fig. 4.4.3. Change in bubble number density over time predicted by the numerical model of the 3.5\$ SOL-B step case, showing results of a Monte Carlo simulation and results of the predictive correlations.

simulated domain has time to saturate before the growth of bubbles in other regions leads to a drop in the dissolved gas concentration below the critical concentration for bubble formation. The number density of bubbles is therefore more uniform across the simulated domain and the system behaviour more closely resembles that predicted by the correlations based on homogeneous parameters.

4.4.2 Effects of Statistical Variation in the Monte Carlo Model

It is necessary to examine the extent to which some of the phenomena attributed to spatial variations may in fact be due to statistical variation in the numerical model. The numerical model uses a Monte Carlo simulation technique and so it is possible to observe some statistical variation in the results. However, the number of fission events simulated in each model is very large. For example, despite the simulated domain having a volume of only $2 \times 10^{-12} \text{ m}^3$, the 2.4\$ SOL-C case discussed in Section 4.4.1 involves over 18 million fission events. Any statistical variation in the simulation results is therefore expected to be small.

In Section 4.4.1 it was discussed that regions with large differences in dissolved gas concentration can appear and then merge during the course of saturation. To examine the possibility that this phenomenon may be subject to statistical variation due to stochasticity in the frequency and location of fission events, the 2.4\$ case in the SOL-C fuel solution was run an additional four times for the time period 0-0.5 seconds. Another simulation was also run with a smaller simulated domain volume to see if the phenomenon might be an artefact of the simulated domain size. The results of both tests

are shown in Figure 4.4.4.

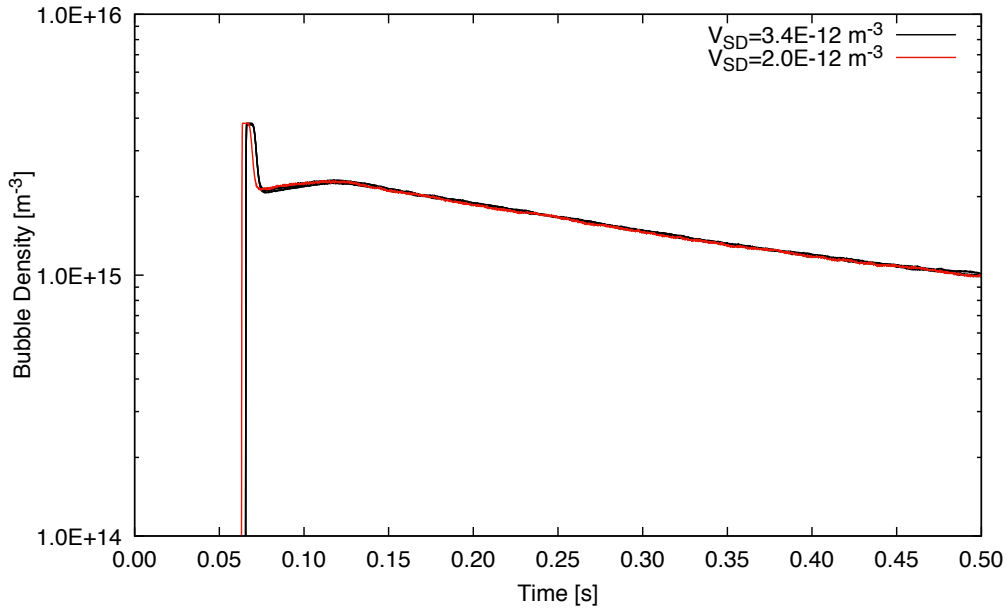


Fig. 4.4.4. Change in bubble number density over time predicted by the numerical model of the 2.4\$ SOL-C step case, showing 5 independent Monte Carlo simulations with two different simulated domain volumes.

The fact that the identical runs of the 2.4\$ SOL-C simulation yield similar results indicates that the previously noted heterogeneity in the dissolved gas concentration is not a chance occurrence subject to statistical variation but a product of the saturation process at certain fission power densities.

4.5 Conclusions

A model has been presented that tracks the number, size and growth or shrinkage of all bubbles formed in a small volume of fissile solution, contained somewhere within a larger volume, during a reactivity excursion. The aim of the model is to examine the competing processes taking place as the solution becomes saturated with dissolved radiolytic gas, with the aim of predicting the number and size of bubbles that survives saturation for a range of different reactivity excursions. The model is most relevant to conditions at the centre of a volume of fissile solution, far away from internal surfaces, where the voids have their largest effect on reactivity, yet void formation is most suppressed, due to the sparsity of nucleation sites.

The results presented have significant implications for accurate modelling of transients in fissile solutions. In particular, they show that there is a significant variation in the size and number of bubbles appearing upon saturation of a fissile solution, and this variation is sufficient to have a substantial

impact on the degree of reactivity feedback produced by a given number of moles of radiolytic gas. A set of empirical and semi-empirical correlations has been presented which can be used to predict the number of stable bubbles present in a given volume of fissile solution, following saturation with dissolved radiolytic gas. These correlations will be used as the basis for a new radiolytic gas treatment in a point kinetics model to be presented in the next chapter.

The size of the stable bubbles that appear after saturation of the fuel solution depends on the number of bubbles that survives the saturation process. The average radius of stable bubbles and the separation distance between these bubbles is therefore dependent on the density of stable bubbles after saturation. In general, cases where the fission power density is lower at the moment of saturation produce larger bubbles. The negative reactivity induced by one mole of radiolytic gas is therefore greater for these cases because larger bubbles have lower internal pressure due to surface tension effects. For smaller reactivity insertions, the average radius of stable bubbles was found to increase with decreasing inserted reactivity, whereas for larger reactivity insertion cases, the average radius of stable bubbles was found to be independent of the inserted reactivity, determined instead by the rate of collapse of the bubbles present.

The concentration of dissolved gas in the model increased to a concentration (the critical concentration) at which the largest of the small bubbles formed along the tracks of fission fragments were able to serve as nucleation sites. Once this concentration is reached, the bubbles expand and the concentration of dissolved gas drops very rapidly. The rate of change in the dissolved gas concentration, and the rate of appearance of voids due to radiolytic gas, depends on the number density of stable bubbles, which determines the diffusion time required for dissolved gas to reach a bubble interface where it can come out of solution. The number density of stable bubbles is therefore a key factor determining the rate of appearance of gas voids.

If the critical concentration in a fissile solution could be reduced by providing nucleation sites for the formation of bubbles, it would result in a smaller power peak, increased void feedback due to a larger average bubble size, and a reduction in the total amount of fission energy released. It may therefore be useful to consider the inclusion of additional nucleation sites, designed to reduce the critical concentration, as one means to mitigate against the risk posed by unplanned criticality excursions in containers used for the storage of fissile solutions.

Chapter 5

A Point Kinetics Model with Physical Representation of Bubble Formation, Growth and Removal

Much of the work presented in this chapter, including tables and figures, is reproduced from Winter et al. (2020b) (submitted for publication).

The following chapter presents a new point kinetics code for the simulation of nuclear criticality transients in aqueous fissile solutions. The new code is developed in FORTRAN and implements a novel model of radiolytic gas, based on the findings presented in Chapters 3 and 4. The code also features a novel treatment of the critical concentration for void formation and a multi-component treatment of radiolysis products. Models of mixing and gas advection have been taken from the literature. A stochastic-deterministic analysis of the 1958 Y-12 accident is presented by combining the results of the new code with the methods presented in Chapter 2.

The purpose of the work presented in the previous chapter was to develop techniques which can be used to improve the accuracy of point kinetics models with respect to radiolytic gas production. The correlations proposed will now be integrated into a point kinetics model to permit the modelling of an entire fuel solution. This will allow the correlations developed to be evaluated against experimental data from experimental criticality transients in fissile solutions to determine their validity.

In Chapter 4 it was shown that the magnitude and timing of void reactivity feedback depends strongly on the mechanics of bubble formation. In particular, the timing is affected by the concentration at which bubbles are able to nucleate, either on the tiny bubbles of hydrogen gas deposited by

fission fragments as they tear through the fuel solution, or on the surface of contaminants in the fuel solution or vessel internals. The magnitude of the reactivity feedback produced depends strongly on the size of the bubbles which form during saturation of the fuel solution. This is due to surface tension effects, which make the internal pressure of the bubbles, and resulting compression of the radiolytic gas, a function of the bubble size. Current models of radiolytic gas often ignore the effect of surface tension on the molar volume of radiolytic gas in a fissile solution. This will result in an over-estimate of the radiolytic gas volume and the resulting reactivity feedback.

Not only does bubble size influence the volume of radiolytic gas voids, it also determines the speed with which these voids advect out of the solution. The number and size of bubbles produced during saturation of a fuel solution is therefore a key factor determining the occurrence and timing of any subsequent rises in fission power following the initial power peak.

It was further shown in Chapter 4 that the number density (and therefore size) of bubbles produced during saturation of a fuel solution is a predictable function of the fission energy deposited during saturation of the solution. The survival of the bubbles formed during saturation was also shown to be a predictable function of the solution properties and the fission power density. This makes it possible to propose a new method for modelling radiolytic gas, in which the formation, growth and removal of stable bubbles is modelled in an attempt to produce a more physically realistic representation of radiolytic gas behaviour.

5.1 Model Description

The model is adapted from that presented in Cooling (2014) and borrows many of the same assumptions and physical representations. It is a point kinetics model coupling zero-dimensional neutronics with one-dimensional thermal hydraulics. Most of the key differences between the model presented here and that of Cooling (2014) relate to the treatment of radiolytic gas and are set out in detail below. Except where indicated, physical properties have been modelled using the same correlations as in Chapters 3 and 4.

The model presented in this chapter does not include boiling and the analysis will therefore be limited to cases where the fuel solution temperature remains below its saturation temperature.

5.1.1 Point Kinetics Equations and Flux Shape

The fission power density is modelled using Equation 4.2.1 where the void and thermal feedback terms have been adapted to calculate global feedback based on the properties of each reactor section.

The rate of change in the temperature of fuel solution in each section is determined using,

$$\frac{\partial T(t, z)}{\partial t} = \frac{P(t)\psi(t, z)}{M_{sol}(t, z)C_p}, \quad (5.1.1)$$

where $\psi(t, z)$ is a function representing the shape of the neutron flux and the other terms have the same meaning as in Equation 4.2.1. The shape of the flux is determined using the following equation adapted from Cooling et al. (2014a),

$$\psi(t, z) = \frac{f(t, z)}{\int f(t, z)dz}; \quad f(t, z) = \frac{\pi \sin\left(\frac{\pi(z+\delta_b)}{H_{ext}}\right) f_{liq}(t, z)}{H_{ext} \left(\cos\left(\frac{\pi\delta_b}{H_{ext}}\right) - \cos\left(\frac{\pi(\delta_b+H_l)}{H_{ext}}\right) \right)}, \quad (5.1.2)$$

where H_l is the height of the fuel solution surface, δ_b and δ_s are the base and surface extrapolation distances, respectively, $H_{ext} = H_l + \delta_b + \delta_s$ is the cosine period comprising the sum of the fuel solution height and extrapolation distances and f_{liq} is the local non-void fraction. The latter term has been added to the original equation from Cooling et al. (2014a) to account for the local reduction in fission rate due to the appearance of radiolytic gas voids. The thermal feedback is evaluated using the mass-weighted average solution temperature,

$$R_{\$,T}(t) = \alpha_T (T_{Av}(t) - T_0), \quad (5.1.3)$$

where T_0 is a reference temperature where $R_{\$,T} = 0$ and the mass-weighted average solution temperature is evaluated using,

$$T_{Av}(t) = \frac{1}{M_{sol}(t)} \sum_z M_{sol}(t, z) T(t, z), \quad (5.1.4)$$

where $M_{sol}(t)$ is the total mass of the fuel solution and $M_{sol}(t, z)$ therefore represents the mass of fuel solution in a discretised volume. Void feedback is evaluated as the sum of feedback contributions from each section of the solution,

$$R_{\$,V}(t) = \sum_z \alpha_V(z) V_{RG}(t, z), \quad (5.1.5)$$

where α_V is the void feedback coefficient and may be a constant or a function of z .

5.1.2 Vertical Discretisation

The model has vertical discretisation to permit a 1D representation of the physical processes important in determining the degree of reactivity feedback. The discretisation works by dividing the fuel solution

into disk-shaped sections of equal mass at the start of the simulation.

The vertical discretisation uses a Lagrangian scheme in which the height and volume of each section is allowed to vary as the fuel solution expands and contracts due to thermal expansion and the appearance of voids. This approach differs from the Eulerian discretisation scheme used in Cooling (2014) where the entire reactor is divided into disk-shaped sections of equal volume and fuel solution is transferred from one section to the next, keeping the volume of each section constant while the fuel solution expands and contracts.

An advantage of Lagrangian discretisation over Eulerian schemes is that the expansion and contraction of each region is fully characterised by the system of ODEs. Conversely, the region size in Eulerian schemes is assumed fixed for each step of the ODE solver, requiring an adjustment to be made where material is redistributed between the regions. This leads to a discretisation error that cannot easily be controlled by the ODE solver and may create a need for small time steps when the solution is rapidly expanding or contracting.

One dimensional vertical discretisation is required as a minimum to capture the saturation of the fuel solution, as regions closer to the centre of the solution (where fission density is highest) saturate first, leading to a saturation front which expands outwards until the consumption of gas by growing bubbles exceeds the rate at which new gas is deposited in the solution by radiolysis.

5.1.3 Bubble Population and Size

The population of bubbles is determined using the equations derived in Chapter 4. Only stable (growing) bubbles are considered, since the results of the numerical model in Chapter 4 indicated that bubbles collapse rapidly once the process of collapse has started, meaning that collapsing bubbles have relatively little influence on the total voidage of the system.

The number of stable bubbles in each section of fuel solution is influenced by the stabilisation and growth of fission track bubbles, mixing within the solution and advection. The collapse of bubbles due to diffusion was a process highlighted by the numerical simulation and Equation 4.3.26 was proposed in Chapter 4 as a means to predict this effect. However, preliminary analysis of criticality excursions in the CRAC, SILENE and TRACY reactors indicates that the extremely high number density of bubbles required for collapse due to diffusion will not occur. The total rate of change in the number of bubbles in a given section at time t is therefore given by,

$$\frac{\partial N_b(t, z)}{\partial t} = \left[\frac{\partial N_b(t, z)}{\partial t} \right]_{\text{stabilisation}} + \left[\frac{\partial N_b(t, z)}{\partial t} \right]_{\text{mixing}} + \left[\frac{\partial N_b(t, z)}{\partial t} \right]_{\text{advection}}. \quad (5.1.6)$$

Bubble break-up and coalescence are not thought to have a significant effect on the number of bubbles in the solution for transients without boiling. The reasons for this are discussed in Section 5.1.3.3.

5.1.3.1 Stable Bubble Formation

Bubbles are continuously added to the solution by radiolysis, in which tiny bubbles are deposited along the tracks of fission fragments travelling through the fuel solution at high velocity (see Chapter 3). These bubbles usually collapse in a time period on the order of microseconds but a proportion of them will be stabilised (and grow to larger size) whenever the local concentration exceeds the critical concentration. The model determines the critical concentration from the local temperature and radiolytic gas generation coefficient (using Equations 3.3.1 and 3.3.7). These parameters affect the size of the largest fission track bubbles and therefore the dissolved gas concentration required to allow these bubbles to grow.

When the local concentration exceeds the critical concentration in a given section of the fuel solution, the model adds stable bubbles to that section of the solution at a rate determined by Equation 4.3.15. The equation is differentiated so that it can be incorporated into the full set of coupled ODEs:

$$\left[\frac{N_b(t)}{V} \right]_{\text{stabilisation}} = k_f \left(\frac{E(t) - E(t_{sat})}{V} \right)^\alpha, \quad (5.1.7)$$

$$\left[\frac{\partial N_b(t, z)}{\partial t} \right]_{\text{stabilisation}} = \alpha V(t, z)^{(1-\alpha)} k_f (E(t, z) - E(t_{sat}, z))^{(\alpha-1)} P(t, z), \quad (5.1.8)$$

where $k_f = 0.05$, $\alpha = 2.5$, $E(t, z)$ is the total fission energy deposited at time t and height z in the fuel solution, $E(t_{sat}, z)$ is the value of $E(t, z)$ at the moment the concentration of dissolved gas in that region exceeded the critical concentration. $P(t, z)$ is the fission power density at time t and height z within the fuel solution. Equation 5.1.8 is only applied while the local concentration of dissolved hydrogen in the fuel solution exceeds the critical concentration.

5.1.3.2 Mixing and Advection

The rates of change due to mixing and advection are calculated in the manner described in Cooling et al. (2014a) for calculating the effect of mixing and advection on the composition of each discretised portion of the fuel solution. In Cooling's model, the number of bubbles was not a variable tracked by the ODE solver, however the equations are easily adapted to the mixing and advection of bubbles.

The mixing term is given by,

$$\left[\frac{\partial N_b(t, z)}{\partial t} \right]_{\text{mixing}} = D_{FS} \frac{\partial^2 N_b(t, z)}{\partial z^2}, \quad (5.1.9)$$

where D_{FS} is a mixing coefficient corresponding to the rate of mixing between adjacent sections of the fuel solution. The advection term is given by,

$$\left[\frac{\partial N_b(t, z)}{\partial t} \right]_{\text{advection}} = -v_b(t, z) \frac{\partial N_b(t, z)}{\partial z}, \quad (5.1.10)$$

where $v_b(t, z)$ is the velocity of bubbles in a given section of fuel solution at time t . The bubble velocity is determined from its radius using the correlations of Celata et al. (2007) as presented in Cooling et al. (2014a).

Bubble sizes are treated as uniform within each section of the fuel solution. The size of bubbles in each section is determined by calculating the number of moles of gas per bubble, then determining the bubble size using Equation 4.2.10. Treating all bubbles within a single section as having the same size is not without physical justification, since bubbles in close proximity to each other will tend to exchange gas by diffusion. This will result in all bubbles in the local region tending towards a radius where the partial pressure of gas inside the bubbles is in equilibrium with the local dissolved gas concentration.

5.1.3.3 Break Up and Coalescence

Bubble break-up would influence the behaviour of radiolytic gas in a fissile solution by increasing the number of bubbles in the system and reducing the average bubble size. Bubble coalescence would influence the behaviour of radiolytic gas by having precisely the opposite effect. Krepper et al. (2008) use the models of Prince and Blanch (1990) to predict the rates of bubble break-up and coalescence in their model of bubbles for multiphase polydispersed flow in pipes. They note that bubble break-up tends to occur close to the edge of the pipe, where there is a significant differential in the superficial velocity of the fluid with respect to the radial direction. The velocity differential creates a shear stress across the bubble, providing the force necessary for break-up.

To predict the rate of bubble break-up with accuracy would require a model of the turbulent flow of the fuel solution so that shear rates that promote bubble break up could be evaluated. This type of fluid modelling is not desirable in a criticality safety code of this type since these calculations are expensive and have only a modest effect on the kinetics of the criticality transient. It is therefore not practical to model the rate of bubble break-up precisely, however it is unlikely that significant error is introduced by neglecting this process for a non-boiling fissile liquid. Prince and Blanch (1990)

demonstrated that the rate of bubble break-up increases with increasing bubble size, and that the rate is close to zero for bubbles whose volume is less than 0.01 cm^3 ($r_b \sim 10^{-3} \text{ m}$). Since bubbles even a fraction of this size would advect very quickly (see Figure 4.2.2), they are likely to have left the system before having a reasonable chance of breaking apart.

Bubble coalescence can occur whenever bubbles collide and remain in contact for long enough for the film separating them to break down to a critical thickness. Once this critical thickness is reached, the separating film breaks down and the bubbles coalesce. The rate at which this occurs depends on the collision rate between bubbles and the proportion of collisions leading to coalescence, the latter quantity being known as the collision efficiency. Bubble coalescence is of particular importance for processes in air-sparged columns, where bubbles are injected into a flowing liquid. In these cases, an increase in the liquid flow rate leads to an increase in bubble coalescence due to a corresponding increase in the bubble collision frequency (Prince and Blanch (1990), Marrucci and Nicodemo (1967)). In a fissile solution undergoing a criticality transient, the liquid phase is not flowing, however there will be movement in the fluid due to thermal expansion and the effect of expanding gas voids.

The coalescence of bubbles in the absence of fluid flow was examined by Kim and Lee (1987), who also examined the effect of adding surface active solutes. They found that the presence of surfactant solutes (which reduce the surface tension of the solution) had an inhibiting effect on the rate of breakdown in the film separating the two bubbles. This led to longer coalescence times and the complete inhibition of coalescence at high solute concentrations. Marrucci and Nicodemo (1967) showed that bubble coalescence is also inhibited by the presence of inorganic solutes that increase surface tension.

Both Kim and Lee (1987) and Marrucci and Nicodemo (1967) found that solutes with the greatest influence on surface tension (with the highest $d\sigma_s/dC$) were found to have the greatest inhibiting effect, regardless of whether the effect on surface tension was positive or negative. Uranyl nitrate in aqueous solutions has a positive effect on solution surface tension; the surface tension increases with increasing uranyl nitrate concentration at a rate of approximately $2.9 \times 10^{-3} \text{ N m}^{-1} \text{ mol}^{-1} \text{ m}^3$ (Grant et al. (1948)). This value of $d\sigma_s/dC$ is higher than any of the solutes tested by Marrucci and Nicodemo (1967). The closest solute reported in their data was CuSO_4 with a value $d\sigma_s/dC = 1.83 \times 10^{-3} \text{ N m}^{-1} \text{ mol}^{-1} \text{ m}^3$. In their experiments, CuSO_4 was found to inhibit bubble coalescence completely at a concentration of less than 100 mol m^{-3} in an experiment where the liquid superficial velocity was 0.5 cm s^{-1} . Increasing the liquid superficial velocity would increase the concentration required to completely inhibit bubble coalescence, however in an experiment using KCl (a weaker surface active solute), bubble coalescence was completely inhibited at a concentration of 250 mol m^{-3} , with liquid

superficial velocities up to 1.48 cm s^{-1} .

As with bubble break-up, accurate determination of the rate of bubble coalescence would require a model of turbulent flow within the fuel solution in order to determine the collision frequency between bubbles, and this is not practical for a criticality safety code of the type presented here. However, experimental studies of the effect of solutes on bubble coalescence in aqueous solutions indicate that the relatively large concentrations of uranyl nitrate present in a typical fuel solution would strongly inhibit bubble coalescence.

In the absence of experimental data examining the rates of bubble break-up and coalescence in fuel solutions of uranyl nitrate it is not possible to rule out with complete certainty some influence due to these processes. However, based on the evidence summarised above it seems likely that these processes can be neglected without introducing significant error into the model, due to the relatively small size of bubbles expected to form in non-boiling fissile solutions and the presence of inorganic solutes in high concentration.

5.1.4 Dissolved Gas Production

Hydrogen gas and hydrogen peroxide are produced through the radiolysis reaction (see Equation 4.1.1) and the model adds these directly to the dissolved phase. In reality, hydrogen gas appears first in the gaseous phase as tiny gas bubbles deposited along the tracks of fission fragments, however these gas bubbles collapse extremely rapidly (on a timescale $\sim 10^{-6}$ seconds) at which point the hydrogen gas they contain is added to the dissolved phase.

The rates of hydrogen gas and hydrogen peroxide production are determined from the radiolytic gas generation coefficient as a function of the fission power:

$$\frac{dC_{\text{H}_2(aq)}(t, z)}{dt} = \frac{P(t, z)G_{\text{H}_2}}{V(t, z)}; \quad \frac{dC_{\text{H}_2\text{O}_2(aq)}(t, z)}{dt} = \frac{P(t, z)G_{\text{H}_2\text{O}_2}}{V(t, z)}, \quad (5.1.11)$$

where the radiolytic gas generation coefficient for hydrogen (G_{H_2}) may be estimated using Equation 3.2.26. The generation coefficient for hydrogen peroxide depends on the degree of recombination of the free radical species produced during radiolysis. Its maximum value is equal to the radiolytic gas generation coefficient for hydrogen (Lane et al. (1958)) so these coefficients will be set as equal in the point kinetics model.

Hydrogen peroxide decomposes to produce water and diatomic oxygen. The rate at which this happens is modelled using the following correlation based on data from Lane et al. (1958). It has been

noted by Cooling (2019) that the data of Lane et al. fits an expression of the following form:

$$k_{\text{H}_2\text{O}_2}(t, z) = 1.578 \times 10^{-20} \exp(1.066 \times 10^{-1} T(t, z)), \quad (5.1.12)$$

where the rate of disappearance of H_2O_2 is determined by,

$$\frac{\partial C_{\text{H}_2\text{O}_2(aq)}(t, z)}{\partial t} = -k_{\text{H}_2\text{O}_2}(t, z) C_{\text{H}_2\text{O}_2(aq)}(t, z), \quad (5.1.13)$$

where $C_{\text{H}_2\text{O}_2(aq)}$ is the local concentration of hydrogen peroxide in solution.

The decomposition of hydrogen peroxide is catalysed by a wide range of chemical species which may be present in the solution. The above correlation is a conservative estimate based on the minimum decomposition rates listed in Lane et al. (1958) for the decomposition of hydrogen peroxide in uranyl sulphate. No data has been found in the literature for the rate of thermal decomposition of hydrogen peroxide in uranyl nitrate solutions however experimental data are available for pure water.

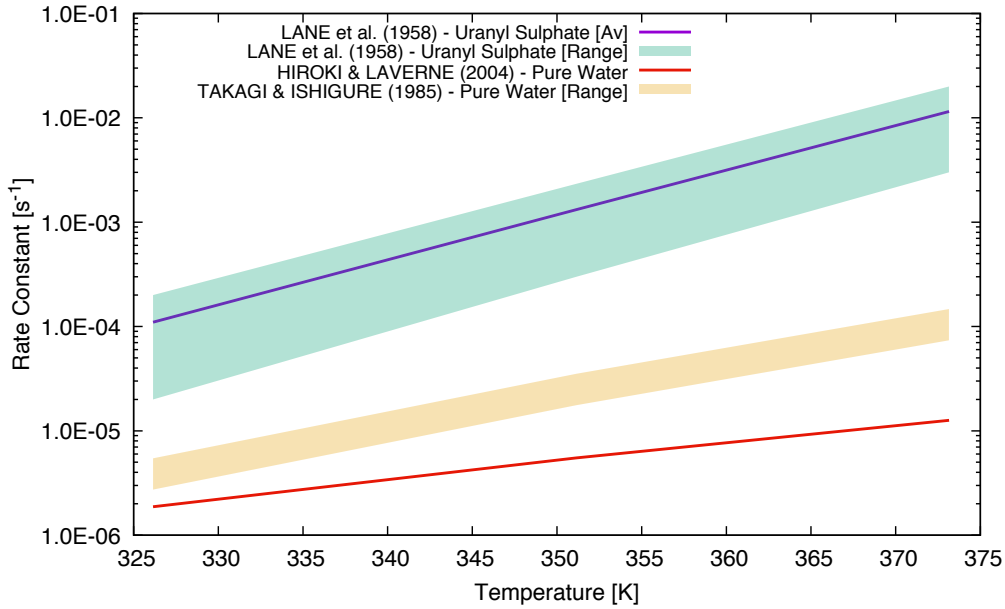
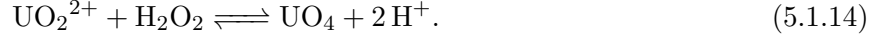


Fig. 5.1.1. Selected rate constants for the decomposition of hydrogen peroxide in pure water and uranyl sulphate solution.

Figure 5.1.1 compares Equation 5.1.12 to the range of maximum and minimum rate constants listed in Lane et al. (1958) for the decomposition of hydrogen peroxide in uranyl sulphate. The figure also shows rate constants experimentally determined by Hiroki and LaVerne (2005) and Takagi and Ishigure (1985) for the decomposition of hydrogen peroxide in pure water. The reason for the range of values from Takagi and Ishigure is that the rate of decomposition is expected to increase from its initial value to a maximum of twice the initial rate once a steady-state concentration of intermediate decomposition products is reached. These data indicate a significant degree of uncertainty in predicting

the rate of decomposition of hydrogen peroxide and confirm that solutes present in solutions of uranyl sulphate act as a catalyst for this process.

One route via which the presence of uranyl sulphate solution may catalyse the decomposition of hydrogen peroxide is by the following reaction noted by Lane et al. (1958):



The presence of the uranyl ion provides a decomposition route with reduced activation energy compared to uncatalysed thermal decomposition. If this is the reason for the rapid decomposition of hydrogen peroxide in uranyl sulphate then the same effect would be expected for solutions of uranyl nitrate. For this reason, Equation 5.1.12 which is based on the decomposition rate for hydrogen peroxide in uranyl sulphate solution, will be used to model the rate of hydrogen peroxide decomposition in the point kinetics model.

5.1.5 Dissolved Gas Mass Transfer

It was shown in Chapter 4 that the rate of mass transfer of dissolved gas from the dissolved phase into the gaseous phases is determined by the number of bubbles available per unit volume of fuel solution. This is because dissolved gas must diffuse towards bubbles where it can come out of solution at the bubble interface, and the time required for diffusion is the rate-limiting step in this process.

The rate of appearance of gas will be modelled using the following equation adapted from Equation 4.3.30 in the previous chapter,

$$\frac{\partial C_{i,(aq)}(t, z)}{\partial t} = -\alpha_c(t, z) (C_{i,(aq)}(t, z) - C_{i,\text{eq}}(t, z)), \quad (5.1.15)$$

where $C_{i,\text{eq}}$ is determined from:

$$C_{i,\text{eq}}(t, z) = y_i(t, z) \left(P_l + \frac{2\sigma_s(t, z)}{r_b(t, z)} \right) H_{i,\text{sol}}(t, z), \quad (5.1.16)$$

where y_i is the mole fraction of component i in the gas phase, σ_s is the fuel solution surface tension and $H_{i,\text{sol}}$ is the Henry's law constant for component i in the fuel solution. The local bubble radius $r_b(t, z)$ is determined from the amount of gas present and the number of bubbles using Equation 4.2.10.

This equation is similar to that used in the CRITEX code (Barbry et al. (nd)) to model the rate of appearance of radiolytic gas, except that in CRITEX the rate constant is a user-specified constant, whereas the constant α_c is time-dependent and evaluated as a function of the local bubble number

density using an equation based on Equation 4.3.32 from the previous chapter.

$$\alpha_c(t, z) = 1.9436 \times 10^{-6} \left(\frac{N_b(t, z)}{V(t, z)} \right)^{0.78926} D_{FS}^{0.5} \quad (5.1.17)$$

Equation 5.1.17 has been modified from Equation 4.3.32 to adjust the mass transfer rate to account for the rate of convective mass transport within the solution. The adjustment is necessary because the numerical simulation of Chapter 4 included mass transport by gaseous diffusion only, whereas a model of a full-scale solution must account for convection. In the current model, this is achieved through the mixing coefficient, D_{FS} (see Section 5.1.9).

Applying two-film theory (see Equation 4.2.11) it can be shown that the mass transfer parameter α_c is related to the interface mass transfer coefficient (k_D) as follows:

$$\alpha_c \equiv \frac{k_D A_b}{V}, \quad (5.1.18)$$

where A_b/V is the interfacial area concentration.

The interfacial area concentration is unaffected by the rate of mass transport of dissolved gas within the solution. However, Equation 4.2.12 predicts that the interface mass transfer coefficient is affected by this parameter, and that in cases where $\sqrt{\pi D_i (r_b/v_b)} \gg r_b$ (i.e. $r_b > 10^{-6}$), the interface mass transfer coefficient will vary with the square root of the diffusion coefficient: $k_D \sim f(D_i^{0.5})$.

An appropriate adjustment to Equation 4.3.32 can therefore be made by multiplying by $(D_{FS}/D_{NS})^{0.5}$ where D_{NS} is the diffusion coefficient applied in the numerical simulation of Chapter 4. The value of D_{NS} was temperature-dependent and therefore varied from one simulation to another, however the average value was approximately $1 \times 10^{-8} \text{ m}^2 \text{ s}^{-1}$. Multiplying Equation 4.3.32 by this correction factor results in Equation 5.1.17 as shown above.

5.1.6 Critical Concentration with Multiple Dissolved Gases

The critical concentration of dissolved gas in a fissile solution has been defined in previous chapters as the concentration at which dissolved gas can come out of solution at the available nucleation sites. While this is true at the macroscopic scale, a definition which more accurately describes the critical concentration at a microscopic scale is the concentration of dissolved gas at which there is zero net flow between the dissolved and gaseous phases at the available nucleation sites.

For a fuel solution containing only a single dissolved gas (e.g. hydrogen), the net flow of gas

between the dissolved and gaseous phases is given by:

$$\frac{dC_{\text{H}_2(aq)}}{dt} = -\alpha_c \left[C_{\text{H}_2(aq)} - \left(P_l + \frac{2\sigma_s}{r_{\text{nucl}}} \right) H_{\text{H}_2,\text{sol}} \right], \quad (5.1.19)$$

where the first term on the right-hand side is the concentration of dissolved gas in the aqueous phase and the second term is the equilibrium concentration, given by the product of the partial pressure of the gas inside a radiolytic gas bubble and the Henry's law constant characterising the solubility of that gas in the fuel solution. The parameter r_{nucl} is the maximum size of fission track bubbles, to be determined from Equation 3.3.6.

In the case of zero net flow between the dissolved and gaseous phases, Equation 5.1.19 can be set to zero and rearranged to give the critical concentration of dissolved gas:

$$C_{\text{H}_2\text{crit}} = C_{\text{crit}} = \left(P_l + \frac{2\sigma_s}{r_{\text{nucl}}} \right) H_{\text{H}_2,\text{sol}}. \quad (5.1.20)$$

The situation is similar if there are multiple gases present. The critical concentration still occurs when there is zero net flow of gas between the dissolved and gaseous phases.

$$\sum_i \frac{dC_{i(aq)}}{dt} = -\alpha_c \left[\sum_i C_{i(aq)} - \left(P_l + \frac{2\sigma_s}{r_{\text{nucl}}} \right) \sum_i H_{i,\text{sol}} y_i \right] = 0, \quad (5.1.21)$$

where i represents all the dissolved gases present (H_2 , O_2 , etc.), $H_{i,\text{sol}}$ is the Henry's law constant of component i in the fuel solution and y_i is the mole fraction of component i in the gas phase.

Rearranging this equation for the critical concentration of dissolved hydrogen results in the following expression for a solution containing multiple dissolved gases:

$$C_{\text{crit}} = \left(P_l + \frac{2\sigma_s}{r_{\text{nucl}}} \right) \sum_i H_{i,\text{sol}} y_i - \sum_j C_{j(aq)}; \quad j \neq \text{H}_2, \quad (5.1.22)$$

where i represents all the dissolved gases present and j represents all dissolved gases present except hydrogen. Since fission track bubbles contain (almost) no gases other than hydrogen, Equation 5.1.22 can be further simplified:

$$C_{\text{crit}} = \left(P_l + \frac{2\sigma_s}{r_{\text{nucl}}} \right) H_{\text{H}_2,\text{sol}} - \sum_j C_{j(aq)}; \quad j \neq \text{H}_2. \quad (5.1.23)$$

Equation 5.1.22 shows that the presence of other dissolved gases in the fuel solution can reduce the critical concentration. This is because the fission track bubbles consist of almost pure hydrogen gas with only a negligible amount of other gases. The partial pressure of gases other than hydrogen inside the radiolytic gas bubbles is therefore very low, which makes it easy for these gases to diffuse into the bubbles, even if they are only present at low concentrations in the fuel solution. While other gases

diffuse into the bubbles, hydrogen gas diffuses out and dissolves into the fuel solution. The critical concentration is the concentration at which the net flow of these gases between the bubble and the solution is zero.

5.1.7 Bubble Velocity

Bubbles formed within the fuel solution will begin to advect upwards due to their buoyancy. Cooling et al. (2014b) used the model of Celata et al. (2007) to predict the velocity of bubble advection in their model of the medical isotope production reactor (MIPR). In doing so, they assumed that the bubbles formed in the reactor reached their terminal velocity rapidly so that acceleration time could be neglected. Let this assumption be referred to as the “terminal velocity assumption”.

The terminal velocity assumption is expected to result in a very small error since the initial acceleration of the bubbles ($a_0 = 9.81 \text{ m s}^{-2}$) is large compared to the terminal velocity and the acceleration time is therefore expected to be very short. This was confirmed using the equations of Celata et al. (2007) to calculate the net force acting on bubbles of various sizes in order to determine the time taken for these bubbles to reach their terminal velocity.

The buoyancy and drag forces acting on a bubble can be calculated from Equations 4.2.5 and 4.2.7, respectively. In the previous chapter, a simple relation for the value of C_D was applied which assumes that the bubble remains spherical as it moves through the liquid. Initially, this assumption is valid, as surface tension forces act to minimise surface area. However, as the bubble becomes larger in size it starts to deform, an effect which starts to have a significant impact on the net force calculated for bubbles larger than $\sim 1 \times 10^{-5} \text{ m}$ in radius. This effect is captured using the following expression for the drag coefficient. This expression is proposed by Celata et al. (2007) for a fully contaminated solution and was applied by Cooling et al. (2014b) in a model of MIPR:

$$C_D = \max \left(\frac{24 (1 + 0.15 Re_b^{0.687})}{Re_b}, \frac{8}{3} \frac{E_0}{E_0 + 4} \right). \quad (5.1.24)$$

The dimensionless Eötvös number is defined by,

$$E_0 = \frac{4gr_b^2 (\rho_s - \rho_g)}{\sigma_s}, \quad (5.1.25)$$

and represents the ratio of viscous, surface tension and inertial forces acting on the bubble. The gas density is determined from the ideal gas law using:

$$\rho_g = \frac{M_{H_2} P_b}{RT}, \quad (5.1.26)$$

where M_{H_2} is the molecular weight of hydrogen gas, P_b is the pressure inside the bubble and R is the universal gas constant. The acceleration of the bubble can be determined from the above equations using $a = F/m$ as follows:

$$a = \frac{F_{\text{buoyancy}} - F_{\text{drag}}}{m_l}. \quad (5.1.27)$$

The terminal velocity of the bubbles is the velocity at which the net force acting on the bubble is zero. This can therefore be determined by finding the velocity at which the buoyancy and drag forces are equal,

$$\frac{4}{3}\pi r_b^3 \rho_s g - \frac{\rho_s v_b^2 C_D \pi r_b^2}{2} = 0. \quad (5.1.28)$$

This expression is solved in the point kinetics model using a Newton-Raphson algorithm.

When the model is run using Equation 5.1.27 to determine the velocity of bubbles it results in a very high degree of stiffness in the system of ODEs. This is due to the very large initial acceleration rate of the bubbles. It is therefore desirable to use the terminal velocity assumption and calculate bubble velocities instead using Equation 5.1.28 provided the error introduced is acceptable.

Figure 5.1.2 shows the rates of acceleration over time, calculated by solving Equation 5.1.27 using the forwards Euler method, for a range of bubbles sizes in an aqueous solution containing 932 mol m⁻³ of uranyl nitrate at 298 K and atmospheric pressure.

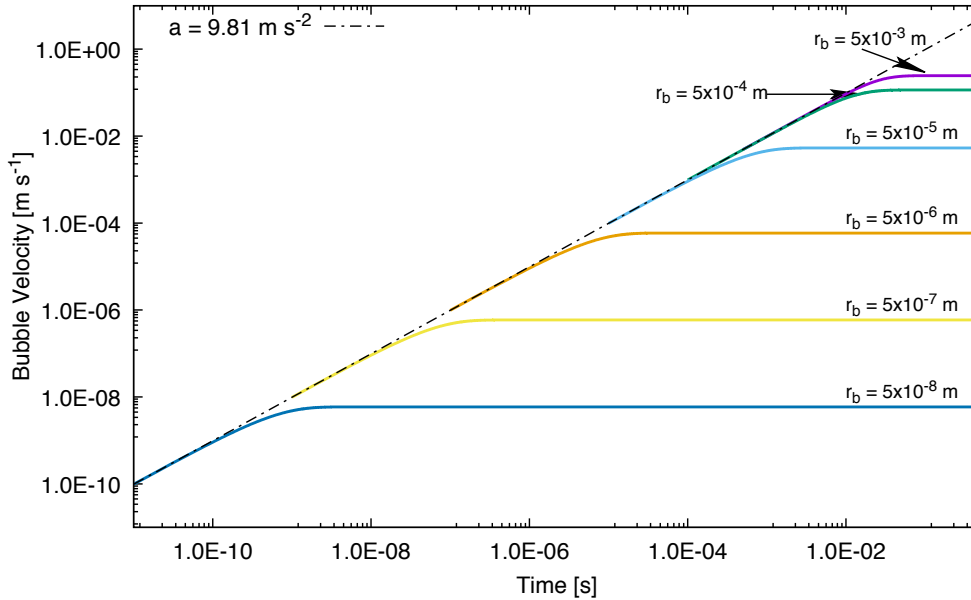


Fig. 5.1.2. Acceleration rate of bubbles as a function of time for bubbles of various radii in uranyl nitrate solution at 298 K. Values calculated using Equation 5.1.27.

Figure 5.1.2 shows that the time to reach terminal velocity increases with the size of the bubble. The error inherent in the terminal velocity assumption also increases with the acceleration time since

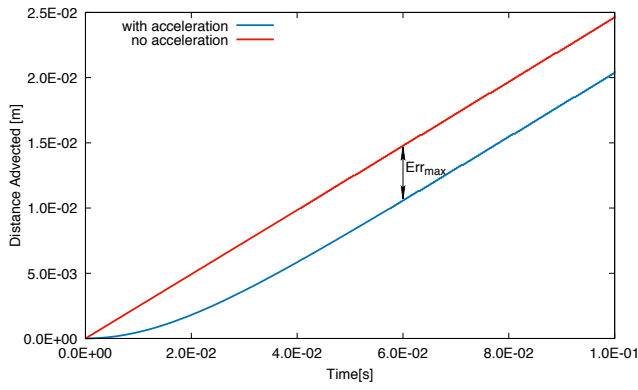


Fig. 5.1.3. Error resulting from the use of the terminal velocity assumption in the case of a radiolytic gas bubble with radius 5×10^{-3} m in uranyl nitrate solution of concentration 932 mol m^{-3} at 298 K.

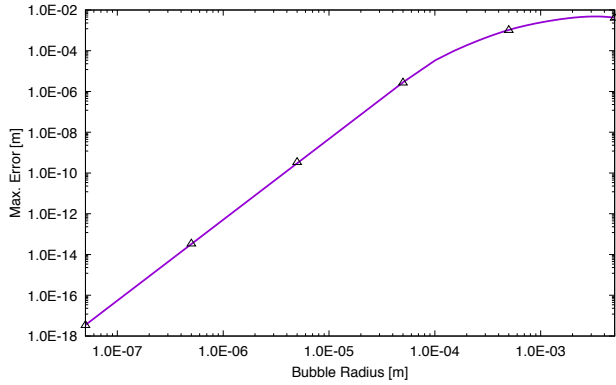


Fig. 5.1.4. Maximum error resulting from the use of the terminal velocity assumption for bubbles of different sizes in uranyl nitrate solution of concentration 932 mol m^{-3} at 298 K.

the error arises from the fact that the velocity of the bubble is overestimated during the period of acceleration. One measure of the error is the difference in the calculated distances advected by the two methods. This value reaches a maximum once the bubble reaches terminal velocity, as shown in Figure 5.1.3.

For newly formed radiolytic gas bubbles measuring approximately 5×10^{-8} m in radius, the calculated terminal velocity is $5.9 \times 10^{-9} \text{ m s}^{-1}$ and bubbles are predicted to reach 95% of this velocity in less than 2×10^{-9} s. In this case, the acceleration time is extremely short and no appreciable error is expected to result from the use of the terminal velocity assumption. However, the error increases for larger bubbles with longer acceleration times.

Figure 5.1.4 shows how the maximum error in the predicted displacement, due to the terminal velocity assumption, varies for bubbles of different sizes in uranyl nitrate solution. The error is shown to increase with increasing bubble size. The increase in the maximum error begins to slow for bubbles with radius $> 5 \times 10^{-4}$ m. This is because the increase in the terminal velocity with increasing bubble size also slows at this point due to the effects of bubble deformation.

Given the computational advantages of using the terminal velocity assumption, and the small size of the error introduced by this assumption, the point kinetics model will use this assumption when calculating the velocities and distances advected by bubbles in the fuel solution.

5.1.8 Heat Loss

The temperature of a fissile solution during a criticality transient depends on the balance of fission energy added to the solution and heat lost to the reactor materials and surroundings. A high rate of heat loss will tend to increase the intensity of the transient by reducing the solution temperature and reducing the amount of thermal feedback.

Later in this chapter, the point kinetics code will be validated against experimental results from the aqueous homogeneous reactors CRAC, SILENE and TRACY. The heat loss processes examined in this section will therefore focus on those which are likely to be significant for these reactors. The sensitivity of transient characteristics to the rate of heat transfer between the solution and its surroundings is relatively modest. Furthermore, exact environmental conditions that may effect the rate of heat transfer are not known in most cases, e.g. the rate of air circulation within the room surrounding the vessel. A rigorous model of heat transfer is therefore not justified for the purposes of the present study. Instead, the following section seeks to obtain a reasonable order of magnitude estimate for the relevant heat transfer coefficients.

5.1.8.1 From the Reactor to the Surroundings

Heat is lost from the external surfaces of an aqueous homogeneous reactor by radiation and natural convection. The maximum rate of heat loss due to radiation can be evaluated by modelling the reactor as a black body, i.e. a perfect absorber and emitter of energy by radiation.

Coulson et al. (1996) describes how the rate of black body radiation can be determined as a function of temperature using the Stefan-Boltzmann equation:

$$E_b = \sigma_{S-B} T^4, \quad (5.1.29)$$

where E_b is the energy emitted per unit area, $\sigma_{S-B} = 5.67 \times 10^{-8} \text{ W m}^{-2} \text{ K}^{-4}$ is the Stefan-Boltzmann constant and T is the temperature of the radiating body. Assuming that the radiation emitted by the reactor at ambient temperature was balanced by the radiation it absorbed, Equation 5.1.29 can be modified to estimate the net increase in radiative heat loss as the temperature of the reactor vessel rises:

$$E_b = \sigma_{S-B} (T_{\text{vessel}}^4 - T_0^4). \quad (5.1.30)$$

The maximum surface temperature for an aqueous homogeneous reactor operating at atmospheric pressure is limited by the boiling point of water. The maximum rate of heat loss due to radiation can therefore be determined by evaluating Equation 5.1.30 at 100°C and an ambient temperature of 20°C.

This gives a maximum heat flux of 680 W m^{-2} .

The radiative heat loss from a black body can be used to estimate the radiative heat loss from a real object by multiplying by the emissivity. The emissivity ($0 < e < 1$) gives the ratio of radiative heat transfer from a real surface to that from an idealised black body surface. Typical emissivity values are given by Coulson et al. (1996) with a value of 0.657 listed for sheet steel. Multiplying the heat flux calculated above by this value for the emissivity of steel results in a maximum heat flux of 447 W m^{-2} at the external reactor surface.

The rate of heat loss due to natural convection from the reactor surfaces can be estimated using an equation of the form:

$$Nu = f(Gr, Pr), \quad (5.1.31)$$

where $Nu = hL/k$ is the Nusselt number, $Gr = \beta g \Delta T l^3 \rho_s^2 / \mu^2$ is the Grashof number and $Pr = C_p \mu / k$ is the Prandtl number. In the definitions of these groups, h is the convective heat transfer coefficient (HTC), l is the characteristic length (e.g. material thickness), k is thermal conductivity, β is the thermal coefficient of expansion and all other symbols are as previously defined.

Evaluating the Grashof number at the external surface of a typical aqueous homogeneous reactor yields a value of 1.1×10^{10} based on a reactor height of 1 m, air of density 1.225 kg m^{-3} and viscosity $1.85 \times 10^{-5} \text{ Pa s}$, an air temperature of 298 K and a surface temperature of 373 K. Evaluating the Prandtl number for typical properties of air gives a value of 0.63, based on a heat capacity of $1008 \text{ J kg}^{-1} \text{ K}^{-1}$, a thermal conductivity of $0.0297 \text{ W m}^{-1} \text{ K}^{-1}$ and the same viscosity as above.

A review of experimental studies in the field of convective heat transfer was conducted by Coulson et al. (1996), who recommended the following Equation by Hiroharu et al. (1968) for vertical cylinders where $Gr > 10^9$:

$$Nu = 0.138 Gr^{0.36} (Pr^{0.175} - 0.55). \quad (5.1.32)$$

This equation gives a convective HTC, $h_{\text{ext}} = 6.29 \text{ W m}^{-2} \text{ K}^{-1}$ for the typical Grashof and Prandtl numbers calculated above. At a reactor temperature of 100°C and an ambient temperature of 20°C this amounts to a heat transfer rate of 503 W m^{-2} . The rate of heat loss due to natural convection is therefore on a similar scale to the expected rate of radiative heat loss.

5.1.8.2 From the Fuel Solution to the Reactor Vessel

Heat generated in the fuel solution is transferred to the reactor vessel walls by convective heat transfer. The convective HTC characterises the rate of this process and depends on many factors, in particular

the speed of any circulating currents within the solution. The HTC can be estimated using correlations based on experimental data. A very large number of correlations have been developed over the years for estimating the convective HTC for different systems. None of these correlations apply directly to the case of an aqueous homogeneous reactor, however it is possible to estimate the HTC for the current model based on similarities to systems for which a heat transfer correlation has been determined.

A correlation by Evans and Stefany (Equation 5.1.33) was used by Pérez et al. (2015) to model the HTC due to natural convection in the aqueous homogeneous reactor ARGUS. Natural convection results from differences in fluid density that occur when a fluid is subject to a temperature gradient. Warmer, less dense fluid rises to the top of the vessel, displacing cooler fluid and setting up a current which keeps the fluid circulating. To assume that convective heat transfer within a fissile solution reactor is entirely due to natural convection is likely to underestimate the true rate of heat transfer but provides a good indication of the minimum possible value for the HTC.

$$Nu_D = \frac{hD}{k} = 0.55 (Gr_L Pr)^{1/4} \quad (5.1.33)$$

The HTC due to natural convection is a function of the liquid level in the vessel, since higher liquid levels are conducive to the formation of stronger convection currents. The values predicted using Equation 5.1.33 are shown in Figure 5.1.5. The HTC depends on the temperature difference between the bulk solution and the vessel wall. The figure shows estimated HTCs due to natural convection for temperature differences of 10 K and 75 K.

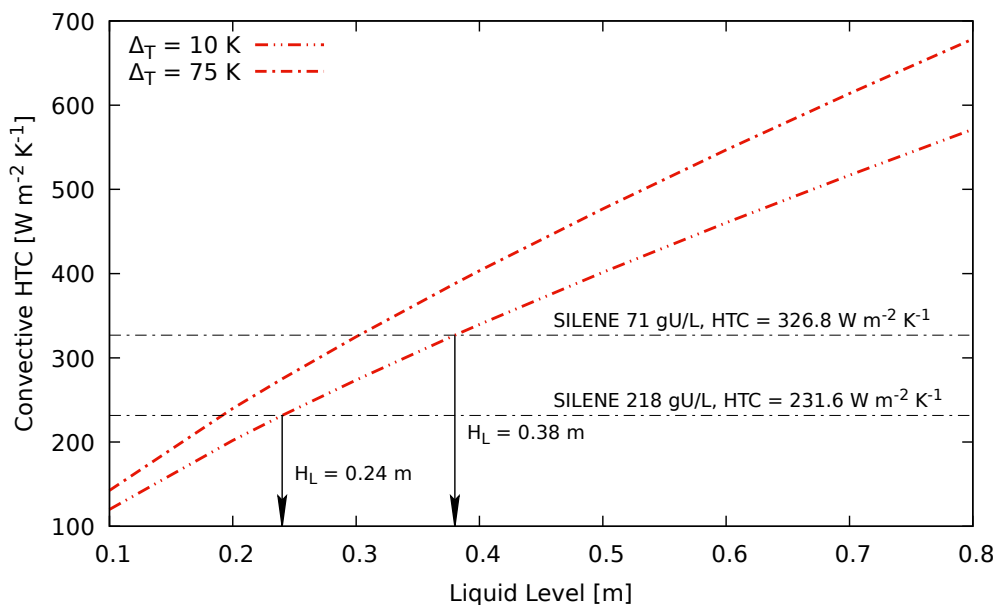


Fig. 5.1.5. Convective heat transfer coefficients for heat transfer between the fuel solution and the vessel wall, calculated using Equation 5.1.33.

Figure 5.1.5 indicates that the heat transfer coefficient between the fuel solution and the vessel walls due to natural convection alone (h_{int}) would be $232 \text{ W m}^{-2} \text{ K}^{-1}$ for a reactor similar to SILENE with a liquid depth of 0.24 m (as in the 218 gU/L configuration) or $337 \text{ W m}^{-2} \text{ K}^{-1}$ for a liquid depth of 0.38 m (as in the 71 gU/L configuration) for a temperature difference of 10 K.

In an aqueous homogeneous reactor it is likely that the degree of agitation will be significantly greater than that due to natural convection, particularly in transients involving the appearance and rapid expansion of radiolytic gas bubbles. In their CFD model of the ARGUS reactor, Pérez et al. (2015) modelled the average fluid velocity with and without accounting for the appearance of radiolytic gas voids. They determined an average fluid velocity of 0.016 m s^{-1} in the absence of gas voids and 0.104 m s^{-1} when gas voids were included. Using these velocities to calculate the Richardson number (Ri) for the fuel solution gives an indication of the relative importance of forced and natural convection in the heat transfer characteristics of the system. The Richardson number is discussed by Laguerre et al. (2017) who note that a value $Ri < 0.1$ indicates that forced convection is dominant, a value $Ri > 10$ indicates that natural convection is dominant, and an intermediate value indicates that both forced and natural convection are significant.

$$Ri = \frac{Gr}{Re^2} \quad (5.1.34)$$

Calculating the Richardson number for the fluid velocities above gives $Ri = 38.7$ for the fluid velocity without gas voids and $Ri = 0.92$ for the fluid velocity with gas voids. These results indicate that natural convection is dominant up to the point at which gas voids appear, after which a combination of natural and forced convection contribute to the heat transfer between the solution and the vessel wall.

An indication of the influence of forced convection on the HTC in an aqueous homogeneous reactor can be gained by considering heat transfer correlations for an agitated vessel with a cooling jacket. The following correlation is proposed by Chilton et al. (1944):

$$Nu \left(\frac{\mu_s}{\mu} \right)^{0.14} = 0.36 Ro^{0.67} Pr^{0.33}, \quad (5.1.35)$$

where $Ro = L^2 N \rho_s / \mu$ is the Roshko number, L is the length of the impeller blade and N is the vortex shedding rate, equivalent to the number of revolutions per second made by the impeller. Using Equation 5.1.35 it is possible to predict the change in the convective HTC as a function of the agitation in the liquid. Figure 5.1.6 shows the calculated HTCs as a function of the impeller revolution rate and impeller size relative to the reaction vessel diameter. The calculated values are for a cylindrical vessel of radius 0.176 m, which was chosen because a circle of this radius has the same area as an annulus

with internal and external radii equal to those of the annular SILENE reactor.

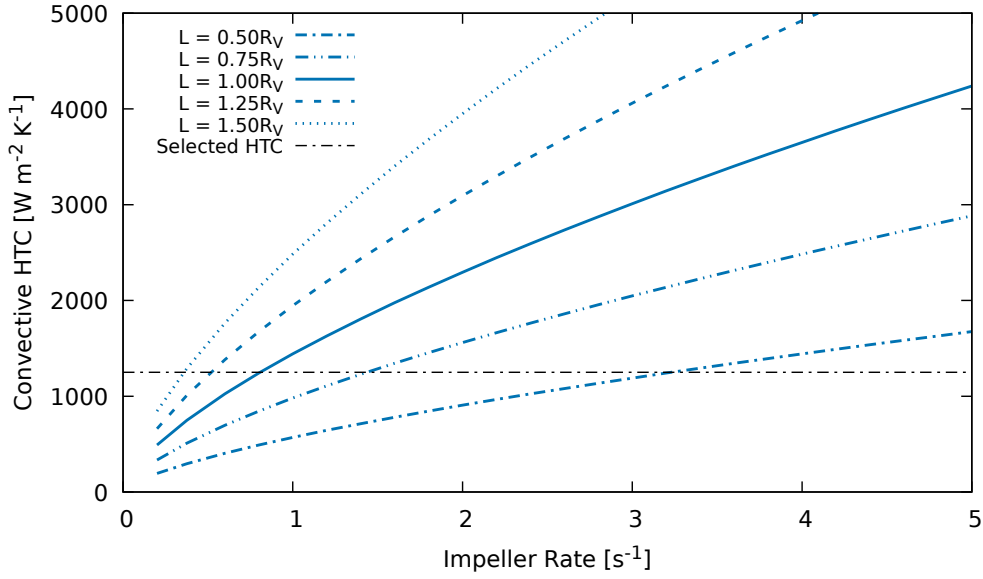


Fig. 5.1.6. Convective heat transfer coefficients for heat transfer between the fuel solution and the vessel wall, calculated using Equation 5.1.35 for stirred reactor vessels with cooling jackets.

Figure 5.1.6 shows that the degree of agitation in the reactor vessel strongly influences the heat transfer coefficient between the fluid and the vessel wall. The degree of agitation in the fuel solution is likely to vary significantly during the course of a transient, due to spikes in the fission rate leading to sudden expansion of the fluid, and the appearance of bubbles which agitate the solution as they expand and advect.

Without the use of a coupled CFD code it is not feasible to model the variation with time in the HTC. Instead an average value will be selected corresponding to a relatively low impeller speed. Figure 5.1.6 shows a selected value h_{int} of $1250 \text{ W m}^{-2} \text{ K}^{-1}$. This value would be expected for a stirred tank containing a relative large impeller ($L=1.5R_V$) turning at a very slow pace $\sim 0.3 \text{ s}^{-1}$, or alternatively a small impeller ($L=0.5R_V$) turning at a faster pace $\sim 3.2 \text{ s}^{-1}$. These agitation rates correspond to average impeller blade velocities of 0.12 m s^{-1} and 0.44 m s^{-1} , respectively, which is of the same order of magnitude as the fluid velocity predicted by the CFD model of Pérez et al. (2015) for systems containing gas bubbles.

5.1.8.3 From the Fuel Solution Surface to the Plenum Gas

A study by Laguerre et al. (2017) examined the heat transfer coefficient between the liquid surface of a hot drink and the surrounding air. In some respects this system is similar to situation at the fuel solution surface in an aqueous homogeneous reactor, in particular the geometries and temperature

concerned are very similar. Laguerre et al. examined correlations for the liquid/air HTC in a system where air flows over and around a cylindrical object. They also examined correlations for a flat plate which is cooled by the air above it.

The same question exists with regards to the HTC at the solution surface as to whether the heat transfer is driven by natural or forced convection. Aqueous homogeneous reactors must be equipped with gas removal systems to prevent an explosive mixture of hydrogen and oxygen forming over in the plenum gas. There must therefore be some degree of forced convection as air is removed from the plenum and treated before returning to the reactor. However, no information on the gas removal rate could be found for the CRAC, SILENE or TRACY reactors. Instead, a sensitivity study will be carried out to determine the potential influence of the plenum gas velocity on the surface heat transfer coefficient.

Laguerre et al. (2017) use two correlations from Incropera and DeWitt (1996) to determine the heat transfer coefficient due to natural and forced convection in the laminar flow regime. Both correlations treat the surface of the liquid as a flat plate. The correlation for natural convection is as follows:

$$Nu_L = 0.54 (Gr_L Pr_L)^{1/4}; \quad \text{for } 10^4 < Gr_L Pr_L < 10^7, \quad (5.1.36)$$

where the characteristic length L in this case is the area of the flat surface divided by its perimeter. The product of the Grashof and Prandtl numbers for the surface of a reactor similar to SILENE was found to be 5.7×10^6 , within the range of validity of Equation 5.1.36. The HTC using this correlation was evaluated at $7.80 \text{ W m}^{-2} \text{ K}^{-1}$.

The correlation for forced convection is as follows:

$$Nu_L = 0.664 Re_L^{1/2} Pr_L^{1/3}; \quad \text{for } Re_L \leq 2500. \quad (5.1.37)$$

The surface HTC resulting from Equation 5.1.37 is plotted in Figure 5.1.7 for a range of gas velocities and Reynolds numbers up to 2500. The results indicate that the HTC due to forced convection is not substantially greater than the HTC due to natural convection, even at gas velocities of 45 cm s^{-1} . The model will therefore use the value calculated above for heat transfer due to natural convection.

The value discussed above was the HTC for heat transfer between the fuel solution surface and the plenum gas. Calculating the overall rate of heat transfer between the fuel solution and the plenum gas requires the overall HTC (U_{surface}) which accounts for the resistance to heat transfer from the solution bulk to the surface and the resistance to heat transfer from the solution surface to the gas.

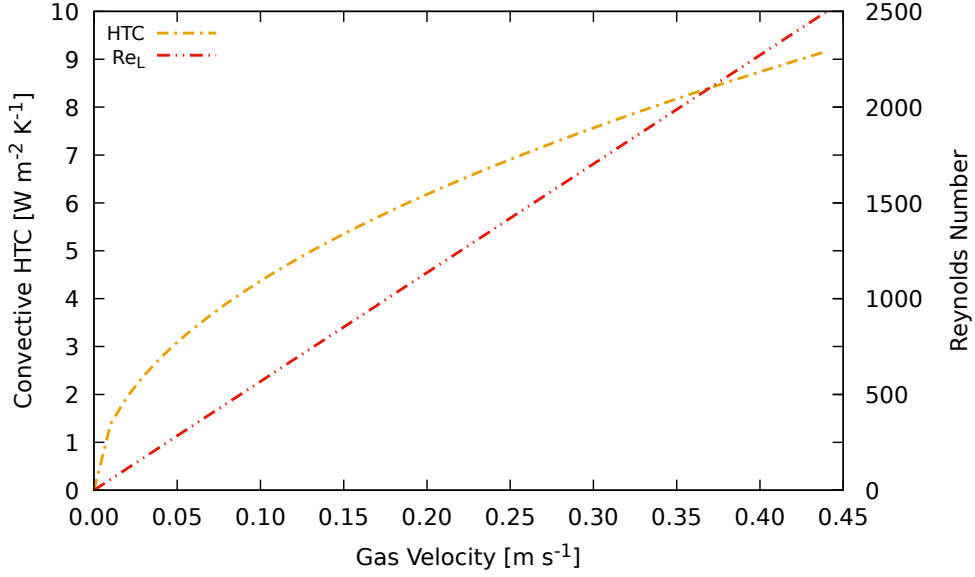


Fig. 5.1.7. Convective heat transfer coefficients for heat transfer between the surface of the fuel solution and the plenum gas, calculated using Equation 5.1.37 based on heat transfer to the air from a flat plate.

The overall HTC is evaluated as follows:

$$\frac{1}{U_{\text{surface}}} = \frac{1}{h_{\text{int}}} + \frac{1}{h_{\text{surface}}}, \quad (5.1.38)$$

where h_{int} is the HTC between the liquid bulk and the surface.

The value of h_{int} will be close to the HTC calculated in Section 5.1.8.2. Using this value to determine the overall heat transfer coefficient results in $U_{\text{surface}} = 7.75 \text{ W m}^{-2} \text{ K}^{-1}$.

5.1.9 Mixing

The simulation uses the mixing model described in Cooling (2014) with some adaptations to account for the Lagrangian discretisation scheme used in this point kinetics code, and also to permit the movement of bubbles between discretised slices of the fuel solution due to mixing. The equations for mixing are included in the summary of equations given in Section 5.1.13.

The rate of mixing in the model of Cooling is characterised by a constant mixing coefficient (D_{FS}). The mixing coefficient has units of $\text{m}^2 \text{s}^{-1}$ and is analogous to the diffusion coefficient or mass diffusivity in gaseous diffusion. It is related to the velocity and radius of a typical eddy as follows:

$$D_{FS} = \frac{v_{\text{eddy}} r_{\text{eddy}}}{\pi}, \quad (5.1.39)$$

where v_{eddy} is the velocity of those eddies and r_{eddy} is their radius.

Both the velocity and characteristic size of eddies for a given system and transient are subject to significant uncertainty. The value of this parameter is assumed constant, however in reality the rate of mixing will actually vary over time and will be affected significantly by solution heating, the appearance and advection of bubbles and the addition of solution to the vessel. Cooling estimated a value of $3.34 \times 10^{-3} \text{ m}^2 \text{ s}^{-1}$ for the Medical Isotope Production Reactor (MIPR) based on a CFD simulation (Buchan et al. (2012)) of the SUPO fissile solution reactor. Given the difficulty in estimating an accurate value for this parameter, and the similarities between MIPR, SUPO and the fissile solution reactors simulated in this chapter, the value estimated by Cooling will be adopted in the present study.

5.1.10 Modelling the Addition of the Fuel to the Solution

One method of initiating a criticality excursion in benchmark experiments is to increase the volume of fuel solution in the reactor vessel. The addition of fuel solution in this way will have a number of physical effects, including increasing the total mass of fuel solution, changing the temperature of the fuel solution and contributing to mixing of the fuel solution. While the fuel solution will typically be added at the top or bottom of the reactor vessel, the momentum of the inflowing fluid would contribute to mixing in the fuel solution and the additional solution is expected to spread out very quickly. The model will therefore simulate inflowing fuel solution as evenly distributed throughout the reactor vessel.

A fraction of the added fuel solution is added to the mass of fuel solution in each vertically discretised section of the reactor:

$$\frac{\partial M(t, z)}{\partial t} = Q_{sol}(t, z), \quad (5.1.40)$$

where $M(t, z)$ is the mass of fuel solution at location z at time t and Q_{sol} is the mass flow rate of the fuel solution. The temperature of the fuel solution was modified in order to account for the difference in temperature between the incoming fuel solution and the fuel solution in the vessel. The temperature was modified as follows:

$$\frac{\partial T(t, z)}{\partial t} = \frac{Q_{sol}(t, z)}{M(t, z)} (T_{\text{ext}} - T(t, z)), \quad (5.1.41)$$

where T_{ext} is the temperature of the solution added, assumed equal to the room temperature. This last expression assumes that the heat capacity of the incoming fuel solution is the same as the heat capacity of the solution already in the reactor vessel. Since the exact room temperature is rarely noted in the experimental reports, a value of 15°C will be assumed.

5.1.11 Solubility of Dissolved Gases

In Chapter 4 it was shown that the the presence of various solutes in aqueous solutions affected the solubility of hydrogen gas. A single value of the Henry's law constant for hydrogen gas was selected by choosing a value in the middle of the range for solution types and concentrations. This approach was suitable for the model presented in Chapter 4 where dynamic variation in the solubility of hydrogen gas was not of interest, however the model presented in the current chapter would benefit from the ability to estimate the Henry's law constants on a time-dependent basis. A crude method for estimating the Henry's law constant for hydrogen gas in solutions of aqueous nitrate salts is presented in Appendix C. This model will be used for estimating hydrogen and oxygen solubility for the point kinetics model.

5.1.12 Radiolytic Gas Generation Coefficient

The radiolytic gas generation coefficients (G_{H_2}) can be estimated using Equation 3.2.26, However, as previously discussed in Section 3.2.3.5, this equation is based on a limited set of relatively old data from Lane et al. (1958) and a more recent study by Yoshida et al. (2019) indicates that radiolytic gas generation coefficients may in fact be somewhat greater than those indicated by Equation 3.2.26.

Further evidence for this can be found in a report (Miyoshi et al. (2009)) comparing the performance of criticality safety codes in reproducing the observed behaviour of the criticality safety benchmark experiments. For pulse experiments on the TRACY reactor, this report recommends a value of $G_{H_2} = 1 \times 10^{-7}$ mol J⁻¹ where the inserted reactivity is less than one dollar and $G_{H_2} = 3 \times 10^{-7}$ mol J⁻¹ where the inserted reactivity is greater than one dollar. The second of these is significantly higher than the maximum possible value indicated in Lane et al. ($G_{H_2} = 1.87 \times 10^{-7}$ mol J⁻¹ for pure water), but has been shown by Miyoshi et al. (2009), and also Liem and Naito (2015), to result in excellent agreement between simulation and experiment.

There is therefore some significant uncertainty in the true value of G_{H_2} for solutions of uranyl nitrate, due in part to a lack of any recent experimental data. The value of G_{H_2} will therefore be selected case-by-case based on the most appropriate available literature estimates or using Equation 3.2.26 where no literature values are available.

5.1.13 Summary of Principal Governing Equations

The following equations are solved using the ODE solver of Shampine and Gordon (1975).

$$\frac{dP(t)}{dt} = \frac{\beta P(t)}{\Lambda} (R_{ex}(t) + \alpha_T(T(t) - T_0) + \alpha_V(V_{RG}(t) - V_{RG,0}) - 1)$$

$$+ \sum_{i=1}^6 \lambda_i C_i(t) + \frac{S(t)\epsilon}{\bar{v}\Lambda}, \quad (5.1.42)$$

$$\frac{dE(t)}{dt} = P(t), \quad (5.1.43)$$

$$\frac{dC_i(t)}{dt} = -\lambda_i C_i(t) + \frac{\beta_i}{\Lambda} P(t), \quad (5.1.44)$$

$$\begin{aligned} \frac{\partial T(t, z)}{\partial t} = & \frac{P(t)\psi(t, z)}{M(t, z)C_p} - \frac{(T(t, z) - T_{\text{vessel}}(t))h_{\text{int}}A(t, z)}{M(t, z)C_p} + D_{FS} \frac{\partial^2 T(t, z)}{\partial z^2}, \\ & + \frac{Q_{\text{sol}}(t, z)(T_{\text{ext}} - T(t, z))}{M(t, z)}, \end{aligned} \quad (5.1.45)$$

$$\frac{\partial T(t, 0)}{\partial t} = 0, \quad (5.1.46)$$

$$\frac{\partial T(t, H_l)}{\partial t} = \frac{(T(t, H_l) - T_{\text{ext}})U_{\text{surface}}A_{\text{surface}}}{M(t, z)C_p}, \quad (5.1.47)$$

$$\frac{\partial T_{\text{vessel}}(t)}{\partial t} = \frac{(T(t, z) - T_{\text{vessel}}(t))h_{\text{int}}A(t, z)}{M_{\text{vessel}}C_{p, \text{vessel}}} - \frac{(T_{\text{vessel}}(t) - T_{\text{ext}})h_{\text{ext}}A_{\text{vessel}}}{M_{\text{vessel}}C_{p, \text{vessel}}}, \quad (5.1.48)$$

$$\frac{\partial N_{i(g)}(t, z)}{\partial t} = \alpha_c(t, z) (C_{i(aq)}(t, z) - C_{i,eq}) V(t, z) - v_b \frac{\partial N_{i(g)}(t, z)}{\partial z} + D_{FS} \frac{\partial^2 N_{i(g)}(t, z)}{\partial z^2}; \quad (5.1.49)$$

$$i = \text{H}_2, \text{O}_2, \quad (5.1.50)$$

$$\frac{\partial N_{\text{H}_2(aq)}(t, z)}{\partial t} = P(t)\psi(t, z)G_{\text{H}_2} - \alpha_c(t, z) (C_{\text{H}_2(aq)}(t, z) - C_{\text{H}_2,eq}) V(t, z) + D_{FS} \frac{\partial^2 N_{\text{H}_2(aq)}(t, z)}{\partial z^2}, \quad (5.1.51)$$

$$\begin{aligned} \frac{\partial N_{\text{O}_2(aq)}(t, z)}{\partial t} = & \frac{1}{2} k_{\text{H}_2\text{O}_2}(t, z) C_{\text{H}_2\text{O}_2(aq)}(t, z) - \alpha_c(t, z) (C_{\text{O}_2(aq)}(t, z) - C_{\text{O}_2,eq}) V(t, z) \\ & + D_{FS} \frac{\partial^2 N_{\text{O}_2(aq)}(t, z)}{\partial z^2}, \end{aligned} \quad (5.1.52)$$

$$\frac{\partial N_{\text{H}_2\text{O}_2(aq)}}{\partial t} = P(t)\psi(t, z)G_{\text{H}_2\text{O}_2} - k_{\text{H}_2\text{O}_2}(t, z)N_{\text{H}_2\text{O}_2(aq)}(t, z) + D_{FS} \frac{\partial^2 N_{\text{H}_2\text{O}_2(aq)}(t, z)}{\partial z^2}, \quad (5.1.53)$$

$$\frac{\partial E_{\text{sat}}(t, z)}{\partial t} = P(t)\psi(t, z) \quad \text{when} \quad C_{\text{H}_2,(\text{aq})}(t, z) \geq C_{\text{crit}}(t, z), \quad (5.1.54)$$

$$E_{\text{sat}} = 0 \quad \text{otherwise},$$

$$\begin{aligned} \frac{\partial N_b(t, z)}{\partial t} = & \delta_1 \alpha V(t, z)^{(1-\alpha)} k_f E_{\text{sat}}(t, z)^{(\alpha-1)} P(t)\psi(t, z) - v_b \frac{\partial N_b(t, z)}{\partial z} + D_{FS} \frac{\partial^2 N_b(t, z)}{\partial z^2}; \\ & \alpha = 2.5, k_f = 0.05, \end{aligned} \quad (5.1.55)$$

$$\delta_1 = \begin{cases} 0 & \text{when } C_{\text{H}_2,(\text{aq})}(t, z) < C_{\text{crit}}(t, z), \\ 1 & \text{otherwise.} \end{cases} \quad (5.1.56)$$

$$(5.1.57)$$

Equations 5.1.42 and 5.1.44 are the standard point kinetics equations. Equation 5.1.45 tracks the change in temperature of the fuel solution based on the rate of heat generation from fission, heat transfer between the fuel solution and the reactor vessel (see Section 5.1.8.2), heat transfer within the fuel solution due to mixing (model of Cooling (2014)) and the temperature difference of any incoming fuel solution (see Section 5.1.10). Equations 5.1.50 to 5.1.52 track the movement of gas between the aqueous and gaseous phases. The rate of mass transfer is based on the parameter α_c which is determined using the correlation developed in Section 4.3.5. Equation 5.1.53 tracks the

rate of formation and decomposition of hydrogen peroxide and the rate of formation of oxygen (see Section 5.1.4). Equation 5.1.54 calculates the amount of fission energy deposited in a given region of the fuel solution while the solution is saturated with dissolved radiolytic gas. This value is used by Equation 5.1.55 to determine the number of bubbles formed during saturation. The formation term in this equation is based on the model described in Section 4.3.3.1 and the collapse term is based on the model described in Section 4.3.3.2. The mixing and advection terms are based on the models described in Cooling (2014).

The following equations are evaluated as required as a function of the current system state:

$$V_{RG}(t, z) = \sum_i N_{i(g)}(t, z) \frac{RT(t, z)}{P_l + \frac{2\sigma_s(t, z)}{r_b(t, z)}}; \quad i = \text{H}_2, \text{O}_2, \quad (5.1.58)$$

$$r_{nucl}(t, z) = r_{b0}(t, z) F_{\text{corr}}, \quad (5.1.59)$$

$$\begin{aligned} r_{b0}(t, z) = & (-2.8632 \times 10^{-15} T(t, z)^2 + 7.3996 \times 10^{-13} T(t, z) - 9.9925 \times 10^{-11}) \dot{E}_{Av}(t, z)^2 \\ & + (8.7907 \times 10^{-14} T(t, z)^2 - 9.7928 \times 10^{-13} T(t, z) + 3.4558 \times 10^{-9}) \dot{E}_{Av}(t, z) \\ & + (9.7683 \times 10^{-14} T(t, z)^2 - 4.0125 \times 10^{-11} T(t, z) + 4.9092 \times 10^{-9}); \end{aligned} \quad (5.1.60)$$

$$\begin{aligned} \dot{E}_{Av}(t, z) = & (1.3387 \times 10^{-6} T(t, z) - 3.4319 \times 10^{-5}) C_U \\ & - (6.6431 \times 10^{-3} T(t, z) - 8.8142), \end{aligned} \quad (5.1.61)$$

$$F_{\text{corr}} = 0.3554 + 0.4264 G_{\text{H}_2} - 0.0400 G_{\text{H}_2}^2, \quad (5.1.62)$$

$$C_{crit}(t, z) = \left(P_l + \frac{2\sigma_s(t, z)}{r_{nucl}(t, z)} \right) H_{\text{H}_2, \text{sol}}(t, z) - C_{\text{O}_2(aq)}(t, z), \quad (5.1.63)$$

$$v_b(t, z) = \begin{cases} \frac{2r_b^2(t, z)\rho_s(t, z)g}{9\mu(t, z)}; & r_b(t, z) < 1 \times 10^{-5} \text{m} \\ \left(\frac{8r_b(t, z)g}{3C_D(t, z)} \right)^{1/2}; & r_b(t, z) \geq 1 \times 10^{-5} \text{m} \end{cases}, \quad (5.1.64)$$

$$C_D(t, z) = \max \left(\frac{24(1 + 0.15 \text{Re}(t, z)^{0.687})}{\text{Re}(t, z)}, \frac{8E_0(t, z)}{3(E_0(t, z) + 4)} \right), \quad (5.1.65)$$

$$E_0(t, z) = \frac{4gr_b^2(t, z)(\rho_s(t, z) - \rho_g(t, z))}{\sigma_s(t, z)}, \quad (5.1.66)$$

$$\text{Re}(t, z) = \frac{2\rho_s(t, z)v_b(t, z)r_b(t, z)}{\mu(t, z)}, \quad (5.1.67)$$

$$\mu(t, z) = 2.411 \times 10^{-3} - 2.887 \times 10^{-4} (T(t, z) - 273.15)^{0.4478}, \quad (5.1.68)$$

$$\alpha_c(t, z) = 1.9436 \times 10^{-6} \left(\frac{N_b(t, z)}{V(t, z)} \right)^{0.78926} D_{\text{FS}}^{0.5}, \quad (5.1.69)$$

$$C_{i,eq}(t, z) = y_i(t, z) H_{i, \text{sol}}(t, z) \left(P_l + \frac{2\sigma_s(t, z)}{r_b(t, z)} \right). \quad (5.1.70)$$

Equation 5.1.58 uses the ideal gas law to calculate the volume of radiolytic gas. The pressure of these gases is determined from the bubbles size and liquid surface tension which is estimated as a function of temperature using Equation 3.2.23. Equation 5.1.59 sets the minimum bubble radius at the estimated size of fission track bubbles (see Section 3.3.5). Equation 5.1.62 is the correction factor due to variation in the radiolytic gas generation coefficient (see Section 3.3.2). Equation 5.1.63 determines

the critical concentration based on the size of fission track bubbles, the solubility of hydrogen gas in the fuel solution and the concentration of dissolved oxygen (see Section 5.1.6). The Henry's law constants for hydrogen and oxygen are calculated using Equations C.2 and C.3. Equation 5.1.64 determines the advection velocity of gas bubbles using the model of Celata et al. (2007). Equation 5.1.68 is a correlation derived by Cooling (2014) from the experimental data of Grant et al. (1948). Equation 5.1.69 was derived in Section 4.3.5 of the previous chapter. The bubble radius is determined by solving Equation 4.2.10.

5.2 Simulation of the SILENE S3-258 Experiment

The SILENE reactor was commissioned in 1974 to continue the work carried out on CRAC at the CEA's Valduc facility in France. The SILENE reactor is annular rather than cylindrical which allowed space for a control rod in the centre of the reactor, useful for rapid reactivity insertion studies. Further details regarding the characteristics and operations of the SILENE reactor can be found in numerous reports, including Barbry et al. (1973), Barbry (1987), Barbry (1993), Barbry (1994) and Barbry et al. (2009).

5.2.1 Reactivity and Delayed Neutrons

Experiment S3-258 was one of the "pulsed" type experiments carried out on SILENE. These experiments were initiated by rapid removal of the control rod. In S3-258 this was done to achieve a reactivity insertion of 1.836\$ in 0.2s (Barbry (1994)). There was no external neutron source used in the experiment so the initiation of the transient can be considered stochastic. For this reason, the model will treat the rapid insertion of the control rod as a step insertion occurring at $t=0.2s$. The control rod is reinserted approximately 10s before the end of the experiment. This does not appear to be detailed in the experimental results although the timing is easily inferred from the fission power profile.

$$R_{ex}[\$] = \begin{cases} 0.0 & t \leq 0.2s \\ 1.836 & 0.2 < t \leq 410.8s \\ 1.836 \left(1 - \frac{t-409.8}{0.2}\right) & 409.8s < t < 410.0s \\ 0.0 & t \geq 410.0s \end{cases} \quad (5.2.1)$$

The delayed neutron precursor parameters are shown in Table 5.1. These are based on data from Barbry (1994) with the values of β_i renormalised so that $\sum_i \beta_i = \beta_{\text{eff}}$. The generation time is

determined to be 3.55×10^{-5} s based on the prompt neutron lifetime given by Barbry (1994).

i th Group	SILENE 71 gU/L	
	β_i	λ_i [s ⁻¹]
1	2.693×10^{-4}	0.0124
2	1.727×10^{-3}	0.0305
3	1.591×10^{-3}	0.111
4	3.106×10^{-3}	0.301
5	9.343×10^{-4}	1.13
6	3.126×10^{-4}	3.0
	$\beta_{\text{eff}} = 0.00794$	

TABLE 5.1

Delayed neutron group yields (β_i) and decay constants (λ_i) for the SILENE fuel solution with a concentration of 71 gU/L based on data from Barbry (1994).

5.2.2 Reactivity Feedback Coefficients

The thermal and void reactivity feedback coefficients for the SILENE reactor with a uranium concentration of 71 gU/L are based on experimental data from Kornreich (1993). These values are -6.4×10^{-2} $\$ \text{K}^{-1}$ for the thermal feedback coefficient and -2281 $\$ \text{m}^{-3}$ for the void feedback coefficient.

5.2.3 Intrinsic Neutron Source and Initiation Time

The strength of the intrinsic neutron source in the SILENE fuel solution is subject to some uncertainty since its exact value depends, not only on the composition of the solution, but on its irradiation history, which is not known, and on the geometry of the container.

Using the same approximations as those adopted in Section 2.3.2, the data of Hankins (1966) and Seale and Anderson (1991) can be used to obtain an approximate estimate. The fuel solution examined by Hankins had a uranium concentration of 53 gU/L and that of Seale and Anderson had a concentration of 420 gU/L, compared to a concentration of 71 gU/L for the SILENE S3-258 fuel solution. Hankins measured a neutron emission rate of 5.6 n/s, and Seale and Anderson measured 21.4 n/s, for 1 L samples of their respective fuel solutions. Both solutions were enriched to 93% ^{235}U , similar to the SILENE S3-258 fuel solution. Interpolating linearly between these two data points would suggest a neutron emission rate of 6.4 n/s L⁻¹, and extrapolating this to the volume of the fuel solution in experiment S3-258 would result in a value of 250 n/s.

The data provided in Hankins (1966) and Seale and Anderson (1991) are experimentally measured values for the rate of neutron emissions from 1 L volumes of uranyl nitrate solution. The measured rate

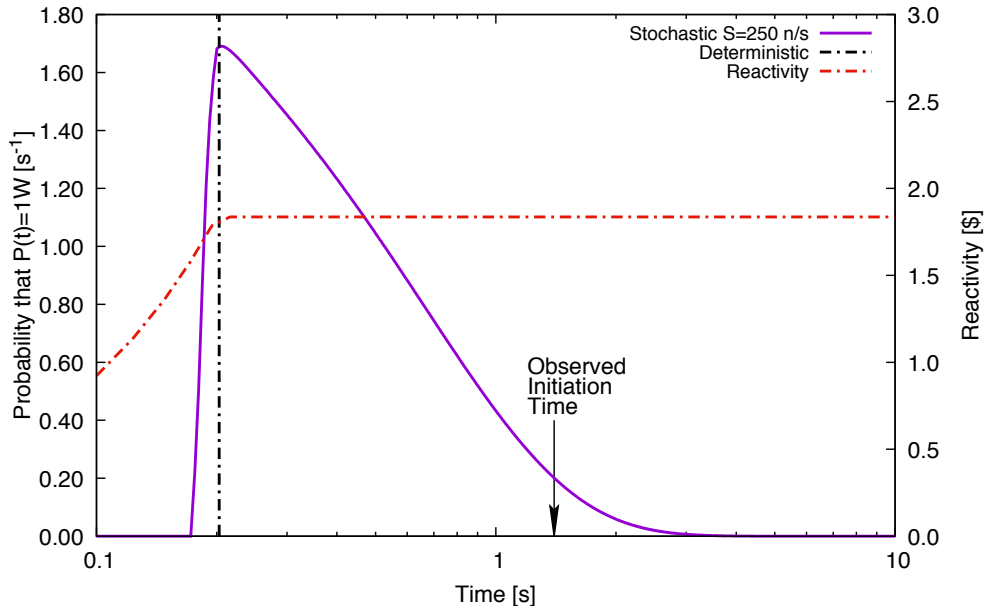


Fig. 5.2.1. Probability distribution of the time to reach a power level of 1 Watt during the SILENE S3-258 experiment assuming an intrinsic neutron source strength of 250 n/s.

of neutron emission will be slightly larger than the true intrinsic neutron source, since the measured value includes some neutron multiplication due to induced fissions, adding further uncertainty to the estimate. However, these data provide a useful indication of the likely order of magnitude.

Figure 5.2.1 shows the probability distribution for the time required for SILENE experiment S3-258 to reach a power level of 1 Watt based on the method described in Section 2.2.2. An intrinsic neutron source of 250 n/s has been assumed for illustrative purposes. Figure 5.2.1 indicates that the fission burst initiated relatively late compared to the deterministic wait-time of 0.2 s. The cumulative probability of the power level having reached 1 W at the experimentally observed time of 1.4 s is 90% for the assumed intrinsic neutron source strength.

Since the burst initiation occurred significantly later in this experiment than a purely deterministic calculation would predict, the intrinsic neutron source strength applied in the point kinetics model will be set to an arbitrarily small value in order to delay the predicted initiation to match that observed during the experiment.

5.2.4 Summary of Inputs

Table 5.2 summarises the input parameters passed to the point kinetics model.

¹The model uses the radius to determine the cross-sectional area, assuming cylindrical geometry. The SILENE reactor is annular so the radius specified has the same cross-sectional area as the area of the SILENE annulus.

Parameter	Symbol	Value or Eq. N°	Units
Intrinsic Neutron Source	S_0	10^{-60}	neutrons per second
Initial Temperature	T_0	293.6	K
External Temperature	T_{ext}	293.6	K
Vessel Pressure	P_l	1.01325×10^5	Pa
Generation Time	Λ	3.548×10^{-5}	s
Thermal Feedback Coefficient	α_T	-6.4×10^{-2}	$\text{\$/K}^{-1}$
Void Feedback Coefficient	α_V	-2281.0	$\text{\$/m}^{-3}$
Energy per fission	ϵ	3.09813×10^{-11}	J
Neutrons per fission	$\bar{\nu}$	2.43	–
Uranyl Nitrate Concentration	C_U	300.89	mol m^{-3}
Nitric Acid Concentration	C_N	2000	mol m^{-3}
Uranium Enrichment	–	92.7%	–
Fuel Solution Mass	M	45.54	kg
Solution Heat Capacity	C_p	3442	$\text{J kg}^{-1} \text{K}^{-1}$
Heat Transfer Coefficient (internal)	h_{int}	1250.0	$\text{W m}^{-2} \text{K}^{-1}$
Heat Transfer Coefficient (external)	h_{ext}	6.29	$\text{W m}^{-2} \text{K}^{-1}$
Heat Transfer Coefficient (surface)	U_{surface}	7.74	$\text{W m}^{-2} \text{K}^{-1}$
Vessel Radius	r_v	0.176^1	m
Vessel Height	H_v	1.0	m
Vessel Mass	M_{vessel}	90.5	kg
Vessel Surface Area	A_{vessel}	1.41	m^2
Flux Extrapolation	δ_b	0.03	–
	δ_s	0.03	–
Solution Mixing Constant	D_{FS}	3.34×10^{-3}	$\text{m}^2 \text{s}^{-1}$
Radiolytic Gas Generation	G_{H_2}	Eq. 3.2.26	–
Fuel Solution Density	ρ_s	Eq. E.2	kg m^{-3}

TABLE 5.2
Summary of model inputs and initial values.

5.2.5 Model Results

The fission power profile predicted by the model is compared to the experimental results in Figure 5.2.2. The results show very close agreement between experiment and prediction. The peak power predicted by the model was 2.03×10^8 W whereas the peak power observed during the experiment was 1.66×10^8 W. The timing of the power peak is offset by approximately one quarter of a second in the model compared to the experiment. This is due to stochasticity resulting from the weakness of the intrinsic neutron source, as discussed in Section 5.2.3. Total energy release at the end of the experiment predicted by the model was 7.53×10^6 J whereas the total energy release measured during the experiment was 7.61×10^6 J. The model accurately predicts the timing and magnitude of the secondary power peak. This is predicted by the model to have a magnitude of 5.80×10^4 W and

to occur at $t=61.6\text{s}$, while the experimental results show the peak occurring with a magnitude of $5.60 \times 10^4 \text{ W}$ at $t=65.1\text{s}$.

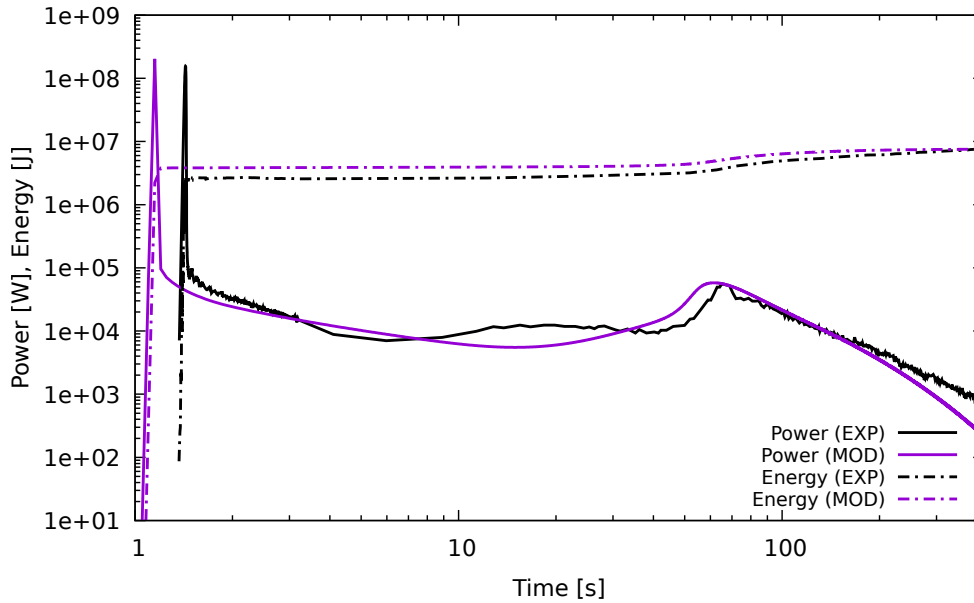


Fig. 5.2.2. Experimental and predicted fission power profiles for SILENE S3-258. Experimental power profile digitised from Barbry (1994).

Figure 5.2.3 shows the concentration of dissolved hydrogen and oxygen in the fuel solution, as well as the critical concentration of hydrogen at which the fission track bubbles become viable nucleation sites. The multiple red lines represent the concentration of dissolved hydrogen in the different discretised regions of the fuel solution. These lines are not intended to be distinguishable and are included to indicate the range of concentrations predicted by the model. The concentration of dissolved hydrogen initially increases sharply as a result of the rapidly rising fission rate. A reduction in the predicted critical concentration occurs at the same time due to the rising solution temperature. When these values meet, bubbles are produced (see Figure 5.2.4) and the concentration of dissolved hydrogen begins to fall as the bubbles grow. The dissolved hydrogen concentration drops most rapidly at the centre of the solution where the number of growing bubbles is greatest, and relatively slowly far away from the centre where the number of growing bubbles is smaller.

Oxygen gas is only produced in small quantities towards the end of the experiment. Oxygen therefore has little effect on the kinetics of the transient, however when it does appear it contributes to decreasing the critical concentration for hydrogen. The concentration of hydrogen begins to rise a second time around $t=50\text{s}$, as gas bubbles advect from the system and the hydrogen produced by radiolysis no longer has a gas/liquid interface at which to come out of solution. However, the concentration of dissolved hydrogen remains below the critical concentration for the rest of the experiment

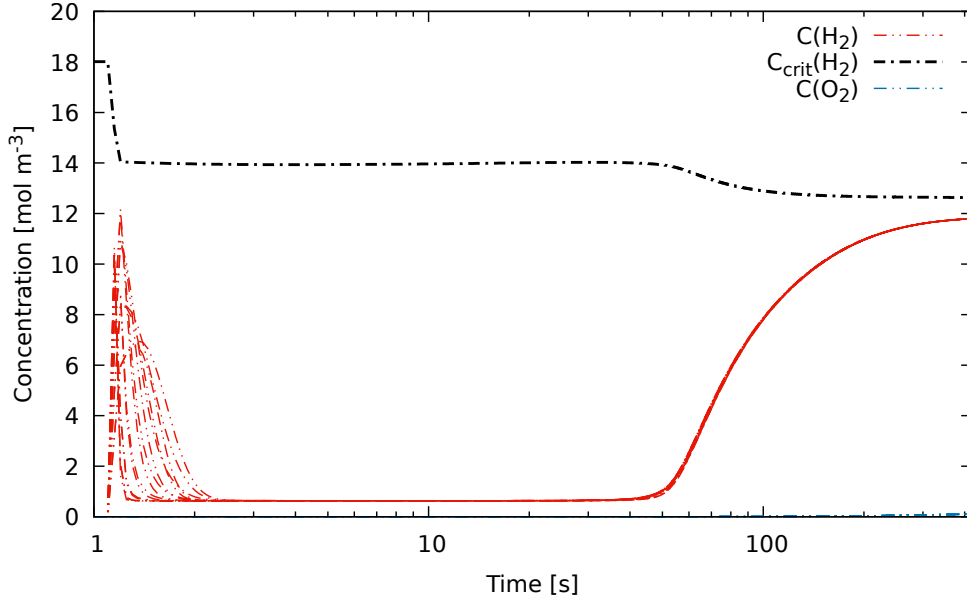


Fig. 5.2.3. Predicted concentrations of dissolved hydrogen and oxygen, as well as the critical concentration, for SILENE experiment n°S3-258. Multiple lines shown to indicate the range of concentrations across each discretised section of the fuel solution.

and the solution does not saturate a second time.

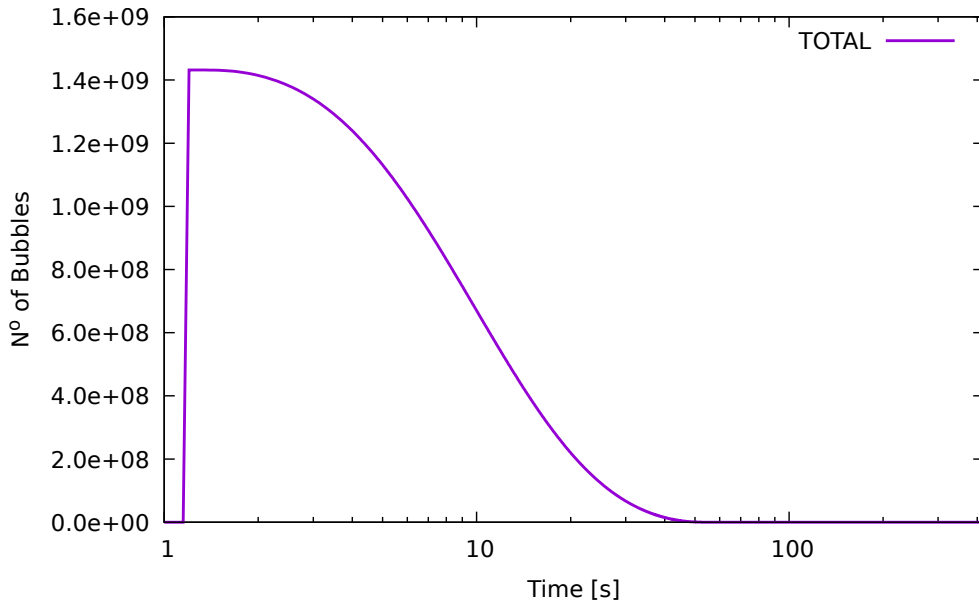


Fig. 5.2.4. Number of bubbles predicted by the model for SILENE experiment n°S3-258.

The average radius of stable bubbles in each vertically discretised section of the fuel solution is shown in Figure 5.2.5. The average bubbles size increases sharply when the fuel solution becomes saturated with dissolved hydrogen. Once the fuel solution has saturated, the size of the radiolytic gas bubbles evens out across the solution at around $r_b = 1.3 \times 10^{-4}$ m. This is due to the evening out of the dissolved gas concentration due to mixing. The size of the gas bubbles begins to increase again

around $t=50$ s as the concentration of dissolved hydrogen begins to increase.

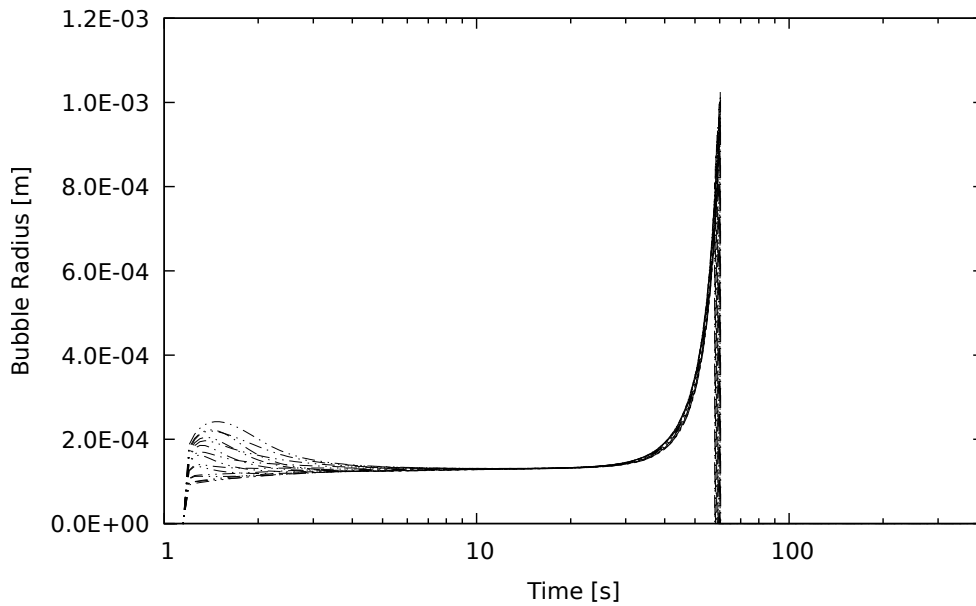


Fig. 5.2.5. Radius of bubbles predicted by the model for SILENE experiment n°S3-258. Multiple lines shown to indicate the range of bubble sizes across each discretised section of the fuel solution.

Figure 5.2.6 compares the fuel solution temperature predicted by the model to the temperature measured during the experiment. There is relatively good agreement between the model and the experiment, providing validation for the choice of heat transfer coefficients in Section 5.1.8. The temperature initially rises very rapidly due to the peak in the fission power output. The experimental measurement peaks at 55°C whereas the model predicts a peak temperature of 44°C . This difference may be due to direct heating from the intense gamma radiation emitted during the fission power peak. Following the initial increase, the temperature remains relatively stable until approximately $t=50$ s before increasing again due to the secondary rise in fission power output.

Figure 5.2.7 shows the various factors contributing to the reactivity, predicted by the point kinetics model. The reactivity initially rises due to rapid removal of the control rod. The overall reactivity then remains relatively constant until the first power peak, except for a small amount of thermal reactivity feedback due to the rise in fuel solution temperature. The appearance of radiolytic gas induces a large negative reactivity, causing the fission power output to peak. This negative reactivity gradually decreases as the bubbles produced during saturation advect from the system, leading to the second increase in fission power when the overall reactivity becomes slightly positive once again. This small positive reactivity is offset by thermal feedback to bring the reactivity back to zero once again.

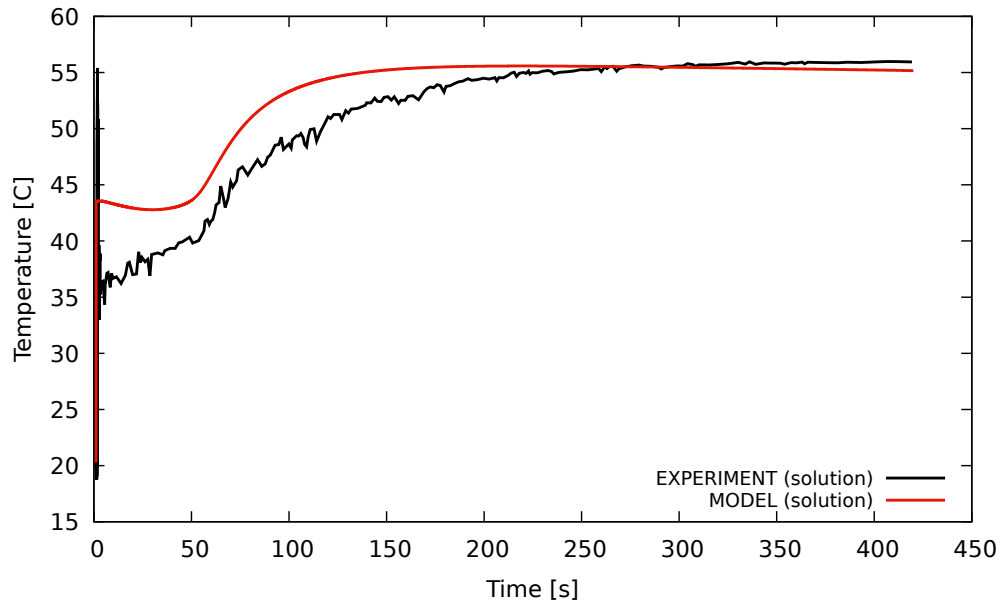


Fig. 5.2.6. Experimental and predicted temperature of the fuel solution and vessel wall for SILENE S3-258. Experimental temperature profile digitised from Barbry (1994).

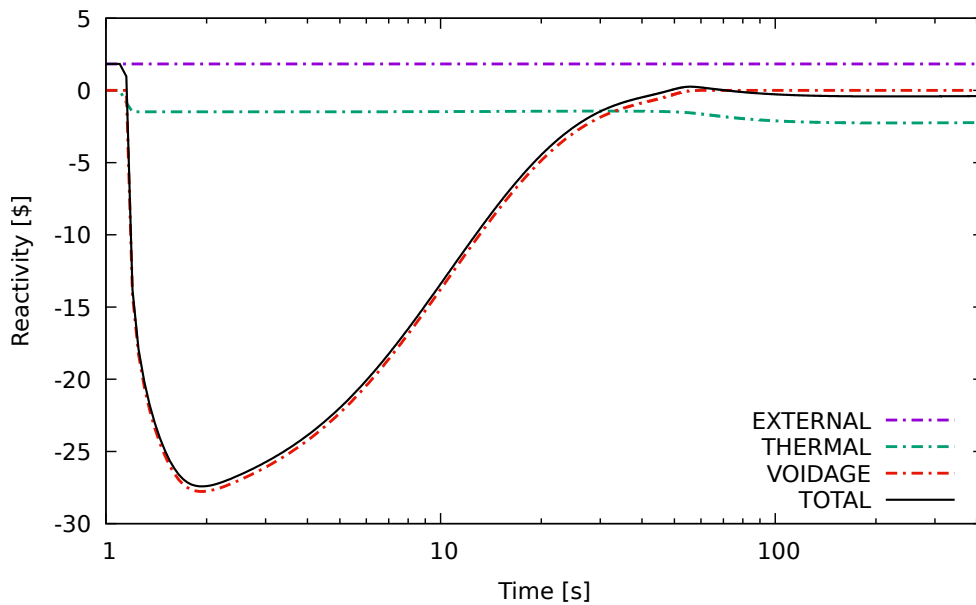


Fig. 5.2.7. Individual contributions and total reactivity predicted by the model for SILENE experiment n°S3-258.

5.3 Simulation of the CRAC-29 Experiment

The CRAC experiments were performed at the Valduc facility of the French *Commissariat à l'Energie Atomique* between 1967 and 1972. The experiments were performed on two reactor cores, both cylindrical open topped vessels, one with an internal diameter of 300 mm, and the other 800 mm in diameter. The CRAC-29 experiment was performed on the 300 mm reactor core. Details of the geometry and composition of this vessel assumed for purposes of MCNP modelling can be found in

Appendix B.

A review covering some of these experiments as well as some performed on the SILENE reactor was published by Barbry et al. (2009). Details of the CRAC-29 experiment, including the fuel solution composition and the experimental procedure are described in a summary document by Barbry et al. (1973).

5.3.1 Delayed Neutrons and Reactivity

The delayed neutron parameters were simulated using MCNP. These values are shown in Table 5.3. The generation time was also modelled using MCNP resulting in a value of 2.707×10^{-5} s.

i th Group	CRAC-29	
	β_i	λ_i [s ⁻¹]
1	3.50×10^{-4}	0.01334
2	1.46×10^{-3}	0.03274
3	1.39×10^{-3}	0.12078
4	3.24×10^{-3}	0.30278
5	1.45×10^{-3}	0.84951
6	5.80×10^{-4}	2.85309
$\beta_{\text{eff}} = 0.00848$		

TABLE 5.3

Delayed neutron group yields (β_i) and decay constants (λ_i) for the CRAC-29 fuel solution modelled using MCNP.

The reactivity insertion that initiated the CRAC-29 experiment was achieved by adding additional solution to the reactor vessel. The initial liquid level in the reactor core was 0.101 m, increasing steadily to 0.635 m over a period of 267 seconds. The experimental reports give a critical solution height of 0.4227 m. A marker on the experimental power profile shows the end of the reactivity ramp at experimental time $t = 103.4$ s, suggesting that the reactor reached the critical solution height at $t = -2.76$ s.

MCNP was used to determine that the reactivity of the reactor as a function of the fuel solution level in the vessel. The MCNP model predicted a critical height of 0.440 m, slightly higher than the critical height noted in the experimental report. This may be the result of differences between the true geometry and that represented in the MCNP model. In particular, the MCNP model does not include the reactor supports or surroundings, which could slightly increase the reactivity of the system due to neutron reflection.

The reactivity profile used for simulation purposes was obtained by shifting the x-axis (liquid level)

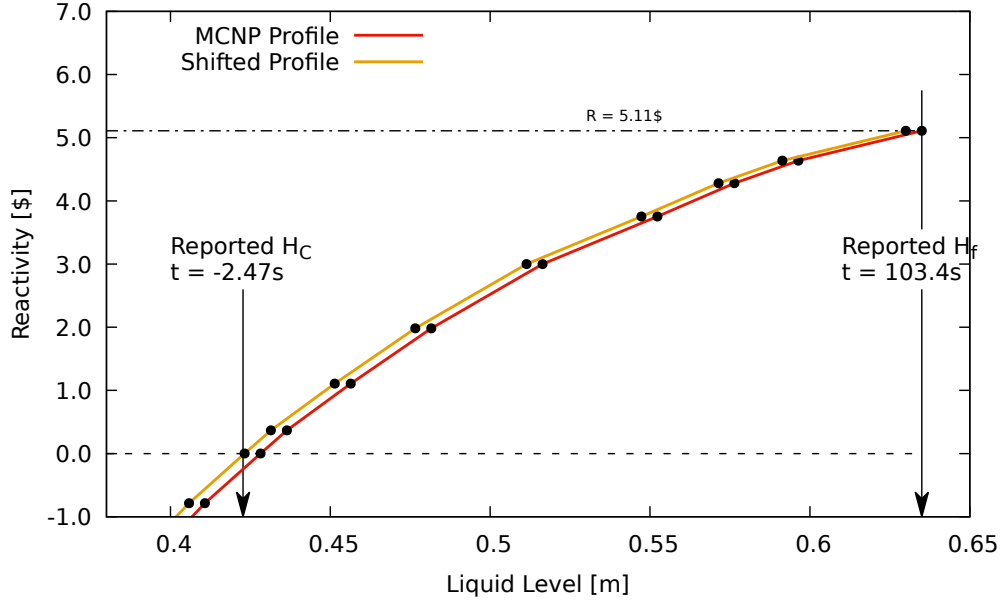


Fig. 5.3.1. MCNP simulation to determine the reactivity of CRAC29 as a function of the fuel solution level in the vessel.

in Figure 5.3.1 so that criticality and the end of the reactivity ramp both occur at the time reported in the experimental report. The resulting reactivity profile is given by Equation 5.3.1:

$$R_{ex}[\$] = \begin{cases} 0.0 & t \leq -2.76s, \\ 0.08969(t + 2.76) & -2.76s < t \leq 1.31s, \\ 0.37 + 0.07398(t - 1.31) & 1.31s < t \leq 11.3s, \\ 1.11 + 0.06917(t - 11.3) & 11.3s < t \leq 24.0s, \\ 1.98 + 0.05867(t - 24.0) & 24.0s < t \leq 41.3s, \\ 3.00 + 0.04187(t - 41.3) & 41.3s < t \leq 59.3s, \\ 3.75 + 0.04375(t - 59.3) & 59.3s < t \leq 71.3s, \\ 4.28 + 0.03572(t - 71.3) & 71.3s < t \leq 81.3s, \\ 4.64 + 0.02370(t - 81.3) & 81.3s < t \leq 103.4s, \\ 5.11 & t > 103.4s. \end{cases} \quad (5.3.1)$$

5.3.2 Void Feedback Coefficient

The void feedback coefficient was estimated using MCNP. The estimated value was $-3344.2 \text{ \$ m}^{-3}$ at the critical liquid level and $-2265.2 \text{ \$ m}^{-3}$ at the final liquid level. The model interpolates linearly between these two values for the time period during which fuel solution is being added to the reactor,

as indicated by Equation 5.3.2.

$$\alpha_V[\$ \text{ m}^{-3}] = \begin{cases} -3344.2 & t \leq -2.76s, \\ -3344.2 + 10.16(t + 2.76) & -2.76 < t \leq 103.4s, \\ -2265.2 & t > 103.4s. \end{cases} \quad (5.3.2)$$

5.3.3 Thermal Feedback Coefficient

The thermal feedback coefficient is a key parameter determining the kinetics of the criticality transient. It is affected by reactor geometry, as well as fuel solution composition and liquid level. The thermal feedback coefficient can be estimated using MCNP, however a study by Kornreich (1993) highlights limitations to this method, showing that Monte Carlo simulations frequently underestimate the magnitude of the thermal feedback coefficients for fissile solutions. This may be due in part to the limited number of cross-section libraries available in the temperature range of interest for fissile liquids, for example neutron cross-sections are typically available at temperature intervals of 300 K, and thermal scattering libraries at intervals of 50 K, creating a need for interpolation. This problem is compounded by the possibility that the thermal feedback coefficient may itself be a function of solution temperature, increasing as the temperature of the solution increases. This phenomenon was observed by Yamane (2015) who showed that the thermal feedback coefficient of the TRACY reactor was best characterised as a quadratic function of the solution temperature.

Despite the reservations noted above, an MCNP model (see Appendix B) was constructed to estimate the thermal feedback coefficient for the reactor configuration corresponding to the CRAC-29 experiment at maximum liquid level. The model evaluates the individual contributions due to Doppler broadening, liquid expansion and changes to thermal scattering cross-sections. This simulation predicted a total thermal feedback coefficient $\alpha_T = -6.7 \times 10^{-2} \$ \text{ K}^{-1}$. Kornreich (1993) provides a list of experimentally determined void and thermal feedback coefficients for various aqueous homogeneous reactors, including three configurations of CRAC. Unfortunately, this list does not include the particular configuration of the CRAC-29 experiment.

The thermal feedback coefficient can be estimated from data in the CRAC-29 experimental report. Figure 5.3.2 shows the temperature and power profiles for the CRAC-29 experiment. There is an initial peak ($t = 13s$) in the fission power, followed by a series of oscillations ($13s < t < 180s$) which eventually die out. The temperature increases sharply with the initial power peak and continues to increase as the power oscillates, tending towards a constant value towards the end of the experiment.

The reactivity inserted by addition of new fuel solution during the experiment is counterbalanced

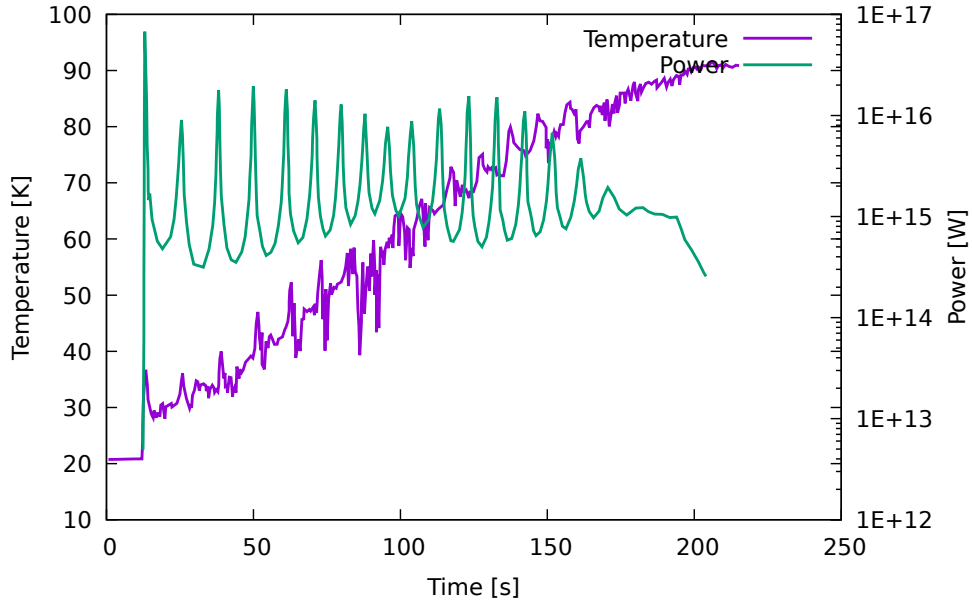


Fig. 5.3.2. Fission power output and solution temperature from experimental reports of the CRAC-29 experiment.

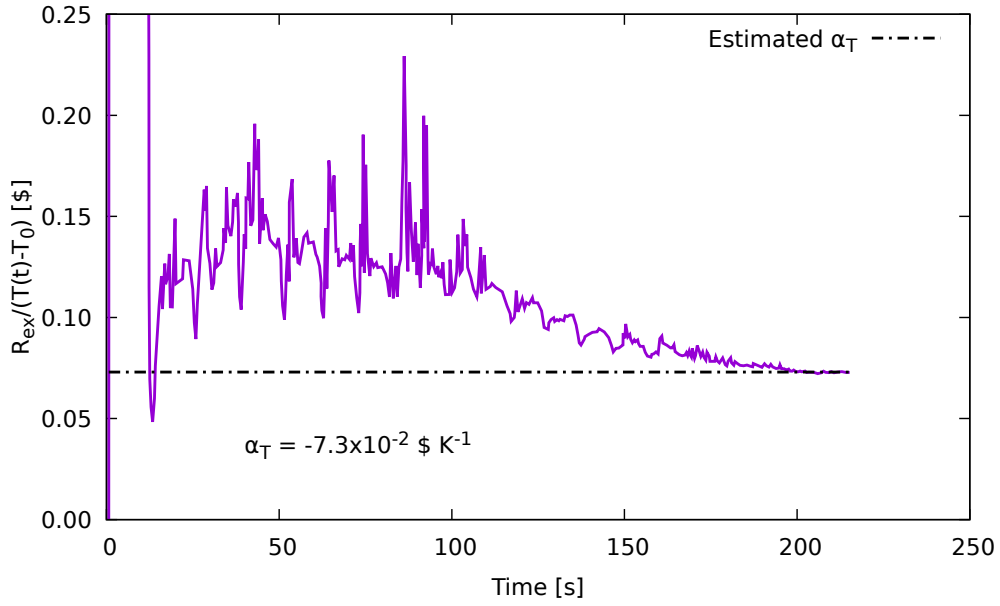


Fig. 5.3.3. Estimate of the thermal feedback coefficient for CRAC-29.

by void and thermal reactivity feedbacks. Voids are constantly removed from the solution due to advection of the gas bubbles (unless new voids are being created) whereas thermal feedback dissipates very slowly due to the low rate of heat transfer between the reactor and its surroundings. Figure 5.3.3 shows the amount of reactivity feedback per Kelvin of temperature rise since the start of the experiment. The feedback per Kelvin is determined using:

$$F_K = \frac{R_{\text{ins}}(t)}{T(t) - T_0}, \quad (5.3.3)$$

where F_K is reactivity feedback per Kelvin of temperature rise, R_{ins} is inserted reactivity due to control rod withdrawal and T_0 is the solution temperature at the start of the experiment. If the system was critical and contained no voids, F_K would be equal to the thermal feedback coefficient, however F_K is initially a function of thermal and void feedback. Figure 5.3.3 shows that the value of F_K tends towards a constant towards the end of the experiment. Unless there is another source of reactivity accounting for the rise in temperature leading up to this period, this fall in the value of F_K must be due to the advection of voids from the system. The final constant value of F_K therefore gives an indication to the thermal feedback coefficient of the reactor. The resulting value is compared to the MCNP estimate in Table 5.4.

	MCNP	Experimental	Units
Estimated α_T	-6.7×10^{-2}	-7.3×10^{-2}	$\$/\text{K}^{-1}$

TABLE 5.4

Thermal feedback coefficients for CRAC-29 at maximum liquid level estimated using MCNP and from experimental data.

5.3.4 Summary of Inputs

Table 5.5 summarises the input parameters for the point kinetics model.

5.3.5 Model Results

Figure 5.3.4 shows the fission power profile for the CRAC-29 experiment and compares it to the predictions of the point kinetics model. The first power peak experimentally observed had a magnitude of 2.09×10^6 W and occurred at 13.0s. The point kinetics model predicts a peak power of 2.76×10^6 W in magnitude occurring at 10.6s. The timing of the initial peak may be subject to some stochastic effects due to the absence of any external neutron source during the experiment, however these are expected to be minimal due to the slow reactivity insertion rate.

The model correctly predicts the appearance of fission power oscillations due to the repeated saturation of the fuel solution followed by advection of radiolytic gas voids. The oscillations observed are too slow to be the result of liquid sloshing (see Appendix D).

Figure 5.3.5 shows the predicted concentrations of dissolved hydrogen and oxygen in the fuel solution, as well as the critical concentration at which gas voids can nucleate on the fission track bubbles. The data show a repeating pattern in which dissolved hydrogen accumulates in the fuel solution, reaches the critical concentration, drops sharply as the bubbles expand and take hydrogen

Parameter	Symbol	Value or Eq. N°	Units
Intrinsic Neutron Source	S_0	1.0	neutrons per second
Initial Temperature	T_0	295.0	K
External Temperature	T_{ext}	288.2	K
Vessel Pressure	P_l	1.01325×10^5	Pa
Generation Time	Λ	2.707×10^{-5}	s
Thermal Feedback Coefficient	α_T	-7.3×10^{-2}	$\text{\$/K}^{-1}$
Void Feedback Coefficient	α_V at $t = -2.76\text{s}$	-3344.2	$\text{\$/m}^{-3}$
	α_V at $t = 103.4\text{s}$	-2265.2	$\text{\$/m}^{-3}$
Energy per fission	ϵ	3.09813×10^{-11}	J
Neutrons per fission	$\bar{\nu}$	2.43	–
Uranyl Nitrate Concentration	C_U	344.31	mol m^{-3}
Nitric Acid Concentration	C_N	2150	mol m^{-3}
Uranium Enrichment	–	93%	–
Fuel Solution Mass	M at $t = -2.76\text{s}$	34.23	kg
	M at $t = 103.4\text{s}$	51.25	kg
Solution Heat Capacity	C_p	3370	$\text{J kg}^{-1} \text{K}^{-1}$
Heat Transfer Coefficient (internal)	h_{int}	1250.0	$\text{W m}^{-2} \text{K}^{-1}$
Heat Transfer Coefficient (external)	h_{ext}	6.29	$\text{W m}^{-2} \text{K}^{-1}$
Heat Transfer Coefficient (surface)	U_{surface}	7.74	$\text{W m}^{-2} \text{K}^{-1}$
Vessel Radius	r_v	0.147	m
Vessel Height	H_v	2.090	m
Vessel Mass	M_{vessel}	45.68	kg
Vessel Surface Area	A_{vessel}	3.35	m^2
Flux Extrapolation	δ_b	0.03	–
	δ_s	0.03	–
Solution Mixing Constant	D_{FS}	3.34×10^{-3}	$\text{m}^2 \text{s}^{-1}$
Radiolytic Gas Generation	G_{H_2}	3.0×10^{-7}	mol J^{-1}
Fuel Solution Density	ρ_s	Eq. E.2	kg m^{-3}

TABLE 5.5
Summary of model inputs and initial values.

out of the solution, before increasing again once the bubbles formed have had time to advect from the solution.

The number of stable bubbles predicted to be in the fuel solution as a function of time is shown in Figure 5.3.6 and the predicted bubble radius is shown in Figure 5.3.7. The appearance of bubbles coincides with the dissolved gas concentration reaching the critical concentration, and the observed increases in the dissolved gas concentration coincide with the disappearance of bubbles from the

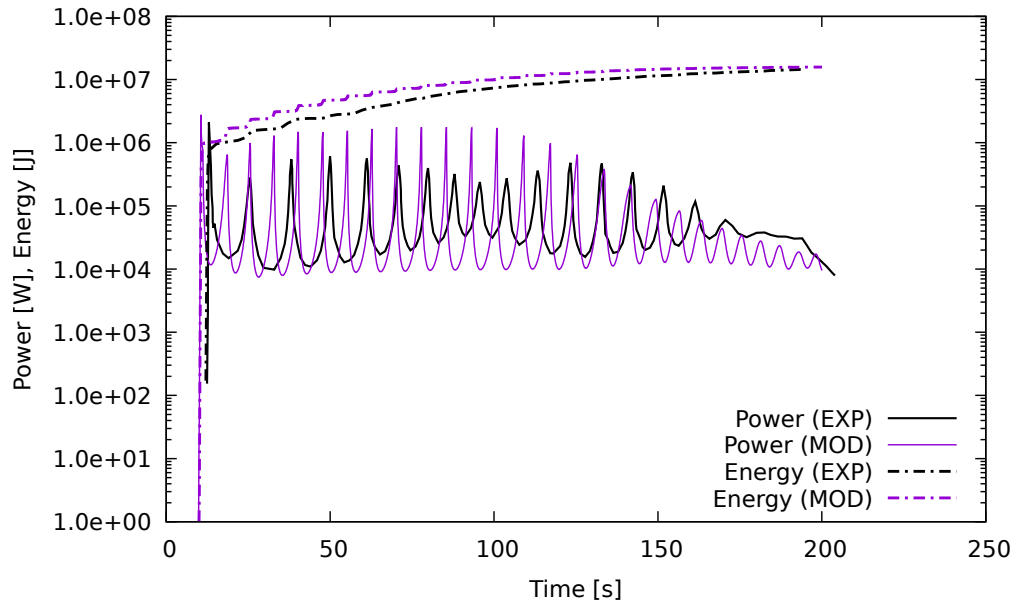


Fig. 5.3.4. Experimental and predicted fission power profiles for the CRAC-29 experiment. Experimental power profile digitised from Barbry et al. (1973).

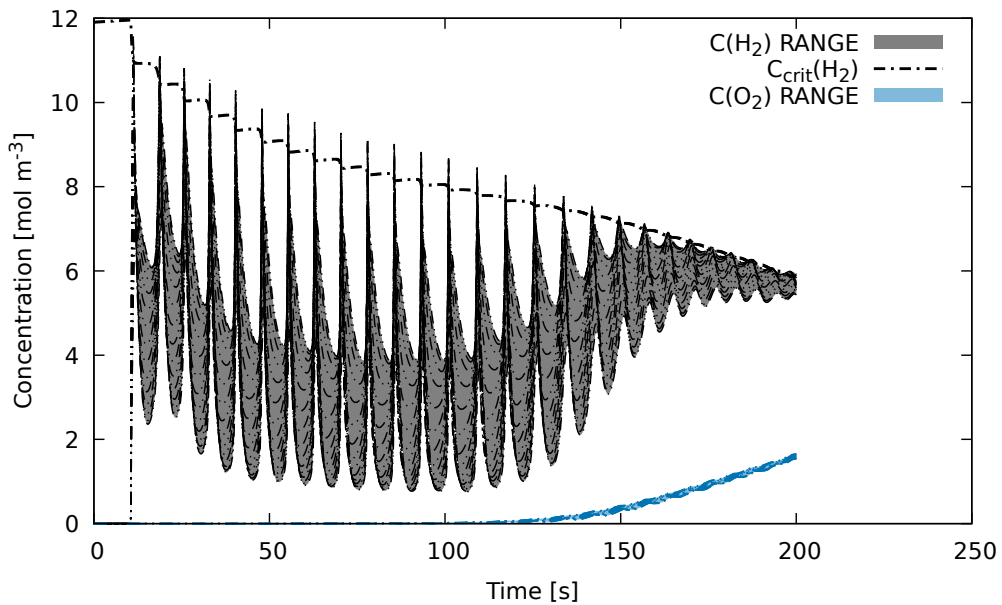


Fig. 5.3.5. Predicted concentrations of dissolved hydrogen and oxygen, as well as the critical concentration, for the CRAC-29 experiment. Area shaded in grey indicates the range of concentrations across each discretised section of the fuel solution.

system. The bubbles are predicted to grow rapidly from the size of fission track bubbles, approximately 5×10^{-8} m, to a size on the order of 10^{-4} - 10^{-3} m. This is because the advecting bubbles continue to consume dissolved gas from the fuel solution as they move towards the surface.

Figure 5.3.8 shows the predicted temperatures of the fuel solution and reactor vessel, as well as the measured values recorded in the experimental report. The temperatures predicted by the model rise

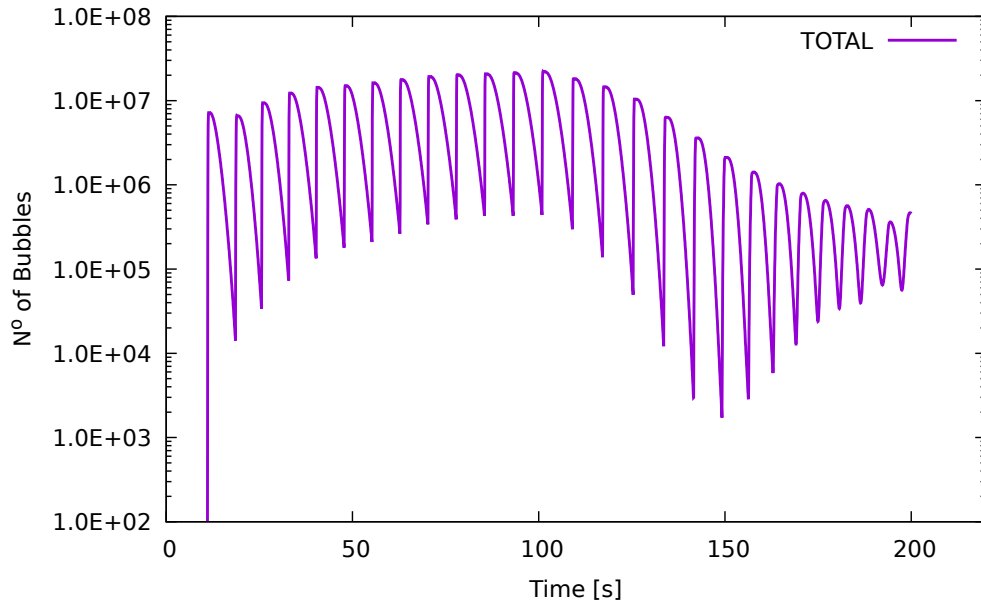


Fig. 5.3.6. Total number of bubbles predicted by the model for the CRAC-29 experiment.

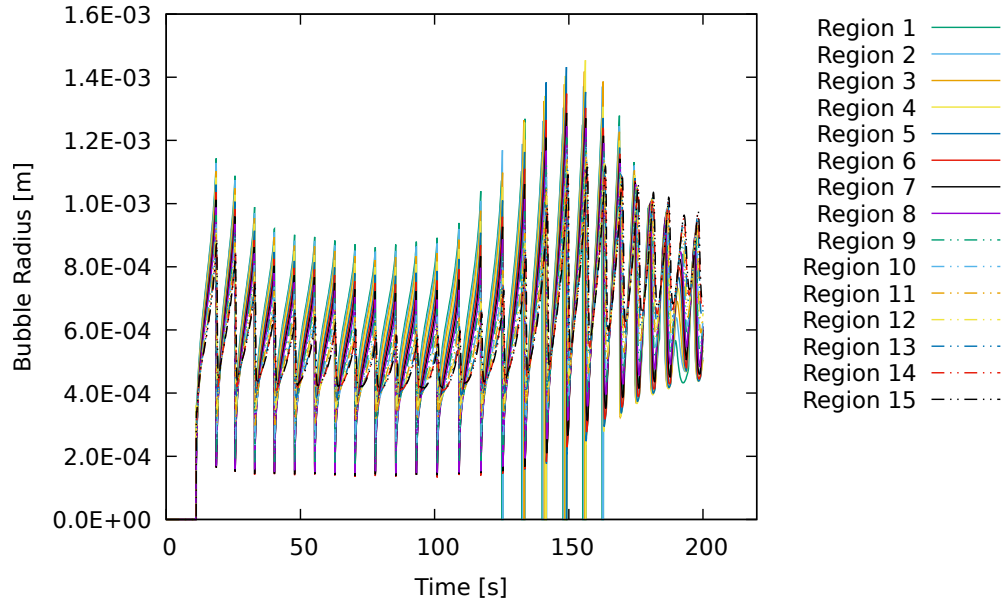


Fig. 5.3.7. Radius of bubbles predicted by the model for the CRAC-29 experiment in each vertically discretised region of the fuel solution. Regions are numbered from the bottom of the fuel solution (Region 1) to the top (Region 15).

slightly faster than the temperature observed during the experiment, however there is relatively close agreement between the model and experiment, and the model is successful in reproducing many of the qualitative features of the experimental results. In particular, the model correctly predicts that the solution temperature increases in a stepwise manner, due to the fission power oscillations discussed above. The model also correctly predicts that the stepwise increase eventually dies out, leading to a plateau at approximately 91°C.

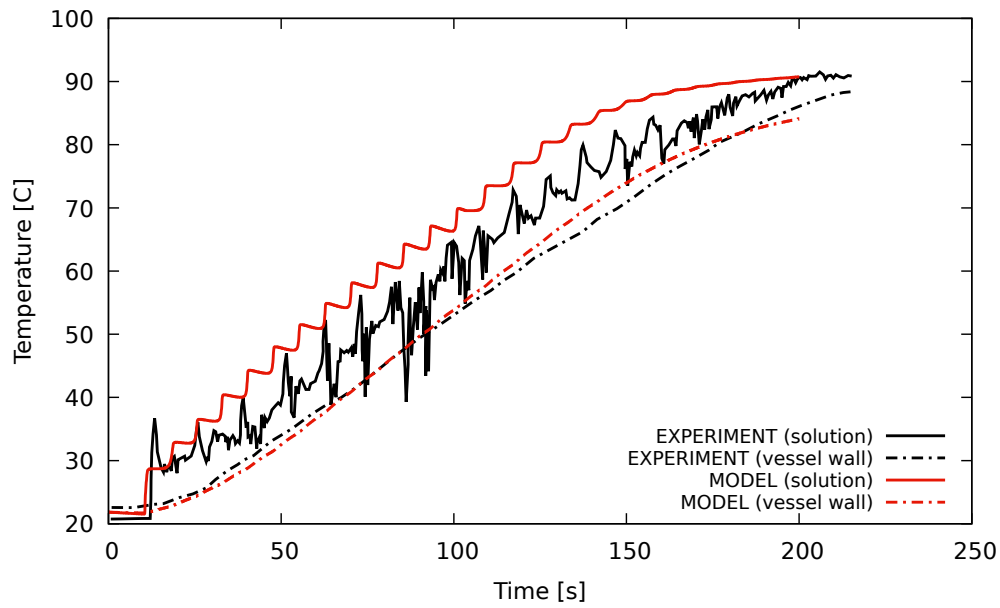


Fig. 5.3.8. Experimental and predicted temperature of the fuel solution and vessel wall for the CRAC-29 experiment. Experimental temperature profile digitised from Barbry et al. (1973).

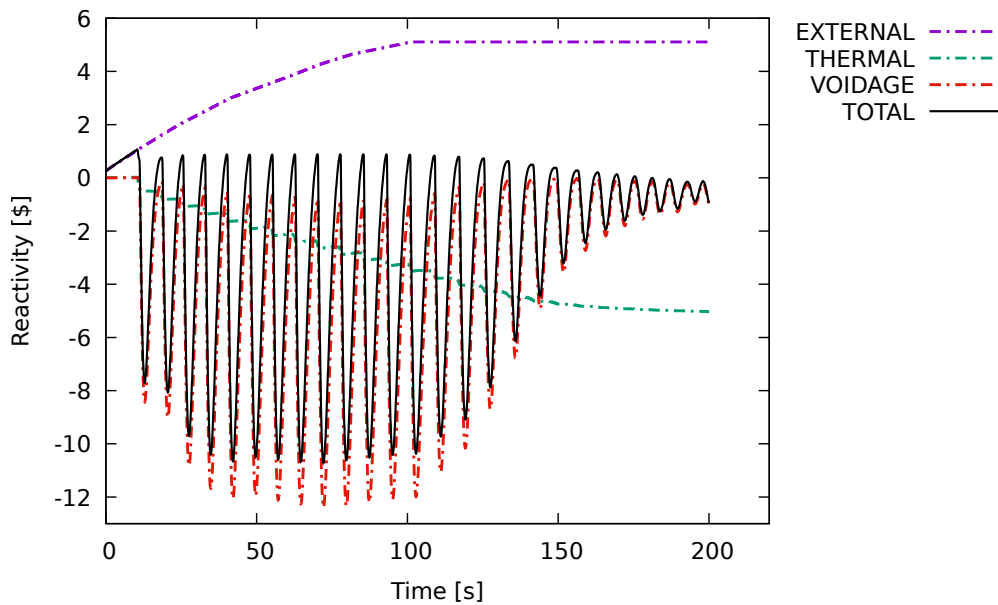


Fig. 5.3.9. Individual contributions and total reactivity predicted by the model for the CRAC-29 experiment.

Figure 5.3.9 highlights that, while thermal reactivity feedback increases smoothly, void reactivity feedback is produced in pulses, which cause oscillations in the fission power output. These power oscillations begin to die away once the temperature has risen to a point at which almost all the inserted reactivity is cancelled out by thermal feedback alone. The experimental data shows that the oscillations die away faster than the model predicts.

The amplitude of the fission power oscillations reflects the amount of radiolytic gas and the number

of bubbles produced, each time the solution becomes saturated with radiolytic gas, before the solution returns to an unsaturated state. This depends partly on the rate at which dissolved gas is transported from the aqueous phase into the bubbles; this rate being characterised in the model by the parameter α_c . It also depends on the rate at which radiolytic gas is generated in the fuel solution, which in turn depends on the current power level and radiolytic gas generation coefficient. The frequency of the fission power oscillations depends on the time taken for the bubbles to advect from the fuel solution. This in turn depends on the number and size of the bubbles produced. The frequency and amplitude are also affected by the amount of oxygen present in the fuel solution, since the presence of dissolved oxygen reduces the critical concentration of hydrogen at which bubbles can appear.

5.3.6 Sensitivity to the Mixing Coefficient

The period of the fission power oscillations due to radiolytic gas effects was found to be influenced by the rate of mixing in the solution. Figure 5.3.10 shows the power profiles for two simulations run with different solution mixing coefficients. Figure 5.3.10a was run with a mixing coefficient of $3.34 \times 10^{-3} \text{ m}^2 \text{ s}^{-1}$ and Figure 5.3.10b was run with a mixing coefficient of $0.1 \text{ m}^2 \text{ s}^{-1}$.

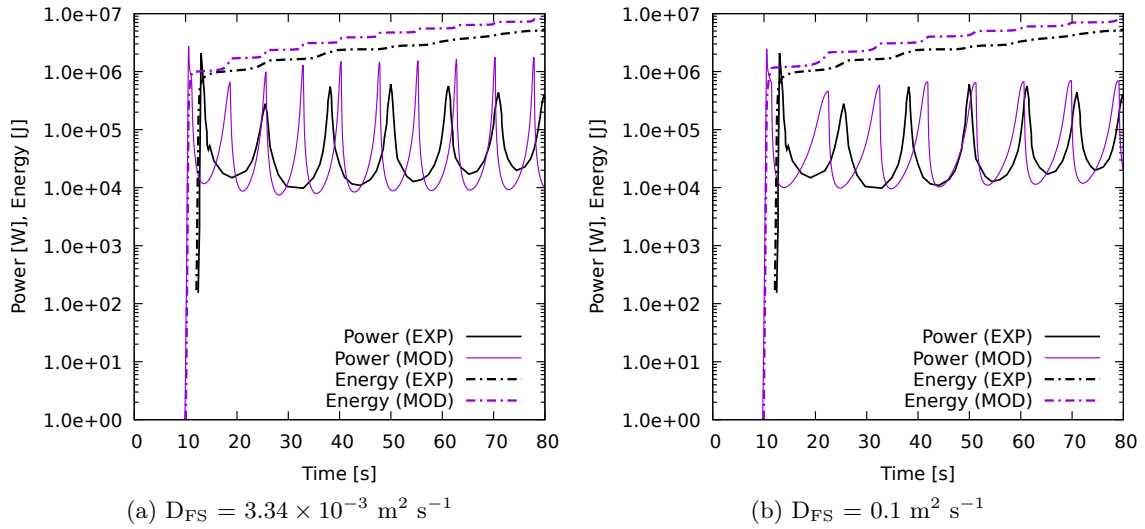


Fig. 5.3.10. Predicted power profiles simulated with two different mixing coefficients.

The reason for the observed sensitivity is that fission track bubbles can only serve as nucleation sites in regions where the dissolved hydrogen concentration exceeds the critical concentration. When the rate of mixing is high, dissolved hydrogen is moved more quickly from areas of high concentration to areas of lower concentration. This delays the time at which the critical concentration is reached and increases the total volume of fuel solution that will reach saturation. These two factors lead to an increase in the total number of bubbles produced during saturation, and because the total amount of

radiolytic gas produced is the same, a reduction in the average bubble size. This affects the period of fission power oscillations because the smaller bubbles advect more slowly leading to a longer period of oscillation. It is possible that the rate of mixing is higher than predicted in the CRAC-29 experiment due to the influence of inflowing fuel solution.

The rate of mixing is an important parameter determining the dynamics of fissile solutions whose behaviour is dominated by radiolytic gas formation. It would be useful to replace the user-defined mixing coefficient with a time-dependent model of turbulent mixing which accounts for agitation of the fuel solution induced by heating, bubble formation and inflow of additional solution. A model which tracks the solution kinetic energy of the fluid may be possible based on the Kolmogorov turbulent cascade theory, a description of which can be found in Cushman-Roisin (1974).

5.4 Simulation of the TRACY R76 Experiment

TRACY is an aqueous homogeneous reactor which was operated by the Japan Atomic Energy Agency. TRACY used a fuel solution comprising uranyl nitrate and nitric acid in aqueous solution, however unlike CRAC and SILENE which used high-enriched uranium (HEU) fuel, the TRACY reactor used low-enriched uranium (LEU). Details of the TRACY reactor, and in particular the R76 experiment, can be found in Miyoshi et al. (2009), Liem and Naito (2015) and Nakajima et al. (2002c).

5.4.1 Reactivity and Delayed Neutrons

The TRACY experimental databook (Nakajima et al. (2002c)) gives details of the reactivity insertion which was achieved by addition of fuel solution to the reactor vessel. The databook provides the following equation for the dependency of the reactivity on the solution height inside the reactor:

$$\rho[\$] = -\frac{C}{2} \left(\frac{1}{(h + \lambda)^2} - \frac{1}{(H_c + \lambda)^2} \right) \quad (5.4.1)$$

where $C = 7.67 \times 10^{10} \$ \text{ mm}^{-2}$ and $\lambda = 102 \text{ mm}$ is the vertical extrapolation distance.

Nakajima et al. (2002c) reports that the reactivity ramp began at $t = 4.25 \text{ s}$ and ended at $t = 115.1 \text{ s}$. The flow rate of fuel solution into the reactor for this experiment is reported in Liem and Naito (2015) as 20 litres per minute. These values and Equation 5.4.1 were used to construct the reactivity profile with respect to time shown in Figure 5.4.1.

The delayed neutron parameters were estimated using a MCNP model of the TRACY R76 experiment with the liquid level at the critical height and the results are shown in Table 5.6. The generation

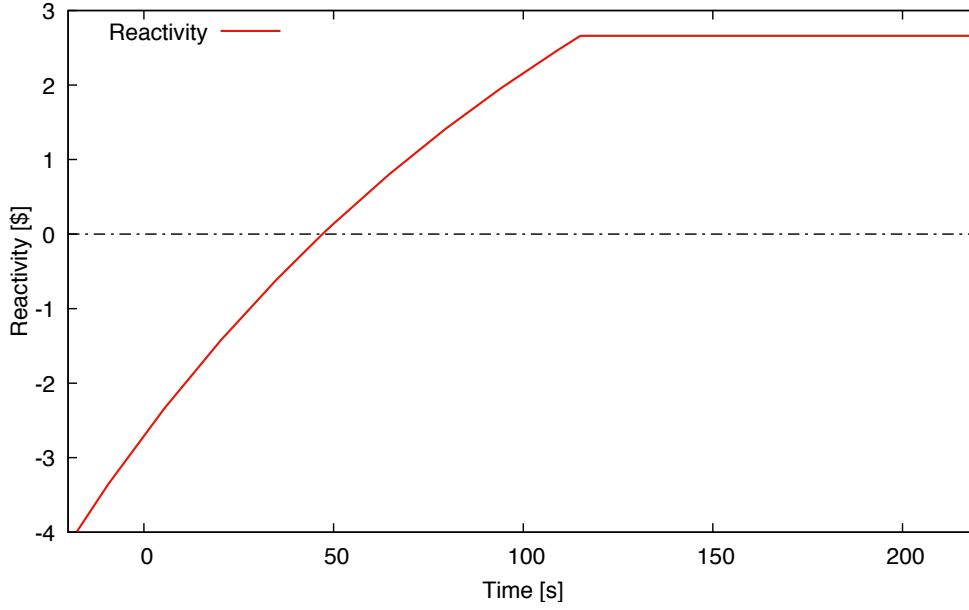


Fig. 5.4.1. Calculated time-dependent reactivity profile for TRACY R76.

time was also estimated using MCNP resulting in a value of 4.84×10^{-5} s.

TRACY R76		
i th Group	β_i	λ_i [s ⁻¹]
1	0.00031	0.01334
2	0.00147	0.03273
3	0.00131	0.12081
4	0.00274	0.30310
5	0.00116	0.85086
6	0.00048	2.85781
$\beta_{\text{eff}} = 0.00747$		

TABLE 5.6

Delayed neutron group yields (β_i) and decay constants (λ_i) for the TRACY fuel solution estimated using MCNP.

5.4.2 Reactivity Feedback Coefficients

The thermal feedback coefficient was obtained from Yamane (2015) and given by the quadratic function shown in Equation 5.4.2. The coefficients shown are the values for TRACY R72 which had a fuel solution composition almost identical to experiment n°76; the uranium concentration was slightly lower at 393.5 gU/L compared to 396.2 gU/L and the nitric acid concentration was the same.

$$\alpha_T[\$] = -0.039\Delta T - 5.1 \times 10^{-4} (\Delta T)^2, \quad (5.4.2)$$

where ΔT is the change in temperature since the start of the transient.

The void feedback coefficient was obtained from Liem and Naito (2015) who used a value equivalent to $-765.1 \text{ } \text{\$ m}^{-3}$ in their model of TRACY R76.

5.4.3 Radiolytic Gas Generation Coefficients

A value of $G_{\text{H}_2} = 1.2 \times 10^{-7} \text{ mol J}^{-1}$ has been determined by Yoshida et al. (2019) for experiments on TRACY.

5.4.4 Summary of Inputs

Table 5.7 summarises the input parameters passed to the point kinetics model.

5.4.5 Model Results

All experimental results in this section were digitised from plots presented in Liem and Naito (2015). The power profile predicted by the model is compared to the experimental power profile in Figure 5.4.2. The peak power predicted by the model was $1.10 \times 10^7 \text{ W}$ compared to an experimentally observed peak power of $3.80 \times 10^6 \text{ W}$. The peak power is therefore overestimated by the model. The power peak appears to occur before the appearance of radiolytic gas voids, indicating that the overestimate may reflect an underestimate in the degree of thermal feedback in the model. The total energy is overestimated as a result of the error in the initial power peak, with a predicted energy release of $4.50 \times 10^7 \text{ J}$ compared to an observed energy release of $1.68 \times 10^7 \text{ J}$.

Despite the errors noted above, the model succeeds in capturing many of the qualitative features of the fission power profile. The fission power initially oscillates due to repeated cycles of saturation with dissolved radiolytic gas followed by advection of bubbles from the system. The predicted period of the oscillations is approximately correct while the amplitude is slightly overestimated. The model correctly predicts that the amplitude of the fission power oscillations decreases from $t \sim 120 \text{ s}$ onwards, leading to their eventual disappearance.

The dissolved gas concentrations shown in Figure 5.4.3 indicate that the concentration of dissolved hydrogen reaches the critical concentration shortly after the initial power peak. The concentration then decreases as bubbles grow and consume the gas from the solution. This cycle repeats several times leading to the fission power oscillations discussed above. After $t \sim 140 \text{ s}$ the oscillations in the dissolved hydrogen concentration cease and the concentration then remains relatively stable at a value close to the critical concentration. The model predicts the accumulation of small quantities of dissolved oxygen

Parameter	Symbol	Value or Eq. N°	Units
Intrinsic Neutron Source	S_0	1.0	neutrons per second
Initial Temperature	T_0	298.1	K
External Temperature	T_{ext}	298.1	K
Vessel Pressure	P_l	1.01325×10^5	Pa
Generation Time	Λ	4.841×10^{-5}	s
Thermal Feedback Coefficient	α_T	$-0.039 - 5.1 \times 10^{-4}(\Delta T)$	K^{-1}
Void Feedback Coefficient	α_V	-765.1	m^{-3}
Energy per fission	ϵ	3.09813×10^{-11}	J
Neutrons per fission	$\bar{\nu}$	2.43	–
Uranyl Nitrate Concentration	C_U	1666.48	mol m^{-3}
Nitric Acid Concentration	C_N	740.0	mol m^{-3}
Uranium Enrichment	–	9.98%	–
Fuel Solution Mass	M at $t=0\text{s}$	119.2	kg
	M at $t=110\text{s}$	294.2	kg
Solution Heat Capacity	C_p	2648	$\text{J kg}^{-1} \text{K}^{-1}$
Heat Transfer Coefficient (internal)	h_{int}	1250.0	$\text{W m}^{-2} \text{K}^{-1}$
Heat Transfer Coefficient (external)	h_{ext}	6.29	$\text{W m}^{-2} \text{K}^{-1}$
Heat Transfer Coefficient (surface)	U_{surface}	7.74	$\text{W m}^{-2} \text{K}^{-1}$
Vessel Radius	r_v	0.247	m
Vessel Height	H_v	1.875	m
Vessel Mass	M_{vessel}	587.9	kg
Vessel Surface Area	A_{vessel}	3.52	m^2
Flux Extrapolation	δ_b	0.03	–
	δ_s	0.03	–
Solution Mixing Constant	D_{FS}	3.34×10^{-3}	$\text{m}^2 \text{s}^{-1}$
Radiolytic Gas Generation	G_{H_2}	1.2×10^{-7}	mol J^{-1}
Fuel Solution Density	ρ_s	Eq. E.2	kg m^{-3}

TABLE 5.7
Summary of model inputs and initial values.

in the fuel solution. The oxygen concentration remains low during the cycles of saturation/advection as the growing bubbles remove dissolved oxygen from the solution. The concentration of dissolved oxygen is predicted to rise more steeply after these oscillations have ceased.

Also shown in Figure 5.4.3 is the critical concentration for the nucleation of new radiolytic gas voids from the fission track bubbles. The critical concentration is initially predicted to be 13.6 mol m^{-3} of dissolved hydrogen at the start of the experiment but its value decreases over time due to the increase in the solution temperature. The concentration of dissolved gas in each region of the fuel solution oscillates due to the competing effects of radiolysis and bubble growth. Radiolysis increases

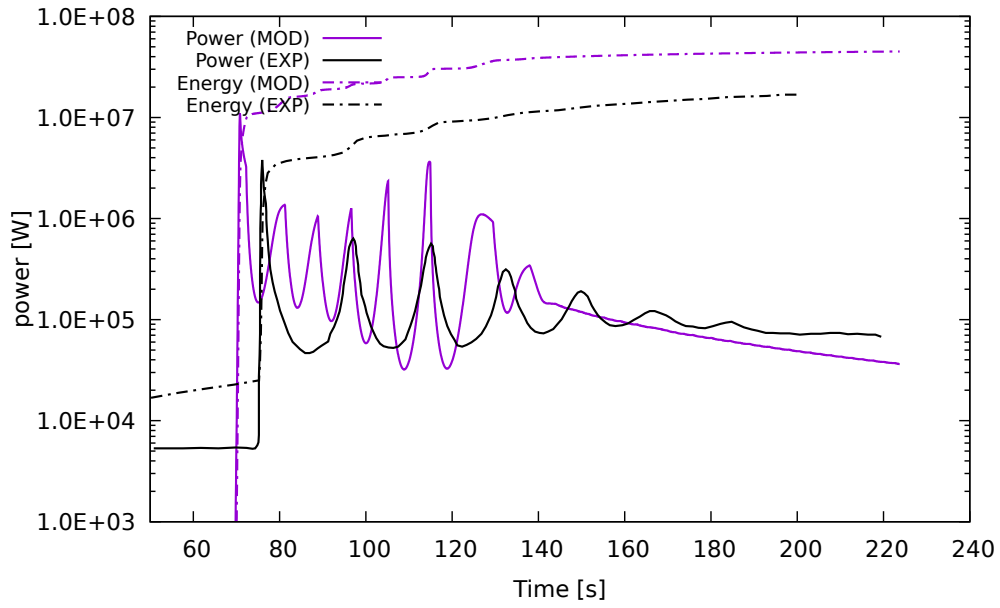


Fig. 5.4.2. Experimental and predicted fission power profiles for the TRACY R76 experiment. Experimental power profile digitised from Nakajima et al. (2002c).

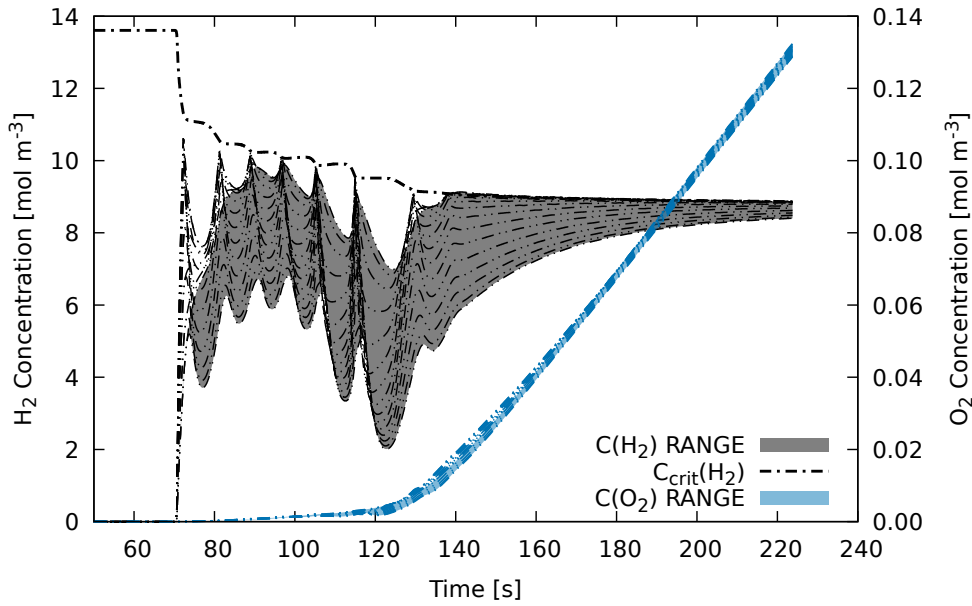


Fig. 5.4.3. Predicted concentrations of dissolved hydrogen and oxygen, as well as the critical concentration, for the TRACY R76 experiment.

concentration of dissolved gas until the critical concentration is reached, at which point the appearance of new radiolytic gas bubbles allows dissolved gas to pass into the gaseous phase, leading to a decrease in the dissolved gas concentration.

Figure 5.4.4 shows the average predicted bubble radius and Figure 5.4.5 shows the total number of bubbles in each vertically discretised region of the fuel solution. A step change in phenomena is noticeable, coinciding with the end of the fission power oscillations. During the fission power

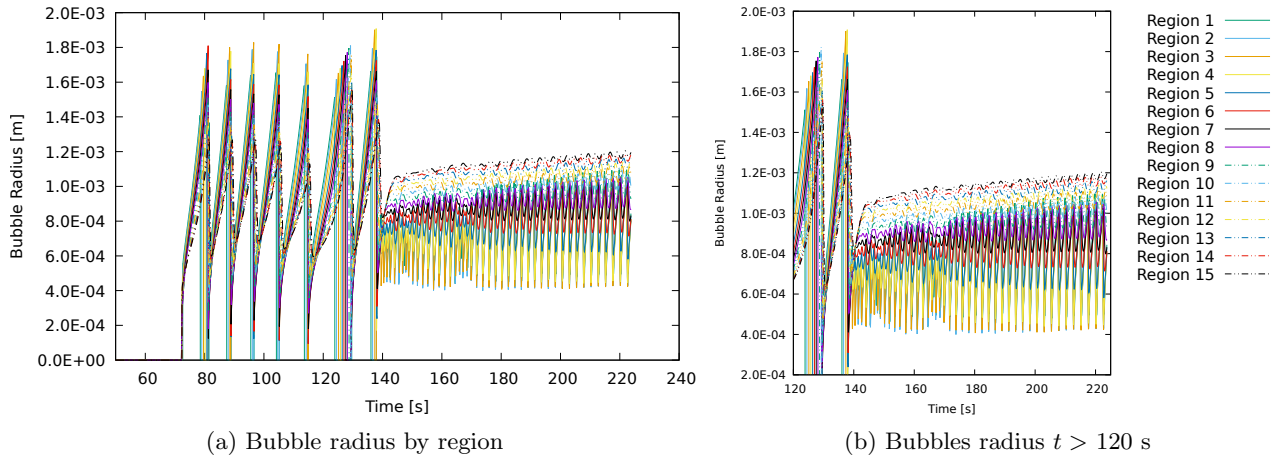


Fig. 5.4.4. Predicted bubble radius in each discretised region of the fuel solution, throughout the duration of the experiment (left) and after the end of fission power oscillations (right). Regions are numbered from the bottom of the fuel solution (Region 1) to the top (Region 15).

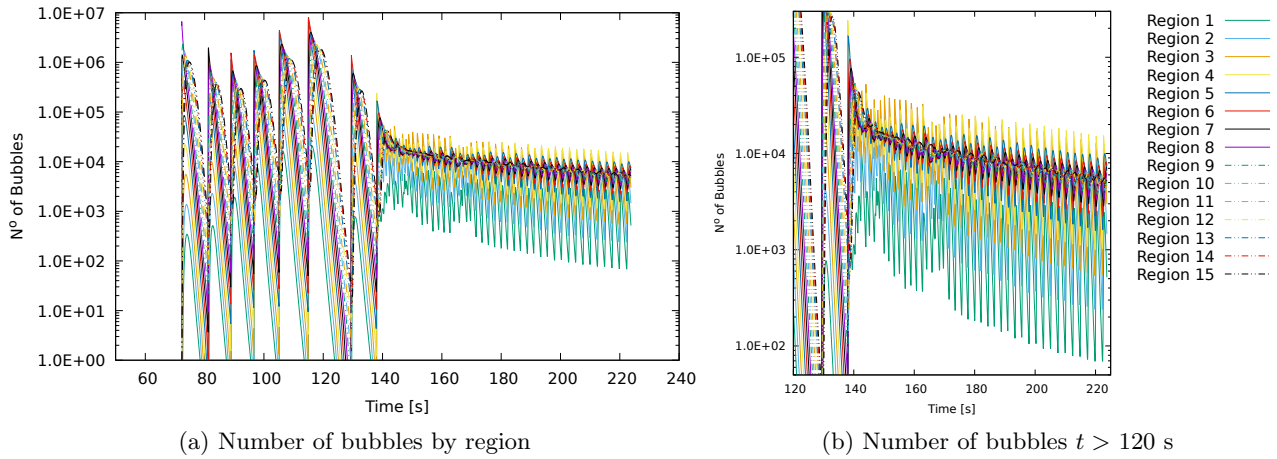


Fig. 5.4.5. Predicted number of bubbles in each discretised region of the fuel solution, throughout the duration of the experiment (left) and after the end of fission power oscillations (right). Regions are numbered from the bottom of the fuel solution (Region 1) to the top (Region 15).

oscillations, the model predicts that the entire solution undergoes cycles of saturation followed by advection of gas bubbles. During this phase, the formation of new bubbles between power spikes is effectively suppressed due to the consumption of dissolved gas by the growth of the bubbles formed during the previous spike. However, after approximately $t = 140$ s, this behaviour enters a new phase where the number of bubbles created during saturation is relatively small and the dissolved gas concentration varies relatively less between power spikes. During this period, the formation of bubbles becomes localised to the regions just below the centre of the solution. Small oscillations in the number and size of bubbles are predicted in regions 1 to 6, whereas in regions 7 to 15 a steady-state is established and the number and size of bubbles remains relatively constant. Once this second “steady-state” phase of bubble formation is reached, the amount of reactivity feedback due to

radiolytic gas voids remains small and relatively constant over time (see Figure 5.4.6), which explains the disappearance of the fission power oscillations observed in the experimental power profile.

The predicted oscillations in the local average bubble radius and the number of bubbles in each region are expected to be largely physical in nature and not purely numerical artefacts of the simulation. This is because new bubbles can only form when the concentration of dissolved gas in the fuel solution exceeds the critical concentration. This leads to repeated bursts of bubble creation, and sharp fluctuations in the interfacial area available for mass transfer of gas from the dissolved phase into the gaseous phase. This, in turn, leads to fluctuations in the size of bubbles, due to rapid growth occurring when the interfacial area is highest, followed quickly by the advection of larger bubbles into the region above or out of the solution altogether.

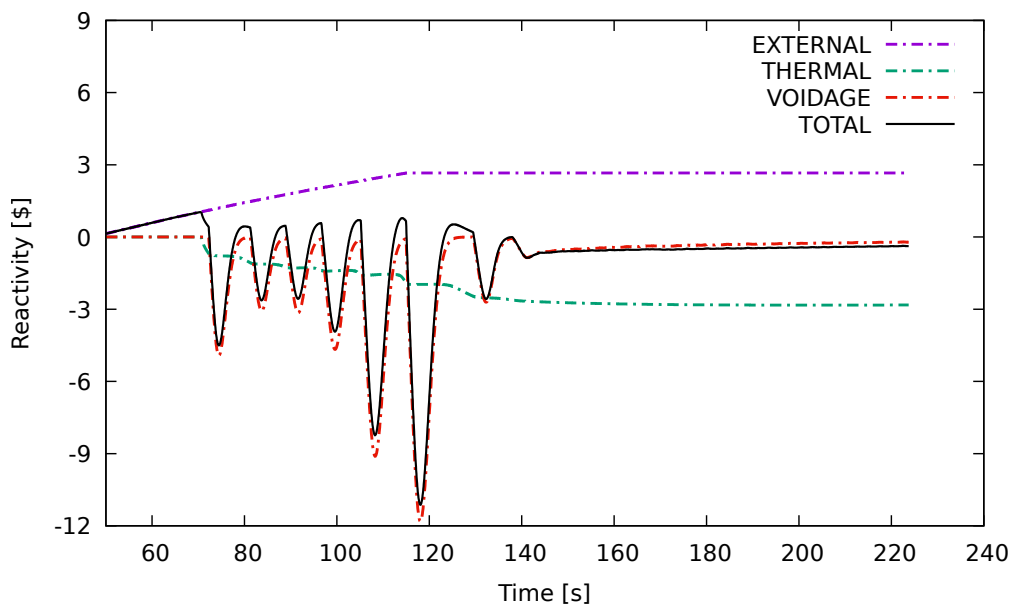


Fig. 5.4.6. Individual contributions and total reactivity predicted by the model for the TRACY R76 experiment.

Figure 5.4.7 compares the temperature profile measured by one of the TRACY reactor thermocouples (TC-C) and the average solution temperature predicted by the model. Thermocouple TC-C is located 250 mm from the reactor bottom and 40 mm away from the wall of the central channel. The maximum liquid level during the experiment is 588 mm so the thermocouple is located just below the centre of the solution. The predicted temperature profile is offset from the experimented profile during the difference in timing and magnitude of the initial power peak, however the qualitative features of the temperature profile are reproduced with step increases in the solution temperature coinciding with spikes in the fission power.

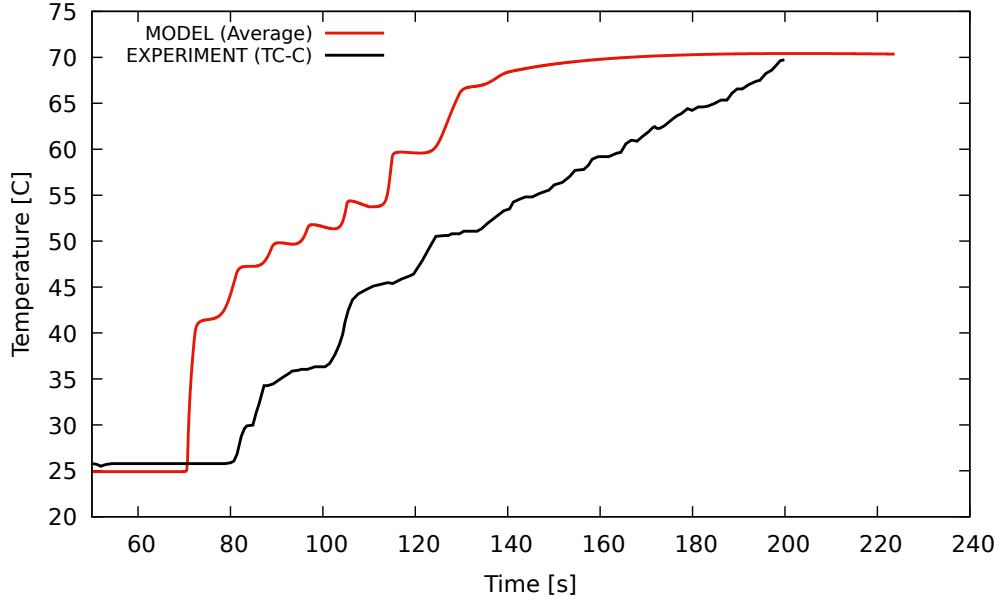


Fig. 5.4.7. Experimental and predicted temperature of the fuel solution for the TRACY R76 experiment. Experimental temperature profile digitised from Nakajima et al. (2002c).

5.5 Application to the Y-12 Accident

The point kinetics code presented in this chapter was applied to a simulation of the Y-12 accident. This accident was described in Chapter 1 and analysed in Chapter 2 where a Monte Carlo uncertainty quantification technique was used to evaluate the influence of uncertainty in the reactivity insertion rate on the resulting wait-time probability distribution of the criticality transient. In this section, the saddlepoint method presented in Chapter 2 will be combined with the point kinetics code presented in this chapter to examine the influence of stochastic uncertainty on the course of the resulting criticality transient.

The input data for the simulations presented below have been taken from Zamacinski et al. (2014), subject to some exceptions and adaptations outlined in Section 5.5.2. The purpose of the work presented here is to build upon the work of Zamacinski et al. by bringing new insights into the influence of stochastic uncertainty and radiolytic gas evolution on the course of the Y-12 criticality accident.

5.5.1 Methodology

Stochastic uncertainty in the initiation time is evaluated using the saddlepoint method described in Section 2.2.2. The fission rate threshold is set at a level equivalent to 1 Watt of power output. The intrinsic neutron source is set at the lower estimate given in Section 2.3.2 of 30 n/s based on the

experimental measurements of Harris (1960). These stochastic calculations will be used to determine the times at which the cumulative probability of exceeding the fission power threshold is equal to 0.05 and 0.95, respectively.

The point kinetics code was set up to simulate the Y-12 criticality transient, using the input data derived by Zamacinski et al. (2014). This includes the time-dependent reactivity profile, reactivity feedback coefficients, radiolytic gas generation coefficient, delayed neutron parameters and generation time.

The initiation time of the simulated transient will need to be adjusted so that the fission power output reaches 1 Watt at the desired moment. This will be achieved by varying the intrinsic neutron source strength to produce a deterministic realisation with the desired initiation time. Using this technique ensures that the populations of the delayed neutron precursors will match their expected values at the moment the fission power output crosses the threshold.

5.5.2 Input Data

The thermal feedback coefficient is adapted from Equation 56 of Zamacinski et al. (2014) which is based on MCNP simulations and gives the thermal feedback coefficient as a function of the absolute temperature of the solution. This equation has been adapted to the following form which returns the thermal feedback coefficient as a function of the rise in temperature since the start of the transient:

$$\alpha_T[\$K^{-1}] = -2.4208 \times 10^{-2}(\Delta T) - 1.74598 \times 10^{-4}(\Delta T)^2 + 4.82338 \times 10^{-7}(\Delta T)^3 - 4.95197 \times 10^{-21}(\Delta T)^4. \quad (5.5.1)$$

The void feedback coefficient is assumed to vary linearly between $-597.2 \$ m^{-3}$ at minimum liquid level and $-430.4 \$ m^{-3}$ at maximum liquid level. These values are taken from Figure 13 of Zamacinski et al. (2014) which shows predicted void feedback coefficient as a function of liquid level based on MCNP simulations.

$$\alpha_V[\$ m^{-3}] = \begin{cases} -597.2 + 0.1668t & 0s < t \leq 1000s, \\ -430.4 & t > 1000s. \end{cases} \quad (5.5.2)$$

The solution composition in Zamacinski et al. (2014) is based on data from Buchan et al. (2013) who estimated an initial uranium content of 38.16 gU/L, equivalent to $171.0 mol m^{-3}$ of uranyl nitrate, decreasing to 26.48 gU/L by the end of the transient. The point kinetics code takes a fixed uranium concentration, from which it determines the solution density, radiolytic gas generation coefficient and

fission fragment LET. The small effect of the change in the uranyl nitrate concentration on these parameters over the course of the transient was therefore neglected.

The change in the fuel solution mass over time was modelled according to the values given in Table 1 of Zamacinski et al. (2014). The heat capacity was estimated based on the initial solution composition using the Equation 4.2.4 and the radiolytic gas generation coefficient was estimated using Equation 3.2.26.

The model inputs are summarised in Table 5.8.

5.5.3 Results

5.5.3.1 Effects of Initiation Time

Using the saddlepoint method to solve the backward form of the generating function for the probability distribution of the neutron population as a function of time, the wait-time was determined for a fission power threshold of 1 W in the presence of an intrinsic neutrons source of 30 n/s. The resulting probability distribution is shown in Figure 5.5.1 alongside the time-dependent reactivity profile.

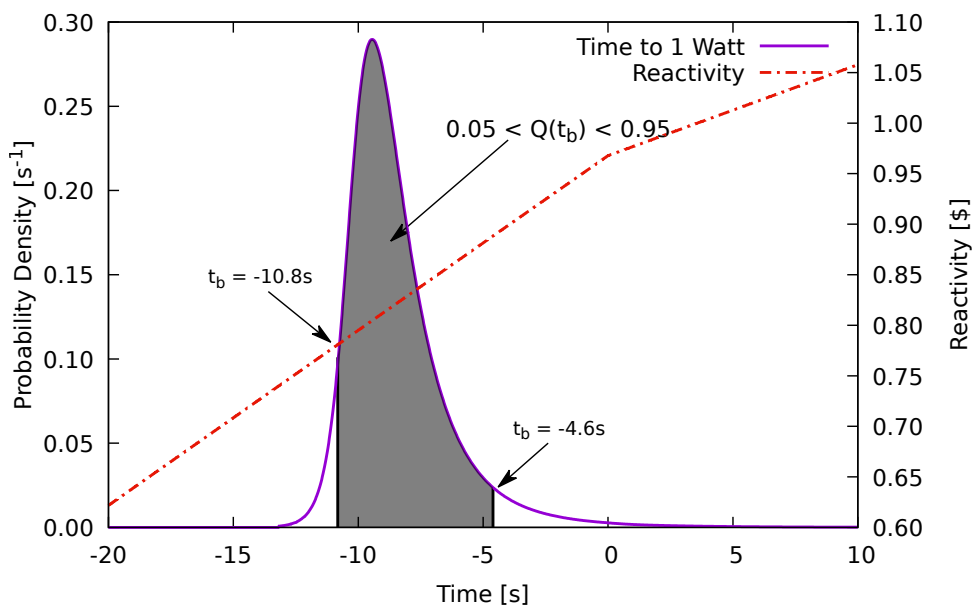


Fig. 5.5.1. Wait-time probability distribution for the fission power during the Y-12 accident to exceed a threshold value of 1 Watt.

The probability distribution was used to determine the times at which the fission power had a 5% and 95% probability, respectively, of having exceeded the fission power threshold. These times were determined to be -10.8 s and -4.6 s. These times are based on the timescale of the reactivity profile

Parameter	Symbol	Value, Eq. N° or Ref.	Units
Intrinsic Neutron Source	S_0 (Q=0.05)	3070	neutrons per second
	S_0 (Q=0.95)	1.10×10^{-2}	neutrons per second
Initial Temperature	T_0	293.0	K
External Temperature	T_{ext}	293.0	K
Vessel Pressure	P_l	1.01325×10^5	Pa
Generation Time	Λ	4.1008×10^{-5}	s
Thermal Feedback Coefficient	α_T	Eq. 5.5.1	$\text{\$ K}^{-1}$
Void Feedback Coefficient	α_V at t=0s	-597.2	$\text{\$ m}^{-3}$
	α_V at t=1000s	-430.4	$\text{\$ m}^{-3}$
Energy per fission	ϵ	3.09813×10^{-11}	J
Neutrons per fission	$\bar{\nu}$	2.43	–
Uranyl Nitrate Concentration	C_U	170.98	mol m^{-3}
Nitric Acid Concentration	C_N	0.0	mol m^{-3}
Uranium Enrichment	–	90%	–
Fuel Solution Mass	M	Table 1 of Zamacinski et al. (2014)	kg
Solution Heat Capacity	C_p	4050	$\text{J kg}^{-1} \text{K}^{-1}$
Heat Transfer Coefficient (internal)	h_{int}	1250.0	$\text{W m}^{-2} \text{K}^{-1}$
Heat Transfer Coefficient (external)	h_{ext}	6.29	$\text{W m}^{-2} \text{K}^{-1}$
Heat Transfer Coefficient (surface)	U_{surface}	7.74	$\text{W m}^{-2} \text{K}^{-1}$
Vessel Radius	r_v	0.286	m
Vessel Height	H_v	0.869	m
Vessel Mass	M_{vessel}	8.8	kg
Vessel Surface Area	A_{vessel}	3.35	m^2
Flux Extrapolation	δ_b	0.03	–
	δ_s	0.03	–
Solution Mixing Constant	D_{FS}	3.34×10^{-3}	$\text{m}^2 \text{s}^{-1}$
Radiolytic Gas Generation	G_{H_2}	1.55×10^{-7}	mol J^{-1}
Fuel Solution Density	ρ_s	1052.7	kg m^{-3}

TABLE 5.8
Summary of model inputs and initial values.

derived by Zamacinski et al. (2014) who predicted that the solution reached a critical configuration at $t = -62.72$ s.

Figure 5.5.2 compares the fission rate and total number of fissions predicted by the model as a function of time for the early and late initiated transients. The peak fission rates and total number of fissions for each transient are shown in Table 5.9 and compared to the values obtained by Zamacinski et al. (2014) and those reported in the original accident report of Patton et al. (1958). The predicted

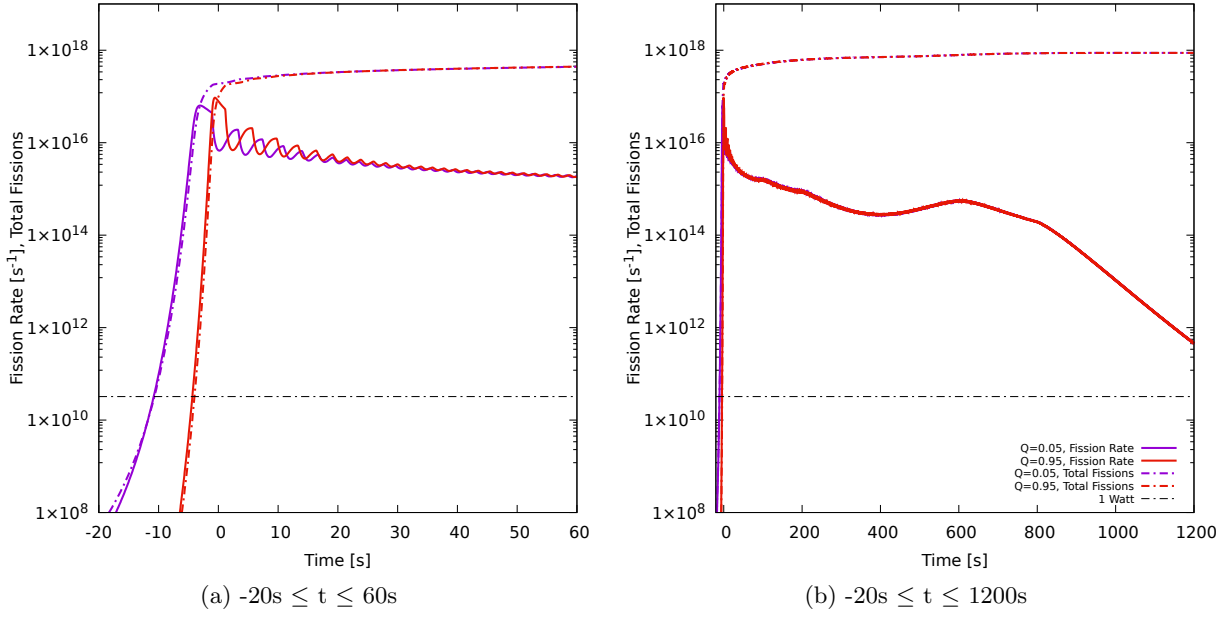


Fig. 5.5.2. Predicted fission power profile of the Y-12 accident.

peak fission rate is 44% higher in the late initiation case than in the early initiation case, however the total energy released up to the power peak is slightly less in the late initiation case. The total energy released at the end of the transient is the same in both cases.

	Early Initiation	Late Initiation	Accident Report	Units
Peak Fission Rate	6.344×10^{16}	9.346×10^{16}	–	s^{-1}
Total Fissions at Peak Power	6.538×10^{16}	4.471×10^{16}	6×10^{16}	–
Total Fissions at t_f	8.741×10^{17}	8.741×10^{17}	1.3×10^{18}	–
Time from 1W to 10^{16} Fissions	6.3	3.0	–	s

TABLE 5.9

Peak fission rate and total number of fissions, values predicted by the point kinetics code compared to those reported in the literature.

Table 5.9 also shows the time taken for the transient to release 10^{16} fissions after crossing the threshold 1W power level. This figure is included to give an indication of the influence of initiation time on the effectiveness of operator evacuation measures upon hearing the Criticality Accident Alarm System (CAAS). If the CAAS would be triggered at a fixed fission rate (e.g. 1 Watt) then this figure indicates the time available before a given radiation dose would be received. The results of this calculation indicate that a modest improvement in the effectiveness of evacuation measures could be expected in the early initiation case compared to the late initiation case, providing a few extra seconds as long as operators evacuated the area promptly upon hearing the alarm.

The initiation time of the transient has very little effect on the temperature of the solution, as shown in Figure 5.5.3. This is because the initiation time has little effect on the course of the transient

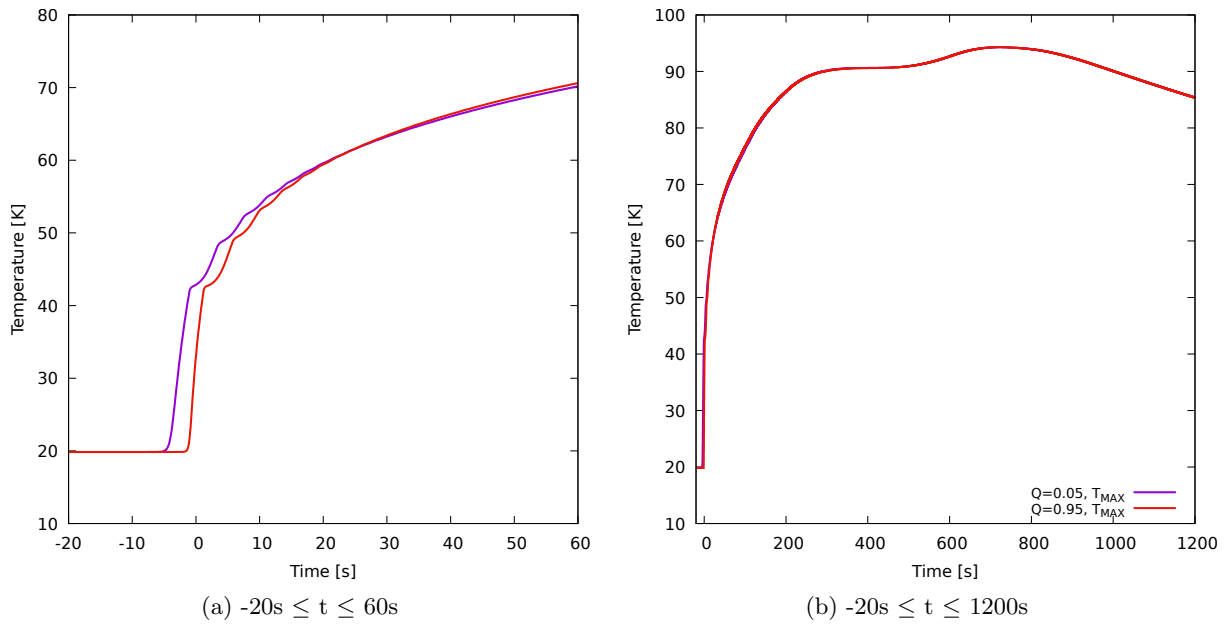


Fig. 5.5.3. Predicted solution temperature as a function of time during the Y-12 criticality accident.

beyond the initial power peak, after which the two transients tend to converge.

5.5.3.2 Predictions of the Radiolytic Gas Model

The power profile predicted by the new code is similar to that presented in the paper of Zamacinski et al. (2014), however the new code predicts small oscillations in the fission power due to the appearance and advection of radiolytic gas voids. The predicted number of bubbles produced due to radiolysis within the fissile solution is shown in Figure 5.5.4 for the early initiation case.

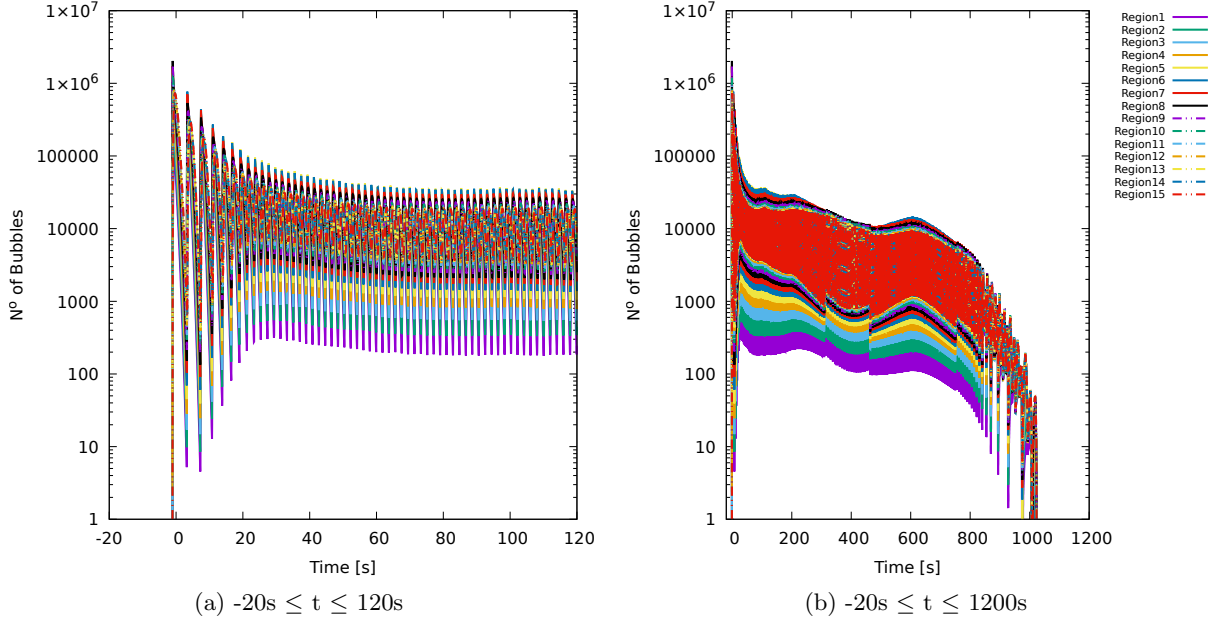


Fig. 5.5.4. Number of bubbles predicted in each vertically discretised region as a function of time during the Y-12 criticality accident. Regions are numbered from the bottom of the fuel solution (Region 1) to the top (Region 15).

The model predicts that the total number of bubbles oscillates between approximately 10^4 and 10^6 during most of the transient. There is a corresponding oscillation in the average bubble radius predicted in each vertically discretised region of the fissile solution. The size of the bubbles oscillates between approximately 0.4 mm and 0.9 mm during most of the transient.

Unlike the CRAC-29 and TRACY R76 benchmark experiments, the repeated cycles of saturation of the fuel solution followed by bubble advection do not contribute to large oscillations in the fission power. This is due to the smaller value of α_V associated with the Y-12 scenario which means that the bubbles produced have a smaller reactivity worth than those produced in the benchmark experiments presented earlier.

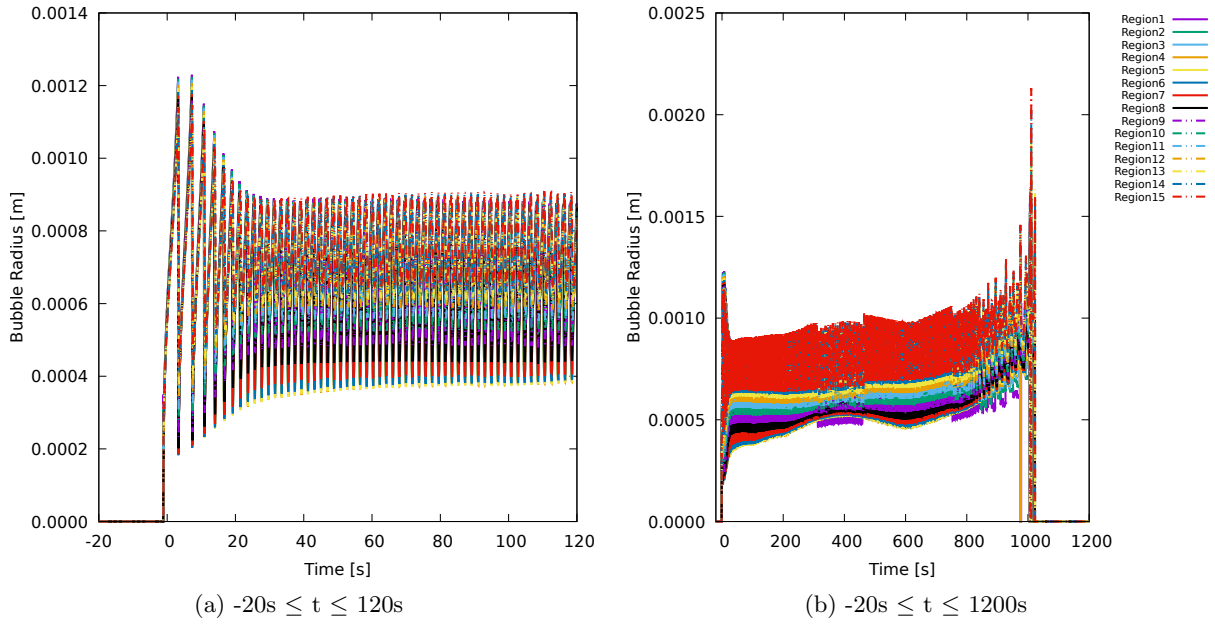


Fig. 5.5.5. Average bubble radius predicted in each vertically discretised region as a function of time during the Y-12 criticality accident. Regions are numbered from the bottom of the fuel solution (Region 1) to the top (Region 15).

5.6 Conclusions

This chapter presents a new method for modelling the formation and behaviour of gas voids in point kinetics models of criticality transients in fissile liquids. The point kinetics code presented includes:

- a new model to predict the number of bubbles produced during saturation of the fuel solution with radiolytic gas based on work presented in previous chapters;
- a model for the rate of mass transfer of gas molecules from the dissolved phase to the gaseous phase based on the number of bubbles per unit volume;
- a basic model of bubble collapse due to simple diffusion;
- prediction of the critical concentration for gas bubble formation based on the solution temperature and its composition, including the presence of any dissolved oxygen.

The model also incorporates a correlation for predicting the Henry's law constants for hydrogen and oxygen gas in solutions of uranyl nitrate, necessary for the accurate prediction of the critical concentration for gas void formation, and a model of oxygen production from the decomposition of hydrogen peroxide.

The models summarised have been incorporated into a point kinetics code and validated against

three criticality benchmark experiments, demonstrating close agreement between the model and the experimental results. A particular feature of the new method is the ability to predict the number and size of radiolytic gas bubbles produced during saturation of a fissile solution with radiolytic gas. This permits an accurate prediction of the rate of gas advection from the system, which in turn allows an accurate prediction of the timing and magnitude of secondary power peaks. This predictive capability has been demonstrated by comparison to an experiment on the SILENE reactor in which a secondary power peak occurs.

The model currently incorporates a mixing model in which the rate at which material is transported between regions of the fuel solution is characterised by a mixing coefficient. The mixing coefficient is assumed constant and estimated based on literature values for average fluid velocities in fissile liquids and the geometry of a particular fuel solution. The value of this coefficient has been shown to have a strong influence on the behaviour of radiolytic gas within the fissile solution and the need for a time-dependent mixing coefficient has been identified as an area of further work required to improve the predictive capabilities of the new point kinetics code.

The new code lends support to the importance of nucleation sites in the timing and rate of appearance of radiolytic gas during nuclear criticality transients in fissile solutions, confirming the role of fission track bubbles in providing suitable nucleation sites. This phenomenon can explain the fission power oscillations observed in many criticality benchmark experiments where the concentration of dissolved radiolytic gas in the fuel solution oscillates about the level at which gas can come out of solution on the fission track bubbles.

The code has been applied, along with stochastic methods presented in an earlier chapter, to an analysis of the Y-12 accident. This analysis examines the importance of transient initiation time on the rate of energy release during the Y-12 criticality accident, indicating that stochastic effects may play a significant role in determining the radiation dose received by workers, as well as the effectiveness of Criticality Accident Alarm Systems (CAAS) in mitigating the consequences of such an accident.

Chapter 6

Conclusions and Future Work

6.1 Thesis Summary

This thesis presents the development of mathematical and computational models for simulating transient nuclear excursions in aqueous fissile solutions. The aim of this research was to develop more fundamentally based, mechanistic, high-fidelity models of the underlying physical phenomena; and as a consequence eliminate some of the assumptions and approximations that have been used to model such systems in the past. As discussed in Chapter 1, there is a need to develop aqueous fissile solution models with predictive capabilities for use in nuclear criticality safety assessment. Currently available models for aqueous fissile solutions require the tuning of adjustable model parameters in order to match the predictions of the model to experimental profiles, thus removing much of their usefulness as predictive tools. Other models that don't require the tuning of parameters rely on simplified approaches that cannot hope to reproduce the complex behaviour of real systems. This is especially true of models of radiolytic gas, which are extremely important in determining the time-dependent characteristics of a criticality transient. Another important area of criticality safety is the quantification of uncertainty when transients are initiated in the presence of a weak intrinsic neutron source. This thesis presents a new method for quantifying the uncertainty in the wait-time probability distributions for criticality transients, including stochastic uncertainty with uncertainty due to epistemic uncertainty in the input parameters.

Chapter 1 presents an overview of the fundamental physics of criticality transients in aqueous fissile solutions as well as setting out the motivation for the work presented in the chapters that follow. Chapter 2 presents the method of uncertainty quantification for criticality transients initiated in the presence of a weak intrinsic neutron source. Chapter 3 goes on to examine the mechanics of

radiolysis in fissile solutions at the level of individual gas bubble formation, resulting in a method to estimate the size and number of gas bubbles deposited along the tracks of fission fragments. This information is used in Chapter 4 to develop a model of bubble growth and collapse in a fissile solution as it becomes saturated with radiolytic gas. Finally, the results of this model are incorporated in Chapter 5 into a point kinetics model of a full scale fissile liquid system which is then successfully validated against the results of three benchmark experiments.

Some of the principal findings of the work are summarised below:

- The gamma distribution method can be used for rapid quantification of uncertainty in wait-time probability distributions for nuclear criticality excursions initiated in the presence of a weak neutron source. The method reduces the calculation time for the wait-time probability distribution for certain scenarios to a fraction of a second, opening up the possibility of uncertainty quantification via the Monte Carlo method.
- An uncertainty of $\pm 10\%$ in the flow rate of the fissile solution in the Y-12 accident would result in a significant broadening of the effective wait-time probability distribution, increasing its standard deviation from 2.1 to 2.9 seconds in the presence of an intrinsic source emitting 30 n/s. A similar effect has been demonstrated for experiments on the Caliban reactor.
- The number, size and location of bubbles containing vapour and radiolytic gas, deposited along the tracks of fission fragments during nuclear criticality transients in aqueous fissile solutions, can be estimated by means of an energy balance over the bubble formation process. Combining this method with LET profiles calculated for the 250 highest-yielding fission fragments of ^{235}U , empirical correlations are presented for rapid determination of maximum bubble size as a function of the temperature and composition of uranyl nitrate solutions. These correlations can be used to estimate the critical concentration of the solution at which gas voids will appear during a nuclear criticality transient.
- The number of bubbles produced during saturation of a fissile solution with radiolytic gas can be estimated as a function of the fission energy deposited in the solution during the saturation process. Correlations are presented that permit the rapid estimation of the bubble number density for use in point kinetics models of fissile solutions.
- The rate of mass transfer of soluble gas between the dissolved and gaseous phases in a fissile solution depends on the number density of bubbles present in the solution. A correlation is presented for the rate constant based on the results of a numerical simulation of the saturation and bubble growth processes.

- A new expression is presented for the critical concentration of dissolved hydrogen gas that must be reached before the appearance of radiolytic gas voids in a fissile solution. The new expression depends on the size of the largest fission track bubbles, which can be estimated from the correlations discussed above, and the concentration of any other dissolved gases present in the solution. The critical concentration, which is often presumed constant, is predicted to vary significantly as a function of solution composition and temperature.
- A novel model of radiolytic gas in aqueous fissile solutions is presented and validated against experimental data. The new model has been shown capable of predicting the onset of fission power oscillations due to radiolytic gas effects in the CRAC-29 and TRACY R76 experiments. It can also predict the approximate timing and magnitude of secondary fission power peaks, as demonstrated by a simulation of experiment S3-258 on the SILENE fissile solution reactor.
- A deterministic-stochastic analysis of the Y-12 accident has shown that the stochastic uncertainty in the initiation time of the excursion can have an important impact on the kinetics of the resulting criticality excursion. In the case of the Y-12 accident, early initiation was found to add valuable seconds between the start of the excursion and the time to peak power. Early initiation also reduced the magnitude of the first power peak compared to late initiation, however the total accident yield remained unchanged.

The model presented in Chapter 5 does not require the tuning of adjustable parameters to experimental results and can therefore be said to have genuine predictive capabilities. However, some areas of additional research have been identified that would improve the reliability of the model across the broadest range of applications. In particular, the need for experimental data permitting the accurate prediction of the radiolytic gas generation coefficient, and the development of a mixing model for fissile solutions that is capable of adjusting the rate of mixing as a function of time.

6.2 Insights Gained

The quantification of uncertainty in the input parameters to calculations of the wait-time probability distribution has demonstrated that relatively small uncertainties in those input parameters can have a significant impact on the resulting probability distribution. The relative importance of a given degree of parametric uncertainty depends on the amount of stochastic uncertainty and therefore the intrinsic neutron source strength of the system.

The models developed in Chapters 3 to 5 offer insights into the physical processes contributing

to the time-dependent behaviour of aqueous fissile solutions during nuclear criticality transients. The number of bubbles produced per unit volume during saturation of a fissile solution has been shown to vary with the amount of fission energy deposited during the saturation process. Furthermore, the rate at which gas is transferred from the dissolved phase to the gaseous phase has been shown to depend on the number density of bubbles in the solution. This insight has permitted the removal of a parameter which is an important tunable user-prescribed input in criticality safety codes such as CRITEX.

Incorporating the saturation model into a point kinetics model of a full scale system has helped to elucidate the mechanisms by which radiolytic gas contributes to oscillations in the fission power produced by a fissile solution. During benchmarking, the model has been shown to successfully predict the timing and appearance of a secondary power peak, thanks to accurate prediction of the number (and therefore size and advection velocity) of bubbles produced during saturation of the solution during the initial power peak.

6.3 Future Work

It has been previously highlighted in Chapter 5 that a time-dependent mixing model would be required in order to accurately predict the period of fission power oscillations due to cycles of saturation/desaturation of the fuel solution with radiolytic gas. Such a model may be possible by means of an energy balance, tracking the addition and dissipation of kinetic energy within the fuel solution. As noted in Chapter 5, kinetic energy will be added to the fuel solution due to the advection of gas bubbles. The addition of fuel solution will also add kinetic energy due to the momentum imparted by the incoming solution. The Kolmogorov cascade theory (Cushman-Roisin (1974)) of energy dissipation in fluid systems could provide the starting point for such a model.

The work presented in Chapters 3 to 5 of this thesis provides new models for accurately characterising the behaviour of homogeneous aqueous fissile solutions. This corresponds to a need of the nuclear industry where aqueous solutions of fissile material have widespread applications. There is also a strong industrial need to develop similar models for more complex, heterogeneous systems, consisting of sludges, slurries, cakes, emulsions and wetted powders. Heterogeneous systems consisting of one or more liquid or solid phases dispersed within a liquid phase are also widespread throughout the nuclear fuel cycle (IAEA (2014)). One example is the processing of uranium ore, where the ore is crushed into a powder, mixed with leaching agents and then filtered to produce an insoluble uranium-rich powder known as yellowcake.

The addition of water to a bed of dry insoluble powder (such as uranium oxides or yellowcake)

involves complex physical processes governing the rate of infiltration of the water. Once wet, the water acts as a moderator, shifting the energy spectrum of neutrons towards thermal energy levels. Whether or not this is sufficient to lead to a criticality excursion will depend on the packing fraction of the material which will determine the H/U ratio achievable. If an excursion were to occur, the action of fission fragments in the aqueous phase would lead to the creation of gases due to radiolysis and the heat produced may lead to steam generation. Unlike in homogeneous liquids, where gas bubbles are free to advect from the system, gas bubbles produced within a wetted particle bed may become trapped in the particle matrix. The infiltration of water in powders has been examined in an experiment on the SILENE reactor (Rozain et al. (1991)) but there is a need to develop methods for simulating these phenomena during nuclear criticality excursions.

An example of a criticality accident in a complex heterogeneous system which has already occurred is the 1970 Windscale criticality accident, descriptions of which can be found in Knief et al. (1985) and McLaughlin et al. (2000). This accident involved the formation of an organic phase rich in plutonium which, unbeknown to the operators, accumulated inside a solution transfer vessel. The partition coefficient for the plutonium compound between the aqueous and organic phases was strongly in favour of the organic phase, leading to the accumulation over months or years of high concentrations of plutonium in the organic phase, and eventually resulting in a criticality excursion. The Windscale accident demonstrates the subtle importance of diverse physical processes in the causation of criticality accidents, in this case, the partitioning and mass transfer of a plutonium compound between separate aqueous and organic phases in direct contact.

The heterogeneous nature of the systems described above may require a move away from point reactor kinetics towards multi-point kinetics, where two or more distinct regions exist, or for more complex geometrical configurations, 2D or 3D spatially-dependent neutronics coupled to phenomenological models of thermal hydraulics.

Another important area of future work is the problem of interacting arrays of fissile material. The majority of advanced techniques for evaluating the consequences of nuclear criticality transients are concerned with events that occur within a single vessel or unit. However, the storage of fissile materials requires that individual units be placed in close proximity to each other. The distance between each unit is determined to minimise the risk of criticality while making efficient use of the available space. However, unforeseen circumstances such as a criticality transient in one of the units, or the flooding of the area containing the units, could lead to a number of storage vessels acting as an interacting array. The problem of interacting arrays could be examined by incorporating the point kinetics code presented in this thesis into a multi-point kinetics model for an arbitrary number of loosely-coupled

units using coupling coefficients based on the theory of Avery (1958).

Stochastic effects may become extremely important in arrays of interacting units, where the intrinsic source of each individual unit will often be weak. A possible extension to the uncertainty quantification technique demonstrated in Chapter 2 would be a space-dependent or multi-point model capable of quantifying the influence of stochastic and parametric uncertainty in an interacting array. By computing neutron number probability distributions for a spherical system using a model that included energy and spatial dependence, Saxby et al. (2018) demonstrated the emergence of complex features in calculated neutron number probabilities that would not have been revealed by a zero-dimensional approach.

The effect of one unit in an array undergoing a criticality transient will be to provide an extrinsic source of neutrons to the other units in the array. Where this extrinsic neutron source is strong enough this could lead to other units in the array behaving as accelerator driven systems (ADS) as the extrinsic neutrons induce fissions within them. The secondary induced transients will also produce bursts of neutrons, potentially leading to oscillatory interactions between the units. The potential for instability in coupled systems has been demonstrated by Murray et al. (1966). Calculation methods which could provide the basis for models of interacting arrays can be found in Ackroyd et al. (1961) and Thomas and Abbey (1973).

Bibliography

- Abate, J. and Whitt, W. (1992). The Fourier-series method for inverting transforms of probability distributions. *Queueing Systems*, 10(1):5–87.
- Ackroyd, R. T., Charlesworth, F. R., and Thomas, A. F. (1961). Methods of calculation for interacting arrays with special reference to storage problems. In *Criticality Control in Chemical and Metallurgical Plant, Karlsruhe Symposium*.
- Allen, A. O. (1961). *The Radiation Chemistry of Water and Aqueous Solutions*. D. Van Nostrand Company, Inc.
- Amaldi, E., Fano, U., Spencer, L. V., Berger, M. J., and Fluegge, S. (1959). *Neutronen und verwandte Gammastrahlprobleme*. Springer-Verlag.
- ANSWERS Software Service (2018). PANTHER - An Advanced 3D Nodal Code for Reactor Core Analysis. <https://www.answerssoftwareservice.com/panther/>. Accessed: 2019-11-01.
- Authier, N., Richard, B., and Humbert, P. (2014). Initiation of persistent fission chains in the fast burst reactor Caliban. *Nuclear Science and Engineering*, 177:169–183.
- Avery, R. (1958). Theory of coupled reactors. In *Second United Nations International Conference on the Peaceful Uses of Atomic Energy*.
- Barbry, F. (1987). Accidents de criticité en solution - synthèse des expériences de mesure d’onde de pression sur SILENE. Technical Report SRSC 87.96, Institut de Radioprotection et de Sécurité Nucléaire.
- Barbry, F. (1993). A review of SILENE criticality experiments. Technical Report SRSC 93.220, Institut de Radioprotection et de Sécurité Nucléaire.
- Barbry, F. (1994). SILENE Reactor - Results of selected typical experiment. Technical Report SRSC 223, Commissariat à l’Énergie Atomique.

- Barbry, F., Fouillaud, P., Grivout, P., and Reverdy, L. (2009). Review of the CRAC and SILENE criticality accident studies. *Nuclear Science and Engineering*, 161(2):160–187.
- Barbry, F., Mangin, D., and Pevol, H. (1973). Récapitulation des résultats expérimentaux. Technical Report S.E.E.S.N.C. 116, Commissariat à l’Energie Atomique.
- Barbry, F., Ratel, R., Rozain, J. P., Bickley, A., Burns, W. G., Harrison, M. I., Mather, D., and Prescott, A. (n.d.). Final report of phase 1 of the study of a criticality accident during the transport or storage of fissile material as a solution. Technical Report CEC 86-B-7015-11-007-17, CEA and UKAEA.
- Basoglu, B., Yamamoto, T., Okuno, H., and Nomura, T. (1998). Development of a new simulation code for evaluation of criticality transients involving fissile solution boiling. Technical report, Japan Atomic Energy Research Institute.
- Beckurts, K.-H. and Wirtz, K. (1964). *Neutron Physics*. Springer-Verlag Berlin Heidelberg.
- Bell, G. I. (1963). Probability distribution of neutrons and precursors in a multiplying assembly. *Annals of Physics*, 21:243–283.
- Bell, G. I. (1965). On the stochastic theory of neutron transport. *Nuclear Science and Engineering*, 21(3):390–401.
- Bidwell, R. M., King, L. D. P., and Wykoff, W. R. (1956). Radiolytic yields of nitrogen and hydrogen in water boilers. *Nuclear Science and Engineering*, 1:452–454.
- Blue, L. R., Hoffman, M., and Dunenfeld, M. (1964). A program for the numerical solution of the space independent reactor kinetics equations for KEWB. Technical Report NAA-SR-7087, Atomics International.
- Bowen, D. G. and Busch, R. D. (2006). Hand calculation methods for criticality safety - a primer. Technical report, Los Alamos National Laboratory.
- Buchan, A., Pain, C., Goddard, A., Eaton, M., Gomes, J., Gorman, G., Cooling, C., Tollit, B., Nygaard, E., Glenn, D., and Angelo, P. (2012). Simulated transient dynamics and heat transfer characteristics of the water boiler nuclear reactor SUPO with cooling coil heat extraction. *Annals of Nuclear Energy*, 48:68 – 83.
- Buchan, A. G., Pain, C. C., Tollit, B. S., Gomes, J. L. M. A., Eaton, M. D., Gorman, G. J., Cooling, C. M., Goddard, A. J. H., Nygaard, E. T., Angelo, P. L., and Smith, P. N. (2013). Simulated spatially

- dependent transient kinetics analysis of the oak ridge Y12 plant criticality excursion. *Progress in Nuclear Energy*, 63:12–21.
- Bunkin, N. F., Shkirin, A. V., Suyazon, N. V., Babenko, V. A., Sychev, A. A., Penkov, N. V., Belosludstev, K. N., and Gudkov, S. V. (2016). Formation and dynamics of ion-stabilised gas nanobubble phase in the bulk of aqueous NaCl solutions. *The Journal of Physical Chemistry*, 120:1291–1303.
- Cacuci, D. G., editor (2010). *Handbook of Nuclear Engineering*. Springer US.
- Casoli, P., Authier, N., and Baud, J. (2009). Calculation of kinetic parameters of Caliban metallic core experimental reactor from stochastic neutron measurements. In *2009 1st International Conference on Advancements in Nuclear Instrumentation, Measurement Methods and their Applications*, pages 1–7.
- Çengel, Y. A. and Boles, M. A. (2015). *Thermodynamics: An Engineering Approach*. McGraw-Hill Education, 8th edition.
- CEA (2015). *Neutronics*. Editions - Le Moniteur.
- Celata, G. P., D’Annibale, F., Marco, P. D., Memoli, G., and Tomiyama, A. (2007). Measurements of rising velocity of a small bubble in a stagnant fluid in one- and two-component systems. *Experimental Thermal and Fluid Science*, 31(6):609–623.
- Chadderton, L. T. (1988). On the anatomy of a fission fragment track. *International Journal of Radiation Applications and Instrumentation. Part D. Nuclear Tracks and Radiation Measurements*, 15(1):11–29.
- Chilton, T. H., Drew, T. B., and Jebens, R. H. (1944). Heat transfer coefficients in agitated vessels. *Industrial and Engineering Chemistry*, 36(6):510–516.
- Clayton, E. D. (1974). Anomalies of criticality. *Nuclear Technology*, 23:14–27.
- Clayton, E. D. (2010). Anomalies of nuclear criticality, revision 6. Technical Report PNNL-19176, Pacific Northwest Laboratory.
- Cooling, C. M. (2014). *Development of a Point Kinetics Model with Thermal Hydraulic Feedback of an Aqueous Homogeneous Reactor for Medical Isotope Production*. PhD thesis, Imperial College London.
- Cooling, C. M. (2019). Private Communication.

- Cooling, C. M., Williams, M. M. R., and Eaton, M. D. (2016). Coupled probabilistic and point kinetics modelling of fast pulses in nuclear systems. *Annals of Nuclear Energy*, 94:655–671.
- Cooling, C. M., Williams, M. M. R., Nygaard, E. T., and Eaton, M. D. (2014a). An extension of the point kinetics model of MIPR to include the effects of pressure and a varying surface height. *Annals of Nuclear Energy*, 72:507–537.
- Cooling, C. M., Williams, M. M. R., Nygaard, E. T., and Eaton, M. D. (2014b). A point kinetics model of the medical isotope production reactor including the effects of boiling. *Nuclear Science and Engineering*, 177(3):233–259.
- Coulson, J. M., Richardson, J. F., Backhurst, J. R., and Harker, J. H. (1996). *Chemical Engineering Volume 1: Fluid Flow, Heat Transfer and Mass Transfer*, volume 1. Elsevier Science, 6th edition.
- Courant, E. D. and Wallace, P. R. (1947). Fluctuations of the number of neutrons in a pile. *Physical Review*, 72:1038–1048.
- Cullen, D. E. (1974). Application of the probability table method to multigroup calculations of neutron transport. *Nuclear Science and Engineering*, 55(4):387–400.
- Cusham-Roisin, B. (1974). *Environmental Fluid Mechanics*. John Wiley and Sons.
- Das, M. and Sawamura, T. (2004). Estimation of nucleation parameter for neutron-induced nucleation in superheated emulsion. *Nuclear Instruments & Methods in Physics Research Section A-Accelerators Spectrometers Detectors and Associated Equipment*, 531:577–584.
- de Oliveira, C. R. E. (1986). An arbitrary geometry finite element method for multigroup neutron transport with anisotropic scattering. *Progress in Nuclear Energy*, 18(1):227–236.
- Deitrich, L. W. and Connolly, T. J. (1973). A study of fission-fragment-induced nucleation of bubbles in superheated water. *Nuclear Science and Engineering*, 50(3):273–282.
- Duval, E., Adichtchev, S., Sirotkin, S., and Mermet, A. (2012). Long-lived submicrometric bubbles in very diluted alkali halide water solutions. *Physical Chemistry Chemical Physics (Incorporating Faraday Transactions)*, 14:4125–4132.
- El-Nagdy, M. M. and Harris, M. J. (1971). Experimental study of radiation-induced boiling in superheated liquids. *Journal of the British Nuclear Society*, 10(2):131–139.
- Engel, D. C., Versteeg, G. F., and van Swaaij, W. P. M. (1996). Solubility of hydrogen in aqueous solutions of sodium and potassium bicarbonate from 293 to 333 K. *Journal of Chemical & Engineering Data*, 41(3):546–550.

- Epstein, P. S. and Plesset, M. S. (1951). On the stability of gas bubbles in liquid-gas solution. *The Journal of Chemical Physics*, 18:1505–1509.
- Fernández-Prini, R., Alvarez, J. L., and Harvey, A. H. (2003). Henry’s constants and vapor-liquid distribution constants for gaseous solutes in H₂O and D₂O at high temperatures. *Journal of Physical and Chemical Reference Data*, 32(2):903–916.
- Feynman, R. P. (1946). Statistical behaviour of neutron chains. Technical Report LA-591, Los Alamos National Laboratory.
- Forehand, H. M. (1981). *Effects of Radiolytic Gas on Nuclear Excursions in Aqueous Solutions*. PhD thesis, University of Arizona.
- Gamble, D. P. (1959). A proposed model of bubble growth during fast transients in the KEWB reactor. Technical report, Atomics International.
- Ghormley, J. A. (1958). Nucleation of bubbles in superheated aqueous solutions by fast particles. *Journal of Nuclear Energy (1954)*, 6(4):300–302.
- Glasstone, S. and Sesonske, A. (1994). *Nuclear Reactor Engineering: Reactor Systems Engineering*. Number 2 in Nuclear Reactor Engineering. Springer US.
- Gönnenwein, F. (2004). Ternary and quaternary fission. *Nuclear Physics A*, 734:213–216.
- Govorkov, A. B. (1963a). Statistical reactor kinetics equations. *Translated from Atomnaya Energiya*, 17(6):474–479.
- Govorkov, A. B. (1963b). Statistical scattering of pulse amplitudes in fast neutron pulse reactors. *The Soviet Journal of Atomic Energy*, 13(2):750–753.
- Grant, W. E., Darch, W. J., Bowden, S. T., and Jones, W. J. (1948). The surface tension and viscosity of solutions of uranyl salts. *The Journal of Physical and Colloid Chemistry*, 52(7):1227–1236.
- Greenfield, M. L., Lipkis, R. P., Liu, C., and Zuber, N. (1954). Studies on density transients in volume-heated boiling systems. Technical Report AECU-2950, United States Atomic Energy Commission.
- Grinstead, C. M. and Snell, J. L. (2012). *Introduction to Probability*. American Mathematical Society, 2nd edition.
- Hall, S. K., Eaton, M. D., and Williams, M. M. R. (2012). The application of isogeometric analysis to the neutron diffusion equation for a pincell problem with an analytic benchmark. *Annals of Nuclear Energy*, 49:160–169.

- Hankins, D. E. (1966). Effect of reactivity addition rate and of weak neutron source on the fission yield of uranium solutions. *Nuclear Science and Engineering*, 26:110–116.
- Hansen, G. E. (1960). Assembly of fissionable material in the presence of a weak neutron source. *Nuclear Science and Engineering*, 8(6):709–719.
- Harris, D. R. (1960). Calculation of the background neutron source in new uranium fueled reactors. Technical report, U.S. Atomic Energy Commission. Bettis Atomic Power Laboratory, Report no. WAPD-TM-220.
- Harris, D. R. (1964). Kinetics of low source level. In *Naval Reactors Physics Handbook*, volume 1, pages 1010–1142. United States Atomic Energy Commission.
- Harvey, A. H. (1996). Semiempirical correlation for Henry’s constants over large temperature ranges. *AIChE Journal*, 42(5):1491–1494.
- Hébert, A. (2009). *Applied Reactor Physics*. Presses Internationales Polytechnique.
- Helmut, P. and Schinner, A. (2003). Judging the reliability of stopping power tables and programs for heavy ions. *Nuclear Instruments and Methods in Physics Research Section B, Beam Interactions with Materials and Atoms*, 209:252–258.
- Hiroharu, K., Niichi, N., and Masaru, H. (1968). On the turbulent heat transfer by free convection from a vertical plate. *International Journal of Heat and Mass Transfer*, 11(7):1117–1125.
- Hiroki, A. and LaVerne, J. A. (2005). Decomposition of hydrogen peroxide at water/ceramic oxide interfaces. *The Journal of Physical Chemistry B*, 109(8):3364–3370.
- Housner, G. W. (1963). The dynamic behaviour of water tanks. *Bulletin of the Seismological Society of America*, 53(2):381–387.
- Humbert, P. (2003). Stochastic neutronics with PANDA deterministic code. In *American Nuclear Society Topical Meeting in Nuclear Mathematical and Computational Sciences*.
- Hurwitz, H., MacMillan, D. B., Smith, J. H., and Storm, M. L. (1963). Kinetics of low source reactor startups. Part I. *Nuclear Science and Engineering*, 15(2):166–186.
- IAEA (1999). Report on the preliminary fact finding mission following the accident at the nuclear fuel processing facility in Tokaimura, Japan. Technical report, International Atomic Energy Agency.
- IAEA (2009). Homogeneous Aqueous Solution Nuclear Reactors for the Production of Mo-99 and other Short Lived Radioisotopes. Technical report, International Atomic Energy Agency.

- IAEA (2014). Criticality safety in the handling of fissile material. Technical Report SSG-27, International Atomic Energy Agency.
- Incropera, F. P. and DeWitt, D. P. (1996). *Fundamentals of heat and mass transfer*. Wiley.
- Jähne, B., Heinz, G., and Dietrich, W. (1987). Measurement of the diffusion coefficients of sparingly soluble gases in water. *Journal of Geophysical Research*, 92:10767–10776.
- Keepin, G. R. (1965). *Physics of nuclear kinetics*. Addison-Wesley series in nuclear science and engineering. Addison-Wesley Pub. Co.
- Keepin, G. R., Wimett, T. F., and Zeigler, R. K. (1957). Delayed neutrons from fissionable isotopes of uranium, plutonium and thorium. *Journal of Nuclear Energy*, 6(1):2–21.
- Kim, J. W. and Lee, W. K. (1987). Coalescence behaviour of two bubbles in stagnant liquids. *Journal of Chemical Engineering of Japan*, 20(5):448–453.
- Knief, R. A., Society, A. N., and Commission, U. N. R. (1985). *Nuclear criticality safety: theory and practice*. American Nuclear Society.
- Kopeikin, V. I., Mikaelyan, L. A., and Sinev, V. V. (2004). Reactor as a source of antineutrinos: Thermal fission energy. *Physics of Atomic Nuclei*, 67(10):1892–1899.
- Kornreich, D. E. (1993). Reactivity feedback mechanisms in aqueous fissile solutions. *Nuclear Science and Engineering*, 115:50–61.
- Krepper, E., Lucas, D., Frank, T., Prasser, H.-M., and Zwart, P. J. (2008). The inhomogeneous MUSIG model for the simulation of polydispersed flows. *Nuclear Engineering and Design*, 238(7):1690–1702.
- Laguerre, O., Osswald, V., Hoang, H. M., Souchon, I., Trelea, C., Hartmann, C., and Flick, D. (2017). Experimental study of airflow and heat transfer above a hot liquid surface simulating a cup of drink. *Journal of Food Engineering*, 197:24–33.
- Lamarsh, J. R. (1975). *Introduction to nuclear engineering*. Addison-Wesley series in nuclear science and engineering. Addison-Wesley Pub. Co.
- Lane, J. A., MacPherson, H. G., and Maslan, F., editors (1958). *Fluid Fuel Reactors*. Addison-Wesley.
- LANL (2017). MCNP User’s Manual. Technical Report LA-UR-17-29981, Los Alamos National Laboratory.
- Levanov, A. V., Isaikina, O. Y., and Lunin, V. V. (2017). Dissociation constant of nitric acid. *Russian Journal of Physical Chemistry A*, 91(7):1221–1228.

- Liem, P. H. and Naito, Y. (2015). TRACY and SILENE Benchmark Phase II evaluation by TRACE code. *Progress in Nuclear Energy*, 85:71–82.
- Livolant, M. and Jeanpierre, F. (1974). Autoprotection des résonances dans les réacteurs nucléaires. Technical Report CEA-R-4533, Commissariat à l'Énergie Atomique.
- Lubetkin, S. D. (2003). Why is it much easier to nucleate gas bubbles than theory predicts? *Langmuir*, 19(7):2575–2587.
- Madland, D. G. (2006). Total prompt energy release in the neutron-induced fission of ^{235}U , ^{238}U , and ^{239}Pu . *Nuclear Physics A*, 772(3):113–137.
- Marrucci, G. and Nicodemo, L. (1967). Coalescence of gas bubbles in aqueous solutions of inorganic electrolytes. *Chemical Engineering Science*, 22(9):1257–1265.
- Mather, D. J. and Shaw, P. M. (1986). CRITEX - a computer program to calculate criticality excursions in fissile liquid systems. Technical Report SRD-R-380, UKAEA.
- McLaughlin, T. P., Monahan, S. P., Pruvost, N. L., Frolov, V. V., Ryazanov, B. G., and Sviridov, V. I. (2000). A review of criticality accidents. Technical Report LA-13638, Los Alamos National Laboratory.
- Meem, J. L. (1964). *Two group reactor theory*. Gordon and Breach.
- Mitake, S., Hayashi, Y., and Sakurai, S. (2003). Development of INCTAC code for analyzing criticality accident phenomena. In *7th International Conference on Nuclear Criticality Safety (ICNC2003)*. JAERI-Conf 2003-019.
- Miyoshi, Y., Yamane, Y., Okubo, K., Reverdy, L., Grivot, P., Konishi, H., Mitake, S., and Liem, P. H. (2009). Inter-code Comparison Exercise for Criticality Excursion Analysis - Benchmark Phase I: Pulse Mode Experiments with Uranyl Nitrate Solution in the TRACY and SILENE Facilities. Technical Report NEA No. 6285, Nuclear Energy Agency.
- Murray, H. S., Schultz, D. G., and Weaver, L. E. (1966). Stability of coupled core reactors by the second method of liapunov. *Journal of Nuclear Energy. Parts A/B. Reactor Science and Technology*, 20(9):729–734.
- Nakajima, K. (2003). Applicability of simplified methods to evaluate consequences of criticality accident using past accident data. In *Proceedings of the International Conference on Nuclear Criticality Safety ICNC 2003*, pages 171–176. Japan Atomic Energy Research Institute.

- Nakajima, K., Yamamoto, T., and Miyoshi, Y. (2002a). Modified quasi-steady-state method to evaluate the mean power profiles of nuclear excursions in fissile solution. *Journal of Nuclear Science and Technology*, 39(11):1162–1168.
- Nakajima, K., Yamane, Y., Ogawa, K., Aizawa, E., Yanagisawa, H., and Miyoshi, Y. (2002b). TRACY transient experiment databook, 1) pulse withdrawal experiment. Technical Report 2002-005, Japan Atomic Energy Research Institute.
- Nakajima, K., Yamane, Y., Ogawa, K., Aizawa, E., Yanagisawa, H., and Miyoshi, Y. (2002c). TRACY transient experiment databook, 3) ramp feed experiment. Technical Report 2002-007, Japan Atomic Energy Research Institute.
- National Nuclear Data Center (2011). 92-U-235 neutron-induced fission yields. <https://www.nndc.bnl.gov/sigma/getFissionYieldsData.jsp?evalid=15579&mf=8&mt=454>. Online, accessed 06-November-2018.
- Neeb, K.-H. (1997). *The Radiochemistry of Nuclear Power Plants with Light Water Reactors*. Walter de Gruyter.
- NNSA (2008). Nuclear safety specialist - qualification standard, reference guide. Technical report, National Nuclear Security Administration.
- Norman, A. and Spiegler, P. (1963). Radiation nucleation of bubbles in water. *Nuclear Science and Engineering*, 16(2):213–217.
- Northcliffe, L. C. and Schilling, R. F. (1970). Range and stopping-power tables for heavy ions. *Atomic Data and Nuclear Data Tables*, 7(3):233–463.
- ONR (2016). Criticality safety. Nuclear safety technical assessment guide, Office for Nuclear Regulation.
- Ornstein, L. S. and Uhlenbeck, G. E. (1937). Some kinetic problems regarding the motion of neutrons through paraffine. *Physica* 4, 4(6):478–486.
- Osborn, R. K. and Natelson, M. (1965). Kinetics equations for neutron distributions. *Journal of Nuclear Energy. Parts A/B. Reactor Science and Technology*, 19(8):619–639.
- Ott, K. O. and Neuhold, R. J. (1985). *Introductory Nuclear Reactor Dynamics*. American Nuclear Society.

- Owens, A. R., Welch, J. A., Kópházi, J., and Eaton, M. D. (2016). Discontinuous isogeometric analysis methods for the first-order form of the neutron transport equation with discrete ordinate (sn) angular discretisation. *Journal of Computational Physics*, 315:501–535.
- Pain, C., Oliveira, C., Goddard, A., Eaton, M., Gundry, S., and Umpleby, A. (2003). Transient analysis and dosimetry of the tokaimura criticality incident. *Nuclear Technology*, 144(1):16–33.
- Pain, C. C., de Oliveira, C. R. E., Goddard, A. J. H., and Umpleby, A. P. (2001). Non-linear space-dependent kinetics for the criticality assessment of fissile solutions. *Progress in Nuclear Energy*, 39:53–114.
- Pál, L. (1958). On the theory of stochastic processes in nuclear reactors. *Nuovo Cimento Divided into Nuovo Cimento A and Nuovo Cimento B*, 10(7). Suppl. No. 1,.
- Patton, F. S., Bailey, J. C., Calliham, Z. D., Googin, J. M., Jasny, G. R., McAlduff, H. J., Morgan, K. Z., Sullivan, C. R., Watcher, J. W., Bernarder, N. K., and Charpie, R. A. (1958). Accidental radiation excursion at the Y-12 plant. Technical Report Y-1234, Union Carbide Nuclear Company.
- Paxton, H. C. and Pruvost, N. L. (1987). Critical dimensions of systems containing U-235, Pu-239 and U-233. Technical report, Los Alamos National Laboratory.
- Pázsit, I. and Pál, L. (2008). *Neutron Fluctuations*. Elsevier, Amsterdam.
- Peñas-López, P., Rodríguez-Rodríguez, M., and van der Meer, D. (2016). The history effect in bubble growth and dissolution. part 1. theory. *Journal of Fluid Mechanics*, 800:180–212.
- Pérez, D. M., Lorenzo, D. E. M., Garcia, L. P. R., Rodríguez, M. C., de Oliveira Lira, C. A. B., Hernández, C. R. G., and Llanes, J. S. (2015). Thermal-Hydraulics Study of a 75kWth Aqueous Homogeneous Reactor for 99Mo Production. *Journal of Thermodynamics*, page 11. Article ID 268034.
- Pray, H. A. and Stephan, E. F. (1953). The solubility of hydrogen in uranyl sulphate solutions at elevated temperatures. Technical Report BMI-870, U.S. Atomic Energy Commission.
- Pray, H. A. and Stephan, E. F. (1954). The solubility of oxygen and hydrogen in uranyl fluoride solutions at elevated temperatures. Technical Report BMI-897, U.S. Atomic Energy Commission.
- Prince, M. J. and Blanch, H. W. (1990). Bubble coalescence and break-up in air-sparged bubble columns. *AIChE Journal*, 36(10):1485–1499.
- Rayleigh, J. W. S. (1945). *The Theory of Sound*, volume 2. Dover Publications Inc., 2nd edition.

- Rozain, J. P., Fouillaud, P., Mather, D. J., and Bickley, A. M. (1991). Criticality excursions in wetted UO₂ powder. volume 63 of *Transactions of the American Nuclear Society*, Orlando, Florida. Annual Meeting of the American Nuclear Society.
- Saxby, J. E. M., Prinja, A. K., and Eaton, M. D. (2017). Diffusion theory model of the neutron number probability distribution in a subcritical multiplying assembly. *Annals of Nuclear Energy*, 109:507–528.
- Saxby, J. E. M., Prinja, A. K., and Eaton, M. D. (2018). Energy dependent transport model of the neutron number probability distribution in a subcritical multiplying assembly. *Nuclear Science and Engineering*, 189:1–25.
- Saxby, J. E. M., Williams, M. M. R., and Eaton, M. D. (2016). The energy dependent plbell equation and the influence of the neutron energy on the survival probability in a supercritical medium. *Annals of Nuclear Energy*, 92:413–418.
- Schulenberg, T. and Döhler, J. (1986). Heating-up, nucleation and boiling of a critical solution of fissile material. *International Journal of Multiphase Flow*, 12(5):759–770.
- Seale, R. L. and Anderson, R. E. (1991). Intrinsic neutron source strengths in uranium solutions. *Transactions of the American Nuclear Society*, 63:226.
- Shampine, L. and Gordon, M. (1975). *Computer Solutions of Ordinary Differential Equations: The Initial Value Problem*. Chapman & Hall.
- Shiroya, S., Mori, M., and Kanda, K. (1996). Analysis of experiment on temperature coefficient of reactivity in light-water-moderated and heavy- water-reflected cylindrical core loaded with highly-enriched-uranium or medium-enriched-uranium fuel. *Journal of Nuclear Science and Technology*, 33(3):211–219.
- Souto, F. J. (2002). *Investigation of the Effects of Radiolytic-Gas Bubbles on the Long-Term Operation of Solution Reactors for Medical-Isotope Production*. PhD thesis, University of New Mexico.
- Spiegler, P., Bumpus, C. F., and Norman, A. (1962). Production of void and pressure by fission track nucleation of radiolytic gas bubbles during power bursts in a solution reactor. Technical Report NAA-SR-7086, Atomics International.
- Stacey, W. M. (2007). *Nuclear Reactor Physics*. John Wiley & Sons, 2nd edition.
- Suzaki, T. and Miyoshi, Y. (1986). Measurements of reactivity effects caused by surface waves excited in nuclear fuel systems having a free surface. *Journal of Nuclear Science and Technology*, 23(9):840–842.

- Takagi, J. and Ishigure, K. (1985). Thermal decomposition of hydrogen peroxide and its effect on reactor water monitoring of boiling water reactors. *Nuclear Science and Engineering*, 89(2):177–186.
- Tavernier, S. (2010). *Experimental Techniques in Nuclear and Particle Physics*. Springer-Verlag Berlin Heidelberg, 1st edition.
- Thomas, A. F. and Abbey, F. (1973). *Calculational Methods for Interacting Arrays of Fissile Material*. Pergamon Press. International Series of Monographs in Nuclear Energy, Volume 108.
- Washburn, E. W. (2003). *International Critical Tables of Numerical Data, Physics, Chemistry and Technology (1st Electronic Edition)*. Knovel.
- Williams, M. M. R. (1966). *The Slowing Down and Thermalization of Neutrons*. North-Holland Publishing Company.
- Williams, M. M. R. (2009). The forward equation of probability balance for neutrons in a medium with randomly time-varying properties: Space and angle dependence. *Progress in Nuclear Energy*, 51(6):689–694.
- Williams, M. M. R. (2016). Burst wait times in the Caliban reactor using the gamma probability distribution function. *Nuclear Science and Engineering*, 183(1):116–125.
- Williams, M. M. R. and Eaton, M. D. (2017). A theory of low source start-up based on the Pál-Bell equations. *Annals of Nuclear Energy*, 102:317–348.
- Williams, M. M. R. and Eaton, M. D. (2018). Spatial effects in low neutron source start-up and associated stochastic phenomena. *Annals of Nuclear Energy*, 111:616–634.
- Winter, G. E., Cooling, C. M., and Eaton, M. D. (2020a). Linear energy transfer of fission fragments of ^{235}U and nucleation of gas bubbles in aqueous solutions of uranyl nitrate. *Annals of Nuclear Energy*, 142:107379.
- Winter, G. E., Cooling, C. M., and Eaton, M. D. (2020b). A semi-empirical model of radiolytic gas bubble formation and evolution during criticality excursions in uranyl nitrate solutions for nuclear criticality safety assessment. Submitted for publication.
- Winter, G. E., Cooling, C. M., Williams, M. M. R., and Eaton, M. D. (2018). Importance of parametric uncertainty in predicting probability distributions for burst wait-times in fissile systems. *Annals of Nuclear Energy*, 119:117–128.

- Yamamoto, T. (1995). Application of time-dependent boundary-fitted curvilinear coordinate system for kinetic analysis of aqueous fuel solution sloshing behaviour. *Nuclear Engineering and Design*, 154:145–155.
- Yamane, Y. (2015). Improvement in estimation of first peak power based on non-linear temperature feedback reactivity in criticality accident with instantaneous reactivity insertion. *Journal of Nuclear Science and Technology*, 52(11):1425–1435.
- Yamane, Y., Miyoshi, Y., Liem, P. H., and Naito, Y. (2000). Analysis of JCO criticality accident (5) - kinetics analysis of initial burst by TRACE code. In *Proceedings of the Spring Annual Meeting of Japan Atomic Energy Society*.
- Yamane, Y., Nakajima, K., Yanagisawa, H., Yamamoto, T., and Miyoshi, Y. (2005). Criticality code identification sheets - agnes. Technical report, Japan Atomic Energy Research Institute.
- Yaws, C. L. (2009). *Transport Properties of Chemicals and Hydrocarbons*. William Andrew Publishing.
- Yeoh, G. H. and Tu, J. (2019). *Computational Techniques for Multiphase Flows*. Butterworth-Heinemann, 2nd edition.
- Yoshida, R., Yamane, Y., and Abe, H. (2019). Estimation of hydrogen gas production at transient criticality in uranyl nitrate solution. In *Global and Top Fuel 2019*.
- Youker, A. J., Chemerisov, S. D., Kalensky, M., Tkac, P., Bowers, D. L., and Vandegrift, G. F. (2013). A solution-based approach for Mo-99 production: Considerations for nitrate versus sulfate media. *Science and Technology of Nuclear Installations*.
- Zamacinski, T., Cooling, C. M., and Eaton, M. D. (2014). A point kinetics model of the Y12 accident. *Progress in Nuclear Energy*, 77:92–106.
- Ziegler, J. F., Ziegler, M. D., and Biersack, J. P. (2010). SRIM - the stopping and range of ions in matter (2010). *Nuclear Instruments and Methods in Physics Research Section B, Beam Interactions with Materials and Atoms*, 268(11):1818–1823.
- Zucker, M. S. and Holden, N. E. (1986). Energy dependence of the neutron multiplicity P_ν in fast neutron induced fission of U-235, U-238 and Pu-239. Technical Report BNL-38491, Brookhaven National Laboratory.

Appendix A

Solubility Unit Conversions

The solubility data in Section 4.2.8 are from Washburn (2003). The original data are expressed in terms of the Bunsen coefficient, α , with salt concentrations expressed as normality, N_c , or molality, M_c . Definitions of these units are provided in Washburn (2003).

The Bunsen coefficient is the volume of gas, reduced to standard temperature and pressure (STP: 0°C and 1 atm), that dissolves in one volume of the solvent when the partial pressure is 1 atm,

$$\alpha = \frac{V_{\text{gas,STP}}}{V_{\text{solvent}}}. \quad (\text{A.1})$$

The Bunsen coefficient varies with temperature so it is important to know the temperature of the experiment. In Washburn (2003) this is indicated by a subscript, for example, α_{20} is the Bunsen coefficient at 20°C. Using the ideal gas law ($V = nRT / P$) to substitute for the volume of gas at STP, the Bunsen coefficient can be expressed as follows, in terms of the number of moles of gas dissolved,

$$\alpha = \frac{n_{\text{gas}}RT_{\text{STP}}}{P_{\text{STP}}V_{\text{solvent}}}. \quad (\text{A.2})$$

The Henry's law constant is the concentration of dissolved gas in the liquid phase, per unit partial pressure in the gas phase (Çengel and Boles (2015)). Henry's law is valid for partial pressures where the liquid phase concentration is directly proportional to the gas phase partial pressure (this ceases to be the case at high partial pressures).

Provided Henry's law is valid at standard pressure (P_{STP}) for a particular gas-solvent combination, the Henry's law constant can be obtained from the Bunsen coefficient by dividing by RT_{STP} ,

$$H_{cp} = \frac{n_{\text{gas}}}{PV_{\text{solvent}}} = \frac{\alpha}{RT_{\text{STP}}}, \quad (\text{A.3})$$

where H_{cp} is the Henry's law constant in $[\text{mol m}^{-3} \text{ Pa}^{-1}]$, R is the universal gas constant in $[\text{J K}^{-1} \text{ mol}^{-1}]$ and T_{STP} is standard temperature in Kelvin (273.15 K).

The normality of a solution is the number of gram-equivalents of solute per litre of solution. A gram-equivalent is the mass of a substance adjusted for its valency so that, for example, one gram-equivalent of any reducing agent will react with one gram-equivalent of any oxidising agent. For monovalent ions the normality is the same as the molarity.

The molality of a solution is the number of moles of solute per kilogram of solvent. This was converted to molarity as follows,

$$M = \frac{M_c M_w}{1 + M_c M_w} \rho, \quad (\text{A.4})$$

where M is the molarity in units of $[\text{mol dm}^{-3}]$, M_c is the molality in $[\text{mol kg}^{-1}]$, M_w is the molecular weight of the solute in $[\text{kg mol}^{-1}]$ and ρ is the solution density in units of $[\text{kg m}^{-3}]$ (supplied in Washburn (2003)).

Appendix B

Details of MCNP Inputs Used to Model the CRAC and TRACY Experimental Reactors

This appendix provides details of the assumed geometry and compositions, and cross-section libraries used for the MCNP models of the benchmark reactors discussed in Chapter 5. The geometries shown represent simplifications compared to the true geometries of the CRAC and TRACY reactors.

B.1 CRAC 300 mm

B.1.1 Geometry and Compositions

The CRAC reactor was modelled as a simple cylinder with a shallow elliptical base. The internal radius of the cylindrical section was 0.147 m and the steel thickness was 3 mm. These dimensions were obtained from Barbry et al. (1973). The base was modelled as a hemiellipse with major radius equal to that of the cylindrical section and a minor radius 0.035 m.

The modelled composition of the fuel solution is shown in Table B.I and is based on a uranium concentration of 81 gU/L, a ^{235}U enrichment of 93% and a density of 1180.8 kg m^{-3} . The vessel material was modelled as Stainless Steel SUS304L and its composition is shown in Table B.II.

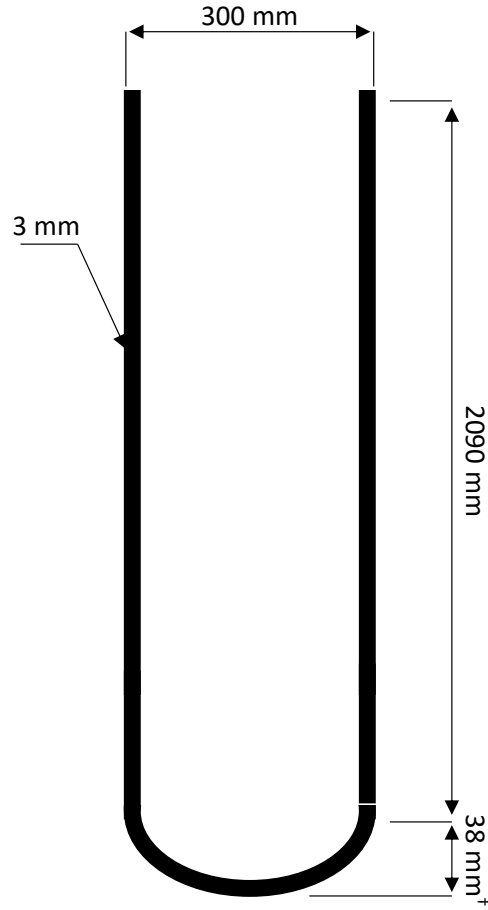


Fig. B.1. Geometry of the CRAC 300 mm core as modelled in MCNP based on dimensions shown in Barbry et al. (1973). [†]Assumed value.

Isotope	Atom Fraction
¹ H	0.62128515
¹⁴ N	0.01708136
¹⁶ O	0.35956159
²³⁵ U	0.00192857
²³⁸ U	0.00014333

TABLE B.I

Fuel solution composition by atom fractions used for MCNP models of CRAC-29.

Isotope	Atom Fraction
¹² C	0.00136945
²⁸ Si	0.01950421
⁵² Cr	0.20015790
⁵⁵ Mn	0.01994123
⁵⁶ Fe	0.65587556
⁵⁸ Ni	0.10263913
³² S	0.00051252

TABLE B.II

Composition of stainless steel SUS304L by atom fractions used for MCNP models.

B.1.2 Thermal Feedback Coefficient

The thermal feedback coefficient was calculated by taking the sum of contributions from Doppler broadening, thermal scattering and the change in density of the solution. The contribution of each of these phenomena is listed in Table B.III.

Thermal Effect	α_T [$\$ K^{-1}$]
Doppler Broadening	-0.00010
Thermal Scattering	-0.01164
Density Change	-0.05553
Total	-0.06727

TABLE B.III

Thermal feedback coefficient using MCNP for the CRAC-29 experiment.

The contribution of Doppler broadening was estimated by comparing the value of k_{eff} using the .70c (293.6 K) and .71c (600 K) cross-section libraries. Thermal scattering was evaluated by comparing the predicted k_{eff} using $S(\alpha, \beta)$ libraries lwtr.20t (293.6 K) and lwtr.23t (450 K). The effect of solution density was evaluated by adjusting the fuel solution density and liquid level to values corresponding to 365 K and 375 K, using Equation E.2 to predict the change in density due to temperature.

B.2 TRACY

B.2.1 Geometry and Compositions

The TRACY reactor was modelled as an annulus of stainless steel. The steel was 80 mm thick in the base, 10 mm thick in the external wall and 3 mm thick in the internal wall. The internal radius of the outer cylinder was 250 mm and the internal radius of the inner cylinder was 38.15 mm. The geometry as modelled in MCNP is shown in Figure B.1. It is based on drawings of the TRACY reactor presented in Nakajima et al. (2002c).

The modelled composition of the fuel solution is shown in Table B.IV and is based on a uranium concentration of 396.2 gU/L, a ^{235}U enrichment of 9.98% and a density of 1553.1 kg m^{-3} . The vessel material was modelled as Stainless Steel SUS304L of the same composition shown in Table B.II.

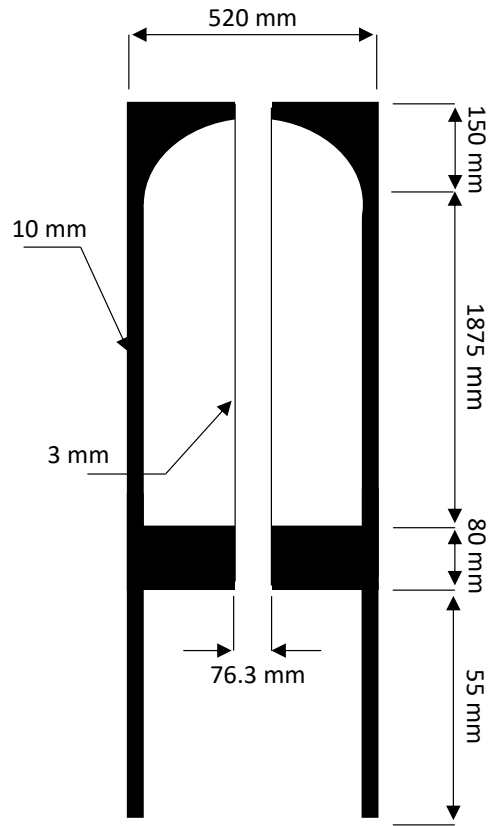


Fig. B.1. Geometry of the TRACY reactor as modelled in MCNP based on dimensions shown in Nakajima et al. (2002c).

Isotope	Atom Fraction
^1H	0.58142607
^{14}N	0.02489199
^{16}O	0.38349710
^{235}U	0.00102814
^{238}U	0.00915671

TABLE B.IV
Fuel solution composition by atom fractions used for MCNP models of TRACY R76.

Appendix C

Estimating the Solubility of H₂ and O₂ in Solutions of Uranyl Nitrate

The solubility of a solute in aqueous solution is generally a function of the composition and temperature of the solution. A correlation presented by Harvey (1996) and Fernández-Prini et al. (2003) permits the Henry's law volatility constants for hydrogen and oxygen gases in pure water to be evaluated as a function of the water temperature. Equation C.1 shows the correlation with some minor adaptations to convert the Henry's law volatility constants to solubility constants. The value of the constants A, B and C are shown in Table C.I.

$$H = \frac{\rho_{\text{H}_2\text{O}}}{M_{\text{H}_2\text{O}}} \left(p^* \exp \left(\frac{1}{T_R} [A + B(1 - T_R)^{0.355}] + CT_R^{-0.41} \exp(1 - T_R) \right) \right)^{-1}, \quad (\text{C.1})$$

where H is the Henry's law solubility constant in units of mol m⁻³ Pa⁻¹, $\rho_{\text{H}_2\text{O}}$ is the density of water and $M_{\text{H}_2\text{O}}$ is its molecular weight, $T_R = T/T_c$ is the relative temperature, p^* is the vapour pressure of water and A , B and C are constants specific to each solute. The results of this correlation for

	H ₂	O ₂
A	-4.73284	-9.44833
B	6.08954	4.43822
C	6.06066	11.42005
	Source: Fernández-Prini et al. (2003)	

TABLE C.I

Constants for use in Equation C.1 to evaluate the Henry's law solubility constants for hydrogen and oxygen in pure water.

hydrogen and oxygen are shown in Figure C.2.¹

¹Mole fractions have been converted to concentrations assuming a constant water density of 997.0 kg m⁻³.

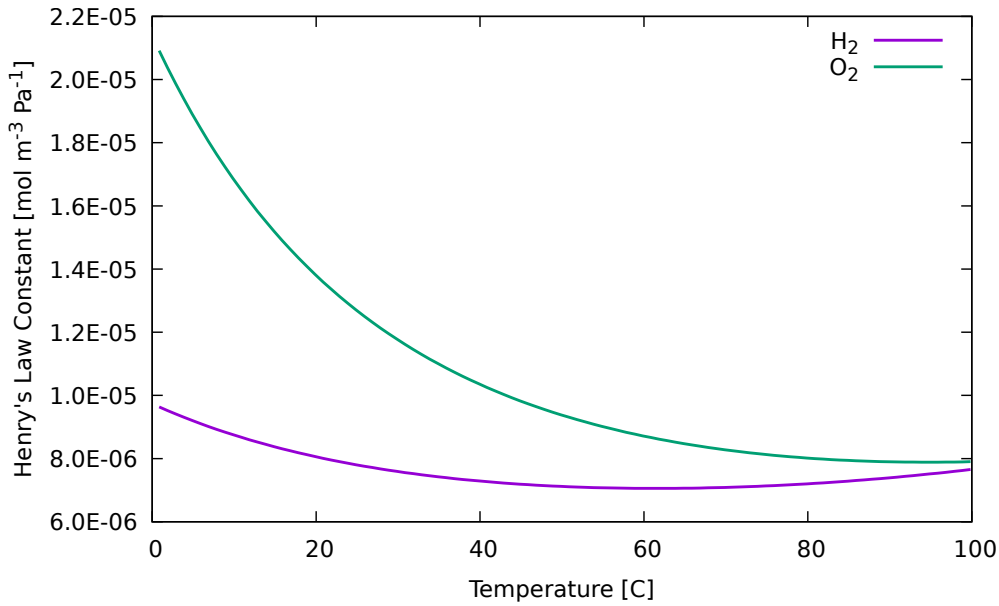


Fig. C.1. Solubility of H₂ and O₂ as a function of temperature in pure water using the correlation of Harvey (1996) and the constants of Fernández-Prini et al. (2003).

The solubility of hydrogen in water passes through a minimum of $7.06 \times 10^{-6} \text{ mol m}^{-3} \text{ Pa}^{-1}$ at 62°C. Apart from this it varies relatively little for liquid water at atmospheric pressure. The solubility of oxygen varies relatively more over the temperature change shown and passes through a minimum of $7.89 \times 10^{-6} \text{ mol m}^{-3} \text{ Pa}^{-1}$ at 94°C.

Despite the smaller degree of variation, changes in the solubility of hydrogen will likely be more significant for the kinetics of a criticality transient in a fissile solution than any changes in the solubility of oxygen. This is because the solubility of hydrogen, through its influence on the critical concentration, directly influences the amount of energy that must be absorbed by the solution before gas voids can appear. The presence of oxygen gas also affects the critical concentration of hydrogen gas but this is not affected by its degree of solubility (see Equation 5.1.22). However, the solubility of oxygen in the fuel solution will have some influence on the kinetics of the transient through its effect on the equilibrium concentration of dissolved oxygen and the rate at which dissolved oxygen passes into the gaseous phase.

Figure C.2 shows the influence of nitric acid on the solubility of hydrogen and oxygen using data from International Critical Tables (Washburn (2003)). The data suggest that nitric acid reduces the Henry's law constant for hydrogen by $-3.1543 \times 10^{-10} \text{ mol m}^{-3} \text{ Pa}^{-1}$ for every mol m^{-3} of nitric acid present. The Henry's law constant for oxygen is reduced by $-7.6603 \times 10^{-10} \text{ mol m}^{-3} \text{ Pa}^{-1}$ for every mol m^{-3} of nitric acid present.

Unfortunately no data was found in the literature for the influence of uranyl nitrate on the solubility

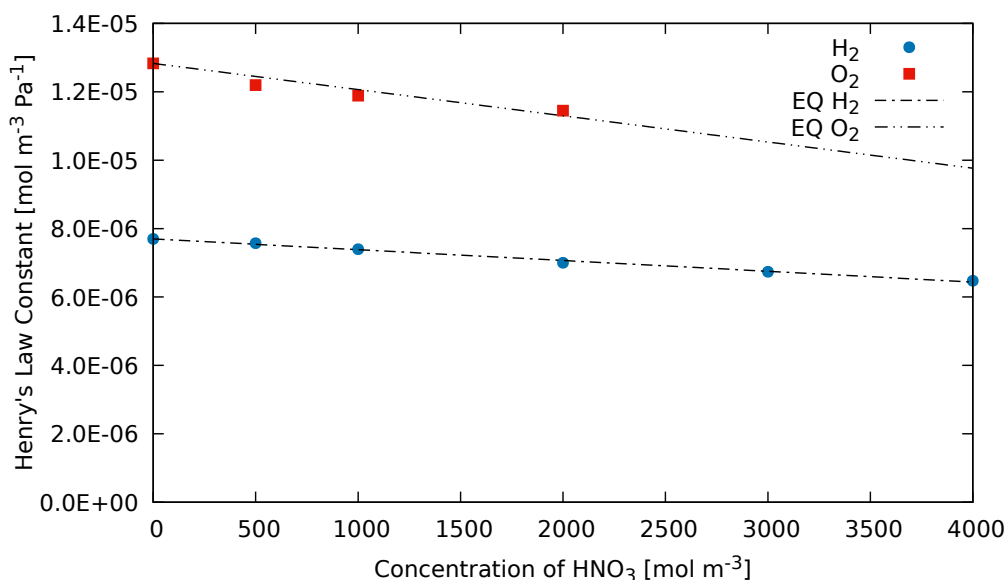


Fig. C.2. Solubility of H_2 and O_2 in nitric acid based on data from International Critical Tables (Washburn (2003)).

of hydrogen or oxygen in aqueous solutions. Data for the influence of other nitrate salts are available for hydrogen but not for oxygen. These data are shown in Figure C.3.

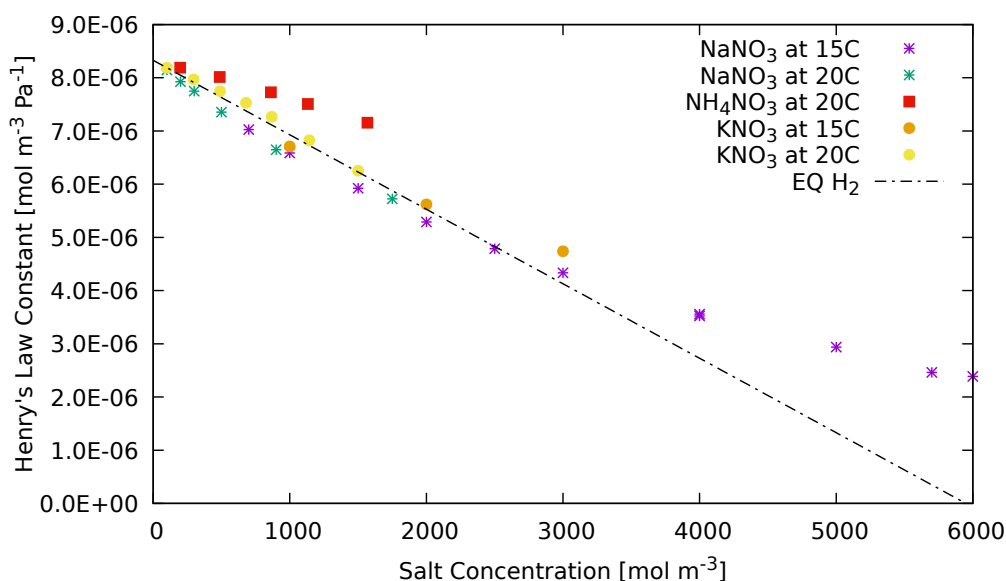


Fig. C.3. Solubility of H_2 in nitrate salts based on data from International Critical Tables (Washburn (2003)).

The data in Figure C.3 show that NaNO_3 and KNO_3 have a very similar effect on the solubility of hydrogen, reducing the Henry's law constant for hydrogen by $1.4 \times 10^{-9} \text{ mol m}^{-3} \text{ Pa}^{-1}$ per mol m^{-3} of salt present in the solution (trend represented by line "EQ H_2 ") up to a concentration of approximately 2500 mol m^{-3} , after which the effect becomes smaller. The NH_4NO_3 salt was found to

be less effective at reducing the solubility of hydrogen, possibly due to its effect on the solution pH.

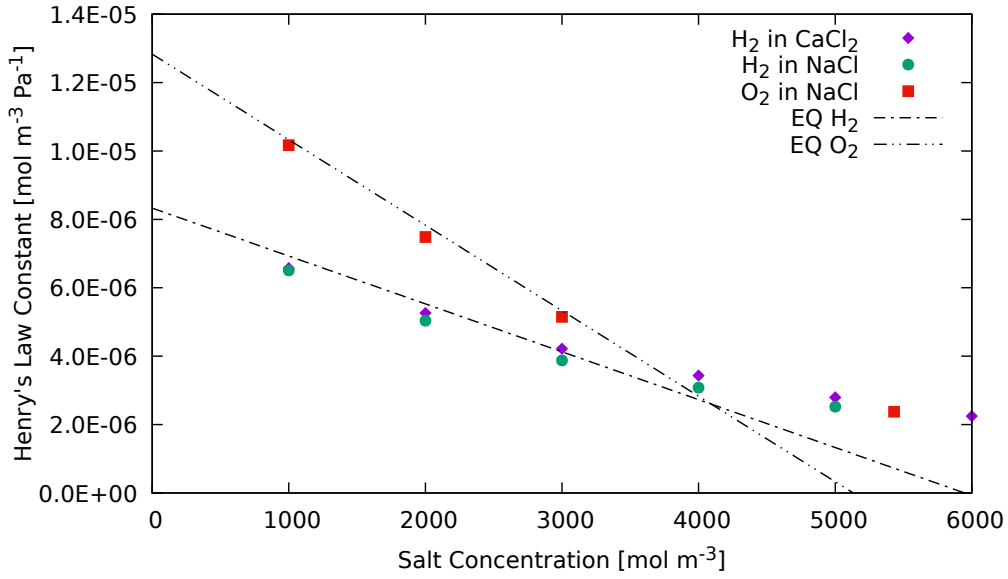


Fig. C.4. Solubility of H₂ and O₂ in chloride based on data from International Critical Tables (Washburn (2003)).

Figure C.4 shows the effect of NaCl on the solubility of both hydrogen and oxygen. The effect of NaCl on hydrogen solubility is very similar to that of NaNO₃ and KNO₃, as indicated by the line “EQ H₂” which also fits the data for NaCl. The presence of NaCl has a greater effect on the solubility of oxygen, reducing the solubility of oxygen by $2.5 \times 10^{-9} \text{ mol m}^{-3} \text{ Pa}^{-1}$ per mol m^{-3} of NaCl present. Also shown in Figure C.4 is the effect of CaCl₂ on the solubility of hydrogen. This salt also has almost an identical effect on the solubility of hydrogen compared to NaNO₃, KNO₃ and NaCl, despite the presence of two chloride anions rather than one.

Given the very similar effects of all the salts examined, apart from NH₄NO₃, on the solubility of hydrogen in solution, it seems reasonable, in the absence of any data specific to uranyl nitrate, to use the values obtained for the nitrate and chloride salts to adjust the Henry’s law constants for hydrogen and oxygen in the model of the fuel solution. This results in the correlations given by Equations C.2 and C.3.

$$H(T)_{\text{H}_2, \text{sol}} = H(T)_{\text{H}_2, \text{H}_2\text{O}} - 3.15 \times 10^{-10} C_{\text{HNO}_3} - 1.4 \times 10^{-9} C_{\text{UO}_2(\text{NO}_3)_2}, \quad (\text{C.2})$$

$$H(T)_{\text{O}_2, \text{sol}} = H(T)_{\text{O}_2, \text{H}_2\text{O}} - 7.66 \times 10^{-10} C_{\text{HNO}_3} - 2.5 \times 10^{-9} C_{\text{UO}_2(\text{NO}_3)_2}, \quad (\text{C.3})$$

where C_{HNO_3} and $C_{\text{UO}_2(\text{NO}_3)_2}$ are less than 2500 mol m^{-3} , $H(T)_{i, \text{sol}}$ is the Henry’s law solubility constant for component i in the solution in units of $\text{mol m}^{-3} \text{ Pa}^{-1}$, $H(T)_{i, \text{H}_2\text{O}}$ is the solubility of component i in pure water at temperature T given by Equation C.1. While this method makes a

number of assumptions which result in a high degree of uncertainty in the predicted value, in the absence of any experimental data for the solubility of hydrogen and oxygen in solutions of uranyl nitrate, the use of these correlations is preferable to ignoring the influence of solute concentrations altogether.

Appendix D

A Note on Sloshing

Liquid sloshing is sometimes discussed as a suspected factor contributing to the fission power oscillations observed in the results of a great number of criticality benchmark experiments. Indeed, Suzaki and Miyoshi (1986) demonstrated that the type of geometric deformation caused by sloshing would result in a significant change in the reactivity of a fissile solution. Yamamoto (1995) used time-dependent neutron diffusion to quantify the effect of sloshing on solutions of uranyl nitrate and plutonium nitrate, and demonstrated that significant reactivity effects are possible. The predicted magnitude of the effect amounted to a few dollars of reactivity. In the simulations of uranyl nitrate, the reactivity effect of sloshing was entirely negative, while the simulations of plutonium nitrate solutions predicted a reactivity profile oscillating from slightly positive to negative, leaving open the possibility of a criticality accident due to sloshing.

Where sloshing occurs it would be expected to produce oscillations in the fission power output. It is also expected that the behaviour of radiolytic gas bubbles may also lead to fission power oscillations, and it is therefore important to be able to distinguish between the two phenomena. One way in which sloshing phenomena may be identified is by the period of oscillations it produces. The natural frequency of sloshing vessels containing liquid has been extensively studied. Simple expressions have been derived for the natural frequency of sloshing in cylindrical vessels, for example, the model of Housner (1963):

$$\tau_{\text{slosh}} = 2\pi \sqrt{\frac{R}{1.8g \tanh^{1.8} H/R}}, \quad (\text{D.1})$$

where R and H are the radius and height of the cylinder, respectively, g is the acceleration due to gravity and τ_{slosh} is the natural period of sloshing.

Figure D.1 shows the natural period of sloshing predicted by Equation D.1 for liquids in a partially

filled cylindrical tank. The natural period varies as a function of the height-to-radius ratio of the cylinder. For benchmark experiments performed on the CRAC reactor with 300 mm internal diameter, the natural period of sloshing would not be expected to exceed one second.

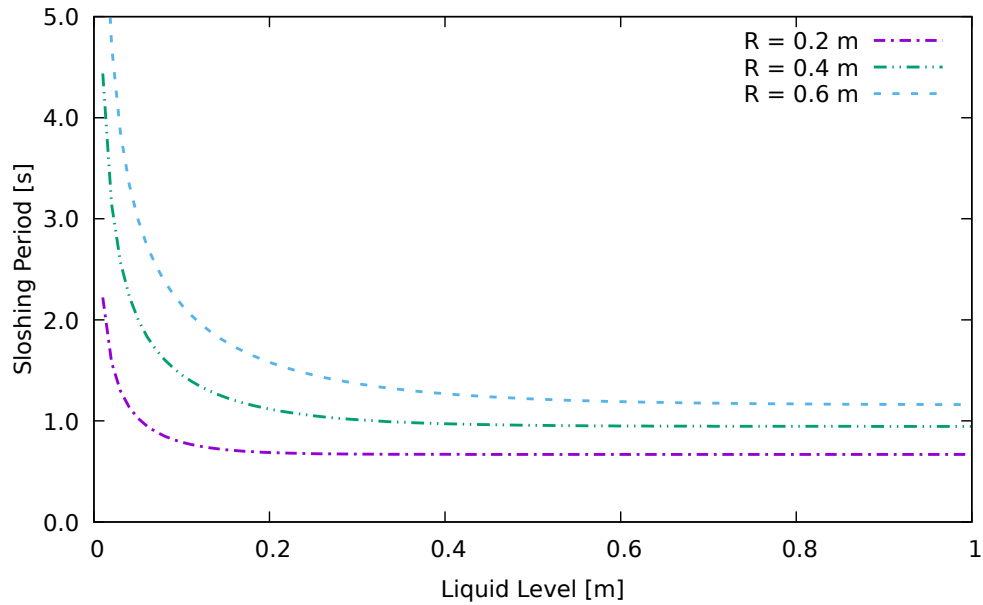


Fig. D.1. Period of sloshing predicted using a correlation from Housner (1963) for liquids in a partially filled cylindrical tank.

While no model of sloshing will be included in the point kinetics model, it is useful to characterise the qualitative effects of sloshing for the interpretation of the results of the benchmark experiments so that the observed behaviour may be linked to the correct underlying physical processes. The oscillations in the fission power profile for the CRAC-29 experiment, shown in Figure 5.3.2, cannot be attributed to sloshing because the period of the observed oscillations is an order of magnitude greater than the natural frequency of sloshing in the CRAC reactor.

Appendix E

Density Correlation for Aqueous Solutions of Uranyl Nitrate

Experimental data presented in Grant et al. (1948) gives the measured densities of aqueous solutions of uranyl nitrate across a range of uranyl nitrate concentrations and solution temperatures. These data are shown in Figure E.1.

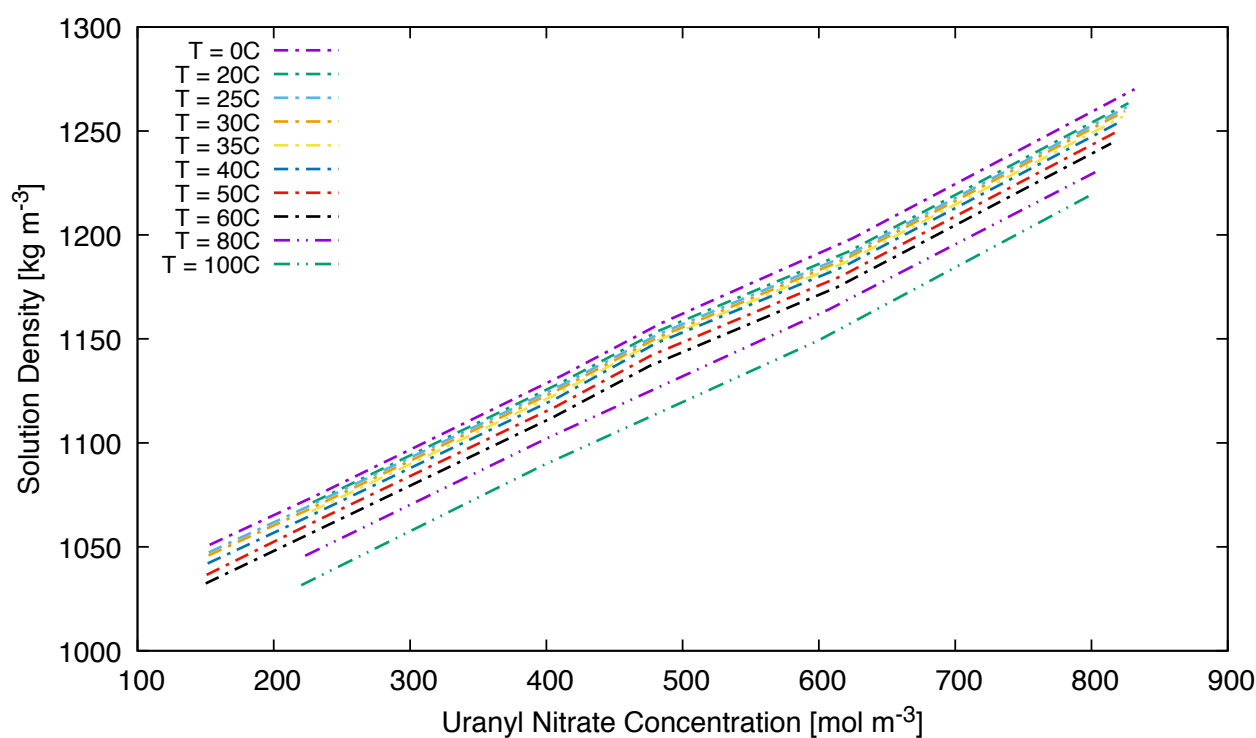


Fig. E.1. Density of aqueous solutions of uranyl nitrate at various temperatures and uranyl nitrate concentrations, Grant et al. (1948)

The data span a range of concentrations from 150 to 800 mol m⁻³ of uranyl nitrate and a range of temperatures from 0°C to 100°C. The concentration of nitric acid in each solution is not reported and it is not known whether or not the solutions tested contained significant quantities of nitric acid.

Using the data shown in Figure E.1 it is possible to derive a correlation for the density of uranyl nitrate solution as a function of temperature and uranyl nitrate concentration. This correlation is shown in Equation E.1.

$$\rho(T, C_{\text{UrN}}) = 0.31635C_{\text{UrN}} - 3.5898 \times 10^{-3}T^2 - 4.7024 \times 10^{-2}T + 1001.0, \quad (\text{E.1})$$

The presence of nitric acid is expected to increase the density of the solution by adding to its mass but it will also change the volume of the solution, which makes the resulting change in density complex to predict. However, if the effect of nitric acid concentration on the solution density can be assumed to have a linear relationship, as is the case for uranyl nitrate, then a coefficient can be determined by fitting to other experimental data.

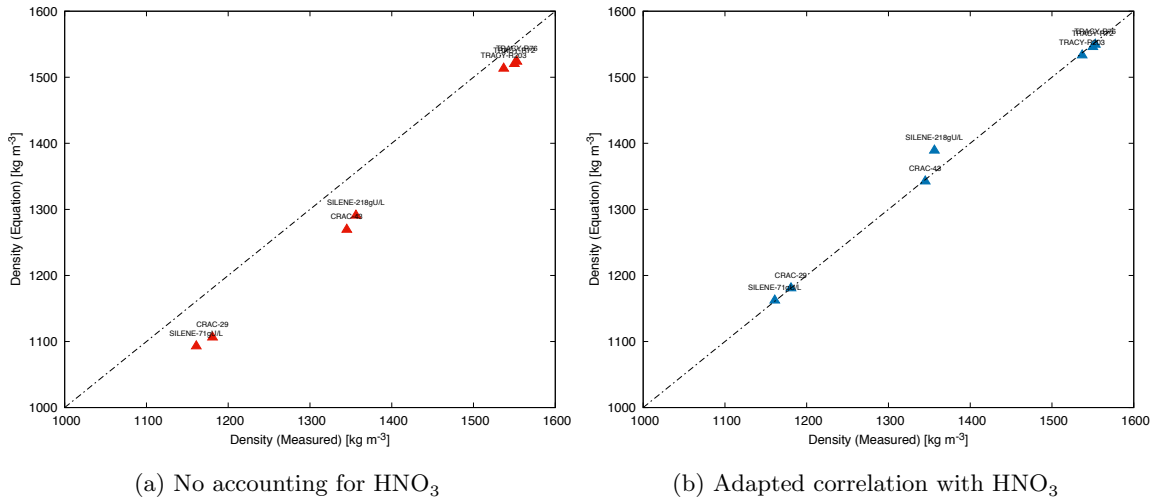


Fig. E.2. Comparison of measured solution densities from fissile solution experiments on CRAC, SILENE and TRACY with densities predicted using Equations E.1 and E.2.

Figure E.2a shows the difference between measured solution densities from fissile solution experiments on CRAC, SILENE and TRACY compared to values predicted using Equation E.1. Adding an additional term to the equation to adjust the predicted density for nitric acid concentration and adjusting the coefficient to minimise the error between measured and predicted density results in Equation E.2.

$$\begin{aligned} \rho(T, C_{\text{UrN}}, C_{\text{HNO}_3}) = & 0.31635C_{\text{UrN}} - 3.5898 \times 10^{-3}T^2 - 4.7024 \times 10^{-2}T \\ & + 3.4663 \times 10^{-2}C_{\text{HNO}_3} + 1001.0, \end{aligned} \quad (\text{E.2})$$

Figure E.2b shows the difference between measured and predicted densities using Equation E.2. The results show close agreement between the measured and predicted solution densities except for the SILENE 218 gU/L fuel solution which appears as an anomaly.

Experiment Name	Uranyl Nitrate Concentration	Nitric Acid Concentration	Temperature	Reported Density	Predicted Density
	mol m ⁻³	mol m ⁻³	°C	kg m ⁻³	kg m ⁻³
CRAC-29	344.3	2150	22.0	1180.8	1181.7
CRAC-43	858.7	2110	22.0	1345.0	1343.0
TRACY-R72	1655.1	740	24.99	1550.0	1550.4
TRACY-R76	1666.5	740	25.07	1553.1	1534.2
TRACY-R203	1632.8	580	25.01	1536.9	1546.8
SILENE (71 gU/L)	300.9	2000	20.0 [†]	1161.0	1163.1
SILENE (218 gU/L)	926.3	2840	20.0 [†]	1356.2	1390.1

TABLE E.I

Composition and density data for various reactor fuel solutions with predicted densities using Equation E.2. Measured data obtained from Barbry et al. (1973), Barbry (1994), Nakajima et al. (2002b) and Nakajima et al. (2002c). [†]Assumed value.

The solution compositions of the experimental reactor fuel solutions are shown in Table E.I. The data span a range of nitric acid concentrations from 580 to 2150 mol m⁻³ (excluding SILENE 218 gU/L). The close agreement between the measured and predicted densities over this range lends credibility to the assumption that nitric acid affects the solution density according to a linear relationship.

The uranyl nitrate concentrations shown in Table E.I are significantly higher than those of the solutions examined by Grant et al. (1948). The accuracy of the predicted solution densities for the CRAC, SILENE and TRACY fuel solutions therefore lends confidence in extrapolating the data of Grant et al. (1948) to higher concentrations.

It has not been possible to evaluate the influence of temperature on solution densities at uranyl nitrate concentrations higher than those examined by Grant et al. (1948) because the densities reported for the experimental reactor fuel solutions are all given at ambient conditions. In the absence of any experimental data, it will be assumed that the effect of temperature on the solution density is independent of the solution composition.